ABSTRACT

Title of Dissertation : INFRARED OPTICAL SENSOR FOR COMBUSTION DIAGNOSTICS USING WAVELENGTH MODULATION SPECTROSCOPY

Mohammadreza Gharavi, Doctor of Philosophy, 2004

Dissertation Directed By: Assistant Professor Steven G. Buckley
Department of Mechanical Engineering

In this dissertation, an optical sensor for combustion diagnostics, basedon near-infrared distributed feedback (DFB) tunable diode lasers, is developed. The sensor is implemented to perform simultaneous species and temperature measurements in a combustion system. The use of optical sensing allows non-intrusive measurements, which are useful particularly in systems sensitive to perturbations caused by external probes. The tunable diode laser sensor is based on absorption spectroscopy, where absorption of laser light by a particular rotational-vibrational absorption feature of a

molecule is related to the molecular concentration. In addition, based on absorption ratio of two particular absorption features of a molecule, temperature is determined.

A TDL sensor was designed, built, and tested in various conditions in the flame and a static cell for CH4 and H2O concentration and for temperature measurement. For high sensitivity, Wavelength Modulation Spectroscopy (WMS) was used. In general, quantification of WMS, particularly in combustion systems, requires detailed spectroscopic information of all absorption features probed by the sensor. Typical absorption features are often overlapped, and therefore measurement of spectroscopic information for individual transitions may be very difficult, or sometimes impossible. The lack of detailed spectroscopic information for the near-infrared transitions of interest, combined with the complexity of WMS technique itself, are the main issue for quantification WMS in combustion systems. In this dissertation, these problems and their solutions are discussed. Following a detailed theoretical study of WMS, new approaches and techniques for concentration and temperature measurement in combustion systems are developed.

INFRARED OPTICAL SENSOR FOR COMBUSTION DIAGNOSTICS USING WAVELENGTH MODULATION SPECTROSCOPY

By

Mohammadreza Gharavi

Dissertation submitted to the Faculty of the Graduate School of the
University of Maryland, College Park, in partial fulfillment
of the requirements for the degree of
Doctor of Philosophy
2004

Advisory Committee:
Assistant Professor Steven G. Buckley, Chairman/Advisor
Professor James M. Wallace
Professor Christopher C. Davis
Associate Professor Gregory S. Jackson
Assistant Professor Bao Yang

DEDICATION

To my wife Simin

ACKNOWLEDGEMENTS

I would like to thank my advisor Professor Steven Buckley for his great support and guidance and his patience during this research work. I would also like to thank the members of my committee for agreeing to be on my committee and for their diligence in reading this thesis. I would like to acknowledge the loving support of my parents. Finally, I would like to thank my wife, Simin, for her understanding, love, and encouragement.

TABLE OF CONTENTENTS

List of Tables ……..……... ix

List of Figures ……..……..…… xi

List of Symbols ….……...…….. xxii

1 Introduction …….....1

1.1 Motivation for use of IR diode-laser diagnostics ……... 2

1.2 Background ……. 3

1.3 Outline of the dissertation ……... 4

2 Theory of Absorption of Electromagnetic Waves by Molecules ……... 6

2.1 Postulates of quantum mechanics ……... 6

2.2 Important Stationary Energy States in Molecular Spectroscopy …… 9

2.2.1 Translational states ……...…….……. 10

2.2.2 Electronic states ……..…….…….. 11

2.2.2.1 Electronic states in atoms ……. 11

2.2.2.2 Electronic states in Molecules …….. 19

2.2.3 Rotational states …….. 21

2.2.3.1 Rotational states of a diatomic molecule …….. 21

2.2.3.2 Rotational states of a polyatomic molecule …….. 24

2.2.4 Vibrational states …… 26

2.2.4.1 Vibrational states for a diatomic molecule ……... 26

2.2.4.2 Vibrational states for a polyatomic molecule ……... 30

2.2.5 Total molecular energy state …….. 33

2.3 Interaction of weak electromagnetic radiation by a molecule …….. 33

2.3.1 Attenuation of radiation beam due to absorption and stimulated emission ……...……... 38

2.3.2 Pressure broadening …… 40

2.3.3 Temperature broadening ……. 42

2.3.4 Voigt line shape function …… 43

2.4 The Selection rules ……... 44

2.4.1 Selection rules for rotational and vibrational transitions …… 44

2.4.2 Selection rule for rotational vibrational absorption ……... 45

2.5 Vibrational-Rotational Spectrum …….. 47

2.6 Beer-Lambert Law …… 50

3 Techniques of Tunable Diode Laser Absorption Spectroscopy ……... 52

3.1 Direct absorption …….. 52

3.2 Wavelength Modulation ……... 56

3.3 Frequency Modulation …….. 58

3.4 Two-tone Frequency Modulation Spectroscopy ……... 66

4 Theory of Wavelength-modulation Spectroscopy ……...……..……71

4.1 Theory of wavelength-modulation spectroscopy …….. 71

4.2 Properties of the in-phase signal at the nth harmonic component, $I_{nf,p}(\bar{\nu})$ .. 81

4.2.1 Properties of $I_{nf,p}(\overline{\nu})$ in the absence of intensity modulation …….. 81

4.2.2 Properties of $I_{nf,p}(\overline{\nu})$ in the presence of intensity modulation …..…. 88

4.3 Methods for concentration and temperature measurement ……... 94

4.3.1 Method for concentration measurement ……. 94

4.3.2 Method for temperature measurement …… 95

4.4 Issues and solutions for concentration and temperature measurement in a combustion system using WMS ……... 98

4.5 Information required for quantification of WMS for combustion diagnostics ……... 100

5 Measurement of spectroscopic parameters of H_2O and CH_4 ……... 102

5.1 Theory of measuring spectroscopic parameters ……. 103

5.2 Measurement of CH_4 spectroscopic parameters ……. 105

5.2.1 Experimental details ……. 106

5.2.2 Line strength at room temperature ……... 109

5.2.3 Line strength at elevated temperature ……... 116

5.2.4 Pressure broadening calculation ……... 118

5.3 Measurement of H_2O spectroscopic parameters ……. 125

5.3.1 Experimental details ……. 126

5.3.2 Line strength measurement and temperature sensitivity of the transitions ……. 128

5.3.3 Pressure broadening calculations ……. 135

5.4 Approximate pressure broadening calculation for some quenching gases 142

6 Temperature and concentration measurements using the WMS sensor … 145

6.1 A Model for simultaneous temperature, CH_4 concentration, and H_2O concentration measurement in combustion systems ……... 145

6.1.1 Calculation of $\hat{I}_{2f}^{H2O}(\nu_I)$ vs.T and $R_{I,II}(T)$ vs.T correlations at optimum conditions …….. 151

6.1.2 Calculation of $\hat{I}_{2f}^{CH4}(\nu_0)$ vs.T correlation at optimum conditions 159

6.2 Comparison of the modeling and experiments ……... 160

6.3 Sensor architecture …….. 167

6.4 In-flame measurements ……... 169

7 Conclusion …….. 177

Appendix A1: A program for simulation of the second harmonic spectra of a Voigt profile when Doppler and Collisional half-width are known 180

Appendix A2: A program for simulation of the second harmonic spectra of the selected H_2O transitions ……... 182

Appendix A3: A program for simulation of the second harmonic spectra of the R(4) manifold of the $2\nu_3$ band of CH_4 …….. 188

Appendix B1: Some spectroscopic parameters of R(3) and R(4) manifolds of the $2\nu_3$ band of CH_4 …….. 192

Appendix B2: Some spectroscopic parameters of the selected H_2O transitions ….. 193

Appendix C: Design and building the Ring Interferometer ……..…… 194

Appendix D: Glass Cell and its accessories ……. 196

Appendix E: Absolute error analysis for linestrength S_T and pressure broadening coefficient γ …… 197

Appendix F: Measurement of amplitude of modulation and intensity-frequency Parameters ……... 201

Appendix G: Temperature correction of the thermocouple measurements for radiation loss ……. 205

References ……..…….. 207

LIST OF TABLES

Table 5.1: Individual line strengths of R(3) at T=296 K ……. 107

Table 5.2: Individual line strengths of R(4) at T=296 K ……. 108

Table 5.3: Variation of S_{tot} in R(3) with temperature …….. 117

Table 5.4: Variation of S_{tot} in R(4) with temperature …….. 117

Table 5.5: Variation of collisional half-width with temperature in R(3) manifold 122

Table 5.6: Variation of collisional half-width with temperature in R(4) manifold 122

Table 5.7: Temperature dependence of collisional broadening line width parameter *n* for different colliding gases. Uncertainty represents the standard deviation in the data …… 124

Table 5.8. Frequency spacing and line strengths at T=977 K (comparison between results of HITRAN 96 and measurement) …… 130

Table 5.9: Variation of collisional half-width with temperature in transition 1 and 2 …… 140

Table 5.10: Variation of collisional half-width with temperature in transition 3 … 140

Table 5.11: Temperature dependence of collisional broadening line width parameter *n* for different quenching gases ……... 142

Table B1.1: Vibrational quantum numbers of the $2\nu_3$ band of R(3) manifold of CH_4 absorption transitions (Extracted from HITRAN database) … 191

Table B1.2: Vibrational quantum number of the $2\nu_3$ band of R(4) manifold of CH_4 absorption transitions (Extracted from HITRAN database) … 191

Table B2.1: Global and local quanta index of the selected H_2O absorption transitions (Extracted from HITRAN database) …….. 192

LIST OF FIGURES

Figure 2.1: A particle confined in a box …… 10

Figure 2.2: The energy levels for a particle in a cube …… 11

Figure 2.3: Quantization of angular momentum *L* (left) and spin angular momentum *S* (right) along the direction of an electric field ……..... 16

Figure 2.4: The first few electronic states of atomic hydrogen ……. 18

Figure 2.5: Definition of the distances involved in the Hamiltonian operator for H_2^+ ……. 20

Figure 2.6a: Variation of energy, *E*, versus inter-nuclear distance, *R*, at ground electronic states for H_2^+ ……..…… 21

Figure 2.6a: A potential energy diagram of O_2 …….. 21

Figure 2.7: Two mass m_1 and m_2 shown rotating about their center of mass …… 22

Figure 2.8: The rotation of a single particle about a fixed point …… 23

Figure 2.9a: Two masses connected to a spring, which is a model used to describe the vibrational motion of a diatomic molecule ……. 27

Figure 2.9b: A mass connected to a wall by a spring …… 27

Figure 2.10: The energy states of a harmonic oscillator (dashed line) and anharmonic oscillator superimposed on a harmonic-oscillator potential and a more realistic internuclear potential ……. 29

Figure 2.11: Normal (vibrational) modes of H_2O ……. 32

Figure 2.12: Two-level system …….. 34

Figure 2.13: The function $F(\omega) = F(2\pi\nu) = \sin^2[(E_2 - E_1 - \hbar\omega)t/2\hbar]/(E_2 - E_1 - \hbar\omega)^2$ which represents the probability of making a $1 \rightarrow 2$ transition in the time interval 0 to t, plotted against frequency ω ……. 36

Figure 2.14: A system with dimension 1 m × 1 m × l m that contains N_0 and N_1 molecules per cubic meter with energies E_0 and E_1, respectively ……. 38

Figure 2.15: The phase of an oscillating dipole moment randomly interrupted by Collision …… 41

Figure 2.16: Interaction of a lane electromagnetic wave with a moving atom …….. 42

Figure 2.17: Normal modes of CO_2 ……... 45

Figure 2.18: The ro-vibrational spectrum of the $0 \rightarrow 1$ vibrational transition of HBr(g) …… 46

Figure 2.19: One of the Parallel band (left trace) and perpendicular band (right trace) in CO_2 ……. 46

Figure 2.20: A typical ro-vibrational transition ……. 49

Figure 2.21: The left graph shows the variation of population density in lower state energy with $J'' > 0$ in a diatomic molecule based on rigid rotor model. Right graph shows the spectrum of a diatomic molecule based on rigid rotor model (the transitions for all possible J'' are considered) ……... 49

Figure 2.22: A typical spectrum of a real diatomic molecule …… 50

Figure 3.1: Typical experimental setup used direct absorption ……. 53

Figure 3.2: Typical data processing used for quantification of direct absorption technique ……. 55

Figure 3.3. A typical experimental setup for wavelength-modulation spectroscopy ……. 56

Figure 3.4: Typical power spectrum of the modulated laser in FMS …… 62

Figure 3.5: The schematic of an experimental setup for FMS ……... 63

Figure 3.6: Output signal in frequency-modulation spectroscopy of Fabry-Perot resonance ……. 64

Figure 3.7: Spectral distribution of the laser field in two-tone frequency modulated diode laser at v_1 and v_2 with β =1.0 and M =0 ……. 67

Figure 3.8: Typical experimental arrangement for two-tone frequency modulation 70

Figure 4.1: Comparison power spectrum between FMS and WMS ……. 72

Figure 4.2: Amplitude of absorption and dispersion of the first harmonic signal as a function of normalized modulation frequency $x_m = f / \Delta\nu_{\text{line}}$ when FM index $\beta = \Delta\nu_m / f = 1$ ……. 72

Figure 4.3: Intensity variation of a typical diode laser as a function of optical frequency …….. 76

Figure 4.4: The functional block diagram of the Stanford Research SR830 lock-in amplifier which was used in this research ……... 78

Figure 4.5: The effect of variation of modulation index *m*, on the spectra of $I_{2f,p}(\bar{\nu})$ for a case of a Voigt line-shape function with $\Delta\nu_D = .05\,\text{cm}^{-1}$, $\Delta\nu_L = .05\,\text{cm}^{-1}$, $\psi = \theta = 0$, and no intensity modulation $(s_{F1} = s_{F2} = s_f = 0)$ ……... 82

Figure 4.6: In-phase signal, $I_{nf,p}(\bar{\nu})$ for the first four harmonic components for the case of a Voigt line-shape function with $\alpha(\nu_0) = .01$, $\Delta\nu_D = .05$ cm^{-1}, $\Delta\nu_L = .05$ cm^{-1}, m=1, $\psi = \theta = 0$, $K' = 1$, and no intensity modulation ($s_{F1} = s_{F2} = s_f = 0$) 83

Figure 4.7: The effect of detection phase on $I_{nf,p}$ 85

Figure 4.8: The effect of detection phase on in-phase signal $I_{nf,p}(\bar{\nu})$ for the case of a Voigt line-shape function with $\alpha(\nu_0) = .01$, $\Delta\nu_D = .05$ cm^{-1}, $\Delta\nu_L = .05$ cm^{-1}, m=1, $\psi = 0$, $K' = 1$, and no intensity modulation ($s_{F1} = s_{F2} = s_f = 0$) 86

Figure 4.9: The effect of modulation index, m, on the maximum of the in-phase signal $I_{2f,p}(\bar{\nu})$ for the case of a Voigt line-shape function with $\alpha(\nu_0) = .01$, $K' = 100$, and no intensity modulation ($s_{F1} = s_{F2} = s_f = 0$), with the optimum detection phase 87

Figure 4.10: The effect of modulation index, m, on the maximum of the in-phase signal $I_{2f,p}(\bar{\nu})$ assuming a Voigt line-shape function with $\alpha(\nu_0) = .01$, $K' = 100$, and no intensity modulation ($s_{F1} = s_{F2} = s_f = 0$), when the detection phase is not optimum 88

Figure 4.11: The effect of the two different mechanisms of intensity modulation on the spectra of $I_{2f,p}(\bar{\nu})$ 90

Figure 4.12: In-phase signal, $I_{nf,p}(\bar{\nu})$ for the first four harmonic components calculated with a Voigt line-shape function with $\alpha(\nu_0) = .01$, $\Delta\nu_D = .05\,\text{cm}^{-1}$ and $\Delta\nu_L = .05\,\text{cm}^{-1}$, m=1, $\psi = \theta = 0$, $K' = 1$, and intensity modulation parameters of ($s_{F1} = -1[1/\text{cm}^{-1}], s_{F2} = 0, s_f = -2[1/\text{cm}^{-1}]$) 91

Figure 4.13: The effect of detection phase on the $I_{2f,p}(\bar{\nu})$ spectra. The calculated results in this figure assume a Voigt line-shape function with $\alpha(\nu_0) = .01, K' = 1$, m=1, $\psi = -20\,\text{deg}$, $\theta = \theta_{\min} = 50\,\text{deg}, s_{F2} = 0$ ... 92

Figure 4.14: The effect of detection phase on in-phase signal $I_{nf,p}(\bar{\nu})$ for a signal with a Voigt line-shape function with $\alpha(\nu_0) = .01$, $\Delta\nu_D = .05\,\text{cm}^{-1}$ and $\Delta\nu_L = .05\,\text{cm}^{-1}$, m=1, $\psi = 0$, $K' = 1$, and linear intensity modulation ($s_{F1} = -1$, $s_{F2} = 0$, $s_f = -2$) 93

Figure 4.15: Second harmonic signal variation as a function of optical frequency for three some arbitrary overlapped absorption transitions 98

Figure 5.1: Line positions and strengths of the $2\nu_3$ band of CH_4 105

Figure 5.2: Schematic diagram of the experiment 107

Figure 5.3: From top to bottom: Ring interferometer signal, absorption signal for R(3), and absorption signal for R(4) 112

Figure 5.4: Measured room temperature (296 K) line strengths for each of the R(3) lines of CH_4, and total line strength at 296 K .....…….. 113

Figure 5.5: Measured room temperature (296 K) line strengths for each of the R(4) lines of CH_4, and total line strength at 296 K …… 114

Figure 5.6: Comparison between the experimental and fitted model results for R(3) transitions (upper trace) and R(4) transitions (lower trace) at room temperature (T=296 K) ……. 115

Figure 5.7: Comparison between the experimental and fitted model results for R(3) transitions (upper trace) and R(4) transitions (lower trace) at high temperature (T= 908 K) ……. 119

Figure 5.8: Collisional broadening half-width of CH_4 by N_2 for R(3) transitions as a function of pressure. Upper trace at room temperature (296 K), and lower trace at high temperature (860 K) ……. 120

Figure 5.9: Collisional broadening half-width of CH_4 by CO_2 for R(3) transitions as a function of pressure. Upper trace at room temperature (296 K), and lower trace at high temperature (908 K) ……. 120

Figure 5.10: Collisional broadening half-width of CH_4 by N_2 for R(4) transitions as a function of pressure. Upper trace at room temperature (296 K), and lower trace at high temperature (952 K) ……... 121

Figure 5.11: Collisional broadening half-width of CH_4 by CO_2 for R(4) transitions as a function of pressure. Upper trace at room temperature (296 K), and lower trace at high temperature (952 K) ……... 121

Figure 5.12: The temperature variation in broadening coefficient half-width of CH_4 by N_2 (top trace) and CO_2 (bottom race) for R(3) transitions ….. 123

Figure 5.13: The temperature variation in broadening coefficient half-width of CH_4 by N_2 (top trace) and CO_2 (bottom race) for R(4) transitions ….. 124

Figure 5.14: Schematic diagram of the experimental set up used to measure line strengths of H_2O ……... 128

Figure 5.15: Transmitted signal (I) and RI signal at different temperature and pressure conditions. The top figure was at T= 468 K, P_{H2O}=24.6 torr and the bottom was at T= 977 K, P_{H2O}=27.6 torr ……... 129

Figure 5.16: Measured and fitted results for H_2O absorbance corresponding to the data shown in Figure 2. The top figure was at T= 468 K, P_{H2O}=24.6 torr and the bottom was at T= 977 K, P_{H2O}=27.6 torr …… 131

Figure 5.17: Comparison between the measured line strengths and HITRAN results. Top trace shows (S_1+S_2) and the bottom trace illustrates S_3 ... 132

Figure 5.18: Comparison between the measured absorption ratio (S_1+S_2)/S_3, and HITRAN results …… 135

Figure 5.19: Measured and fitted results for H_2O absorbance at different pressure for calculating pressure broadening coefficient due to N_2 at T=483 K …… 136

Figure 5.20: Measured and fitted results for H_2O absorbance at different pressure for calculating pressure broadening coefficient due to N_2 at T=999 K …… 137

Figure 5.21: Collisional broadening half-width of H_2O transitions by N_2 as a function of pressure. Upper trace at room temperature (483 K), and lower trace at high temperature (999 K) …….. 138

Figure 5.22: Collisional broadening half-width of H_2O transitions by CO_2 as a function of pressure. Upper trace at room temperature (483 K), and lower trace at high temperature (860 K) …….. 139

Figure 5.23: The temperature variation in broadening coefficient half-width of H_2O by N_2 for transitions 1 and 2 (top trace) and transition 3 (bottom trace) ……..... 141

Figure 5.24: The temperature variation in broadening coefficient half-width of H_2O by CO_2 for transitions 1 and 2 (top trace) and transition 3 (bottom trace) ……... 141

Figure 6.1: Flow diagram of the main steps performed for quantification of the sensor for temperature and species measurement in combustion system with a multiplexed WMS sensor …… 146

Figure 6.2: Typical second harmonic signal of H_2O related to the selected H_2O transitions ……... 149

Figure 6.3: Typical second harmonic signal of CH_4 related to the selected CH_4 transitions …….. 149

Figure 6.4: Variation in $R_{I,II}$ vs. T curve at different modulation depths and optimum detection phase $\theta = 155^\circ$ for CH4/air flame with φ=1 …… 152

Figure 6.5: Calculated spectra of $\hat{I}_{2f}^{H2O}(\bar{\nu} - \nu_I)$ as a function of modulation depth, $\Delta\nu_m$, for CH_4/air flame with φ=1 at condition: T=500 K, $\theta = 155^\circ$ and optical path of L=10 cm …… 153

Figure 6.6: Calculated spectra of $\hat{I}_{2f}^{H2O}(\overline{\nu}-\nu_I)$ as a function of modulation depth, $\Delta\nu_m$, for CH_4/air flame with φ=1 at condition: *T*=2000 K, $\theta = 155^\circ$ and optical path of L=10 cm …… 154

Figure 6.7: The modeled effect of the 4th transition in $\hat{I}_{2f}^{H2O}(\overline{\nu}-\nu_I)$ on the third transition for a CH_4/air flame with φ=1 at $\Delta\nu_m = 0.09\ \text{cm}^{-1}$ ($\theta = 155^\circ$, and optical path L=10 cm) ……..…… 157

Figure 6.8: The modeled effect of the 4th transition in $\hat{I}_{2f}^{H2O}(\overline{\nu}-\nu_I)$ on the third transition for a CH_4/air flame with φ=1 at $\Delta\nu_m = 0.16\ \text{cm}^{-1}$ ($\theta = 155^\circ$, and optical path L=10 cm) ……... 157

Figure 6.9: Variation of $\hat{I}_{2f}^{H2O}(\nu_I)$ with temperature at two different modulation depths for a CH_4/air flame with φ=1, at detection phase of $\theta = 155^\circ$ and optical path of L=10 cm …….. 158

Figure 6.10: Variation of $\hat{I}_{2f}^{CH4}(\nu_0)$ with temperature at three different modulation depths for a CH_4/air flame with φ=1, at detection phase of $\theta = 140^\circ$ and an optical path of L=10 cm ……... 159

Figure 6.11: Calculated spectra of $\hat{I}_{2f}^{CH4}(\overline{\nu}-\nu_0)$ for R(4) transitions at T=500 and 2000 K for a CH_4/air flame with φ=1, at condition: $\theta = 140^\circ$ and optical path of L=10 cm …… 160

Figure 6.12: Comparison between measured and calculated 2f spectra of the selected H_2O absorption transitions for a mixture of N_2-H_2O in the gas cell …… 161

Figure 6.13: Comparison between measured and calculated 2f spectra of the selected H_2O absorption transitions for a mixture of CO_2-H_2O in the gas cell ……... 162

Figure 6.14: Comparison between measured and calculated 2f spectra of the selected H_2O absorption transitions for pure H_2O vapor in the gas cell ……. 163

Figure 5.15: Comparison between a set of (T , $R_{I,II}$) measured by experiment in the gas cell and corresponding values calculated by the modeling results ……... 164

Figure 6.16: Comparison between measured and calculated 2f spectra of the selected CH_4 absorption transitions, R(4), for a known CH_4-N_2 mixture in the gas cell …….. 166

Figure 6:17: Schematic of the sensor architecture ……... 168

Figure: 6.18: Simplified Figure of the setup of the in-flame measurement ……..… 170

Figure 6.19: Pre-calculated correlations, $\hat{I}_{2f}^{H2O}(\nu_I)$ vs.T , $\hat{I}_{2f}^{CH4}(\nu_0)$ vs.T , and $R_{I,II}$ vs.T , for the CH_4/air flame with φ=1.70. The 2f signals are normalized by the 1f signal at the central absorption frequencies ….... 172

Figure 6.20: Calculation of K by comparing the measured second harmonic signal at know temperature and concentration in the gas cell and calculated second harmonic signal with unit gain ……... 173

Figure 6.21: Temperature variation at different height above the burner surface using the optical sensor ……... 174

Figure 6.21: Variation of the H_2O and CH_4 concentrations at different heights above the burner surface using the optical sensor …….. 175

Figure C.1: Schematic of the ring interferometer …… 193

Figure D.1: From top to bottom: Glass Cell and heater assembly, heater dimensions, and Glass Cell and its accessories dimensions ……. 195

Figure F.1: Ring interferometer signal of the H_2O laser when it is modulated around ν_{II}=6771.47 cm^{-1} at f=10 kHz …… 201

Figure F.2: Ring interferometer signal of the H_2O laser when it is modulated around ν_{II}=6771.47 cm^{-1} at F=10 Hz ……..……... 202

LIST OF SYMBOLS

$\psi(\vec{r})$	Time-independent Wave function
$\psi^*(\vec{r})$	Complex conjugate of $\psi(\vec{r})$
$\hat{H}$	Hamiltonian operator
h	Plank's constant
$V(x,y,z)$	Potential energy at location (x,y,z)
m	Mass of a particle
$\hat{A}$	Operator
ψ_n	Eigenfunctions of $\hat{A}$
a_n	Eigenvalues of $\hat{A}$
E_n	Eigenvalues of Hamiltonian operator
$\langle a \rangle$	Average value of the observable corresponding to $\hat{A}$
$\Psi(\vec{r},t)$	Time-dependent wave function
t	Time
n_x, n_y, n_z	Quantum numbers of a particle confined in a box
$\psi_{n_x n_y n_z}$	State functions of a particle confined in a box
$E_{n_x n_y n_z}$	Ttranslational energy states of a particle confined in a box
Z	Number of protons in a nucleolus
N	Number of electrons in a atom/molecule, number of atoms in a molecule
m_e	Mass of electron

e	Electrical charge of electron
$\vec{r}_j$	Position of electron j in a molecule
$G_j(\vec{r}_1, \vec{r}_2, \ldots, \vec{r}_z)$	Potential energy of electron j due to presence of electron 1 at position $\vec{r}_1$, electron 2 at position $\vec{r}_2$,… and electron z at position $\vec{r}_z$
n	Priciple quantum number
l	Angular quantum number
m_l	Magnetic quantum number
m_s	Spin quantum number
L	Magnitude of the orbital angular momentum of electron, length, optical path
S	Magnitude of the spin angular momentum of electron
E	Energy of electron
σ	Spin variable, absorption cross section
$\alpha(\sigma)$	Spin eigenfunctions corresponding to m_s= 1/2
$\beta(\sigma)$	Spin eigenfunctions corresponding to m_s= -1/2
$\Psi(\vec{r}, \sigma)$	Spin orbital wavefunctions
ω	Angular velocity
I	Moment of inertia, radiation intensity
μ	Reduced mass
J	Rotational quantum number
g	Degeneracy in energy level
$\tilde{A}, \tilde{B}, \tilde{C}$	Rotational constants
$\tilde{D}$	Centrifugal distortion constant

k	Spring constant
ν	Fundamental vibrational frequency, optical frequency
υ	Vibrational quantum number
$\tilde{x}_e$	Anharmonicity constant
$\vec{\mu}$	Net dipole moment of a moleucule
$P_{1\leftarrow 0}$	Probability of absorption which causes transition from state 0 to state 1
μ_{10}	Transition dipole moment between states 0 and 1
$\rho(\nu)$	Radiation density
$B_{1\leftarrow 0}$	Einstein coefficient for absorption
$B_{1\rightarrow 0}$	Einstein coefficient of stimulated emission
c	Speed of light in vaccum
N_j	Population density at state j
F	Neutron flux, ramp (saw tooth) frequency
$g(\nu-\nu_0)$	Line-shape function
$\vec{\mathrm{M}}$	Dipole moment of a system
T_2	Average time between collisions
$\Delta\nu_L$	Collisional (Lorentzian) half-width
$\vec{\mathbf{v}}$	Velocity
$\vec{\mathbf{k}}$	Wave vector
$g_L(\nu-\nu_0)$	Lorentzian line-shape function (related to collisional effect)
$g_D(\nu-\nu_0)$	Gaussian line-shape function (related to Doppler effect)

T	Temperature
M	Molecular weight, AM index
$\Delta\nu_D$	Doppler half-width
$g_V(\nu-\nu_0)$	Voigt line-shape function
$Q(T)$	Partition function at temperature T
k_B	Boltzmann constant
$k(\nu)$	Absorption coefficient
P_{abs}	Partial pressure of absorbing species
$\phi(\nu-\nu_0)$	Line-shape function
$S(T)$	Line strength
N_L	Loschmidt's number
E''	Lower-state energy level
f	Oscillator strength, modulation frequency
I_{nf}	n^{th} harmonic signal
$H_2(\nu-\nu_0)$	Second harmonic component of the modulated normalized line-shape (with a maximum of 1.0)
α_0	Maximum absorbance (absorbance at the central absorption frequency)
$I_{2f,max}$	Peak of the second harmonic signal
ω_m	Modulation angular frequency
f_m	Modulation frequency
ω_0	Laser carrier angular frequency
β	FM index

ψ	Phase difference between intensity/amplitude and frequency modulation
$E(t)$	Amplitude of electric field
T_n	Complex transmission function
η_n	Refractive index at $\omega_0 + n\omega_m$
α_n	Absorbance at $\omega_0 + n\omega_m$
δ_n	Amplitude attenuation at $\omega_0 + n\omega_m$
ϕ_n	Optical phase shift at $\omega_0 + n\omega_m$
Ω	Intermediate frequency
i(t)	Diode laser injection current
$\bar{\nu}$	Laser center frequency
s_{F1}, s_{F2}	Intensity-frequency parameters at saw tooth frequency F
s_f	Intensity-frequency parameter at modulation frequency f
Δi	Amplitude of current modulation
ΔI	Amplitude of intensity modulation
$\bar{I}$	Average intensity
$\Delta \nu_m$	Amplitude of frequency of modulation
K	Opto-electrical gain
$I_D(\nu)$	Photodetector signal
θ	Detection phase
$I_{nf,p}(\bar{\nu})$	nth harmonic of the in–phase signal
γ_i	Pressure broadening coefficient

y_i	Mole fraction of species *i*
$\hat{I}_{2f}$	Normalized second harmonic signal
$R_{I,II}$	Ratio of two absorption peaks of the H_2O selected transition

1 Introduction

In this dissertation, an optical sensor based on near-infrared distributed feedback (DFB) tunable diode lasers for combustion diagnostics is developed. The sensor is implemented to perform simultaneous species and also temperature measurements in a combustion system. The use of optical sensing allows for a non-intrusive measurement, which is very important for systems sensitive to perturbations caused by external probes. The sensor is based on absorption spectroscopy, where absorption of laser light by a particular rotational-vibrational absorption feature of a molecule is related to the molecular concentration. In addition, based on absorption ratio of two particular absorption features of a molecule, temperature is calculated.

In this dissertation, a sensor based on absorption spectroscopy was designed, built, and tested in various conditions in the flame and a static cell for CH_4 and H_2O concentration and for temperature measurement. For high sensitivity, Wavelength Modulation Spectroscopy (WMS) was used. In general, quantification of WMS technique, particularly in combustion systems, requires detailed spectroscopic information of all absorption features probed by the sensor. Usually many absorption features are overlapped, and therefore measuring spectroscopic information of individual transitions may be very difficult, or sometimes impossible. The lack of detailed spectroscopic information for the near-infrared transitions of interest, combined with the complexity of WMS technique itself are the main issue for quantification WMS in combustion systems. In this dissertation, the problems and

also their solutions will be discussed. Following a detailed theoretical study of WMS technique explained in this dissertation, new approaches and techniques for concentration and temperature measurement in combustion systems developed herein are presented.

For temperature and H_2O concentration measurement, a set of H_2O transitions with significant variation in line strength ratio with temperature, accessible by a single tunable diode laser within the telecommunication S band operating around 1477 nm, has been identified. The main spectroscopic properties of H_2O absorption lines of the selected transitions, including absorption line strengths and pressure broadening parameters, with respect to the most important combustion species such as CO_2, O_2, N_2, CH_4, and H_2O, were measured. For CH_4 measurement a distributed feedback laser operating around 1650 nm suitable for measuring R(3) and R(4) transitions of $2\nu_3$ rotational-vibrational band of CH_4 was used. For these transitions also all important spectroscopic properties required for WMS quantification, including line strengths and broadening coefficients at different temperatures were measured. The measured properties then used in a high-temperature model for flame measurement.

1.1 Motivation for use of IR diode-laser diagnostics

The need for real-time and *in-situ* measurements for process control in combustion systems is primary motivated for this work. Also, for emission control and theoretical study of combustion physics the need for fast and sensitive methods of combustion diagnostics is well recognized. Non-intrusive and non-perturbing

methodologies may enhance both the speed and accuracy of a diagnostic method. In addition, since combustion processes generally deal with harsh environments, the capability of remote control is another parameter which important for sensor selection. And finally, cost may be a significant factor in the choice of a sensor. All the aforementioned requirements can be realized in IR diode-laser sensors. DFB lasers and related components, which are used in telecommunication systems, are among the best options for combustion diagnostics sensors. High speed current modulation, for absorption measurements on many species using strong ro-vibrational transitions in the infrared, yields great potential for fast and sensitive measurement. Also, the availability of fiber pigtailed lasers and related optical fiber components allows us to use them for remote sensing and control. In addition, because of massive investment by the telecommunication industry (Steele 1997) DFB lasers, IR detectors, and all related products, for optical design and signal processing, are relatively accessible and inexpensive.

As will be discussed later, there are different techniques of modulations and analysis for Tunable Diode Laser Absorption Spectroscopy (TDLAS), which can be used for combustion diagnostics. Among these techniques, wavelength modulation is considered to be the best method in which a simple hardware design and the capability of fast measurements are combined with highly sensitive measurements.

1.2 Background

The use of diode laser for species measurement began shortly after the demonstration of direct current injection semiconductor lasers in the late 1960s. The

first atmospheric measurement was realized in 1975 by employing a long open path (Ku and Hinkley 1975; Henkley 1976) and this technique is still used today. In 1977, diode lasers found application to *in-situ* combustion diagnostics (Hanson, Kuntx et al. 1977). Since that time much research has been conducted to apply diode laser spectroscopy for combustion measurements. Today, diode lasers are common measurement tools, used for sensitive laboratory-based spectroscopic measurements in the post flame region and for remote sensing and atmospheric measurements (CHou, Baer et al. 1997; Milhalcea, Baer et al. 1997; Nelson 1998). Advances in detection methods (e.g. wavelength modulation spectroscopy, one- and two-tone frequency modulation spectroscopy) over the past decade have greatly increased the sensitivity of diode laser absorption spectroscopy measurements (Reid and Labrie 1981; Lenth, Ortiz et al. 1982; Pokrowsky, Zapka et al. 1983; Cooper and Gallagher 1985; Janik, Carlise et al. 1985; Whittaker, Shum et al. 1988; Bomse, Silver et al. 1992; Feher and Martin 1995; Avetisov and Kauranen 1996).

1.3 Outline of the dissertation

In the second chapter, the theory of absorption of electromagnetic waves by molecules is discussed. In this chapter at the beginning, different electronic states of a molecule based on quantum mechanics are explained. Then absorption of electromagnetic radiation by molecules, which causes molecules to go to different energy states, based on simple semi-classical theory is explained. Following that, Beers's law, which is the main governing equation in absorption spectroscopy, will be derived. In this chapter, the physical meaning of spectroscopic properties of a

molecule including, rotational-vibrational energy states and spectra, absorption line strength, line-shape function, etc. has been outlined.

Third chapter reviews different techniques of absorption spectroscopy using tunable diode laser; measurement methods including direct absorption, wavelength modulation, and also frequency modulation are briefly explained. In the fourth chapter, detailed theory of a model developed for this work, based on Wavelength Modulation Spectroscopy (WMS) for temperature and concentration measurement suitable for combustion diagnostics is explained. The measurement of spectroscopic parameters required for quantification of the sensor data, for combustion measurements, is discussed in the fifth chapter. In the sixth chapter, the sensor architecture, experimental results and also the data processing models developed in this research are presented and discussed. And finally the seventh chapter summarizes all important results and new findings in this dissertation.

2 Theory of Absorption of Electromagnetic Waves by Molecules

In this chapter the physical phenomena of absorption of electromagnetic waves by gas-phase molecules (particularly in the gas) will be discussed. The materials covered in this chapter, are mainly extracted from (McQuarrie and Simon 1997) and (Bernath 1995) and are presented such that the physics behind the absorption phenomena is better understood. At the beginning of this chapter, I will review some aspects of quantum-mechanics that form the basis for absorption theory. For example, different quantized modes of energy storage leading to observed spectroscopic transitions of molecules, including translational, electronic, vibrational, and rotational transitions will be briefly explained. Following this, the process of absorption of electromagnetic waves by molecules which leads to the so-called "selection rules" governing transitions will be reviewed. Finally, based on these development, the Beer-Lambert Law, which is the key equation for absorption spectroscopy, will be discussed. The material covered in this chapter will enable a basic understanding of some important spectroscopic properties, such as the transition line strength, line shape, absorption spectra, partition function, etc.

2.1 Postulates of quantum mechanics (McQuarrie and Simon 1997)

Based on the first postulate of quantum mechanics, the quantum-mechanical state of a closed system, meaning an isolated system or a system which does not interact with an external field, is completely specified by a wave function $\psi(\vec{r})$,

which depends on the coordinate of the particle in the system. As in classical mechanics, the state of a system at particular time is determined by the position of a particle, and its velocity or momentum at that time. Based on the first postulate, the wave function has the important property that $\psi(\vec{r})\psi^*(\vec{r})dxdydz$ is the probability that the particle lies in the volume element *dxdydz* at position $\vec{r}$, where $\psi^*(\vec{r})$ is the complex conjugate of $\psi(\vec{r})$.

According to the second postulate, to every observable (a measurable dynamic variable such as energy, momentum, and etc.) in classical mechanics there corresponds a linear operator in quantum mechanics. For instance, the quantum-mechanical operator for the energy, which is called Hamiltonian operator $\hat{H}$, is defined as:

$$\hat{H} \equiv -\frac{\hbar^2}{2m}\left(\frac{\partial^2}{\partial x^2}+\frac{\partial^2}{\partial y^2}+\frac{\partial^2}{\partial z^2}\right)+V(x,y,z) \equiv -\frac{\hbar^2}{2m}\nabla^2+V(x,y,z) \qquad (2.1)$$

where *m* is the mass of the particle and $\hbar = h/2\pi$, in which *h* is plank's constant, and *V*(*x*,*y*,*z*) is the potential energy of the particle in the system.

According to the third postulate, in any measurement of the observable associated with the operator $\hat{A}$, the only values that will ever be observed are the eigenvalues a_n, which satisfy the following equation,

$$\hat{A}\psi_n = a_n\psi_n \qquad (2.2)$$

For example, the quantum-mechanical operator corresponding to the energy is the Hamiltonian operator $\hat{H}$, which is defined in (2.1). Therefore, based on the third

postulate, the only measurable energies of a particle with mass m and potential energy of $V(x,y,z)$ will be the eigenvalues of the following equation:

$$-\frac{\hbar^2}{2m}\nabla^2\psi + V(x,y,z)\psi = E\psi \qquad (2.3)$$

Equation (2.3) represents the time-independent Schrödinger equation. The eigenvalues of this equation, E_n, will be the only possible energies that we can experimentally measure. One of the properties of Hamiltonian operator is that if it can be written as a sum of independent terms, the total wave function will be a product of individual wave functions and the energy will be a sum of independent energies.

Also, based on the fourth postulate of quantum mechanics, if a system is in a state described by a wave function ψ, then the average value of the observable corresponding to $\hat{A}$ is given by

$$\langle a \rangle = \int_{all\ space} \psi^* \hat{A}\, \psi\ dxdydz \qquad (2.4)$$

The fifth postulate of quantum mechanics specifies the variation of wave function of a system with time. It states, the wave function, or state function, of a system evolves in time according to time-dependent Schrödinger equation

$$\hat{H}\Psi(\vec{r},t) = i\hbar\frac{\partial\Psi(\vec{r},t)}{\partial t} \qquad (2.5)$$

if the operator $\hat{H}$ dos not contain time explicitly, we can write the wave function $\Psi(\vec{r},t)$ as $\Psi(\vec{r},t) = \psi(\vec{r})\, f(t)$ (2.6)

in which $\psi(\vec{r})$ is the spatial wave function obtained from (2.3). Doing the separation of variables as in (2.6) we can directly calculate *f(t)* and therefore relate $\Psi(\vec{r},t)$ and $\psi(\vec{r})$ by

$$\Psi(\vec{r},t) = \psi(\vec{r})e^{-iEt/\hbar} \qquad (2.7)$$

It should be stressed here Equation (2.7) is only valid for closed, stationary system, where the operator $\hat{H}$ dose not depend on time.

The time-independent Shrödinger Equation (2.3) can be used for calculating the stationary states in a closed system such as atoms or molecules; however, Equation (2.5) is applied for a system undergoing external interaction. For example, the interaction of an external electromagnetic field with molecules could be studied using the time-independent Schrödinger equation.

2.2 Important Stationary Energy States in Molecular Spectroscopy (McQuarrie and Simon 1997)

As was mentioned above, the stationary states of a closed system can be obtained from the time-independent Schrödinger Equation (2.3). Based on the geometry, potential energy, and the boundary conditions of a given system, Equation (2.3) can (in principle) be solved. The solution of Equation (2.3) will be a set of eigenfunctions ψ_n, corresponding to eigenvalues E_n. Based on the third postulate of quantum-mechanics, the only observable energy for the system will be E_n. Using the forth postulate, one can also show that the variance of the energy, E_n, will be zero, indicating that the only measurable value is E_n. In the following, the energy levels E_n of some important systems in molecular spectroscopy are explained.

2.2.1 Translational states

If Equation (2.3) is applied to a molecule (or any other particle) with mass *m* confined in a rigid cubic box (container) with the dimensions of *a* (Figure 2.1), translational energy states $E_{n_x n_y n_z}$, and state functions $\psi_{n_x n_y n_z}$, which are the eigenvalues and eigenfunctions of (2.3) respectively, will be calculated by

$$E_{n_x n_y n_z} = \frac{h^2}{8ma^2}(n_x^2 + n_y^2 + n_z^2) \qquad n_x, n_y, n_z = 1,2,\ldots$$
$$\psi_{n_x n_y n_z} = \left(\frac{8}{a^3}\right)^{1/2} \sin\frac{n_x \pi x}{a} \sin\frac{n_y \pi y}{a} \sin\frac{n_z \pi z}{a} \qquad (2.8)$$

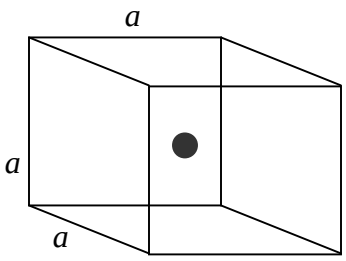

Figure 2.1: A particle confined in a box.

The combinations of n_x, n_y, and n_z corresponding to allowed translational energy states of a molecule in the box, based on Equation (2.8) are shown in Figure 2.2.

For each set of n_x, n_y, and n_z, there is a corresponding wave function $\psi_{n_x n_y n_z}$, which specifies the translational state of the molecule in the box. Different states (different state functions) which have the same energy are called *degenerate states*.

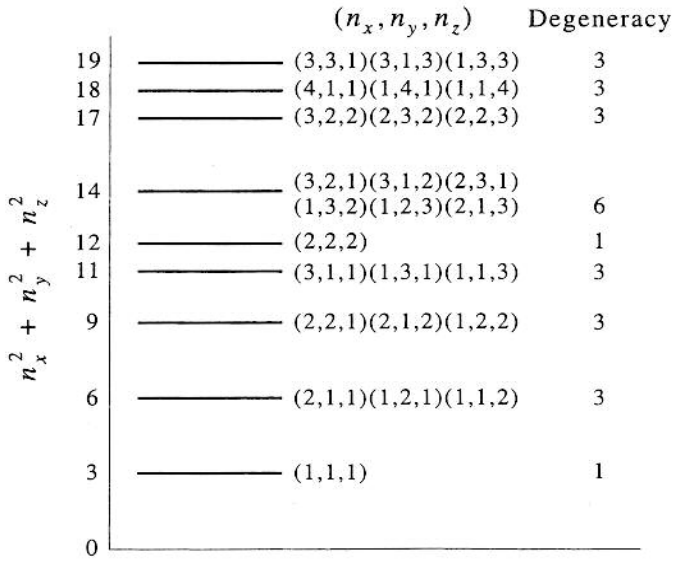

Figure 2.2: The energy levels for a particle in a cube. The degeneracy of each level is also indicated from (McQuarrie and Simon 1997).

2.2.2 Electronic states

The electronic states of a molecule are based on the electronic states of the constituent atoms, hence the electronic states of atoms are discussed as a prelude to discussion of molecular electronic states.

2.2.2.1 Electronic states in atoms

Assume an atom with Z protons in a fixed nucleus (zero kinetic energy) contains Z electrons which are around the nucleus. Using the time-independent Schrödinger equation, the energy of the atom can be obtained from

$$\left(-\frac{\hbar^2}{2m_e}\nabla_1^2-\frac{\hbar^2}{2m_e}\nabla_2^2-\cdots-\frac{\hbar^2}{2m_e}\nabla_z^2\right)\psi(\vec{r}_1,\vec{r}_2,\ldots,\vec{r}_z)+$$
$$\left(-\frac{Ze^2}{4\pi\varepsilon_0 r_1}-\frac{Ze^2}{4\pi\varepsilon_0 r_2}-\cdots-\frac{Ze^2}{4\pi\varepsilon_0 r_z}\right)\psi(\vec{r}_1,\vec{r}_2,\ldots,\vec{r}_z)+ \qquad (2.9)$$
$$\left[G_1(\vec{r}_1,\vec{r}_2,\ldots,\vec{r}_z)+G_2(\vec{r}_1,\vec{r}_2,\ldots,\vec{r}_z)+\cdots+G_z(\vec{r}_1,\vec{r}_2,\ldots,\vec{r}_z)\right]\psi(\vec{r}_1,\vec{r}_2,\ldots,\vec{r}_z)$$
$$=E\psi(\vec{r}_1,\vec{r}_2,\ldots,\vec{r}_z)$$

In Equation (2.9), m_e is the mass of electron and ∇_j^2 is the Laplacian operator with respect to the position of the electron j coordinates. The term $Ze^2/4\pi\varepsilon_0 r_j$ represents potential energy of electron j with respect to the nucleus, and $G_j(\vec{r}_1,\vec{r}_2,\ldots,\vec{r}_z)$ is the potential energy of electron j due to presence of electron 1 at position $\vec{r}_1$, electron 2 at position $\vec{r}_2$,… and electron z at position $\vec{r}_z$ (inter-electronic repulsion). By solving equation (9) and finding the eigenvalues, one finds the all possible electronic energy states of the atom. Except for hydrogen-like atoms (atoms with Z protons in nucleus and one electron in orbital), this equation can not be solved analytically. However, if the effect of the interelectronic repulsion $G_j(\vec{r}_1,\vec{r}_2,\ldots,\vec{r}_z)$, is ignored, Equation (2.9) can be simplified as

$$\psi(\vec{r}_1,\vec{r}_2,\ldots,\vec{r}_z)=\psi(\vec{r}_1)\psi(\vec{r}_2)\ldots\psi(\vec{r}_z) \qquad (2.10)$$

where, $\psi(\vec{r}_j)$ is wave function of electron j in the hydrogen-like atom. In fact, $\psi(\vec{r}_j)$ is the eigenfunction of

$$-\frac{\hbar^2}{2m_e}\nabla_j^2\psi(\vec{r}_j)+\frac{Ze^2}{4\pi\varepsilon_0 r_j}\psi(\vec{r}_j)=E_j\psi(\vec{r}_j) \qquad (2.11)$$

Solving Equation (2.11) yields the energy levels and also wavefunctions of all possible states that one electron in a hydrogen-like atom can have. In fact, there is an analytical solution for Equation (2.11). The eigenfunctions of this equation, which specifies the state functions (wave functions) of the electron in hydrogen-like atom, depend upon three different quantum numbers (similar to those quantum numbers for translational states of the particle in the box). These quantum numbers are principal quantum number n, angular quantum number l, and magnetic quantum number m_l. Based on the solution of Equation (2.11), these quantum numbers can only have certain values as shown in (2.12), which completely specify the state function of the electron for a particular energy state.

$$\begin{aligned} &n = 1,\ 2,\ \ldots \\ &l = 0,\ 1,\ 2,\ \ldots,\ n-1 \\ &m_l = -l,\ -l+1,\ \ldots,\ 0,\ 1,\ \ldots,\ l-1,\ l \end{aligned} \tag{2.12}$$

Here, n represents the orbits in which the electron can be found around the atom nucleus. l is used to calculate L, the magnitude of the orbital angular momentum of the electron, given by

$$L = \hbar\sqrt{l(l+1)} \tag{2.13}$$

The Z component of the orbital angular momentum of the electron is determined by m_l through Equation (2.14).

$$L_z = m_l\hbar \tag{2.14}$$

where Z is the direction of the electric field the axis. Based on the solution of equation (2.11), the electron in hydrogen-like atom can have energies given only by

$$E = -\frac{Z^2 m_e e^4}{32\pi^2 \varepsilon_0^2 \hbar^2 n} \qquad (2.15)$$

which shows that the energy of the electron for the hydrogen-like atom, only depends on principal quantum number *n*. This means that all states with same *n* but different *l* and m_l are degenerate.

Briefly, the solution of Equation (2.11) gives us some important information about the property of the electron in the hydrogen-like atom, indicating that the electron can have only certain energies and orbital angular momenta while it is confined in the atom. In other words, the magnitude of the energy and orbital angular momentum of the electron are quantized. Also the direction of the orbital angular momentum of the electron is quantized.

Equation (2.15) agrees very well with experiments for hydrogen-like atoms. As discussed above, for multi-electronic atoms, if the inter-electronic repulsion terms $G_j(\vec{r}_1, \vec{r}_2, \ldots, \vec{r}_z)$, in Equation (2.9) were negligible, we could use Equation (2.10) to calculate wave functions $\psi(\vec{r}_j)$ and energy states E_j of each electron. If that was the case, the energy states of each electron in a multi-electron atom could be found from Equation (2.15), and also the total electronic energy states of the atom could be found from:

$$E = \sum_{j=1}^{Z} E_j = -Z\frac{Z^2 m_e e^4}{32\pi^2 \varepsilon_0^2 \hbar^2 n} \qquad (2.16)$$

It turns out that Equation (2.16) does not agree with experiment. For example, the electronic ground state energy (*n*=1) for helium atoms is overestimated by 38% using Equation (2.16), indicating that the inter-electronic repulsion term $G_j(\vec{r}_1, \vec{r}_2, \ldots, \vec{r}_z)$ in

Equation (2.9) makes a significant contribution in the total potential energy and cannot be neglected. This means that the simplified form of the state function suggested by equation (2.10) is not valid for multi-electron atoms. Hence, to solve Equation (2.9), we must resort to approximate methods. Fortunately, different approximation methods (e.g. perturbation theory and variational method, etc.) have been used and these methods can yield extremely good results.

Although the Schrödinger equation is quite successful in predicting or explaining the results of the most experiments, it can not explain a few phenomena, such as doublet yellow line in the atomic spectrum of sodium. In this regard, in addition to the three quantum numbers obtained directly from the solution for hydrogen-like atoms, it was suggested by Goudsmit and Uhlenbeck that an electron behaves like a spinning top, contributing its own z components of spin angular momentum. This electronic angular momentum is quantized into two ("up" or "down") values of $\pm \hbar / 2$ and motivate the fourth quantum number m_s, which is called spin quantum number and can only be $\pm 1/2$ for each electron. Thus the spin quantum number m_s, is used to calculate the z component of the spin angular momentum S_z by

$$S_z = m_s \hbar \quad , \; m_s = 1/2, \; -1/2 \qquad (2.17)$$

Therefore the magnitude of spin angular momentum S, similar to orbital angular momentum, is

$$S = \sqrt{s(s+1)} = \frac{\sqrt{3}}{2}\hbar \quad , \; s = 1/2 \qquad (2.18)$$

Figure (2.3) shows examples of the z components of the orbital and spin angular momenta.

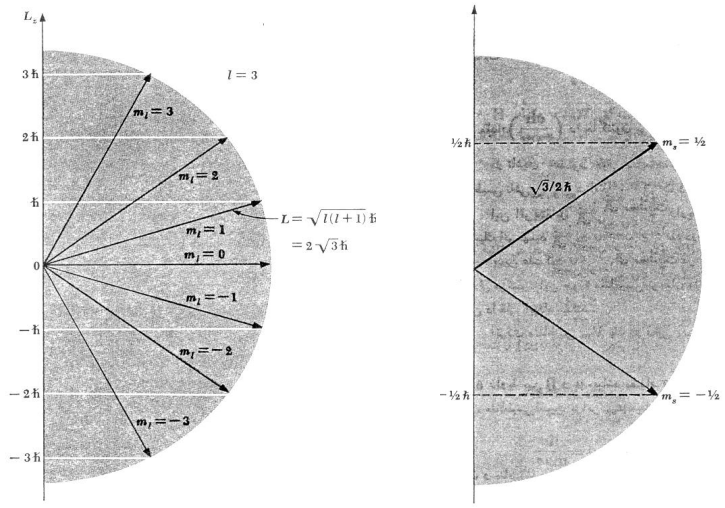

Figure 2.3: Quantization of angular momentum *L* (left) and spin angular momentum *S* (right) along the direction of an electric field.

Based on the spin angular momentum, the one-electron wave function also includes the spin function and it is postulated that the spatial and spin parts of its wave function are independent and therefore the wave function is defined by

$$\Psi(\vec{r},\sigma) = \psi(\vec{r})\alpha(\sigma) \qquad or \qquad \Psi(\vec{r},\sigma) = \psi(\vec{r})\beta(\sigma) \qquad (2.19)$$

in which σ is spin variable, $\alpha(\sigma)$ and $\beta(\sigma)$ are (orthogonal) spin eigenfunctions corresponding to m_s= 1/2 and -1/2 respectively. The spatial and also the complete form of one-electron wave functions $\psi(\vec{r})$ and $\Psi(\vec{r},\sigma)$ are called *orbital* and *spin orbital* wavefunctions, respectively.

As explained above, the spin orbital wavefunction for each electron in an atom depends on four quantum numbers *n*, *l*, m_l, and m_s. Based on *Pauli Exclusion*

Principle, no two electrons in an atom can have the same values of all four quantum numbers. Using this postulate and also the fact that electrons are indistinguishable, the wave function of an atom containing N electrons is usually specified by

$$\Psi(1,\ 2,\ \ldots,\ N) = \frac{1}{\sqrt{N!}}\begin{vmatrix} \varphi_1(1) & \varphi_2(1) & \cdots & \varphi_N(1) \\ \varphi_1(2) & \varphi_2(2) & \cdots & \varphi_N(2) \\ \vdots & \vdots & \vdots & \vdots \\ \varphi_1(N) & \varphi_2(N) & \cdots & \varphi_N(N) \end{vmatrix} \qquad (2.20)$$

where φ's in Equation (2.20) are spin orbitals. Based on *Pauli Exclusion Principle*, all φ's are different; otherwise, the wave function of the atom will be zero.

Each φ_i in Equation (2.20) is dependent on a set of quantum numbers n, l, m_l, and m_s and also depends on the inter-electronic repulsions. As a result, for each electron the wave function can be written as a function of the quantum numbers as

$$\varphi_i = \varphi(n_i, l_i, m_{l_i}, m_{s_i}, \alpha_{1_i}, \alpha_{2_i}, \ldots, \alpha_{p_i}) \qquad (2.21)$$

where the arbitrary parameters $\alpha_{1_i}, \alpha_{2_i}, \ldots, \alpha_{p_i}$ are used to account for inter-electronic repulsions affecting the selected electron. Considering the effect of inter-electronic repulsions for each electron the *orbital energy* ε_i is defined by

$$\hat{F}_i \varphi_i = \varepsilon_i \varphi_i \qquad (2.22)$$

where the energy operator $\hat{F}_i$ includes all inter-electronic repulsions due to other electrons and can be found from Equation (2.20) when the other spin orbitals φ, ,are known. Using a trial and error procedure (called self-consistent method), the spin orbital φ_i (or atomic orbital ψ_i), and the orbital energy ε_i, can be found where every atomic orbital and spin orbital are related by

$$\varphi_i = \psi_i \alpha(\sigma) \quad \text{, if } m_s = 1/2$$
$$\varphi_i = \psi_i \beta(\sigma) \quad \text{, if } m_s = -1/2 \tag{2.23}$$

Briefly, we can see from (2.20), for an atom with *N* electrons, each electron can take a set of quantum numbers given by Equations (2.12) and (2.17), and based on this configuration the atom will have particular wave function (state function) and therefore particular energy state ("electronic state") corresponding to the quantum numbers of its electrons. For example the electronic energy states of the hydrogen atom are shown in Figure 2.4.

Electron configuration	Term symbol	Energy/cm^{-1}
$1s$	$1s\ ^2S_{1/2}$	0.00
$2p$	$2p\ ^2P_{1/2}$	82 258.917
$2s$	$2s\ ^2S_{1/2}$	82 258.942
$2p$	$2p\ ^2P_{3/2}$	82 259.272
$3p$	$3p\ ^2P_{1/2}$	97 492.198
$3s$	$3s\ ^2S_{1/2}$	97 492.208
$3p, 3d$	$3p\ ^2P_{3/2}, 3d\ ^2D_{3/2}$	97 492.306
$3d$	$3d\ ^2D_{5/2}$	97 492.342
$4p$	$4p\ ^2P_{1/2}$	102 823.835
$4s$	$4s\ ^2S_{1/2}$	102 823.839
$4p, 4d$	$4p\ ^2P_{3/2}, 4d\ ^2D_{3/2}$	102 823.881
$4d, 4f$	$4d\ ^2D_{5/2}, 4f\ ^2F_{5/2}$	102 823.896
$4f$	$4f\ ^2F_{5/2}$	102 823.904

Figure 2.4: The first few electronic states of atomic hydrogen from (McQuarrie and Simon 1997).

2.2.2.2 Electronic states in Molecules

The electronic energy states of molecules can be explained with the same concepts developed for atoms. The wave function for a closed-shell molecule with N electrons (N must be an even number) is given by

$$\Psi(1,\ 2,\ \ldots,\ N) = \frac{1}{\sqrt{N!}} \begin{vmatrix} \phi_1(1)\alpha(1) & \phi_1(1)\beta(1) & \cdots & \phi_{N/2}(1)\alpha(1) & \phi_{N/2}(1)\beta(1) \\ \phi_1(2)\alpha(2) & \phi_1(2)\beta(2) & \cdots & \phi_{N/2}(2)\alpha(2) & \phi_{N/2}(1)\beta(2) \\ \vdots & \vdots & & \vdots & \vdots \\ \phi_1(N)\alpha(N) & \phi_1(N)\beta(N) & \cdots & \phi_{N/2}(N)\alpha(N) & \phi_{N/2}(N)\beta(N) \end{vmatrix}$$

(2.24)

where the individual entries are product of (one-electron) molecular orbitals ϕ_i's and spin functions α and β. The same as atomic orbitals φ's, molecular orbitals ϕ_i's specify the spatial probability density of each electron around the molecule. Usually, the ith molecular orbital is obtained from linear combination of atomic orbitals by

$$\phi_i = \sum_{j=1}^{M} c_{ji}\varphi_j \qquad (2.25)$$

in which M is the number of atomic orbitals used to construct a molecular orbital. The atomic orbitals for each atom are obtained from the procedure outlined in the previous section. Again using a trial and error procedure, the constant c_{ji} and therefore the (one-electron) molecular orbital ϕ_i's are calculated. It should be stressed that each molecule contains multiple atoms. Based on the spacing between atoms in a molecule, from Equation (2.25), it is clear that the molecular orbital ϕ_i's will be also a function of atomic spacing. Knowing that for each set of molecular orbitals $\phi_1, \phi_2, \ldots, \phi_{N/2}$, the molecule has a certain electronic energy, we realize that the electronic energy of a polyatomic molecules also depends on its atomic spacing.

To clarify this more, consider the molecular orbitals of H_2^+ which are the simplest orbitals among all polyatomic molecules. Generally, it is a good approximation that the nuclear motion of atoms in molecules can be neglected. Using this approximation for H_2^+, the time-independent Schrödinger equation for this system (one electron molecule H_2^+ as shown in Figure 5) can be written as

$$-\frac{\hbar^2}{2m_e}\nabla^2\psi + (-\frac{e^2}{4\pi\varepsilon_0 r_{1A}} - \frac{e^2}{4\pi\varepsilon_0 r_{1B}} + \frac{e^2}{4\pi\varepsilon_0 R})\psi = E\psi \qquad (2.26)$$

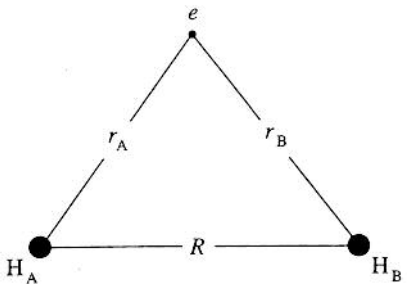

Figure 2.5: Definition of the distances involved in the Hamiltonian operator for H_2^+ from (McQuarrie and Simon 1997).

It is obvious from Equation (2.26) for each state *j*, the molecular orbital ψ_j and therefore energy E_j, eigenfunction and eigenvalue of (2.26), will depend on atomic distance *R*. The inter-nuclear distance between the atoms at particular electronic state where the energy of molecules is minimum, is called *bond length*. As an example, the variation of energy, *E*, versus inter-nuclear distance, *R*, at ground electronic states for H_2^+, is shown in Figure 2.6a. Also, in figure 2.6b some electronic states of the oxygen molecule O_2 are illustrated. Hence, just as atoms, molecules have many different electronic states, which are derived from equation (2.25).

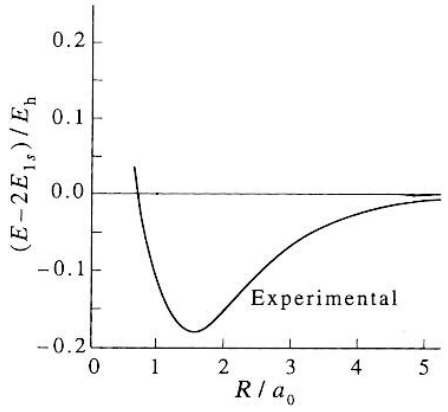

Figure 2.6a: Variation of energy, *E*, versus inter-nuclear distance, *R*, at ground electronic states for H_2^+ from (McQuarrie and Simon 1997).

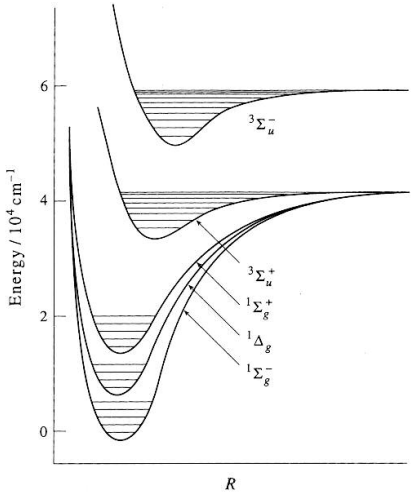

Figure 2.6a: A potential energy diagram of O_2 from (McQuarrie and Simon 1997).

2.2.3 Rotational states

Rotational states of molecules are most easily understood through a discussion of the simpler states of diatomic molecules, after which the discussion can be easily extended to polyatomic molecules.

2.2.3.1 Rotational states of a diatomic molecule

Assume a diatomic molecule contains two atoms with mass m_1 and m_2 at fixed distances r_1 and r_2 from their center of mass (the bond length r is assumed to be constant, Figure 2.7) rotates at angular velocity ω. For such rigid system, the total kinetic energy will be

$$K = \frac{1}{2}m_1 v_1^2 + \frac{1}{2}m_2 v_2^2 = \frac{1}{2}(m_1 r_1^2 + m_1 r_1^2)\omega^2 = \frac{1}{2}I\omega^2 \qquad (2.27)$$

where *I is* called the *moment of inertia,* given by

$$I = m_1 r_1^2 + m_2 r_2^2 \tag{2.28}$$

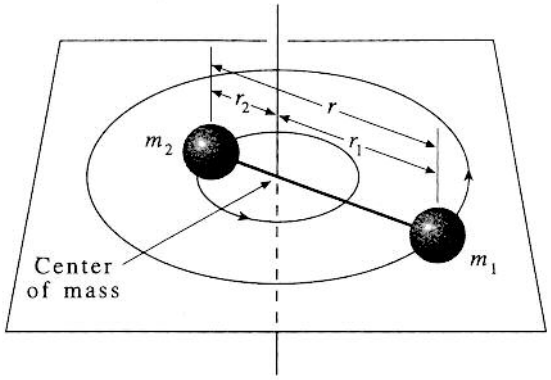

Figure 2.7: Two mass m_1 and m_2 shown rotating about their center of mass, from (McQuarrie and Simon 1997).

The two-body system can be transformed to a single-body system consisting of an effective mass μ rotating at a distance r from a fixed center (which is the center of mass of the two-body system given by $m_1 r_1^2 = m_2 r_2^2$). Figure 2.8. In this new, simpler system, the moment of inertia is given by

$$I = \mu r^2 \tag{2.29}$$

in which μ is *reduced mass* defined by

$$\mu = \frac{m_1 m_2}{m_1 + m_2} \tag{2.30}$$

This model is called the *rigid rotor* model for a molecular system. Writing the time-independent Schrödinger equation for the transformed one-body system, the total rotational kinetic energy of the molecule will be

$$E_J = \frac{\hbar^2}{2I} J(J+1) \qquad J = 0, 1, 2, \ldots \tag{2.31}$$

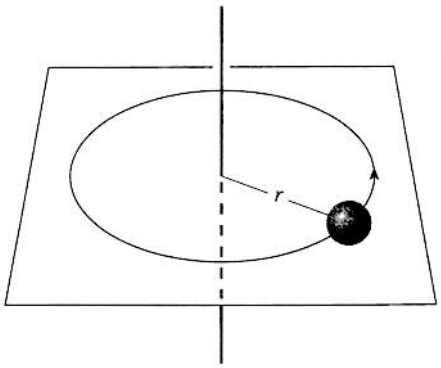

Figure 2.8: The rotation of a single particle about a fixed point, from (McQuarrie and Simon 1997).

Equation (2.31) says that a diatomic molecule with a fixed bond length *r* has only a set of discrete allowed energies and can not have any energy. Also, based on the solution of the Schrödinger equation for such system, each allowed energy level has a degeneracy g_J given by

$$g_J = 2J + 1 \qquad (2.32)$$

Usually, energy in molecular spectroscopy is expressed in units of cm^{-1}, related to energy in Joules as:

$$E(cm^{-1}) = \frac{E(Joules)}{hc} \qquad (2.33)$$

Using Equation (2.33), the rotational energy of the diatomic molecule in cm^{-1} is written by

$$E_J = \frac{\hbar^2}{2Ihc} J(J+1) = \frac{h}{8\pi^2 cI} J(J+1) \qquad J = 0, 1, 2, \ldots \qquad (2.34)$$

Per the rigid rotor model assumptions, Equation (2.34) is only valid when the bond length r is constant. It turns out as molecule rotates more energetically (increasing J), the centrifugal force causes the bond to stretch slightly. If this small variation in r is treated with perturbation theory, the rotational energy (in cm^{-1}) becomes

$$E_J = \tilde{B}J(J+1) - \tilde{D}J^2(J+1)^2 \qquad J = 0, 1, 2, \ldots \tag{2.35}$$

where $\tilde{B} = h/8\pi^2 cI$ and $\tilde{D}$ (the centrifugal distortion constant) for each molecule are usually obtained by fitting Equation (2.35) to the experimental data.

2.2.3.2 Rotational states of a polyatomic molecule

For simplicity, we first assume a polyatomic molecule can be considered as a rigid network of N atoms. For such a system, the *moment of inertia* I_{xx} with respect to any chosen Cartesian axes can be defined as

$$I_{xx} = \sum_{j=1}^{N} m_j[(y_j - y_{cm})^2 + (z_j - z_{cm})^2] \tag{2.36}$$

where m_j s the mass of the jth atom situated at point x_j, y_j, z_j and x_{cm}, y_{cm}, z_{cm} are the coordinates of the center of mass of the molecules. Similar definations are applied to two other moments of inertia I_{yy} and I_{zz}. Also for this system the *product of inertia* I_{xy} is defined by

$$I_{xy} = -\sum_{j=1}^{N} m_j(x_j - x_{cm})(y_j - y_{cm}) \tag{2.37}$$

and as in Equation (2.37), I_{xz} and I_{yz} are defined similarly.

There is a theorem saying that for such a system there will always be a particular set of Cartesian axes *X, Y, Z,* called the *principal axes,* passing through the center of mass of the system such that the products of inertia vanish. The moments of inertia with respect to the principal axes are called *principal moments of inertia*. The principal moments of inertia of the polyatomic molecules are usually denoted by I_A, I_B, I_C such that $I_A \leq I_B \leq I_C$.

The principle axes of molecules with some degree of symmetry are more easily found. Usually an axis of symmetry of a polyatomic molecule is a principal axis. Principal moments of inertia are usually expressed in terms of rotational constants in units of cm^{-1}, defined by

$$\tilde{A} = \frac{h}{8\pi^2 c I_A}, \qquad \tilde{B} = \frac{h}{8\pi^2 c I_B}, \quad \text{and} \quad \tilde{C} = \frac{h}{8\pi^2 c I_C} \tag{2.38}$$

Since $I_A \leq I_B \leq I_C$, the rotational constants always satisfy $\tilde{A} \geq \tilde{B} \geq \tilde{C}$.

Basically, the characteristics of a prototypical rigid polyatomic molecule are determined by its three principal moments. If all principal moments are equal, the molecule is called *spherical top*; if only two of them are equal, it is called a *symmetric top*; and if all three are different, the molecule is called an *asymmetric top*. For example, CH_4 and SF_6 are spherical tops: NH_3 and C_6H_6 are symmetric tops; and H_2O is an asymmetric top.

The rotational energy states for a spherical top and symmetric top can be obtained analytically from the time-independent Shrödinger equation, however, for a asymmetric top molecule, the rotational energy sates are very complicated and there is no analytical expression. The rotational energy states for a spherical top molecules

($\tilde{A} = \tilde{B} = \tilde{C}$) are exactly the same as for a diatomic molecule given by Equation (2.34).

Polyatomic atomic molecules are usually less rigid than diatomic molecules and therefore the centrifugal distortion effect is more important. For this reason, as for a diatomic molecule, the effect of centrifugal force in rotational energy states of a polyatomic is treated by perturbation theory. Again, for spherical top and symmetric top molecules there are analytical solutions for rotational energy states where centrifugal distortion are included. For example, the rotational energy states of a spherical top polyatomic molecule are given by Equation (2.35), which again is exactly the same as for diatomic molecules.

2.2.4 Vibrational states

In addition to translational, electronic, and rotational energy states, a molecule can also have vibrational energy states. As for rotational energy states, the vibrational energy states for the simplest molecules (diatomic molecules) are discussed first, and then the results are extended to polyatomic molecules.

2.2.4.1 Vibrational states for a diatomic molecule

We will consider the so-called "harmonic oscillator" model of a diatomic molecule with two atoms with mass m_1 and m_2, located at x_1 and x_2 respectively, Figure 2.9a.

The basis of the harmonic oscillator model is that the internuclear (repulsion and attraction) forces between the two atoms are symmetric and are proportional to the

displacement from equilibrium ($F = k\Delta x$), as in a simple spring system. If this is true, then the equations of motion of the atoms are given by

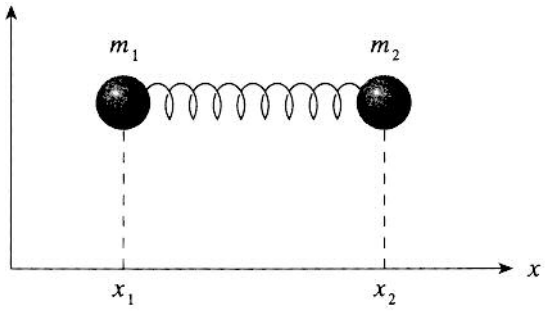

Figure 2.9a: Two masses connected to a spring, which is a model used to describe the vibrational motion of a diatomic molecule, from (McQuarrie and Simon 1997).

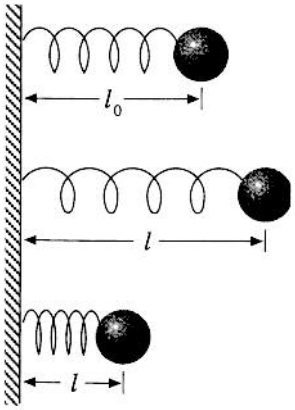

Figure 2.9b: A mass connected to a wall by a spring, from (McQuarrie and Simon 1997).

$$m_1 \frac{d^2 x_1}{dt^2} = k(x_2 - x_1 - r)$$
$$m_2 \frac{d^2 x_2}{dt^2} = -k(x_2 - x_1 - r) \qquad (2.39)$$

Since the motion of the two atoms in harmonic oscillator model only depends on the relative separation between the atoms $x = x_2 - x_1$, it is better to transform the above two-body system to a one-body system illustrated in Figure 2.9b. The equation of motion (2.39) becomes

$$\mu \frac{d^2 x}{dt^2} + kx = 0 \qquad (2.40)$$

where μ is reduced mass of the molecule given by equation (2.30).

The vibrational energy states for a diatomic molecule predicted from the harmonic oscillator model can be obtained from the time-independent Schrödinger

equation, when the potential energy function *V(x)* is known. The potential energy for this system can be easily obtained form

$$V(x) = -\int F(x)dx + c = \frac{k}{2}x^2, \quad \text{Assuming } V(0) = 0 \qquad (2.41)$$

If this potential is put in the time-independent Schrödinger equation, for the aforementioned one-body system, the eigenvalues, or vibrational energy states, will be (below it should say "where E_J is in Joules")

$$\begin{aligned} E_\upsilon &= h\nu\left(\upsilon + \frac{1}{2}\right) \qquad \upsilon = 0, 1, 2, \ldots \qquad \text{where } E_J \text{ is in Joule} \\ E_\upsilon &= \tilde{\nu}\left(\upsilon + \frac{1}{2}\right) \qquad \upsilon = 0, 1, 2, \ldots \qquad \text{where } E_J \text{ is in } cm^{-1} \end{aligned} \qquad (2.42)$$

in which E_υ is the vibrational energy state, an allowable value for vibrational energy $E_\nu = p^2/2\mu + kx^2/2$), and ν, or $\tilde{\nu}$, is the *fundamental vibrational frequency* defined by

$$\nu = \frac{1}{2\pi}\left(\frac{k}{\mu}\right)^{1/2} \qquad \text{or} \qquad \tilde{\nu} = \frac{1}{2\pi c}\left(\frac{k}{\mu}\right)^{1/2} \qquad (2.43)$$

The harmonic oscillator model embodied by equation (2.42) predicts that vibrational energy states for a diatomic molecule are equally separated. If the vibrational energy states are obtained precisely by experiment, it is observed that they are not equally separated.

To calculate vibrational energy states for a diatomic molecule more precisely, the potential energy in the time-independent Schrödinger equation must be the real potential energy of a diatomic molecule, incorporating nonlinearities not in the Hookian spring model. The real inter-nuclear potential energy obtained from electronic state energy diagram (such as Figure 2.6a and 2.6b) illustrates how the actual potential energy of a diatomic molecule varies as the inter-nuclear separation

changes. It turns out the potential energy diagram of a molecule in a particular electronic state is not a simple parabola. To obtain a more accurate vibrational energy, the higher orders of relative displacement x is considered in the potential energy equation such as

$$V(x) = \frac{k}{2}x^2 + c_1x^3 + c_2x^4 + \cdots \qquad (2.43)$$

If the anharmonic terms in (2.43) are treated separately by applying perturbation theory the time-independent Schrödinger equation, then the modified vibrational energy states will be given by

$$E_\upsilon = \tilde{\nu}_e(\upsilon + \frac{1}{2}) - \tilde{x}_e\tilde{\nu}_e(\upsilon + \frac{1}{2})^2 + \cdots \qquad \upsilon = 0, 1, 2, \ldots \qquad (2.44)$$

where $\tilde{x}_e$ is called the *anharmonicity constant*. The energy levels determined by Equation (2.44) are not equally separated, and in fact match with experiment. Figure 2.10 shows the vibrational energy states for a diatomic molecule using harmonic oscillator model, equation (2.42) and more precise model, given by (2.44).

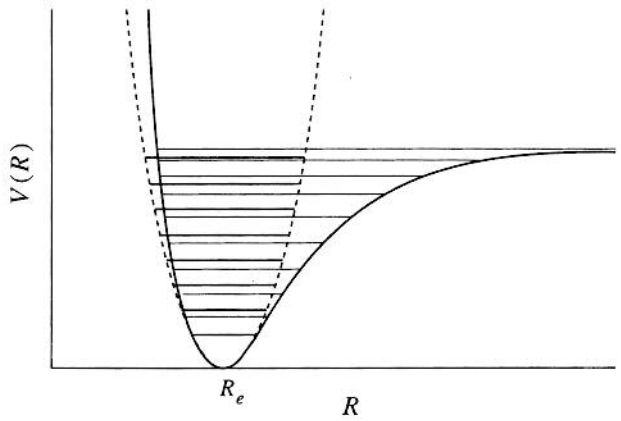

Figure 2.10: The energy states of a harmonic oscillator (dashed line) and anharmonic oscillator superimposed on a harmonic-oscillator potential and a more realistic internuclear potential, from (McQuarrie and Simon 1997).

It should be stressed that in Equation (2.44) different electronic states have different potential energy diagrams, and therefore the constants $\tilde{\nu}_e$ and $\tilde{x}_e$ are unique to each electronic state. For each molecule, these constants are usually obtained by fitting the results of measured vibrational states with Equation (2.44).

2.2.4.2 Vibrational states for a polyatomic molecule

As for diatomic molecules, the key factor in determining vibrational states of a polyatomic molecules is the potential energy of the molecule. In this section, the vibrational energy of a polyatomic molecule based on harmonic oscillator approximation is discussed.

A complete specification of an *N*-atom molecule in space requires *3N* coordinates, each atom requires three coordinates. In this regard, the *N*-atom molecule has *3N degrees of freedom*. Three of these coordinates are used to specify the center of mass of the molecule. Because motion along these coordinates corresponds to translational motion, we can say the molecule has three *translational degrees of freedom*. Two coordinates are required to specify the orientation of a linear molecule about its center of mass, and three coordinates to specify the orientation of a nonlinear molecule about its center of mass. Since motion along these coordinates corresponds to rotational motion, we can say linear and nonlinear molecules have two and three *rotational degrees of freedom*, respectively. The remaining coordinates (*3N-5* for a linear molecule and *3N-6* for a nonlinear molecule) specify the relative position of the *N* nuclei. Since the vibrational motion depends on the relative position

of the nuclei in a polyatomic molecule, we say that a linear and nonlinear molecule have *3N-5* and *3N-6 vibrational degrees of freedom*.

As explained in Section 2.2.2.2, the potential energy of a polyatomic molecule, in the absence of external fields, only depends upon the relative position of the nuclei. Therefore, the potential energy will be only a function of *3N-5* or *3N-6* vibrational coordinates. If we let the displacements about the equilibrium values of these coordinates be denoted by $q_1, q_2, \ldots, q_{N_{vib}}$, where N_{vib} is the number of vibrational degrees of freedom, then the potential energy for the molecule is given by

$$\begin{aligned} V(q_1, q_2, \ldots, q_{vib}) &= V(0,0,\ldots,0) + \frac{1}{2}\sum_{i=1}^{N_{vib}}\sum_{j=1}^{N_{vib}}\left(\frac{\partial^2 V}{\partial q_i \partial q_j}\right) q_i q_j + \cdots \\ &= \frac{1}{2}\sum_{i=1}^{N_{vib}}\sum_{j=1}^{N_{vib}} f_{ij} q_i q_j + \cdots \end{aligned} \tag{2.45}$$

where Equation (2.45) is a generalized form of Equation (2.41) for a multidimensional case. As we can see, the anharmonic terms are not considered here and therefore Equation (2.45) represents potential energy for the *N*-atom molecule with the harmonic-oscillator approximation. The presence of cross terms in Equation (2.45) makes the solution of the corresponding Schrödinger equation very difficult to obtain. However, by using a particular transformation (mapping $\{q_i\}$ coordinates to $\{Q_j\}$ coordinates), the potential energy is related to new coordinates by

$$V(Q_1, Q_2, \ldots, Q_{N_{vib}}) = \frac{1}{2}\sum_{j=1}^{N_{vib}} F_j Q_j^2 \tag{2.46}$$

These new coordinates are called *normal coordinates* and corresponding *3N-5* or *3N-6* vibrations are referred to as *normal modes of vibration*. In normal modes of vibration, the nuclei move in phase, and the motions of nuclei in a normal mode are

such that the center of mass dose not move and the molecule as a whole does not rotate. Sometimes, several modes have identical vibrational frequencies and are referred as *degenerate modes*.

The Hamiltonian operator $\hat{H}$ for the vibrational energy of the *N*-atom molecule with the harmonic-oscillator approximation in terms of normal coordinates can be written as

$$\hat{H}_{vib} = \sum_{j=1}^{N_{vib}} \left(-\frac{\hbar^2}{2\mu_j} \frac{d^2}{dQ_j^2} + \frac{1}{2} F_j Q_j^2 \right) = \sum_{j=1}^{N_{vib}} \hat{H}_{vib,j} \qquad (2.47)$$

According to the property of Hamiltonian operator, mentioned in Section 2.1, the vibrational energy states of the molecule can be written as

$$E_{vib} = \sum_{j=1}^{N_{vib}} h\nu_j (\upsilon_j + \frac{1}{2}) \qquad \text{each } \upsilon_j = 0, 1, 2, \ldots \qquad (2.48)$$

This means that under the harmonic oscillator approximation, the vibrational motion of a polyatomic molecule appears as N_{vib} independent harmonic oscillators, each vibrating with a fundamental frequency ν_j. For example the normal modes of H_2O are shown in Figure 2.11.

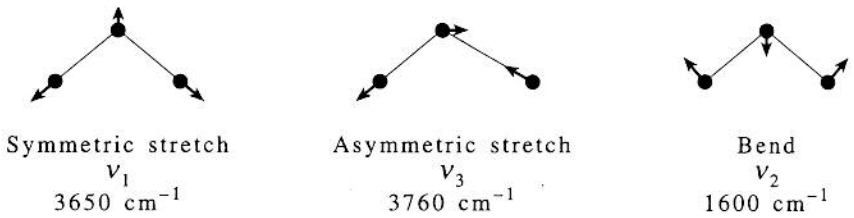

Figure 2.11: Normal (vibrational) modes of H_2O, from (McQuarrie and Simon 1997).

As mentioned above, Equation (2.48) only considers the quadratic term in the potential energy Hamiltonian. If the anharmonic terms (cubic, quartic,… terms) in the potential energy are considered, then modified vibrational energy states are obtained:

$$E_{vib} = \sum_{j=1}^{N_{vib}} \tilde{\nu}_{e,j}(\upsilon_j + \frac{1}{2}) + \sum_{j=1}^{N_{vib}} \sum_{k \geq j}^{N_{vib}} \tilde{x}_{e,jk}(\upsilon_j + \frac{1}{2})(\upsilon_k + \frac{1}{2}) + \cdots \quad (2.49)$$

As explained for diatomic molecules, the anharmonicity coefficients $\tilde{\nu}_{e,j}$ and $\tilde{x}_{e,jk}$ are obtained by fitting the experimental results to Equation (2.49).

2.2.5 Total molecular energy state

The total energy of a molecule, in general, is the sum of translational, electronic, vibrational, and rotational energy. The translational energy states in the molecules are very closely spaced and can not be probed using molecular spectroscopy; hence, they are neglected here. Based on the discussion above, the total energy of a polyatomic molecule is given by

$$E = E_{elect} + E_{vib} + E_{rot} \quad (2.50)$$

2.3 Interaction of weak electromagnetic radiation by a molecule (Bernath 1995)

In this section a semi-classical model for the interaction of a weak electromagnetic wave with a molecule, leading to absorption of electromagnetic energy is discussed. In this model, the energy levels of the molecules are obtained from the time-independent Schrödinger equation, as explained in the proceeding sections, and the electromagnetic wave is treated classically.

Consider a molecule with only two states, with lower and upper state function ψ_0 and ψ_1 and corresponding energy levels E_0 and E_1, as shown in Figure 2.12. Such

a two level system is a good approximation for weak electromagnetic wave where the electric field strengths are low enough such that there is a negligible buildup of population in the exited state{Bernath, 1995 #59}. According to the Bohr condition, an electromagnetic wave with frequency ν such that $E_1 - E_0 = h\nu$ can be absorbed by a molecule and induce a transition from E_0 to E_1.

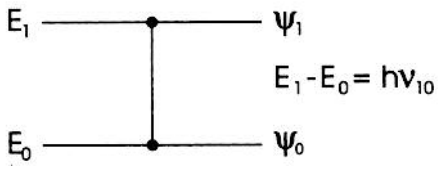

Figure 2.12: Two-level system, from (Bernath 1995).

The nature of such transition is a time-dependent phenomenon and therefore this transition probability is obtained from the time-dependent Shrödinger equation by

$$i\hbar \frac{\partial \Psi(\vec{r},t)}{\partial t} = \hat{H}(t)\Psi(\vec{r},t) = \left[\hat{H}^{(0)} + \hat{H}^{(1)}\right] \Psi(\vec{r},t) \qquad (2.51)$$

where $\hat{H}^{(0)}$ is Hamiltonian operator for an isolated system, given in Equation (2.3), which we used to obtain different stationary states in a molecule. $\hat{H}^{(1)}$ is a time-dependent term of $\hat{H}(t)$ in equation (2.51), due to the interaction of the electromagnetic wave with molecule, representing the time variation of potential energy in the system due to electromagnetic radiation and obtained by

$$\hat{H}^{(1)} = -\vec{\mu} \,.\, \vec{E}(t) = -\vec{\mu} \,.\, \vec{E}_0 \cos(K.r - 2\pi\nu t) = -\mu E_0 \cos(2\pi\nu t) \qquad (2.52)$$

Equation (2.52) is valid if the oscillating electric field and the net dipole moment are in the same direction and the wavelength of electromagnetic wave is much bigger than the dimension of the system, such that there is an equal electric field strength at

every point in the molecule. In Equation (2.52), E_0 and ν represent the amplitude and frequency of the electromagnetic radiation, and μ is the net dipole moment of the system (nuclei and electrons), calculated by

$$\vec{\mu} = \sum q_i \vec{r}_i \qquad (2.53)$$

where $\vec{r}$ is the coordinate of the particle i (nuclei and electrons) relative to the center of mass of the molecule and q_i is the charge of the particle.

Assume that the system is initially in state 0 and the interaction of electromagnetic radiation with the molecule occurs at t=0. Based on *time-dependent perturbation theory* the state function of the system at any time t will be a linear combination of state function of stationary states 0 and 1, $\Psi_0(\vec{r},t)$ and $\Psi_1(\vec{r},t)$. Therefore one can calculate the state function of the system from

$$\Psi(\vec{r},t) = a_0(t)\Psi_0(\vec{r},t) + a_1(t)\Psi_1(\vec{r},t) \qquad (2.54)$$

where $a_0(t)$ and $a_1(t)$ are to be determined. In such a linear combination $a_i(t)\ a_i(t)^*$ is the probability that the molecule is in state i, where the asterisk denotes the complex conjugate. Using Equation (2.7) in (2.54) and then solving Equation (2.51) with initial condition of

$a_0(t) = 1$ and $a_1(t) = 0$

and also assuming the electromagnetic field vector and dipole moment vector are in the same direction, solution is possible for $a_1(t)$, and therefore $a_1(t)\ a_1(t)^*$, which is the probability of absorption or intensity of absorption. The final results will be

$$P_{1\leftarrow 0} = a_1(t)a_1(t)^* = \mu_{10}{}^2 E_0{}^2 \frac{\sin^2\left[\left(E_1 - E_0 - h\nu\right)\ t/2\hbar\right]}{\left(E_1 - E_0 - h\nu\right)^2} \qquad (2.55)$$

where μ_{10} is *called transition dipole moment* between states 0 and 1 and is defined by

$$\mu_{10} = \int \psi_1^* \mu \, \psi_0 d\tau \qquad (2.56)$$

From (2.55), it is observed that the maximum probability of absorption, in the time interval 0 to t, occurs when $h\nu = E_1 - E_0$. A plot of $a_1(t)\ a_1(t)^*$ based on (2.55) is shown in Figure 2.13.

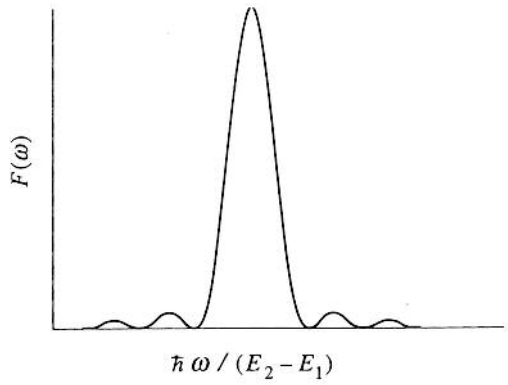

Figure 2.13: The function $F(\omega) = F(2\pi\nu) = \sin^2[(E_2 - E_1 - \hbar\omega)t/2\hbar]/(E_2 - E_1 - \hbar\omega)^2$ which represents the probability of making a $1 \rightarrow 2$ transition in the time interval 0 to t, plotted against frequency ω. This function peaks when $E_2 - E_1 = \hbar\omega = h\nu$, from (Bernath 1995).

Equation (2.55) is somewhat inconsistent because it assumes monochromatic radiation and short interaction time, which are incompatible with one another according to Heisenberg uncertainty principle:

$$\Delta E \, \Delta t \geq \hbar \quad \text{or} \quad \Delta\nu \, \Delta t \geq \frac{1}{2\pi} \qquad (2.57)$$

Equation (2.57) says if monochromatic radiation is applied to the system for a time Δt, then the system sees radiation of bandwidth $\Delta\nu = 1/2\pi\Delta t$ in frequency space, which is certainly not monochromatic.

Considering broadband radiation with radiation density $\rho(\nu) = \varepsilon_0 E^2 / 2$, where $\rho(\nu)$ is assumed to be slowly varying near $\nu_0 = (E_1 - E_0)/h$, the total transition probability over all radiation frequencies can be calculated as

$$\begin{aligned} P_{0\leftarrow 1} &= \frac{2\mu_{10}^{\ 2}}{\varepsilon_0}\int \rho(\nu)\frac{\sin^2\left[\left(E_1 - E_0 - h\nu\right)\ t/2\hbar\right]}{\left(E_1 - E_0 - h\nu\right)^2}\,d\nu \\ &= \frac{2\mu_{10}^{\ 2}}{\varepsilon_0}\rho(\nu_0)\int \frac{\sin^2\left[\left(E_1 - E_0 - h\nu\right)\ t/2\hbar\right]}{\left(E_1 - E_0 - h\nu\right)^2}\,d\nu \\ &= \frac{\mu_{10}^{\ 2}}{2\varepsilon_0\hbar^2}\rho(\nu_0)\,t \end{aligned} \qquad (2.58)$$

Equation (2.58) has been derived using plane wave radiation traveling in a particular direction parallel to the dipole moment of the molecule. In general, for radiation oriented at some arbitrary direction with respect to the molecule, only the component of the radiation aligned with the molecular axis will be absorbed, and therefore in general case we should divide Equation (2.58) by 3. Therefore the absorption rate per molecule with a population density of N_0 and N_1 (as number of molecules per unit volume in states E_0 and E_1 respectively) can be calculated as

$$\frac{dP_{1\leftarrow 0}}{dt} = \frac{dN_1}{dt} = \frac{2\pi^2}{3\varepsilon_0 hc^3}N_0\mu_{10}^{\ 2}\rho(\nu_0) = B_{1\leftarrow 0}\rho(\nu_0)N_0 \qquad (2.59)$$

in which $B_{1\leftarrow 0}$ is Einstein coefficient for absorption. In addition to absorption, there is another important interaction of light with molecules, suggested by Einstein in 1917, called *stimulated emission*. In this process, a photon of energy hν corresponding to the transition $E_1 \rightarrow E_0$ induces an atom or molecule in the upper E_2 state to relax to the lower state by emitting a second photon of energy hν, in phase with the incident photon. This is the process by which a laser achieves gain, through stimulated

emission in the lasing medium. The change of population in state E_1 due to stimulated emission is given by

$$\frac{dN_1}{dt} = -B_{1\to 0} N_1 \rho(\nu_0) \qquad (2.60)$$

It can be shown that $B_{1\to 0}$, Einstein coefficient of stimulated emission, is equal to $B_{1\leftarrow 0}$ and therefore can be obtained from (2.59). Using (2.59) and (2.60), the total change rate of the population in state E_1 due to stimulated emission and absorption can be obtained by

$$\begin{aligned}\frac{dN_1}{dt} &= (N_0 - N_1) B_{1\leftarrow 0} \rho(\nu_0) \\ &= (N_0 - N_1) \frac{2\pi^2}{3\varepsilon_0 hc^3} \mu_{10}{}^2 \rho(\nu_0)\end{aligned} \qquad (2.61)$$

2.3.1 Attenuation of radiation beam due to absorption and stimulated emission

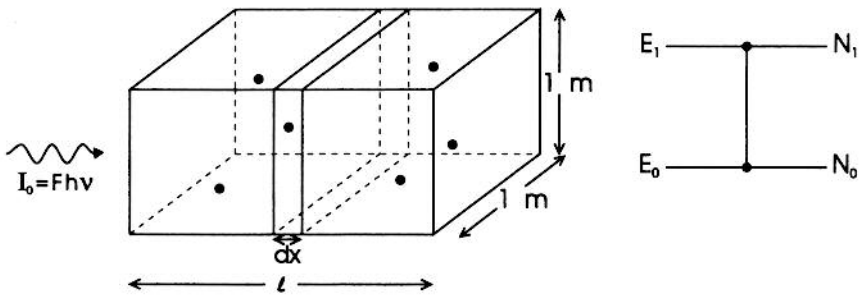

Figure 2.14: A system with dimension 1 m × 1 m × l m that contains N_0 and N_1 molecules per cubic meter with energies E_0 and E_1, respectively, from (Bernath 1995).

Consider a system containing N_0 molecules per cubic meter in the ground state (with energy E_0) and N_1 molecules per cubic meter in the excited state (with energy E_1), as shown in Figure 2.14. If a flux of photons with $F = c\rho(\nu_0)/h\nu = I_0/h\nu$ (photons/m^{2}s) is incident upon the system from the left, the photons will be either absorbed as they travel through the system or will stimulate emission. In this case, the rate of change of population at state E_1 can be obtained by

$$\frac{dN_1}{dt} = \frac{2\pi^2 \mu_{10}{}^2 \nu}{3\varepsilon_0 hc} F(N_0 - N_1) = \sigma F(N_0 - N_1) \qquad (2.62)$$

The parameter σ, called the absorption *cross section* with has units of m^2, is measure of the effective area that a molecule presents to absorb photons. The absorption of photons (which is always accompanied with stimulated emission) by molecules causes an attenuation of flux by dF when it passes through element with thickness dx. Therefore the change in flux caused by traveling through element with thickness of dx is

$$dF = -\sigma F(N_0 - N_1)dx \quad \text{or} \quad dI = -\sigma I(N_0 - N_1)dx \qquad (2.63)$$

By taking the integral with respect to x, the transmitted (attenuated) intensity I due to absorption after travel of L (m) through the absorbing media is given by

$$I = I_0 e^{-\sigma(N_0 - N_1)L} \qquad (2.64)$$

in which I_0 is the incident light intensity. Typically $N_0 >> N_1$, and therefore $N \approx N_0 + N_1$ and the effect of stimulated emission in absorption spectroscopy, particularly at low temperatures, is negligible.

In (2.61), many phenomena, such as collisions and also the effect of molecular motions have been ignored. When these phenomena are considered, the molecular

absorption line shape changes from an infinitely sharp and narrow Dirac delta function $\delta(\nu-\nu_0)$ to a real molecular line shape function $g(\nu-\nu_0)$. [Note that Figure 2.13 does not show a delta function …] Based on Equation (2.61), a realistic absorption cross section can be defined as

$$\sigma = \sigma(\nu) = \frac{2\pi^2 {\mu_{10}}^2 \nu}{3\varepsilon_0 hc} g(\nu-\nu_0) \qquad (2.65)$$

It is this cross section that should be considered in equations (2.62) to (2.64) for applications to real systems.

2.3.2 Pressure broadening

Consider a two-level system as described in Section 2.3. In the absence of radiation the state of the system is given by

$$\begin{aligned}\Psi &= a_0\Psi_0 + a_1\Psi_1 \\ &= a_0\psi_0 e^{-iE_0 t/\hbar} + a_1\psi_1 e^{-iE_1 t/\hbar}\end{aligned} \qquad (2.66)$$

In such system, a_0 and a_1 are constants because no electromagnetic radiation is present in the system. It can be shown that the dipole moment of the system $\vec{M}$ naturally oscillates at the Bohr frequency, $\nu_0 = (E_1 - E_0)/h$, in the expression

$$\begin{aligned}\vec{M} &= \int \Psi^* \mu \ \Psi d\tau = 2a_0 a_1 \mu_{10} \cos(2\pi\nu_0 t) \\ &= \vec{M}_0 \cos(2\pi\nu_0 t)\end{aligned} \qquad (2.67)$$

The variation of the dipole moment of the system with time specifies the line shape function, which can be easily obtained by a Fourier transform of the dipole moment of the system. In the absence of collisions, the dipole moment oscillates exactly at the

Bohr frequency v_0, and therefore the line-shape function would be $\delta(\nu - \nu_0)$ since the Fourier transform of the infinite cosine wave (2.67) yields a frequency of exactly v_0. However, in the case of intermolecular collisions, the phase of the oscillating dipole moment is altered in a random manner. If the average time between collisions is T_2 , as shown in Figure 2.15, then the infinite cosine wave is broken into pieces of average length of T_2. The Fourier transform of such oscillating dipole moment will be a Lorentzian function with a full width at half maximum (FWHM) given by

$$\text{FWHM} = 2\Delta\nu_L = \frac{1}{\pi T_2} \qquad (2.68)$$

and therefore the line-shape function will be:

$$g_L(\nu - \nu_0) = \frac{\Delta\nu_L / \pi}{(\Delta\nu_L)^2 + (\nu - \nu_0)^2} \qquad (2.69)$$

Since the average time between collisions is proportional to the reciprocal of the pressure *p*, therefore

$$\text{FWHM} = 2\Delta\nu_L = bp \qquad (2.70)$$

where *b* is called pressure broadening coefficient and can be calculated through the experiment.

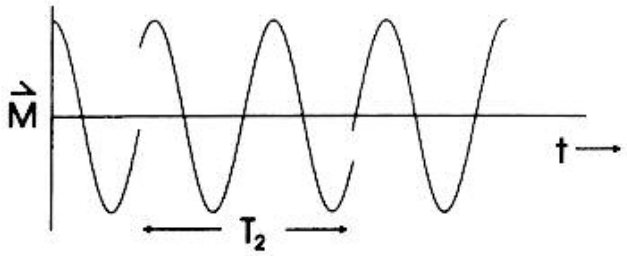

Figure 2.15: The phase of an oscillating dipole moment randomly interrupted by collision, from (Bernath 1995).

2.3.3 Temperature broadening

Consider further an atom with velocity $\vec{\mathbf{v}}$ interacting with a plane wave with frequency ν and a wave vector $\vec{\mathbf{k}}$, as in Figure 2.16. In this case the atom sees a Doppler-shifted frequency $\nu' = \nu(1 \pm \mathrm{v/c})$ depending on if the atoms and plane wave are moving in the same direction (-) or the opposite direction (+). In general when the two vectors **v** and **k** are not parallel, the Doppler shifted frequency can be calculated by

$$\nu' = \nu\left(1 - \frac{\mathrm{v.k}}{\mathrm{c}|\mathrm{k}|}\right) \qquad (2.71)$$

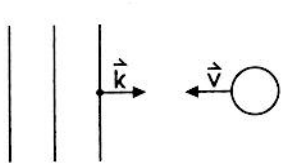

Figure 2.16: Interaction of a lane electromagnetic wave with a moving atom, from (Bernath 1995).

In the frame of the moving molecule, the frequency of the absorbed or emitted electromagnetic wave is unshifted at ν_0, but the in the laboratory frame the resonance frequency (of the atom moving at velocity v) has been shifted to the new value of

$$\nu_0' = \frac{\nu_0}{1 \pm \mathrm{v/c}} \qquad (2.72)$$

At a given temperature T, the molecules in a gaseous system at equilibrium have Maxwell-Boltzmann velocity distribution given by

$$p(\mathrm{v})d\mathrm{v} = \left(\frac{m}{2\pi k\mathrm{T}}\right)^{1/2} e^{(-m\mathrm{v}^2)/(2k\mathrm{T})} d\mathrm{v} \qquad (2.73)$$

in which m is the mass of a molecule and k is the Boltzmann constant. Using $d\mathrm{v} = (\mathrm{c}/\nu_0)d\nu_0'$ from (2.72), the velocity distribution function of molecules given in (2.73), yields a normalized frequency distribution for a fixed resonance frequency ν_0 in the laboratory frame of

$$\mathrm{g}_D(\nu - \nu_0) = \frac{1}{\nu_0}\left(\frac{m\mathrm{c}^2}{2\pi k\mathrm{T}}\right)^{1/2} e^{[-m\mathrm{c}^2(\nu-\nu_0)^2]/(2k\mathrm{T}\nu_0^2)} \qquad (2.74)$$

As shown in (74), the Doppler effect causes a Gaussian line-shape. It can be easily shown that the FWHM in (74) is

$$\Delta\nu_D = 2\nu_0\sqrt{\frac{2k\mathrm{T}\ln(2)}{m\mathrm{c}^2}} = 7.1\times10^{-7}\nu_0\sqrt{\frac{\mathrm{T}}{\mathrm{M}}} \qquad (2.75)$$

where, T is in K, M in amu, ν_0 in cm^{-1} and $\Delta\nu_0$ is in cm^{-1}. Using (2.75), the Gaussian line-shape function in (2.74) can be simplified as

$$\mathrm{g}_D(\nu - \nu_0) = \frac{2}{\Delta\nu_D}\sqrt{\frac{\ln(2)}{\pi}} e^{-4\ln 2[(\nu-\nu_0)^2/\Delta\nu_D]^2} \qquad (2.76)$$

2.3.4 Voigt line shape function

In many systems both Doppler broadening and collisional broadening are important, and therefore the line-shape function is affected by both of these broadening mechanisms. Consider a system containing molecules with resonance frequency ν_0 related to a particular absorption transition. As the result of the Doppler effect, the resonance frequency ν_0 will be shifted to ν_0'. Therefore probability that a

system has a resonance frequency in the interval between ν_0' to $\nu_0' + d\nu_0'$ is $g_D(\nu_0' - \nu_0)d\nu_0'$. Including the effect of collisions, the shifted frequency ν_0' will itself become broadened. In this case, the probability of a frequency shift from ν_0' to the interval between ν and $\nu + d\nu$ is given by

$$g_V(\nu - \nu_0)d\nu = \int_{\nu_0'=-\infty}^{\nu_0'=+\infty} g_D(\nu_0' - \nu_0)g_L(\nu - \nu_0')d\nu_0'd\nu \qquad (2.77)$$

where the line-shape function $g_V(\nu - \nu_0)$, which is a convolution of a Lorentzian and a Gaussian function is called the *Voigt function.* This can be written as:

$$g_V(\nu - \nu_0) = \int_{-\infty}^{+\infty} g_D(\nu_0' - \nu_0)g_L(\nu - \nu_0')d\nu' \qquad (2.78)$$

The Voigt function is a very common line-shape function used in spectroscopy.

2.4 The Selection rules (Bernath 1995; McQuarrie and Simon 1997)

One of the most important results from equation (2.55) is the fact that molecular transitions will occur upon interaction of a molecule with electromagnetic radiation only if the transition dipole moment between the lower and upper state energies, μ_{10}, is not zero. General rules, incorporating quantum mechanics, indicating transitions for which $\mu_{10} \neq 0$ are given by *selection rules*. Below selection rules for some important transitions are explained.

2.4.1 Selection rules for rotational and vibrational transitions

Using the rigid-rotor model as explained in section 2.3, upon calculating a state function, the transition dipole moment can be determined. In this case, for the

transition dipole moments μ_{10} to have a non-zero value requires $\Delta J = \pm 1$, where ΔJ is difference between rotational quantum number of upper and lower states. Also, the molecule must have a permanent dipole moment, $\mu \neq 0$. These are the selection rules corresponding to a harmonic oscillator.

A selection rule for vibrational absorption is that the dipole moment of the molecule must vary during the normal mode motion. When this happens, the normal mode is said to be *infrared active*. Otherwise, it is *infrared inactive.* For example, CO_2 has four normal modes, shown in Figure 2.17. The completely symmetric motion, which does not result in a change in the dipole moment, is infrared active.

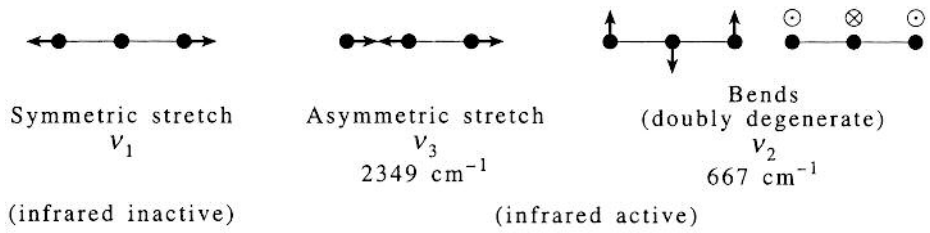

Figure 2.17: Normal modes of CO_2, from (McQuarrie and Simon 1997).

2.4.2 Selection rule for rotational-vibrational absorption

The selection rules for rotational-vibrational absorption mainly depend on how the dipole moment oscillates with respect to the molecular axis. If the dipole moment oscillates parallel to the molecular axis, the selection rule is given by

$$\Delta \upsilon = +1 \quad \text{and} \quad \Delta J = \pm 1 \qquad (2.79)$$

in this case the rotational-vibrational spectrum consists of a *R branch* (rotational-vibrational transition with $\Delta J = +1$) and a *P branch* (rotational-vibrational transition

with $\Delta J = -1$). Such absorption band is called *parallel band*. It should be mentioned that all diatomic molecules fall in this category. Figure 2.18 shows R and P branch of $0 \rightarrow 1$ vibrational spectrum of HBr.

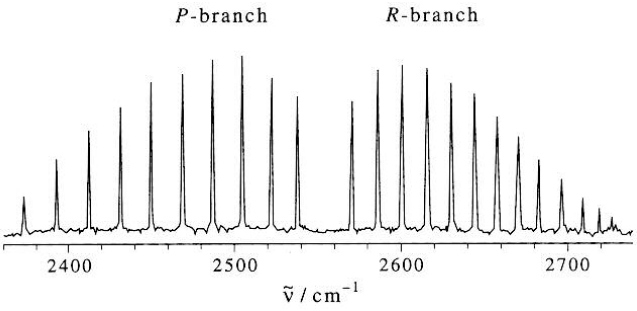

Figure 2.18: The ro-vibrational spectrum of the $0 \rightarrow 1$ vibrational transition of HBr(g). The R branch and P branch are indicated in the figure, from (McQuarrie and Simon 1997).

If the dipole moment oscillates perpendicular to the molecular axis, the selection rule is

$$\Delta \upsilon = +1 \text{ and } \Delta J = 0, \pm 1 \qquad (2.80)$$

in this case in addition to R branch and P branch, the absorption spectrum consists a *Q branch* (rotational-vibrational transition with $\Delta J = 0$) and the absorption band is called a *perpendicular band*. Figure 2.19 shows a parallel and a perpendicular band of CO_2.

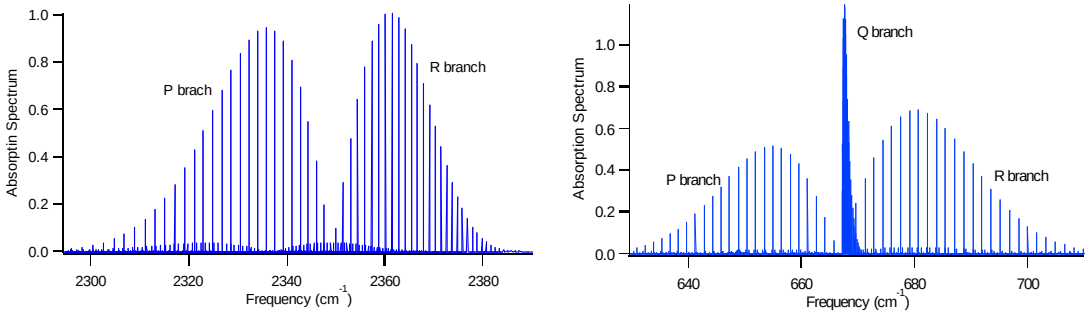

Figure 2.19: One of the Parallel band (left trace) and perpendicular band (right trace) in CO_2.

2.5 Vibrational-Rotational Spectrum (MIT(website); Bernath 1995; Nagali, Chou et al. 1996; McQuarrie and Simon 1997)

As explained in Section 2.3.2, based on Equation (2.64), the attenuation of a radiation beam due to absorption depends on absorption cross section, the population difference, $\Delta N = N_0 - N_1$, and the optical path length. The integral of the cross section as a function of frequency represents the oscillator strength and is a fixed quantity for a particular transition. The oscillator strength depends primarily on the upper and lower state functions and the dipole moment(s) of the molecule. However, the relative population between upper and lower states depends on temperature, and this controls the shape of an absorption spectra looks like. Here I try to draw a simple picture of vibrational-rotational spectra for a very simple case (a diatomic molecule based on harmonic oscillator and rigid rotor). As a definition, when a molecule absorbs infrared radiation, the vibrational transition is accompanied by a rotational transition. This kind of transition is called *vibrational-rotational* or a *ro-vibrational* transition. (Figure 2.20).

Consider a system comprised of N particular molecules having different electronic, vibrational and rotational energy levels at temperature T. Based on a *Boltzmann distribution*, at thermal equilibrium, the number of molecules at particular energy state E_i can be calculated by

$$N_i = \frac{N}{Q(T)} g_i \exp(-E_i / k_B T) \qquad (2.81)$$

where, g_i and k_B are degeneracy of the i^{th} state and Boltzmann constant respectively. *Q(T)* is the partition function of the molecule and is defined by

$$Q(T) = \sum_i g_i \exp(-E_i / k_B T) \qquad (2.82)$$

Now, lets consider a particular ro-vibrational transition, which takes molecules from state E_i to E_f. Suppose E_i and E_f are energy of states with quantum numbers of (v'', J'') and (v', J') respectively. Using the fact that, in many cases there is no appreciable thermal population in upper state (v', J') , and also molecules are usually at their vibrational ground state, only transitions initiating from ground vibrational state shown in Figure 2.20 are assumed to occur, and the corresponding change in population will be:

$$\begin{aligned} \Delta N &= N(v'', J'') - N(v', J') \\ &\propto g(J'') \exp(-E_{J''} / k_B T) \\ &= (2J'' + 1) \exp[-hc\tilde{B}J''(J'' + 1) / k_B T] \end{aligned} \qquad (2.83)$$

where the rotational degeneracy and rotational for a diatomic molecule based on rigid rotor from Section 2.2.3.1 are used. Therefore the absorption spectrum, which is proportional to the change in population, can be obtained from (2.83) and the results would appear as in Figure 2.21.

In Figure 2.21, the vibrational-rotational spectrum is comprised of equally spaced lines and is symmetric. In fact, as discussed in Section 2.2.3, the vibrational and rotational transitions are not independent and a real spectrum looks like figure 2.22.

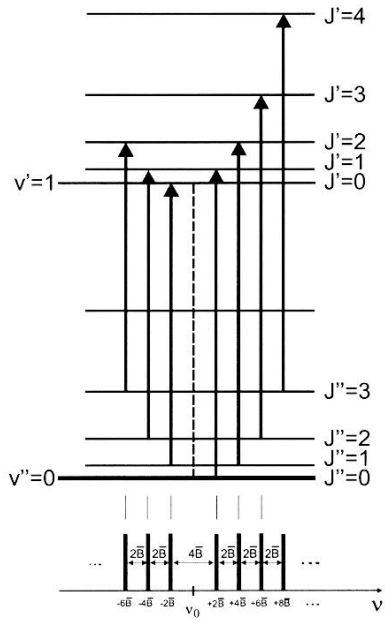

Figure 2.20: A typical ro-vibrational transition, from (MIT(website)).

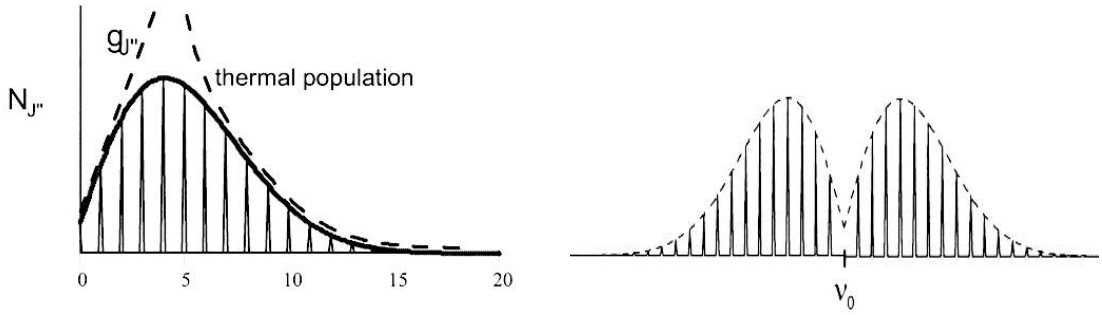

Figure 2.21: The left graph shows the variation of population density in lower state energy with $J'' > 0$ in a diatomic molecule based on rigid rotor model. Right graph shows the spectrum of a diatomic molecule based on rigid rotor model (the transitions for all possible J'' are considered (MIT(website)).

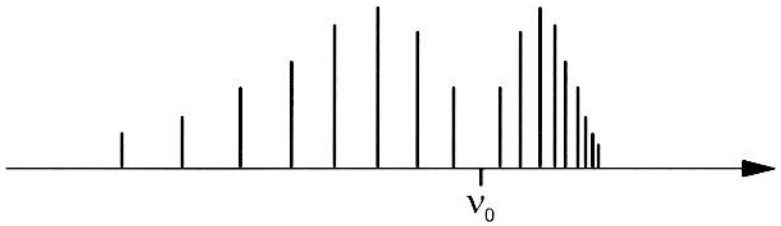

Figure 2.22: A typical spectrum of a real diatomic molecule (MIT(website)).

2.6 Beer-Lambert Law

Based on discussions provided in previous sections, the attenuation of a radiation beam through a region can be calculated from equation (2.64). This equation may be written as

$$I = I_0 e^{-k(\nu)L} \qquad (2.84)$$

where $k(\nu) = (N_0 - N_1)\sigma(\nu)$ (2.85)

is called absorption coefficient. For a ro-vibrational transition, as explained in Section 2.4, if the effect of stimulated emission is neglected, then the population change will be proportional to

$$\Delta N = N_0(\nu'', J'') - N_1(\nu', J') \approx N_0(J'') = \frac{g_{J''}}{Q(T)} \exp(-hcE''/k_B T)N \qquad (2.86)$$

where, $g_{J''}, Q(T)$, and E'' are lower-state degeneracy, molecular partition function at T and lower-state energy. If the effect of stimulated emission also is considered, then the right hand side of Equation (2.86) must be multiplied by $1 - \exp(-hc\nu_0 / k_B T)$.

Considering above assumptions, and writing the absorption coefficient based on the partial pressure of absorbing gas P_{abs} (instead of molecular number density N), Equation (2.84) can be written as

$$I = I_0 e^{-S(T)P_{abs}\phi(\nu-\nu_0)L} \qquad (2.87)$$

Equation (2.87) is called the Beer-Lambert Law. In this equation *S(T)* is called absorption line strength, which is purely a temperature dependent parameter and may be expressed by

$$S(T) = N_L\left(\frac{273}{T}\right)\left(\frac{\pi e^2}{m_e c^2}\right)\frac{g_{J'}}{Q(T)}\exp\left(-\frac{hcE''}{k_B T}\right)f\left[1-\exp\left(-\frac{hc\nu_0}{k_B T}\right)\right] \qquad (2.88)$$

where N_L (cm^{-3}), e (e.u.), and m_e (g) are Loschmidt's number, the electron charge, and electron mass, respectively; c (cm s^{-1}) is the speed of light; *Q(T)* is the molecular partition function; h (J s) is Planck's constant; k_B (J K^{-1}) is Boltzmann's constant; and $g_{J''}, E''$, and f are the lower-state degeneracy, the lower-state energy level, and the oscillator strength for the transition, respectively. $\phi(\nu-\nu_0)$ in Equation (2.87) is line-shape function and in general, as explained in previous sections, it depends on temperature and pressure and usually expressed by a Voigt function.

3 Techniques of Tunable Diode Laser Absorption Spectroscopy

Absorption spectroscopy using tunable diode lasers (TDLs) is based on tuning of the laser optical frequency across a selected absorption transition of a particular species. In general, tunable diode lasers have very narrow line widths and their optical frequencies can be tuned by changing the laser temperature or laser injection drive current. Several techniques for laser modulation and signal interpretation exist; these are the subject of this chapter. In the implementation of all of the techniques, the laser frequency is kept around the center of the transition frequency by adjusting the laser temperature. Then, the frequency of laser light is tuned by changing the injection current. As we will explain in next sections, based on the type of current modulation, different methods of absorption spectroscopy are realized.

3.1 Direct absorption

In this technique (Ku and Hinkley 1975; Hanson, Kuntx et al. 1977; Nagali, Chou et al. 1996; Mihalcea, Webber et al. 1998; Durry and Megie 1999) the wavelength of the tunable diode laser is tuned across the selected transition by ramp-modulating the injection current. A simple experimental set up is shown in Figure 3.1. Typically the emitted laser light is split into three beams by use of two optical beam splitters and one mirror. According to Figure 3.1, the first beam is directed through a probe region and the attenuated beam is detected by the first photodiode detector. The second beam is sent to an interferometer (e.g. ring interferometer) and is detected by the second detector. The signal from the second detector is used to track the

wavelength tuning of the laser with time, to enable the transfer of time domain information to the frequency domain. Finally, the third beam is passed through the ambient and is detected by a third detector. The output signal from the third detector provides relevant information about the background signal.

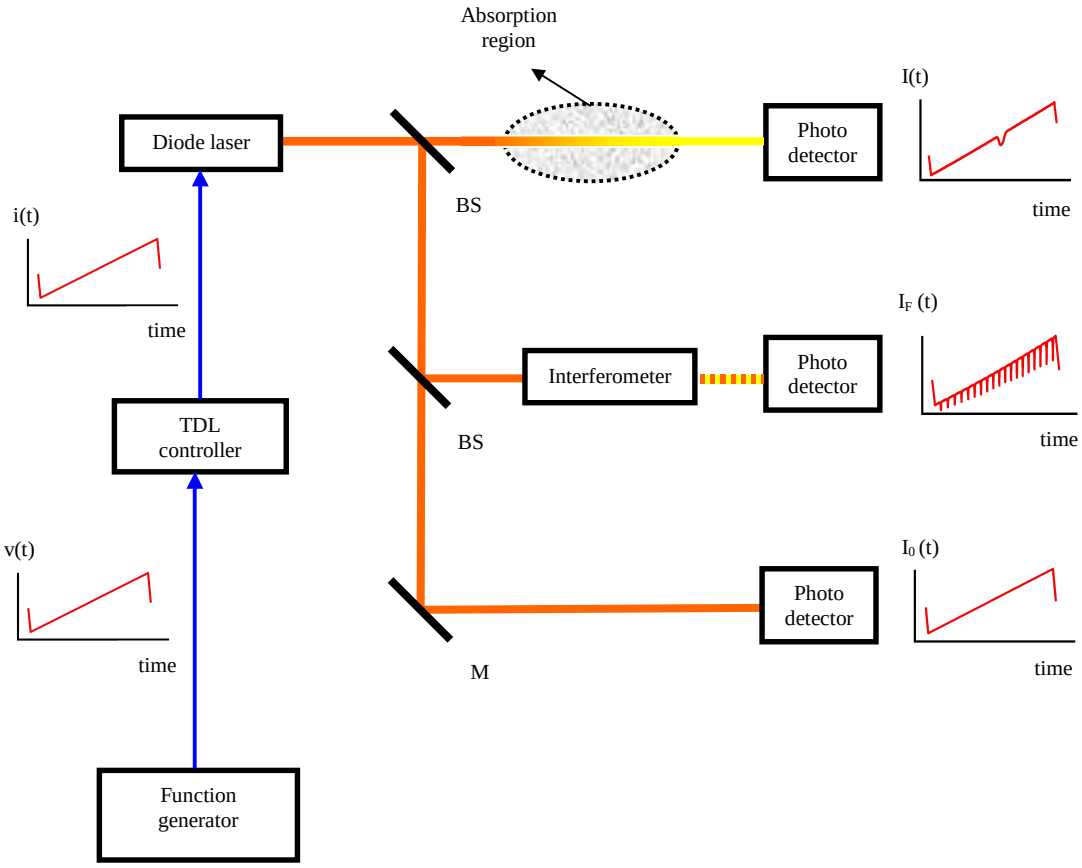

Figure 3.1: Typical experimental setup used direct absorption.

As shown in Figure (3.2), for quantification of the measurements (after background correction), first the absorbance of laser light at time t, $\ln(I_0 / I)$, is determined from the measured transmitted intensity I(t), normalized by the un-attenuated signal $I_0(t)$. By comparison of the attenuated signal I(t) and interferometer signal $I_F(t)$, the absorption of the light as the laser is scanned is obtained. Using the results from step one and two, the measured absorbance as a function of time is converted to absorbance as a function of frequency. Upon obtaining absorbance v.s optical frequency, the measured absorbance is fit with suitable line shape (*e.g.* Voigt function) that can describe the line-broadening processes. Using the fact that the integral of line-shape function is unity, $\int g(\nu - \nu_0) d\nu = 1$, the integral of the fitted curve is used to calculate the absorber concentration (Equation. 2.6).

$$P_{abs} = \frac{1}{S(T)L} \int_{\nu} \ln(\frac{I_0}{I}) d\nu \qquad (3.1)$$

where line strength *S(T)* is only a temperature dependent parameter and is obtained from a database (e.g. HITRAN) or from experiment. It should be mentioned that if the signal to noise ratio (S/N) of measured absorbance is large enough, (S/N > 100), the absorbance integral can be calculated directly from measured absorbance and therefore fitting is no longer required.

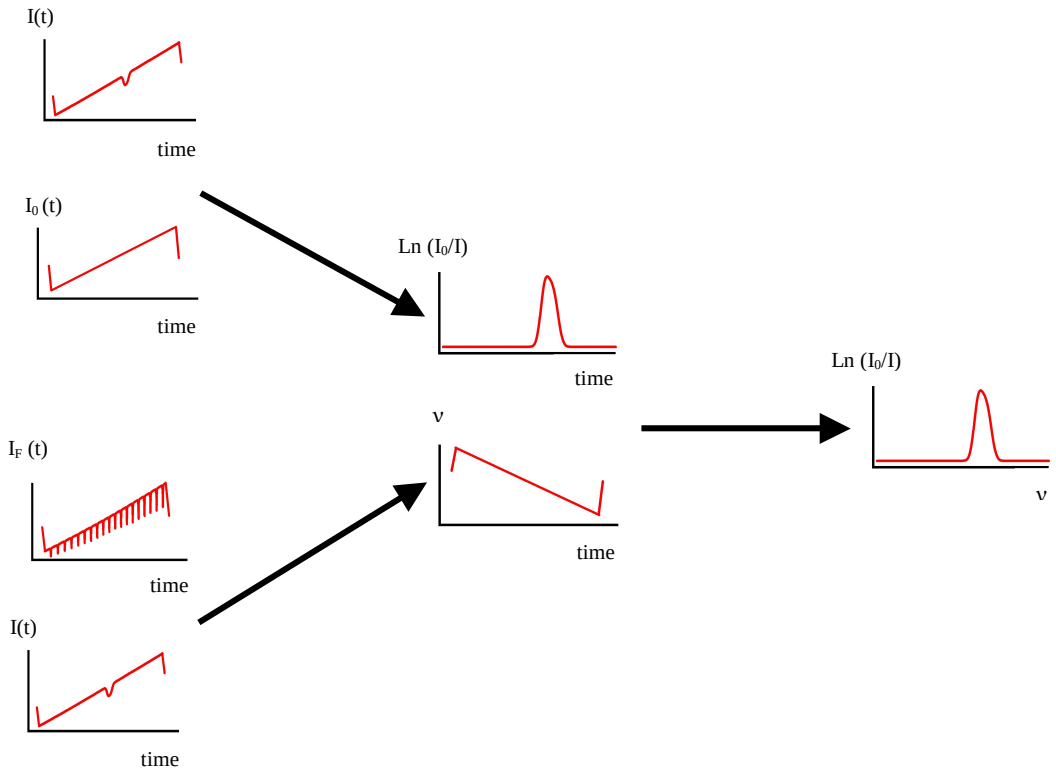

Figure 3.2: Typical data processing used for quantification of direct absorption technique

A direct absorption technique is thus very simple and the quantification of the measurement is straightforward but there are two main drawbacks. First, it requires integration over the whole spectra, which is not always possible, either due to interference between transitions or spectral broadening. Second, the primary disadvantage is the low sensitivity of direct absorption. In addition, quantification of this technique is very sensitive to the measured reference signal and therefore any miscalculation of reference signal causes an error in the concentration calculation.

3.2 Wavelength Modulation

In Wavelength Modulation Spectroscopy (WMS), (Reid and Labrie 1981; Bomse, Silver et al. 1992; Philippe and Hanson 1993), the injection current is usually swept at sweep frequency (50-200 Hz) and a small sinusoidal modulation (10-50 kHz) or "dither" (Uehara and Tai 1992; Jin, Xu et al. 1997) is superimposed upon the sweep signal. Figure 3.3. shows a typical setup for wavelength-modulation spectroscopy. Traditional WMS, as discussed in the literature, is confined to the regime in which the modulation frequency is much smaller than the frequency of the absorption half-width.

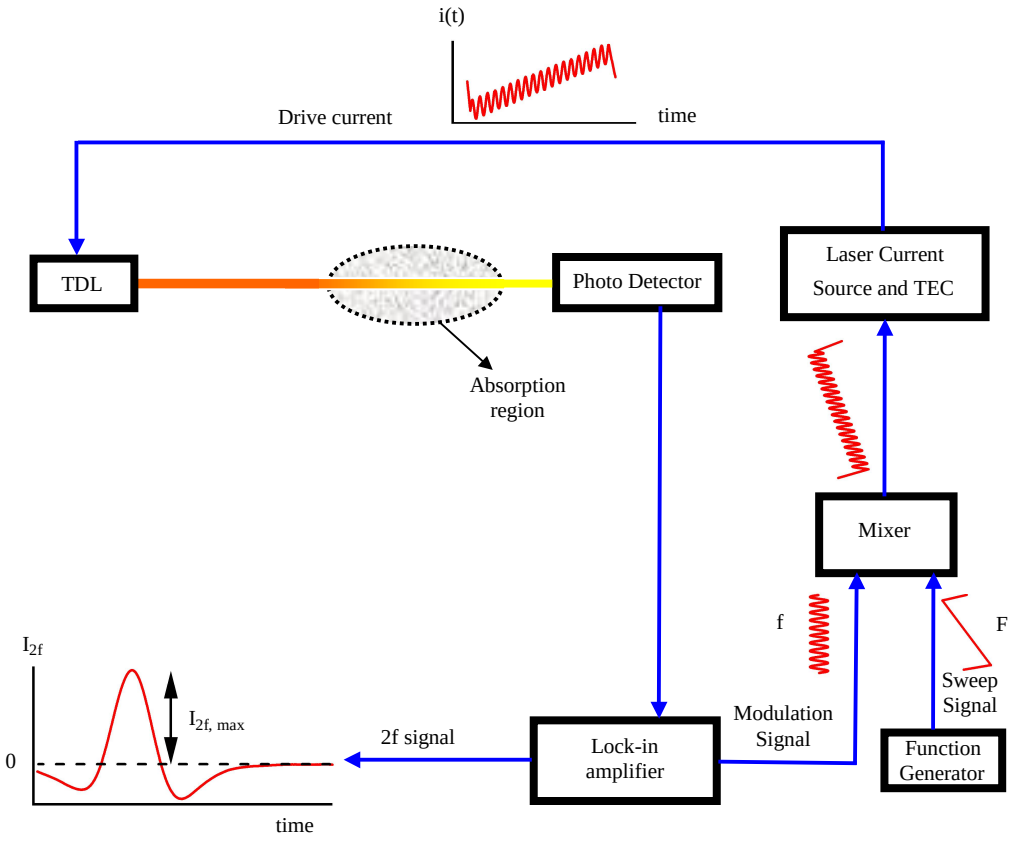

Figure 3.3. A typical experimental setup for wavelength-modulation spectroscopy.

This modulation allows increased sensitivity compared with direct absorption, through the rejection of lower frequency noise by employing a relatively high dither frequency (decreasing 1/f laser noise), and also by decreasing the detection bandwidth by use of lock-in amplifier. It has been demonstrated that WMS, may improve sensitivities up to three orders of magnitude over conventional direct absorption method (Reid and Labrie 1981).

As shown in Figure 3.3, the absorption signal is detected by a photodector and the voltage signal from the detector, *I*, is locked at twice (or for times, etc.) of fundamental frequency, *f*, and corresponding harmonic signal (I_{2f} , I_{4f} , etc.) is captured by a lock-in amplifier. In a simple picture, for small absorption, $\alpha(\nu) = S\, g(\nu - \nu_0)\, L\, P_{abs} < 0.1$, the output signal from lock-in amplifier, I_{2f}, is related to absorber pressure by

$$\begin{aligned} I_{2f}(\nu) &= K\, H_2(\nu - \nu_0)\, S\, g(\nu_0 - \nu_0)\, L\, P_{abs} \\ &= K\, H_2(\nu - \nu_0)\, \alpha_0 \end{aligned} \qquad (3.2)$$

where $H_2(\nu - \nu_0)$ is the second harmonic component of the modulated normalized line-shape (with a maximum of 1.0) and *K* is electro-optical gain. In this equation, $\alpha_0 = S\, g(\nu_0 - \nu_0)\, L\, P_{abs}$ represents the maximum absorbance in the transmitted light. Parameters $H_2(\nu - \nu_0)$ and α_0 both depend on the line-shape function and therefore depend upon temperature and gas species concentrations. $H_2(\nu - \nu_0)$ also depends on the modulation index. In WMS, the peak of second harmonic signal $I_{2f,max}$ is related to the absorbing specie concentration by

$$I_{2f,\max} = K\, H_2(\nu_0)\, S\, g(\nu_0 - \nu_0)\, L\, P_{abs} \qquad (3.3)$$

where, $H_2(\nu_0)$ is the second harmonic of modulated normalized line-shape function at the center of absorption feature.

Equation (3.3), only requires information at the center of absorption line for concentration calculation. If this information is available, there is no need to transform temporally-acquired signal to optical frequency, and hence typically in WMS an interferometer is not required.

In general, the second harmonic signal, I_{2f}, is more complicated than as expressed Iin Equation (3.2), but this equation shows the main properties of the second harmonic signal. For example, Equation (3.2) illustrates that for quantification of one species, the line-shape function and therefore concentration of all species in the system and temperature must be known. This is an enormous challenge and represents a large hurdle for quantification of WMS, particularly in combustion systems where the concentrations of all species are generally unknown. In the next chapter main issues and solutions for quantification of WMS will be addressed, along with a more advance treatment of WMS theory.

3.3 Frequency Modulation

Frequency Modulation Spectroscopy (FMS) is an offshoot of WMS, in which the modulation frequency is larger than the absorption half-width frequency (Silver 1992). The rationale for this approach is that, at such frequencies (typically at least several hundred megahertz) the laser source (excess) noise term is negligible (Lenth 1983; Gehrtz, Lenth et al. 1986). This translates to potential sensitivities of 10^{-7}-10^{-8} absorbance with a 1-Hz detection bandwidth (Silver 1992). In contrast to the theory

of WMS, which is based on the perturbation in the intensity of laser light, FMS theory is based on how a laser electric fields being transmitted through an absorptive (and dispersive) medium. This approach retains phase information, unlike WMS theory, which uses an intensity rather than electric field. In addition, FMS theory includes residual amplitude modulation (AM) effects. Thus the FMS derivation provides a richer picture of the results and these results are applicable to the WMS regime as well (Silver 1992; Avetisov and Kauranen 1997).

When laser current of a diode laser is modulated at frequency $\omega_m=2\pi f_m$, simultaneous AM and FM of electric field occurs such that (Lenth 1983):

$$E(t) = E_o\left[1 + M\sin(\omega_m t + \psi)\right]\exp\left[i\omega_0 t + i\beta\sin(\omega_m t)\right] \qquad (3.4)$$

in which, ω_0, M, and β are the laser carrier frequency, and the AM and FM index respectively. Also the phase difference between AM and FM is denoted ψ and has been found to have a value of $\pi/2$ in number of experiments for frequency modulation $f_m < 750\ MHz$ (Lenth 1984; Gehrtz, Lenth et al. 1986). The instantaneous optical frequency is $\omega(t) = \omega_0 + \beta\omega_m\cos(\omega_m t)$. Since the intensity is proportional to the square of electric field, the total light intensity is (Silver 1992):

$$I(t) = I_0\left[1 + 2M\sin(\omega_m t)\right] \qquad (3.5)$$

where I_0 is detected intensity at ω_0 and the AM index can be obtained from the following equation:

$$M = \frac{\left|I_0 - I_{\max}\right|}{2I_0} \qquad (3.6)$$

The phase modulation component can be expanded in terms of Bessel functions $J_n(\beta)$ as (Abramowitz and Stegun 1972)

$$\exp[i\beta\sin(\omega_m t)] = \sum_{n=-\infty}^{n=+\infty} J_n(\beta)\exp(in\omega_m t) \qquad (3.7)$$

By expanding the AM term in (3.4) in terms of exponentials, then $E(t)$ can be written as

$$E(t) = E_0\exp(\omega_0 t)\sum_{n=-\infty}^{n=+\infty} r_n\exp(in\omega_m t) \qquad (3.8)$$

where (Cooper and Warren 1987)

$$\begin{aligned} r_n(\beta, M, \psi) &= J_n(\beta) + \frac{M}{2i}[\exp(i\psi)J_{n-1}(\beta) - \exp(-i\psi)J_{n+1}(\beta)] \\ &= \sum_{k=-1}^{1} a_k . J_{n-k}(\beta) \end{aligned} \qquad (3.9)$$

with

$$a_0 = 1, \quad a_{\pm 1} = \frac{\pm M}{2i}\cdot\exp(\pm i\psi) \qquad (3.10)$$

Based on Equation (3.8), as result of modulation, the radiation field will no longer contain only the single optical frequency ω_0, but it includes other frequency components with frequency $\omega_0 + n\omega_m$ and amplitude of r_n given in (3.9) (with $n = 0, \pm 1, \pm 2, \ldots$). The frequency ω_0 is carrier frequency and the other frequencies are called sideband frequencies. While the carrier frequency has the maximum amplitude, the amplitude of sidebands decreases by increasing the absolute of *n*.

For a better understanding of the absorption phenomena in FMS, consider a modulation with small M and β. Then the radiation field given in (3.8) as first described by(Lenth 1983) will be simplified as:

$$E(t) = E_0\left[e^{i\omega_0 t} + (\frac{\beta}{2} + \frac{M}{2i}e^{i\psi})e^{i(\omega_0+\omega_m)t} + (-\frac{\beta}{2} - \frac{M}{2i}e^{-i\psi})e^{i(\omega_0-\omega_m)t} \right] \quad (3.11)$$

Therefore for small modulation index, the radiation field is described by a strong carrier frequency at ω_0 and two weak sidebands at $\omega_0 \pm \omega_m$.

If $\psi = 0$ or π, then:

$$E(t) = E_0\left[e^{i\omega_0 t} + (\frac{\beta}{2} + \frac{M}{2i})e^{i(\omega_0+\omega_m)t} - (\frac{\beta}{2} + \frac{M}{2i})e^{i(\omega_0-\omega_m)t} \right] \quad (3.12)$$

If this radiation is detected by a square-law wave photodetector, in which the photodetector generates output signal proportional to the input optical power or square of amplitude of electric field, then the two side bands each beats with the central component to produce signals at ω_m. These two beat signals are 180^o out of phase, and since the side bands are of equal intensity the beat signals cancel exactly and giving no signal component at ω_m. However; if $\psi \neq n\pi$, the detected radiation will have always a component at ω_m. The schematic of a typical power spectrum of the modulated laser (when M and β are small) is shown in Figure 3.4.

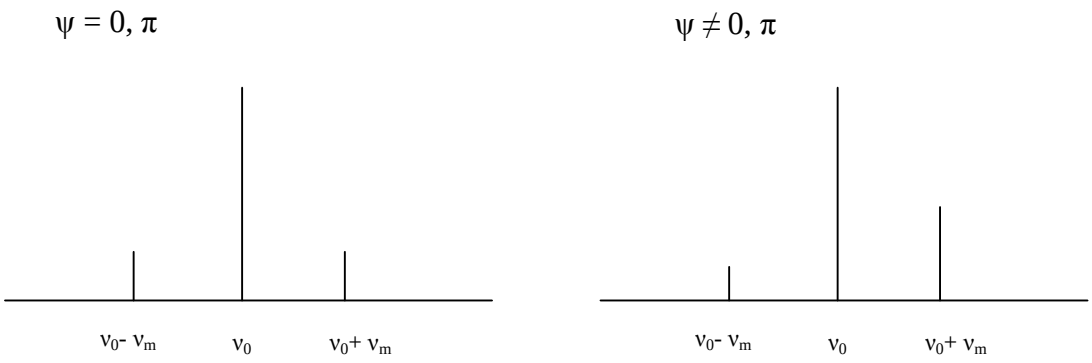

Figure 3.4: Typical power spectrum of the modulated laser in FMS

If the modulated laser light passes through absorptive medium, each of the sidebands is attenuated differently and the transmitted radiation field will be:

$$E(t) = E_0\left[T_0 e^{i\omega_0 t} + T_1\left(\frac{\beta}{2} + \frac{M}{2i}e^{i\psi}\right)e^{i(\omega_0+\omega_m)t} + T_{-1}\left(-\frac{\beta}{2} - \frac{M}{2i}e^{-i\psi}\right)e^{i(\omega_0-\omega_m)t}\right] \quad (3.13)$$

where, T_n is the complex transmission function and is defined as:

$$T_n = e^{-\delta_n - i\phi_n} \qquad n = -1, 0, 1 \qquad (3.14)$$

in which, δ_n and ϕ_n are amplitude attenuation and optical phase shift at $\omega_0 + n\omega_m$ and are calculated as:

$$\delta_n = \frac{\alpha_n}{2}, \quad \phi_n = \frac{\eta_n L(\omega_0 + n\omega_m)}{C} \qquad n = -1, 0, 1 \qquad (3.15)$$

in which α_n and η_n are absorbance and refractive index of the probe region at frequency $\omega_0 + n\omega_m$ respectively. L is length of probe region and C represent light velocity in vacuum. The transmitted light intensity $I_T(t)$ impinging onto the photodetector is proportional to $\left|E_T^2(t)\right|$. Under the further assumption that the absorption losses and phase shifts experienced by the two sidebands and the carrier

are small, *i.e.* $|\delta_0 - \delta_{\pm 1}| \ll 1$, and $|\phi_0 - \phi_{\pm 1}| \ll 1$ the transmitted intensity is readily obtained as (Lenth 1983)

$$I_T(t) \propto I_0[1 + \beta(\delta_{-1} - \delta_1)\cos\omega_m t + M(\phi_{-1} - \phi_1)\cos(\omega_m t + \psi) + M(2 - 2\delta_0 - \delta_1 - \delta_{-1})\sin(\omega_m t + \psi) + \beta(\phi_{-1} + \phi_1 - 2\phi_0)\sin(\omega_m t)] \quad (3.16)$$

Using a radiofrequency (rf) mixer, one can select any of the terms in (3.16) by adjusting the phase at the rf mixer. A typical experimental setup to detect these components is schematically illustrated in Figure 3.5.

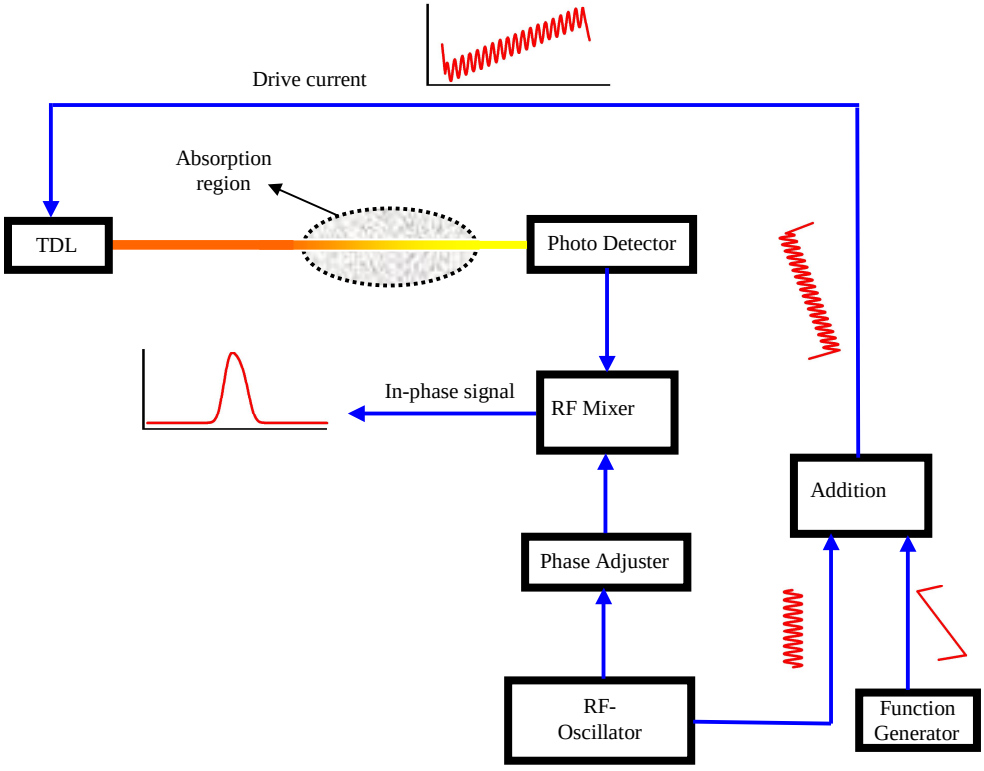

Figure 3.5: The schematic of an experimental setup for FMS

Based on the experimental setup shown in Figure 3.5, a single mode diode laser is used as a light source. The diode drive current consists of a DC bias current, a relatively slow saw-tooth signal, of a few hundred *Hz* up to a few hundred *KHz*,

which allows the frequency tuning of laser along absorption transition, and also, a sinusoidal rf signal, in the range of a few hundred *MHz* to a few *GHz*. The modulated laser light is directed to absorbing medium and is detected by a fast photodetector. The output of the detector is phase-sensitive detected by a double balanced mixer, a passive circuit that forms the product of two analog waveforms, and can be controlled by phase adjuster. This adjustment allows us to pick either absorption (signal containing δ_n terms) or dispersion signal (signal containing ϕ_n terma) from the output of the photodetector (Lenth 1983; Gehrtz, Lenth et al. 1986). And finally, the resulting signal is displayed on a digital oscilloscope or computer for signal processing. Typical results of FMS are shown in Figure 3.6. Regarding the detection of the photodetector signal using rf mixer, the component of the photodetector signal which is exactly in-phase with the modulation signal is called in-phase signal, and the component with 90 phase difference is called quadrature signal.

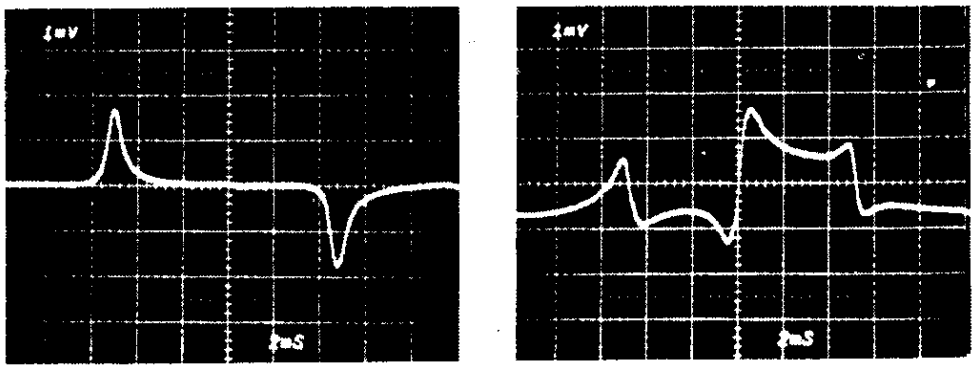

Figure 3.6: Output signal in frequency-modulation spectroscopy of Fabry-Perot resonance: left trace shows in-phase component, right trace shows quadrature component (Lenth 1983).

For quantification, based on Equation (3.16), one can relate the in-phase component (terms with $\cos\omega_m t$) to the concentration. As an example, in a condition when $\psi = \pi/2$, where $\omega_m >> FWHM$ of the absorption feature, each absorption spectra (of Figure 3.6), would purely represent the absorption of each sideband (say $\omega_0 + \omega_m$) and therefore the other frequency components (carrier frequency and the other sideband frequency) would not contribute to the in-phase signal (because $\delta_0 = \delta_{-1} = 0$). Under this condition, the in-phase component can be given by

$$I_{\text{in-phase}} \propto 1 - \beta\delta_1(\nu) + M[2 - \delta_1(\nu)] = 1 + 2M - (\beta + M)\delta_1(\nu) \qquad (3.17)$$

in which, using Equation (3.15), δ_1 is related to partial pressure of the absorbing species by

$$\delta_1(\nu) = \frac{1}{2}\alpha_1(\nu) = \frac{1}{2}S(T)g(\nu - \nu_1)P_{abs}L \qquad (3.18)$$

In Equation (3.17), β and M are laser properties, and depends on the amplitude and the frequency of the modulation current to laser, and can be obtained experimentally. Usually the frequency modulation index is much larger than the intensity modulation index and a typical value of $\beta/M \approx 20$ is reported in (Lenth 1983).

For trace gas detection for improving the detection limit, larger values of β are usually used (e.g. $\beta \sim 1.0$), and this results in the presence of higher order sidebands $n = \cdots, -2, -1, 0, 1, 2, \cdots$. Also, the FMS condition that ω_m is much greater than the absorption line width is not always met because of the difficulty of achieving the necessary detection bandwidth. In this regard the theory of Two-Tone Frequency

Modulation Spectroscopy (TTFMS) was introduced, which is explained briefly in the following section.

3.4 Two-tone Frequency Modulation Spectroscopy

In discussions of TTFMS (Janik, Carlisle et al. 1986; Cooper and Warren 1987; Avetisov and Kauranen 1996), the conventional FMS is termed as Single-Tone Frequency Modulation Spectroscopy (STFMS). In TTFMS, a diode laser is two-tone frequency modulated by imposing two closely spaced RF signals $\omega_1 = \omega_m + \Omega/2$ and $\omega_2 = \omega_m - \Omega/2$ directly to the diode laser drive current. In general, the generator frequency ω_m and $\Omega/2$ are chosen such that ω_m is comparable with or larger than the absorption half width (a few *GHz*) to obtain optimum sensitivity, and the intermediate frequency $\Omega = \omega_1 - \omega_2$ that is detected is small in comparison with the modulation frequency but large enough to avoid low frequency *(1/f)* noise, i.e., typically *5-20 MHz*.

Similar to discussion provided for single tone FMS in Section 3.3, injection current modulation of a diode laser at two closely spaced frequencies $\omega_1 = \omega_m + \Omega/2$ and $\omega_2 = \omega_m - \Omega/2$ produces the electric field

$$E(t) = E_o\left[1 + M_1 \sin(\omega_1 t + \psi_1)\right]\left[1 + M_2 \sin(\omega_2 t + \psi_2)\right] \times \exp\left[i\omega_0 t + i\beta_1 \sin(\omega_1 t)\right] \exp\left[i\omega_0 t + i\beta_2 \sin(\omega_2 t)\right] \tag{3.19}$$

where ω_0 is laser carrier frequency. As the modulation frequencies, ω_1 and ω_2, are generally selected very close to each other, the phase difference ψ, and the FM and AM indices of the diode laser at the two modulation frequencies are nearly the same

and therefore the following approximation is adopted in Equation (3.19), as in (Avetisov and Kauranen 1996)

$$M_1 \cong M_2, \quad \beta_1 \cong \beta_2, \quad \psi_1 \cong \psi_2 \qquad (3.20)$$

Following the same procedure explained for single tone FMS in section 3.3, and using approximation given in (3.20), the electric field in (3.19) can be simplified by

$$E(t) = E_0 \exp(i\omega_0 t) \sum_{n,m=-\infty}^{+\infty} r_n r_m \exp[i(n\omega_1 + m\omega_2)] \qquad (3.21)$$

where r_n and r_m can be obtained from (3.9). A schematic of the spectral distribution of the two-tone frequency-modulated laser field for β=1.0 and M=0 is shown in Figure 3.7. In this figure, spacing between different side bands is greatly exaggerated for illustration. The central component in ($n = m = 0$) is the laser carrier frequency, $\nu_0 = \omega_0 / 2\pi$, and the sidebands are $\nu_0 + n\nu_1 + m\nu_2$.

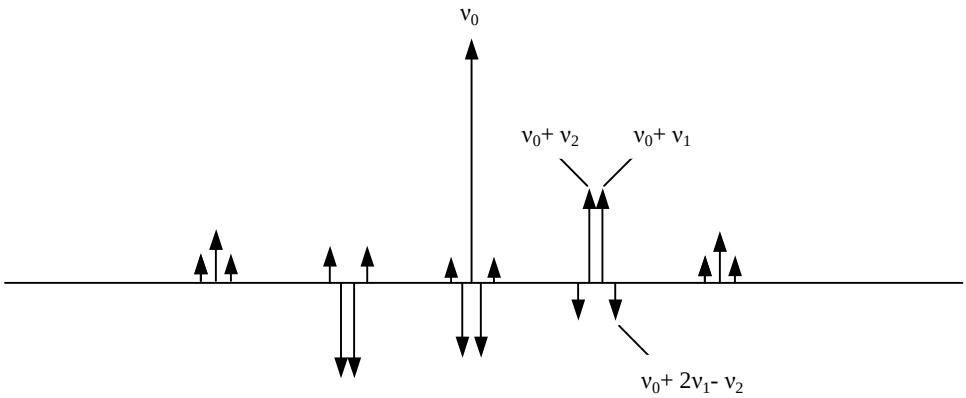

Figure 3.7: Spectral distribution of the laser field in two-tone frequency modulated diode laser at v_1 and v_2 with β =1.0 and M =0.

As result of the interaction of the electric field given in Equation (3.21), with a sample containing absorbing molecules, the electric field is perturbed according to (Avetisov and Kauranen 1996)

$$E(t) = E_0 \exp(i\omega_0 t) \sum_{n,m=-\infty}^{+\infty} r_n r_m \exp[i(n\omega_1 + m\omega_2)] \exp(-1/2\alpha_{n,m} - i\phi_{n,m}) \qquad (3.22)$$

where $\alpha(\nu)$ and $\phi(\nu)$ are defined as

$$\begin{aligned} \alpha_{n,m} &= \alpha(\nu_0 + n\nu_1 + m\nu_2) = S(T) P_{abc} \mathrm{g}(\nu_0 + n\nu_1 + m\nu_2) L \\ \phi_{n,m} &= \phi(\nu_0 + n\nu_1 + m\nu_2) = \frac{\eta(\nu_0 + n\nu_1 + m\nu_2) L(\nu_0 + n\nu_1 + m\nu_2)}{c} \end{aligned} \qquad (3.23)$$

The intensity detected by a photodetector $I(t) = c\varepsilon_0 EE^* / 2$ is given by (Avetisov and Kauranen 1996)

$$\begin{aligned} I(t) = \frac{c\varepsilon_0}{2} {E_0}^2 \sum_{\substack{n,m,\\ n',m'}} r_n r_m r_{n'}^* r_{m'}^* \exp[i(n-n')\omega_1 t + i(m-m')\omega_2 t] \\ \times \exp[-1/2(\alpha_{n,m} + \alpha_{n',m'}) - i(\phi_{n,m} - \phi_{n',m'})] \end{aligned} \qquad (3.24)$$

where c and ε_0 are light velocity and permeability in air respectively. The component of time varying intensity given in (3.24), arising from the heterodyning (mixing the detected and modulation signals to obtain particular frequency component of the detected signal at modulation frequency) of adjacent frequency sidebands at $\pm\Omega$, are obtained for $n - n' = \pm 1$ and $m - m' = \mp 1$. Summing the beat signals at Ω of Equation (3.23) makes

$$\begin{aligned} I_\Omega(t) = \frac{c\varepsilon_0}{2} {E_0}^2 \exp(-i\Omega t) \sum_{n,m} r_n r_m r_{n+1}^* r_{m-1}^* \\ \times \exp[-1/2(\alpha_{n,m} + \alpha_{n+1,m+1}) - i(\phi_{n,m} - \phi_{n+1,m-1})] + \text{c.c.} \end{aligned} \qquad (3.25)$$

where c.c. is complex conjugate of the right hand side in Equation (3.25). As a general approximation in TTFMS, the frequency Ω is chosen small enough that sidebands spaced at Ω experience the same absorption and dispersion. This yields the approximation $\nu_1 \approx \nu_2 \approx \nu_m = \omega_m / 2\pi$. Upon applying this approximation, the dispersion component (terms with phase $\phi_{n,m}$ information) in Equation (3.25) vanishes. If $I_\Omega(t)$ is detected by a phase-sensitive detector driven by frequency Ω, the in-phase component of $I_\Omega(t)$ can be obtained experimentally. Considering the approximation mentioned above, the in-phase component of $I_\Omega(t)$ based on Equation (3.25) will be related to the intensity absorption coefficient $\alpha(\nu)$, by

$$\text{In phase component signal} \propto \sum \text{Re}(r_n r_m r_{n+1}^* r_{m-1}^*) \exp\{-\alpha[\nu_0 + (n+m)\nu_m]\} \qquad (3.26)$$

In (3.26), the only unknown is $\alpha(\nu)$ which is related to concentration of absorbing molecule, line shape function and line strength (Equation 3.23). By tuning the laser carrier frequency across an absorption feature, the in-phase component of signal, given in (3.26), is obtained over the whole absorption spectra. Using a simple least square fitting to the detected in-phase component, the partial pressure of absorbing gas can be easily calculated by using a proper line-shape function (when the line strength is known.) Figure (3.8) shows a simple experimental setup and typical output signal observed in TTFMS.

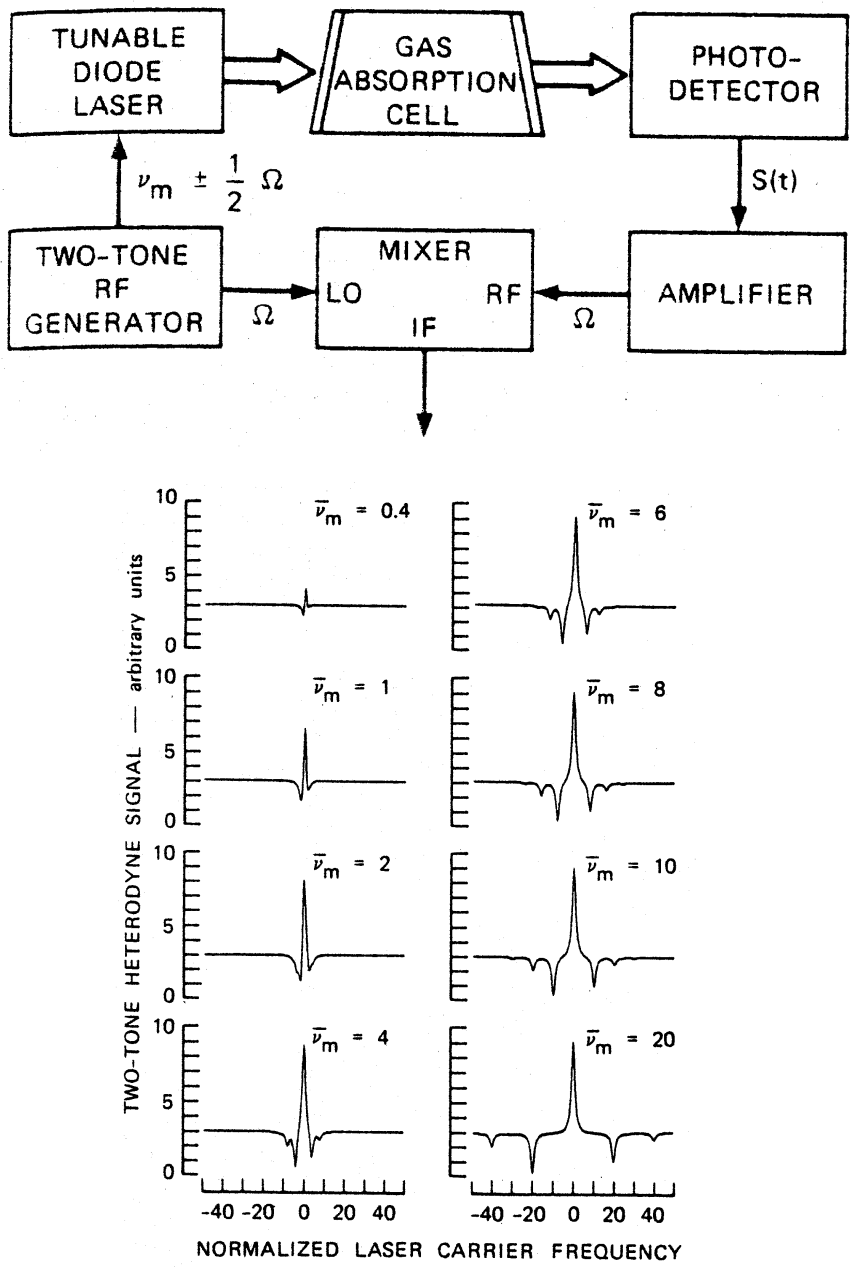

Figure 3.8: Typical experimental arrangement for two-tone frequency modulation (top trace). Bottom trace shows calculated absorption signal at the output of RF mixer (v.s normalized laser frequency) at different average modulation frequency ν_m, with β=0.9, M=.064 and $\psi = \pi/2$ using a lorentzian line shape with a maximum absorbance of $\alpha_0 = 0.01$. The normalized frequency of the laser carrier frequency is defined as $\bar{\nu} = |\nu - \nu_0| / \text{HWHM}$. Also normalized average modulation frequency $\bar{\nu}_m$, is defined by $\bar{\nu}_m = \nu_m / \text{HWHM}$ (Cooper and Warren 1987). Regarding the mixer iput/out, they are defined as: LO is Local Oscillator signal, RF is Radio Frequency signal, and IF is Intermediate Frequency signal.

4 Theory of Wavelength-modulation Spectroscopy

In this chapter, the detail of a general theoretical model of wavelength-modulation spectroscopy, developed in this research is discussed. In the second section, the properties of the WMS output signal, which represents the nth harmonic of the photodetector signal, are studied in depth. Following that, based on the theoretical formalism presented in the first section, methods for concentration and temperature measurement are presented. In the fourth section, major issues and corresponding solutions for concentration and temperature measurements using WMS at high temperatures in a combustion system are discussed. The fifth section, summarizes all required information (including laser and absorption transition parameters) needed for quantification of WMS for combustion diagnostics; measurement of these parameters will be addressed in detail in Chapter 5.

4.1 Theory of wavelength-modulation spectroscopy

As explained in Chapter 3, in WMS (as opposed to FMS) the modulation frequency f is much smaller than absorption feature line-width (f usually is in the order of tens or hundreds of KHz). At these modulation frequencies, the strong sidebands are so close to the carrier frequency that they can not be distinguished. Therefore in WMS, in contrary with FMS, the spectrum of laser light remains unchanged during modulation (Figure 4.1). As result of this property, WMS is preferably described in terms of intensity (rather than electric field) as no phase

information is required. Also because of the relatively low frequency modulation in WMS, dispersion is negligible and therefore only absorption is considered. The former assumption can be justified by looking at Figure 4.2. According to the this Figure, by decreasing the modulation frequency, the contribution of the dispersion in the first harmonic signal drops much faster than absorption. Therefore, in WMS regime the dispersion term will be negligible compare to absorption. As we will see in the following, these properties of WMS help us to some extent simplify the formalism of absorption phenomena.

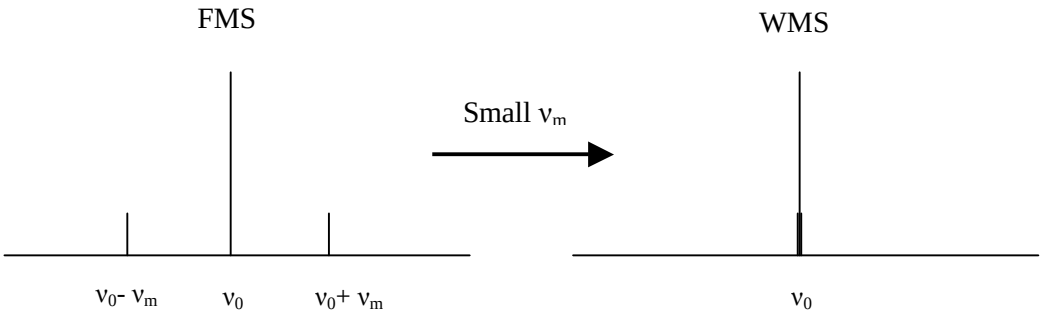

Figure 4.1: Comparison power spectrum between FMS and WMS

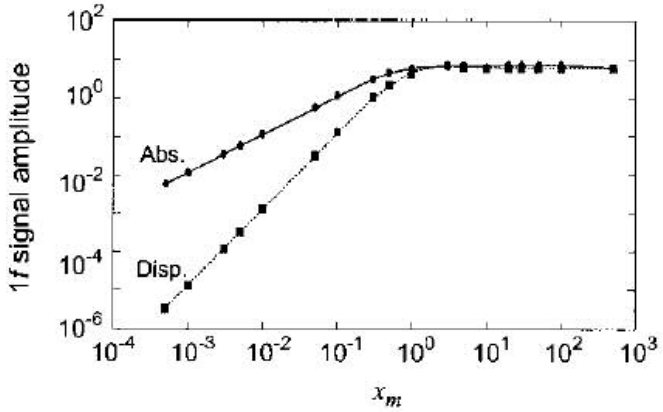

Figure 4.2: Amplitude of absorption and dispersion of the first harmonic signal as a function of normalized modulation frequency $x_m = f / \Delta\nu_{\text{line}}$ when FM index $\beta = \Delta\nu_m / f = 1$(Schilt, Thevenaz et al. 2003).

Theoretical models related to quantification of WMS have been studied by several authors. Wahlquist (Wahlquist 1961) was the first to derive an analytical formula for the first three harmonic components of a modulated Lorentzian absorption line. Arndt (Arndt 1965) generalizes Wahlquist formula for all of harmonic components of Lorentzian line shape using a different mathematical approach. Wilson (Wilson 1963) uses numerical integration to obtain the first three harmonics for both Lorentzian and Gaussian line shapes. In these papers no detailed experimental data confirming the formula were released. Reid and Labrie (Reid and Labrie 1981) using a modulated diode laser, compared calculated second harmonics of different line shapes (including Lorentzian, Gaussian, and Voigt functions) with experimental data and confirmed the earlier theoretical models.

Until the early 1990's, all theoretical models were based on wavelength (frequency) modulation only. However, in diode lasers, modulation of laser current, typically used to cause wavelength modulation, also causes intensity modulation. In 1993, Louis and Hanson (Philippe and Hanson 1993) derived a formula to include the effect of intensity modulation in WMS. Their model neglects the effect of change in intensity of diode laser as it is tuned slowly across an absorption transition during modulation. Schilt, et al. (Schilt, Thevenaz et al. 2003) presented a general theoretical model applicable to WMS using a diode laser, for Lorentzian absorption lines. Their theory is general, including detection phase, intensity modulation, frequency (wavelength) modulation, phase difference between frequency and intensity modulation, and as well as the effects of intensity variation of diode laser when it is tuned slowly across a selected transition. Their model is based on Arndt's model, but

it is generalized to the case when the frequency modulation is accompanied with intensity modulation. The main limitation of their model is that, it is only applicable for Lorentzian line shapes. At the same time, higher order nonlinearity in the intensity variation is not included. Parallel to the studies cited above, there have been other investigations based on Fourier decomposition of the detected signal, in which the presence of various background signals, also included in the theoretical model (Kluczynski and Axner 1999; Kluczynski, Lindberg et al. 2001; Kluczynski, Lindberg et al. 2001). In addition, Dore (Dore 2003) presented a model based on Fast Fourier Transformation of the detected signal to calculate any arbitrary line shape function when it is frequency modulated. However, this model does not include intensity modulation.

In the following, a very general theoretical model for quantification of WMS technique, particularly suitable for combustion measurement, is presented. This model is applicable for any line-shape function and it also includes higher order nonlinearity in the intensity.

If injection current i of a diode laser is modulated at frequency f (with angular frequency $\omega = 2\pi f$) as

$$i(t) = i_0 + \Delta i \cos \omega t \qquad (4.1)$$

(where are i_0 and Δi DC offset and amplitude of modulated current respectively) then the intensity of laser light I and also optical frequency ν will be modulated by

$$I(t) = \bar{I} + \Delta I \cos \omega t \qquad (4.2)$$

$$\nu(t) = \bar{\nu} - \Delta\nu_m \cos(\omega t + \psi) \qquad (4.3)$$

in which $\Delta\nu_m$ is the amplitude of the frequency modulation, ψ is phase difference between intensity and frequency modulation, $\bar{I}$ and, ΔI are average intensity and amplitude of intensity modulation respectively. As can be seen from (4.2) and (4.3), there is a linear relationship between intensity and optical frequency. This is only true when the modulation depth is relatively small - in WMS $\nu_m < 0.1\,\mathrm{cm}^{-1}$ is typical, and with this small tuning range a linear behavior is observed by almost all diode lasers.

According to the discussion of WMS in Chapter 3, as the optical frequency of a diode laser is modulated fast with frequency *f* (typically tens of KHz), simultaneously the laser center frequency $\bar{\nu}$ is tuned slowly across an absorption line by superimposing a low frequency ramp (triangular) injection current with frequency *F*, which is usually ~1/1000 of the modulation frequency *f*. The maximum tuning range of diode lasers with a low frequency current signal is typically about 1 cm^{-1}. At this maximum tuning range there is usually a nonlinear one-to-one relationship between intensity and optical frequency. In the following model a second order nonlinearity is considered, although it could be easily extended to higher order with little modification.

The low frequency current signal causes the intensity of the laser to vary parabolically as

$$I_0(\bar{\nu}) = I_0\left[1 + s_{F1}(\bar{\nu} - \bar{\nu}_0) + s_{F2}(\bar{\nu} - \bar{\nu}_0)^2\right], \qquad (4.4)$$

in which I_0 is the intensity of the laser light at arbitrary frequency $\bar{\nu}_0$. For simplicity we can choose $\bar{\nu}_0$ at the central frequency of the absorption peak, ν_0. In Equation (4.4) s_{F1} and s_{F2} are coefficients to fit the observed intensity-frequency relationship for the particular laser used, at ramp frequency F in 1/cm^{-1} and 1/cm^{-2} respectively. See Figure 4.3.

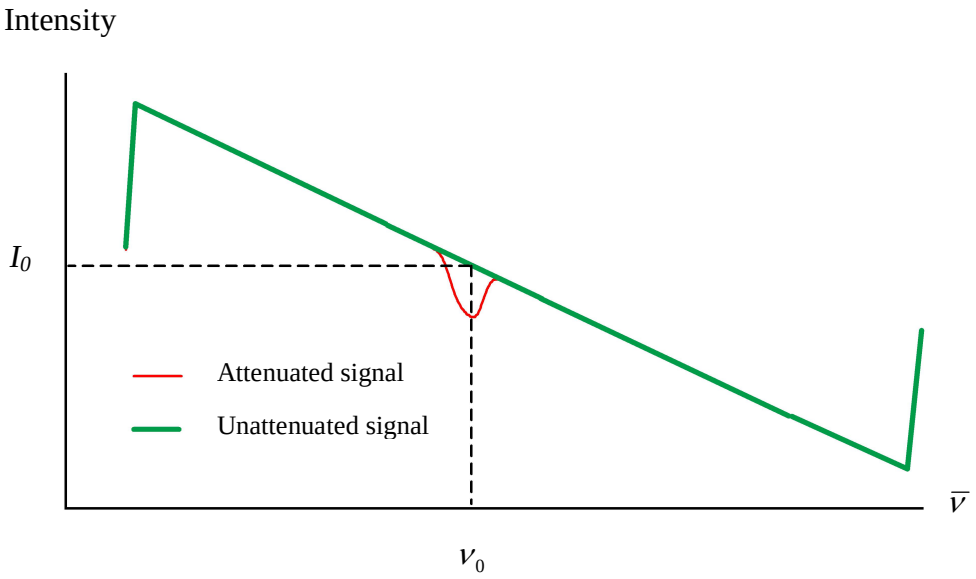

Figure 4.3: Intensity variation of a typical diode laser as a function of optical frequency.

When both injection currents (modulation and ramp) are superimposed on each other, From (4.2) and (4.4), the intensity of laser light will vary as

$$I_0(\nu) = I_0\left[1 + s_{F1}(\bar{\nu} - \bar{\nu}_0) + s_{F2}(\bar{\nu} - \bar{\nu}_0)^2 - s_f \Delta\nu_m \cos\omega t\right] \qquad (4.5)$$

where, s_f is laser intensity-frequency parameter at modulation frequency f in 1/cm^{-1}. As noted above, the laser intensity-frequency parameters strongly depend on the frequency of injection current.

According to Beer's law, if laser light with intensity $I_0(\nu)$ given in Equation (4.5) passes through an absorbing region with absorbance of $\alpha(\nu)$, then the transmitted light will be

$$I(\nu) = I_0(\nu)\exp[-\alpha(\nu)] \qquad (4.6)$$

Usually WMS is applied in situations with small absorbance, where $\alpha(\nu) < 0.1$. Under this condition, Equation (4.6) can be approximated by

$$I(\nu) = I_0(\nu)[1-\alpha(\nu)] \qquad (4.7)$$

If the transmitted light $I(\nu)$ is detected by a wide bandwidth photodetector, it generates a voltage signal proportional to the intensity $I(\nu)$, given by

$$\begin{aligned} I_D(\nu) = K\Big[1 + s_{F1}(\bar{\nu}-\bar{\nu}_0) + s_{F2}(\bar{\nu}-\bar{\nu}_0)^2 - s_f \Delta\nu_m \cos\omega t\Big] \\ \times\Big\{1-\alpha[\bar{\nu} - \Delta\nu_m \cos(\omega t + \psi)\Big\} \end{aligned} \qquad (4.8)$$

in which K is an opto-electrical gain, depending on the laser power impinging on the surface of the photodiode and the amplification gain. If the photodetector signal $I_D(\nu)$ is expressed in a Fourier series we will have

$$I_D(\nu) = K\left[\sum_{n=0}^{\infty} a_n(\bar{\nu})\cos(n\omega t) + \sum_{n=0}^{\infty} b_n(\bar{\nu})\sin(n\omega t)\right] \qquad (4.9)$$

In WMS the photodetector signal $I_D(\nu)$ is sent to a lock-in amplifier, where two operations are performed:

The photodetector signal $I_D(\nu)$ is multiplied by $A_r\cos(n\omega t + \theta)$ and $A_r\cos(n\omega t + \theta + \pi/2)$ voltage signals (where n is the order of the harmonic

component, θ is detection phase, and A_r is amplitude of reference signal) at two separate Phase Sensitive Detectors (PSD). In Figure 4.4 a functional block diagram of a lock-in amplifier is shown.

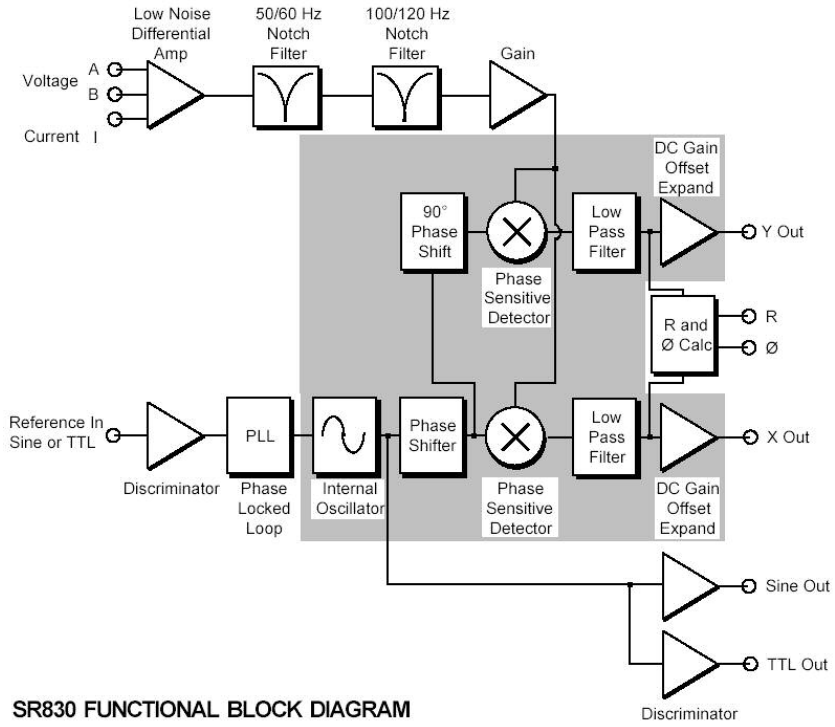

Figure 4.4: The functional block diagram of the Stanford Research SR830 lock-in amplifier which was used in this research, from the reference manual online: http://www.srsys.com/downloads/PDFs/Manuals/SR830m.pdf

Based on the Fourier expansion of $I_D(v)$ given in Equation 4.9, the resulting signal will have a time-dependent term and a DC term proportional to $A_r a_n(\bar{v})\cos(\theta)$ and $A_r b_n(\bar{v})\sin(\theta)$ at the output of the two PSDs. The output signals from each PSD is then low-pass filtered. Since the time-varying term at the output of the PSD is in fact a summation of infinite multiplied orthogonal functions, as results of lowpass filtration, they vanish. Therefore, at the output of the two lowpass filters, only $A_r a_n(\bar{v})\cos(\theta)$ and $A_r b_n(\bar{v})\sin(\theta)$ signals survive. These two signals are sent to

two output channels (X an Y). The signal at the output channel X which is proportional to $A_r a_n(\bar{\nu})\cos(\theta)$ is called the in-phase signal while the other output signal at channel Y which is proportional to $A_r b_n(\bar{\nu})\sin(\theta)$ is named the quadrature signal.

Either in-phase or quadrature signal is used for WMS quantification. In the following, we only discuss the properties of the in-phase signal in depth as this signal was considered for the quantification of the sensor developed in this research.

From the above, the in-phase signal of the photodetector signal $I_D(\nu)$ at the output of lock-in amplifier is given by

$$I_{nf,p}(\bar{\nu}) = K' \int_{-\pi}^{+\pi} \begin{matrix} \left[1 + s_{F1}(\bar{\nu} - \bar{\nu}_0) + s_{F2}(\bar{\nu} - \bar{\nu}_0)^2 - s_f \Delta\nu_m \cos\omega t\right] \\ \times\left\{1 - \alpha[\bar{\nu} - \Delta\nu_m \cos(\omega t + \psi)]\right\} \cos(nwt + \theta)\, d(\omega t) \end{matrix} \tag{4.10}$$

where, $I_{nf,p}(\bar{\nu})$ is the in-phase signal at the nth harmonic component of photodetector signal. As explained in Chapters 2 and 3, the absorbance $\alpha(\nu)$ in Equation (4.10) is given by

$$\begin{aligned} \alpha(\nu) &= \alpha\left[\bar{\nu} - \Delta\nu_m \cos(\omega t + \psi)\right] \\ &= S(T)\, g\left[\bar{\nu} - \nu_0 - \Delta\nu_m \cos(\omega t + \psi)\right] LP_{abs} \end{aligned} \tag{4.11}$$

Therefore, through Equation 4.10 one can relate the measured $I_{nf,p}(\bar{\nu})$ to the absorbing species partial pressure, P_{abs}. The main difficulty in quantification using (4.10) is, the line shape function must be known. As explained in Chapter 2, the most general line shape is given by the Voigt function, which is a convolution of Lorentzian and Gaussian functions. Voigt function $g_V(\nu - \nu_0)$ defined by

$$
\begin{aligned}
&g_V(\nu-\nu_o) = AK(x,y),\\
&A = \frac{1}{\Delta\nu_D}\sqrt{(\ln(2)/\pi},\\
&K(x,y) = \frac{y}{\pi}\int_{-\infty}^{\infty}\frac{\exp(-t^2)}{y^2+(x-t)^2}dt, \qquad (4.12)\\
&y = \frac{\Delta\nu_L}{\Delta\nu_D}\sqrt{(\ln 2},\\
&x = [(\nu-\nu_0)/\Delta\nu_D]\sqrt{\ln 2}
\end{aligned}
$$

where $\Delta\nu_L$ and $\Delta\nu_D$ (in cm^{-1}) are pressure and Doppler broadening half-widths at half-maximum of the transition centered at ν_0, and *t* is a variable of integration. The Doppler half-width of a molecule with molecular weight *M* at temperature *T* (K) can be calculated from

$$\Delta\nu_D = 3.581\times10^{-7}\nu_0\sqrt{T/M} \qquad (4.13)$$

The integral in (4.12) is difficult to evaluate, and simplified expressions are typically used. The expression given by Whiting (Whiting 1968) is often used for approximating the Voigt function. Using Whiting's expression, the absorption cross-section, which is the product of *S(T)* and $g_V(\nu-\nu_0)$, based on Voigt profile, is given by:

$$
\begin{aligned}
\sigma_V(\nu) = \sigma_V(\nu_0)\Bigg\{&(1-x)\exp(-0.693y^2) + \frac{x}{1+y^2}\\
&+ 0.016(1-x)x\left[\exp(-0.0841y^{2.25}) - \frac{1}{1+0.0210y^{2.25}}\right]\Bigg\}
\end{aligned}
$$

(4.14)

where $x = \Delta\nu_L / \Delta\nu_V$, $y = |\nu - \nu_0| / \Delta\nu_V = |\bar{\nu} - \nu_0 - \Delta\nu_m \cos(\omega t + \psi)| / \Delta\nu_V$. $\Delta\nu_V$ is the Voigt profile half-width at half-maximum, given by (Olivero and Longbothum 1977):

$$\Delta\nu_V = 0.5346\Delta\nu_L + (0.2166\Delta\nu_L^2 + \Delta\nu_D^2)^{0.5} \qquad (4.15)$$

In equation (4.14), $\sigma_V(\nu_0)$ is the cross-section at absorption line center which is given by

$$\sigma_V(\nu_0) = \frac{S(T)}{2\Delta\nu_V(1.065 + .447x + 0.058x^2)} \qquad (4.16)$$

It should be noted that, if Lorentzian half-width or Gaussian half-width becomes zero, the Voigt function is converted to a Gaussian or a Lorentzian line shape respectively.

4.2 Properties of the in-phase signal at the nth harmonic component, $I_{nf,p}(\bar{\nu})$

In the following, the principle properties of $I_{nf,p}(\bar{\nu})$ are explained. For better clarity, these properties are being explained through examples with analytical explanations included to the extent that they facilitate the discussion. The examples shown are the results of calculations based on Equations 4.11 (for line shape), 4.14 (for absorbance) and 4.10 for $I_{nf,p}(\bar{\nu})$. A computer program in C++ was written for performing these calculations. (see Appendix A1).

4.2.1 Properties of $I_{nf,p}(\bar{\nu})$ in the absence of intensity modulation

In the absence of intensity modulation, $I_{nf,p}(\bar{\nu})$ is simplified as

$$I_{nf,p}(\bar{\nu}) = K'' \int_{-\pi}^{+\pi} \alpha\left[\bar{\nu} - \Delta\nu_m \cos(\omega t + \psi)\right] \cos(nwt + \theta)\, d(\omega t) \qquad (4.17)$$

this implies that for very small modulation index $m << 1$, defined by

$$m = \frac{\Delta\nu_m}{\Delta\nu_V} \qquad (4.18)$$

$I_{nf,p}(\bar{\nu})$ becomes proportional to the nth-order derivatives of the line shape profile (Wilson 1963). When modulation index is not very small, $I_{nf,p}(\bar{\nu})$ will no be longer proportional but it dose resemble the nth-order derivatives of the line-shape function (see Figure 4.5).

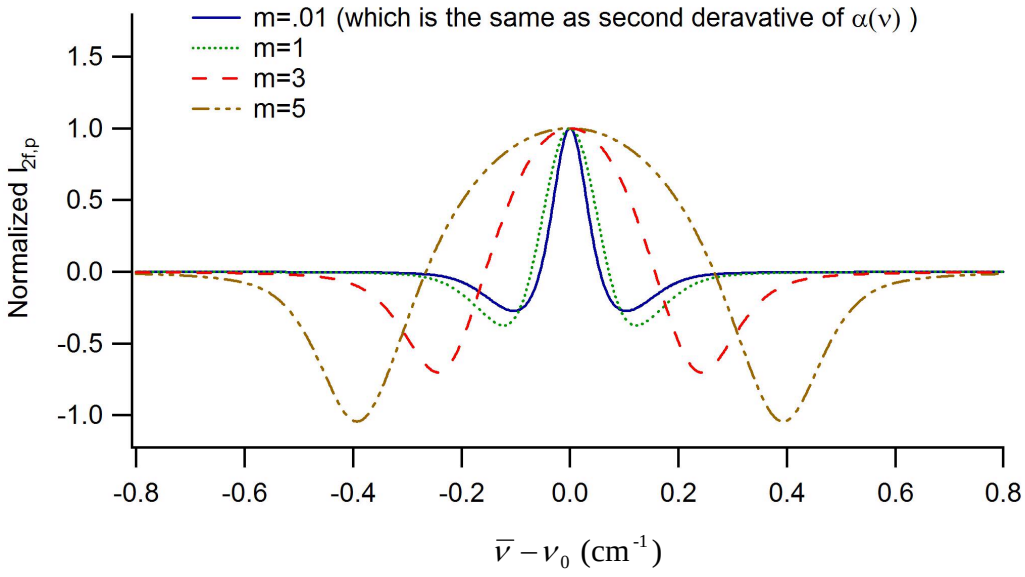

Figure 4.5: The effect of variation of modulation index *m*, on the spectra of $I_{2f,p}(\bar{\nu})$ for a case of a Voigt line-shape function with $\Delta\nu_D = .05\,\text{cm}^{-1}$, $\Delta\nu_L = .05\,\text{cm}^{-1}$, $\psi = \theta = 0$, and no intensity modulation ($s_{F1} = s_{F2} = s_f = 0$).

Also, in Equation (4.17) since the absorbance $\alpha(\nu)$ is symmetric with respect to resonance absorption frequency ν_0, it can be easily realized that $I_{nf,p}(\bar{\nu})$ for *n*=even (e.g. *n*=2, 4, …) is symmetric with respect to ν_0 and it is anti-symmetric for *n*=odd (e.g. *n*=1, 3, …). Applying these simple but important results leads to expectation that at the resonance frequency ν_0 when *n* is even, , the amplitude of $I_{nf,p}(\bar{\nu})$ is maximum and when *n* is odd, the amplitude of $I_{nf,p}(\bar{\nu})$ is zero. These results can be seen in Figure 4.6, where the first four harmonic components of the in-phase signal $I_{nf,p}(\bar{\nu})$ are shown.

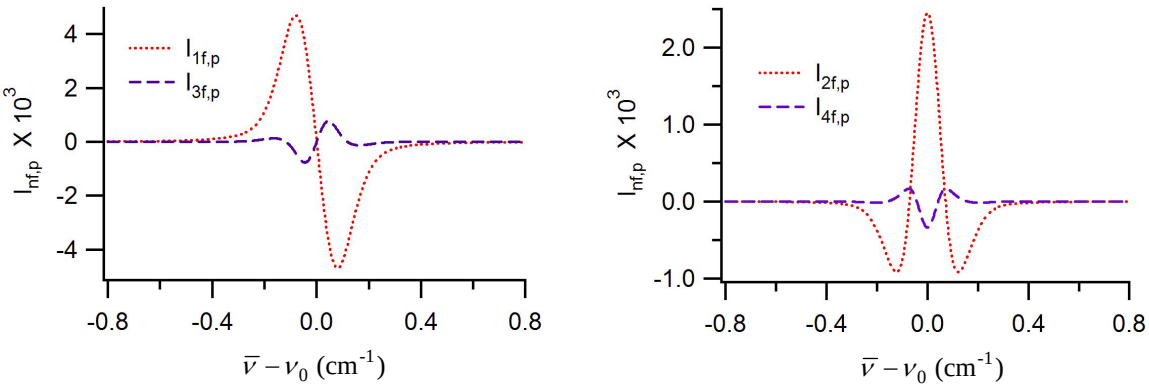

Figure 4.6: In-phase signal, $I_{nf,p}(\bar{\nu})$ for the first four harmonic components for the case of a Voigt line-shape function with $\alpha(\nu_0) = .01$, $\Delta\nu_D = .05\,\text{cm}^{-1}$, $\Delta\nu_L = .05\,\text{cm}^{-1}$, *m*=1, $\psi = \theta = 0$, $K' = 1$, and no intensity modulation ($s_{F1} = s_{F2} = s_f = 0$).

Based on these properties, always the even harmonic components are used for quantification, and in practice usually the peak of $I_{nf,p}(\bar{\nu})$, with even *n*, is related to concentration.

One of the other important properties of $I_{nf,p}(\bar{\nu})$ is: it strongly depends on the detection phase θ; the magnitude of the signal $I_{nf,p}(\bar{\nu})$ varies periodically with the detection phase. As will be explained in the following, the magnitude of this signal will be maximum and minimum at the detection phases given by

$$\theta_{n,\max} = n\psi + k\pi,$$
$$\theta_{n,\min} = n\psi + (2k+1)\pi/2 \qquad (4.19)$$

Equation (4.17) illustrate why at detection phases given in Equation (4.19) the magnitude of $I_{nf,p}(\bar{\nu})$ is a maximum or minimum. Using the definition of $I_{nf,p}(\bar{\nu})$, this signal is proportional to

$$I_{nf,p}(\bar{\nu}) \propto \cos(n\omega t + n\psi)\cdot\cos(n\omega t + \theta) \qquad (4.20)$$

and from Equation (4.20), the maximum amplitude (regardless of the polarity of $I_{nf,p}(\bar{\nu})$ signal) only happens when there is 0 or 180 degree phase difference between $\cos(n\omega t + n\psi)$ and $\cos(n\omega t + \theta)$. Therefore $I_{nf,p}(\bar{\nu})$ is maximum when $\theta = n\psi + k\pi$ and with the same argument $I_{nf,p}(\bar{\nu})$ is minimum, when there is 90 or 270 degree phase shift between $\cos(n\omega t + n\psi)$ and $\cos(n\omega t + \theta)$ or when $\theta = n\psi + (2k+1)\pi/2$. (See Figure 4.7)

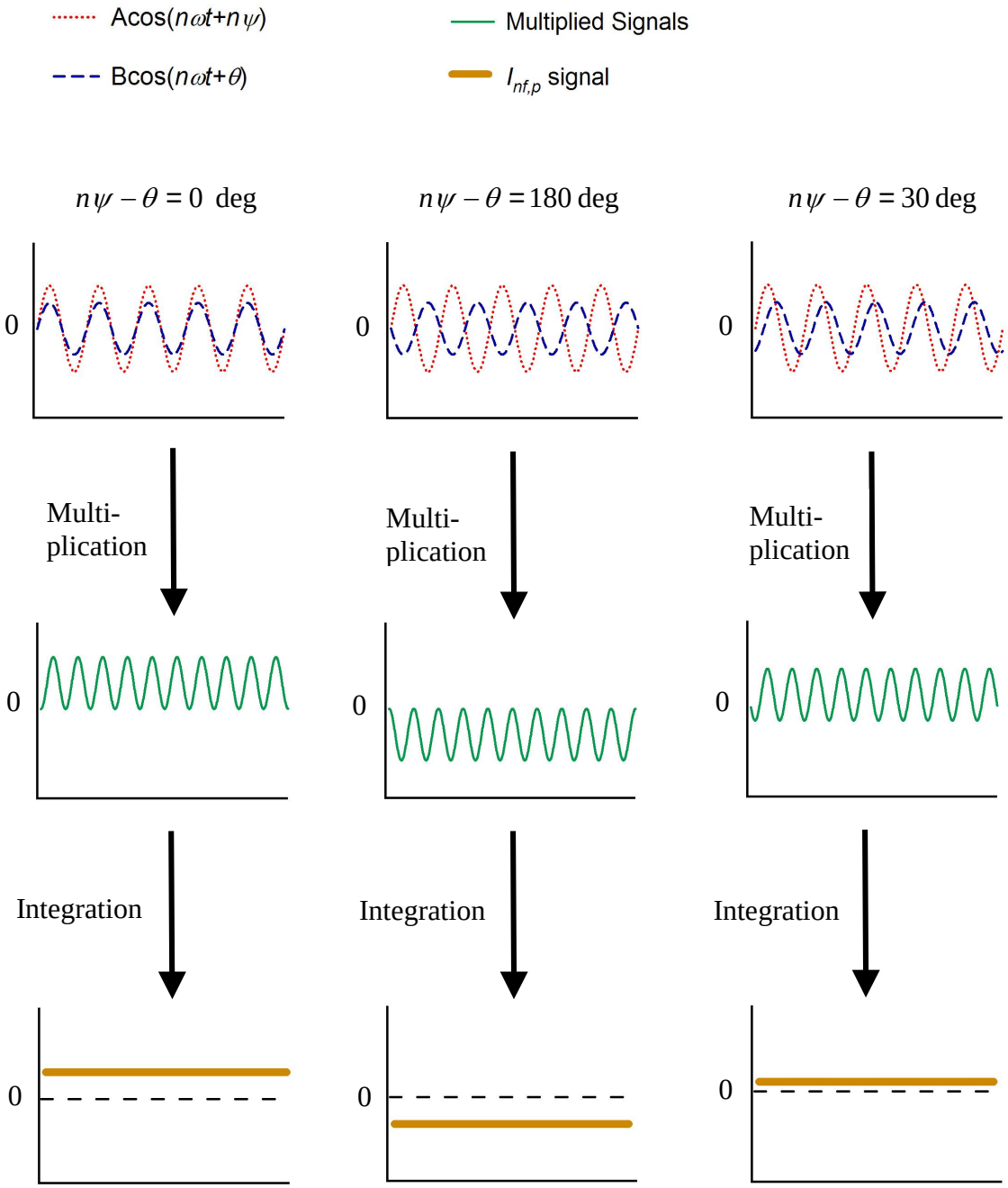

Figure 4.7: The effect of detection phase on $I_{nf,p}$.

In Figure 4.8 variation of $I_{nf,p}(\bar{\nu})$ signals (for n=1,2,3,4) at three different detection phases are shown.

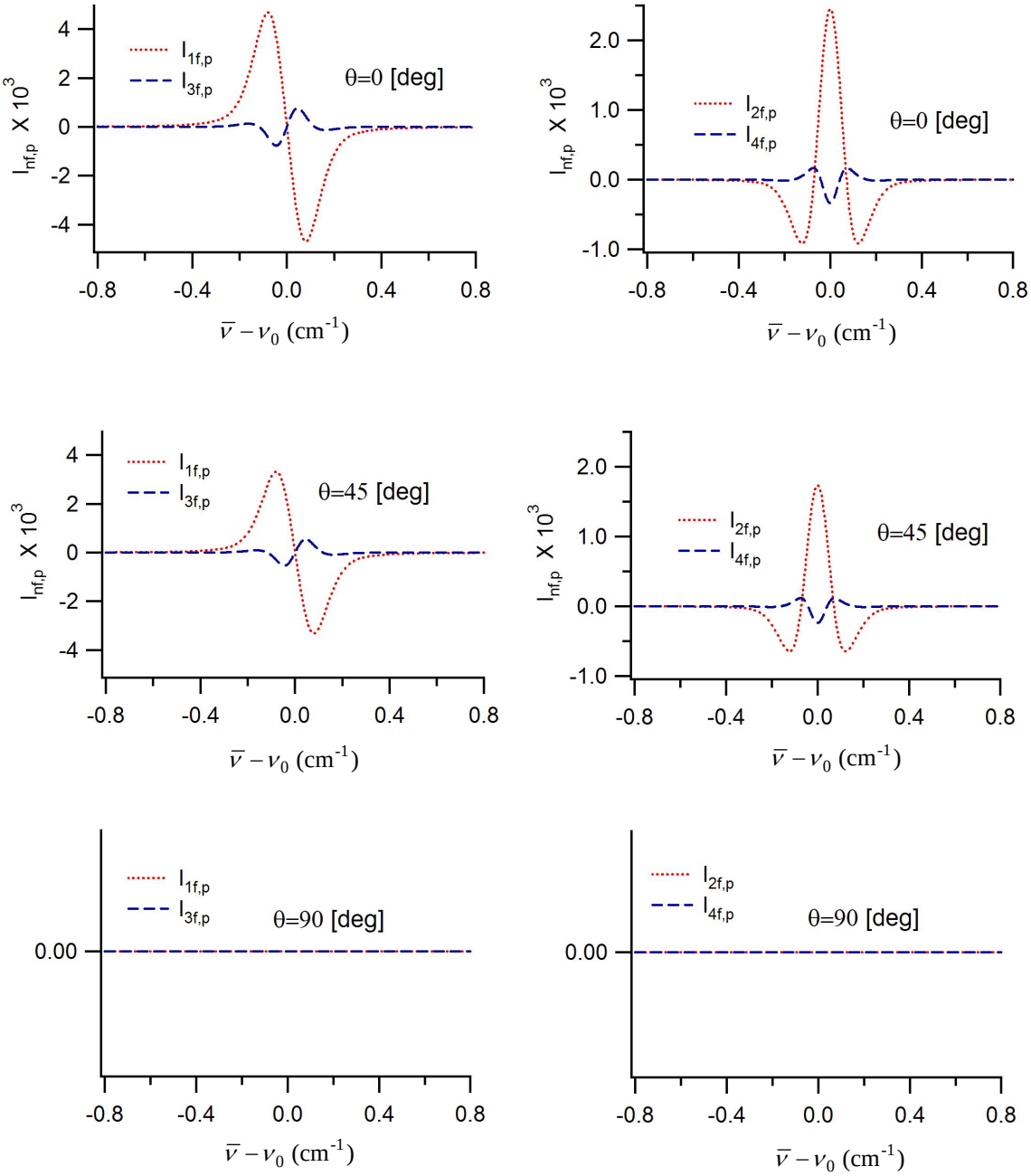

Figure 4.8: The effect of detection phase on in-phase signal $I_{nf,p}(\bar{\nu})$ for the case of a Voigt line-shape function with $\alpha(\nu_0) = .01$, $\Delta\nu_D = .05\,\text{cm}^{-1}$, $\Delta\nu_L = .05\,\text{cm}^{-1}$, m=1, $\psi = 0$, $K' = 1$, and no intensity modulation ($s_{F1} = s_{F2} = s_f = 0$).

At the detection phase $\theta_{n,\min}$ given by 4.19, the amplitude of the in-phase signal $I_{nf,p}(\bar{\nu})$ vanishes.

Another important property of $I_{nf,p}(\bar{\nu})$ is that by changing the modulation depth *m*, in addition to spectra (as shown in Figure 4.5) the amplitude of $I_{nf,p}(\bar{\nu})$ at the peak varies. This variation depends on the line-shape function (see Figure 4.9).

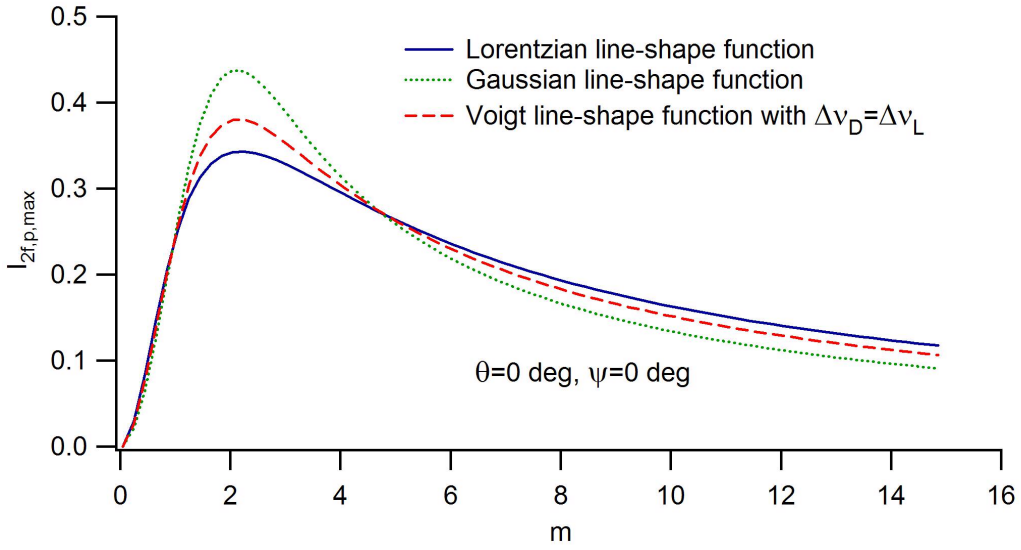

Figure 4.9: The effect of modulation index, *m*, on the maximum of the in-phase signal $I_{2f,p}(\bar{\nu})$ for the case of a Voigt line-shape function with $\alpha(\nu_0) = .01$, $K' = 100$, and no intensity modulation ($s_{F1} = s_{F2} = s_f = 0$), with the optimum detection phase.

As shown in Figure 4.9, at a modulation index of *m*=2.2, the in-phase signal is maximum for different line-shape functions. These results are obtained for the case where the detection phase is optimum. Similar results were first obtained by Reid et al. (Reid and Labrie 1981) where in their analysis they only considered frequency modulation. In Figure 4.10, the in-phase signal versus *m* when the detection phase is

not optimum is shown. Comparing Figures 4.9 and 4.10 illustrates that even at a non-optimum detection phase, the in-phase signal is still maximum at *m*=2.2.

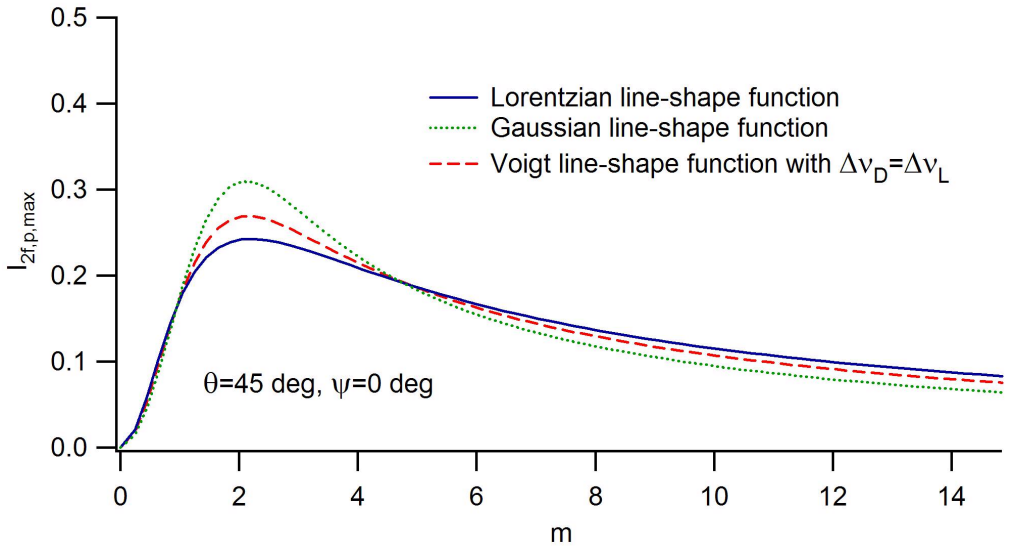

Figure 4.10: The effect of modulation index, *m*, on the maximum of the in-phase signal $I_{2f,p}(\bar{\nu})$ assuming a Voigt line-shape function with $\alpha(\nu_0) = .01$, $K' = 100$, and no intensity modulation ($s_{F1} = s_{F2} = s_f = 0$), when the detection phase is not optimum.

4.2.2 Properties of $I_{nf,p}(\bar{\nu})$ in the presence of intensity modulation

As mentioned before, when the injection current of a diode laser is modulated, the optical frequency and the intensity of the emitted light are modulated. To better understand the effect of intensity modulation, the properties of the in-phase signal $I_{nf,p}(\bar{\nu})$ (particularly the second harmonic signal $I_{2f,p}(\bar{\nu})$), which was investigated in the previous section, will be examined here for the case when both frequency and intensity modulation are taken into account.

In the presence of intensity modulation, the $I_{nf,p}(\bar{\nu})$ spectra will no longer be a symmetric or anti-symmetric (when *n* is even or odd respectively). This asymmetry is

caused by two different mechanisms. The first mechanism is due to the fact that when the central optical frequency $\bar{\nu}$ varies, the intensity of the laser light varies. Therefore, depending on this variation, the spectra of $I_{nf,p}(\bar{\nu})$ obtained for pure FM (frequency modulation) must be multiplied by a function that represents the variation of intensity $I_0(\bar{\nu})$ with $\bar{\nu}$. In this research, we adopted a parabolic variation for $I_0(\bar{\nu})$, given in Equation 4.4, though in many cases a linear variation suffices. The second mechanism is due to the intensity modulation with amplitude of $s_f \Delta\nu_m$ when the optical frequency is modulated with the amplitude of $\Delta\nu_m$. In the absence of the first mechanism ($s_{F1} = s_{F2} = 0$), from Equation (4.10) it can be seen that the term $s_f \Delta\nu_m \cos(\omega t)$ alone can cause a major change in the spectra of $I_{nf,p}(\bar{\nu})$. As result of this term, the spectra of $I_{nf,p}(\bar{\nu})$ will be no longer proportional to the *n*th harmonic of absorbance $\alpha(\bar{\nu})$. By a simple trigonometric manipulation one can see that under this condition, $I_{nf,p}(\bar{\nu})$ spectra will be proportional to a linear combination of the *n*-1, *n*, and *n*+1th harmonic components of $\alpha(\bar{\nu})$. Figure 4.11 illustrates the contribution of each of these two mechanisms on the real spectra of $I_{nf,p}(\bar{\nu})$ when intensity modulation is also considered, using a linear model for the first mechanism for illustration.

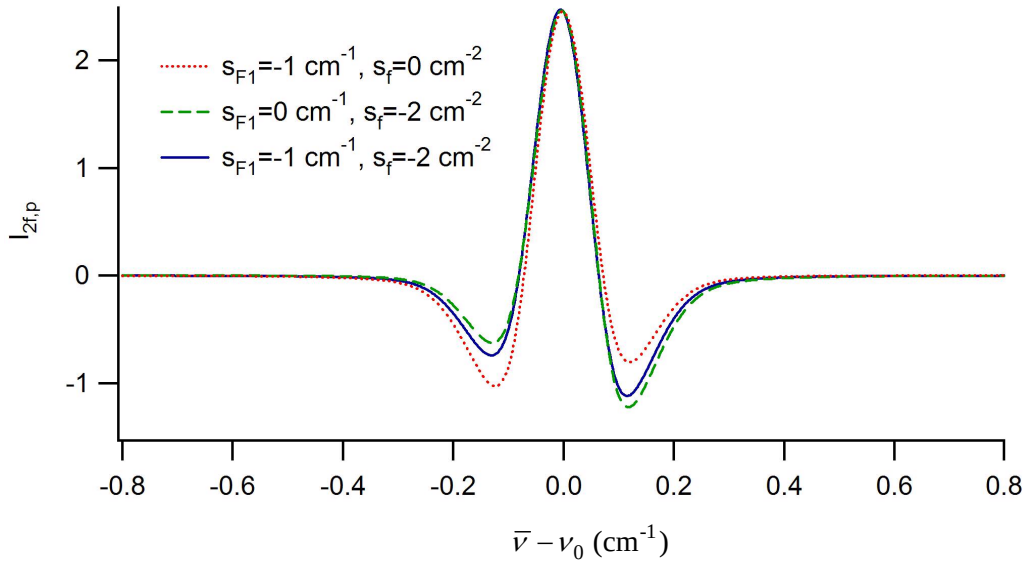

Figure 4.11: The effect of the two different mechanisms of intensity modulation on the spectra of $I_{2f,p}(\bar{\nu})$. The calculated results in this figure used a Voigt line-shape function with $\alpha(\nu_0) = .01$, $K' = 1000$, m=1, $\psi = \theta = 0$, $s_{F2} = 0$.

In comparison to the results given in Figure 4.6, in which intensity modulation was neglected, the first four harmonic components of the in-phase signal $I_{nf,p}(\bar{\nu})$ are presented in Figure 4.12, for which intensity modulation parameters for a typical diode laser are chosen.

One of the important effects of intensity modulation of diode lasers is that as result of intensity modulation the first harmonic component of the in-phase signal $I_{1f,p}(\bar{\nu})$ contains an offset. See Figure 4.12. From Equation 4.8, the magnitude of the offset of $I_{1f,p}(\bar{\nu})$ is calculated by

$$I_{1f,p}(\bar{\nu})\Big|_{Offset} = -K' s_f \Delta\nu_m \cos(\theta) \qquad (4.21)$$

According to the parameters chosen for the spectra in Figure 4.12, the offset in this Figure can be computed as

$$I_{1f,p}(\bar{\nu})\Big|_{Offset} = -K's_f \Delta\nu_m \cos(\theta) = -K's_f m\Delta\nu_V \cos(\theta)$$

$$= -(1)(-2[\text{in } 1/\text{cm}^{-1}])(1)(0.082[\text{in cm}^{-1}])\cos(0) = 0.164\times10^{-3}$$

which is exactly the same as the offset calculated numerically in Figure 4.12. In the above calculation the Voigt half-width, $\Delta\nu_V$, is calculated from 4.15 using $\Delta\nu_D = \Delta\nu_L = 0.05\,\text{cm}^{-1}$ which gives $\Delta\nu_V = 0.082\,\text{cm}^{-1}$

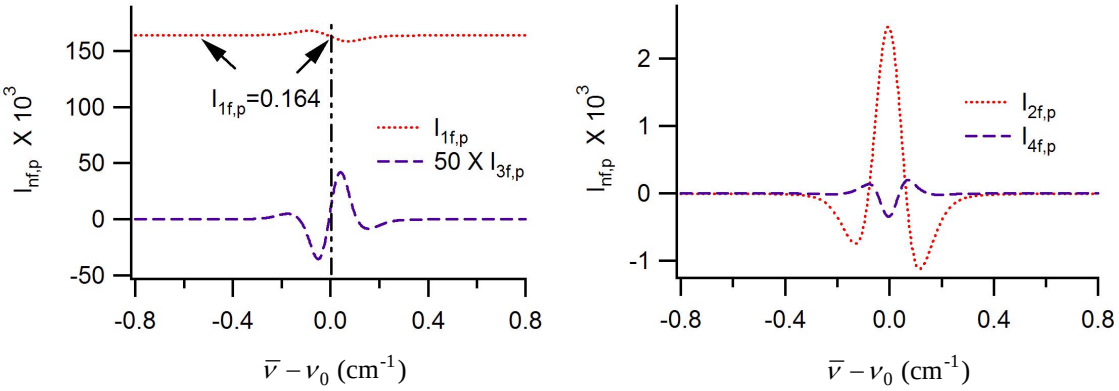

Figure 4.12: In-phase signal, $I_{nf,p}(\bar{\nu})$ for the first four harmonic components calculated with a Voigt line-shape function with $\alpha(\nu_0) = .01$, $\Delta\nu_D = .05\,\text{cm}^{-1}$ and $\Delta\nu_L = .05\,\text{cm}^{-1}$, m=1, $\psi = \theta = 0$, $K' = 1$, and intensity modulation parameters of ($s_{F1} = -1[1/\text{cm}^{-1}], s_{F2} = 0, s_f = -2[1/\text{cm}^{-1}]$).

The importance of this effect is that it allows the use of the first harmonic signal to calculate the laser power. At a fixed detection phase, based on Equation (4.21), the offset is proportional to K' and K' is proportional to laser power. The significance of this property can be better understood in th context of diode laser measurements in harsh media where as result of light scattering or beam steering, the laser power impinging on the photodetector fluctuates with time. In such applications the first

harmonic of the signal can be continuously used to measure the intensity while the even harmonics can be employed for concentration measurement using the intensity information from first harmonic signal.

The effect of the detection phase on the in-phase signal with both intensity and frequency modulation is nearly the same as the case of pure frequency modulation discussed in section 4.2.1. The primary difference is that at the detection phase in which $n\psi - \theta = \pi/2$, the even harmonics of in-phase signal no longer resemble the nth derivative. For example, at condition $2\psi - \theta_{2,\min} = \pi/2$, the in-phase second harmonic of the photodetector signal, $I_{2f,p}(\bar{\nu})$ resembles the first (rather than the second) derivative of the absorption line-shape function (see Figure 4.13).

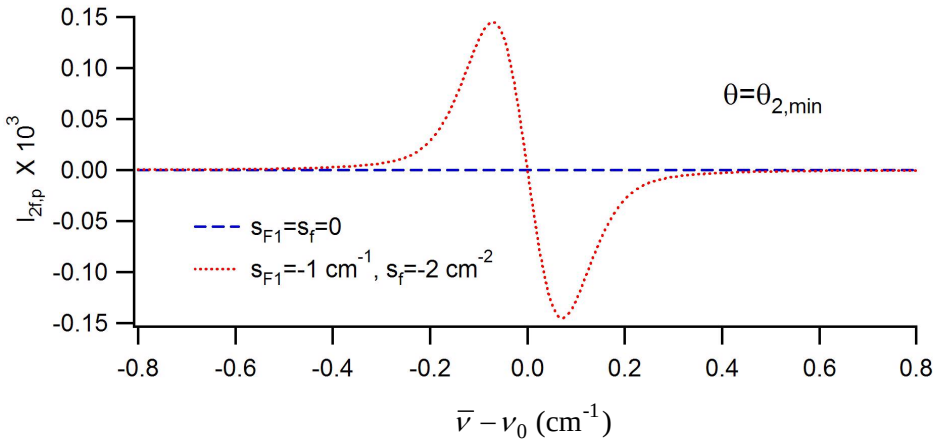

Figure 4.13: The effect of detection phase on the $I_{2f,p}(\bar{\nu})$ spectra. The calculated results in this figure assume a Voigt line-shape function with $\alpha(\nu_0) = .01, K' = 1$, m=1, $\psi = -20\,\text{deg}$, $\theta = \theta_{\min} = 50\,\text{deg}, s_{F2} = 0$. Dotted line shows the second harmonic signal when intensity modulation is not considered (zero), whereas the dashed line represents the same spectra when intensity modulation is taken into account.

The effect of detection phase on $I_{nf,p}(\bar{\nu})$ when both intensity and frequency modulation are considered is shown in Figure 4.14.

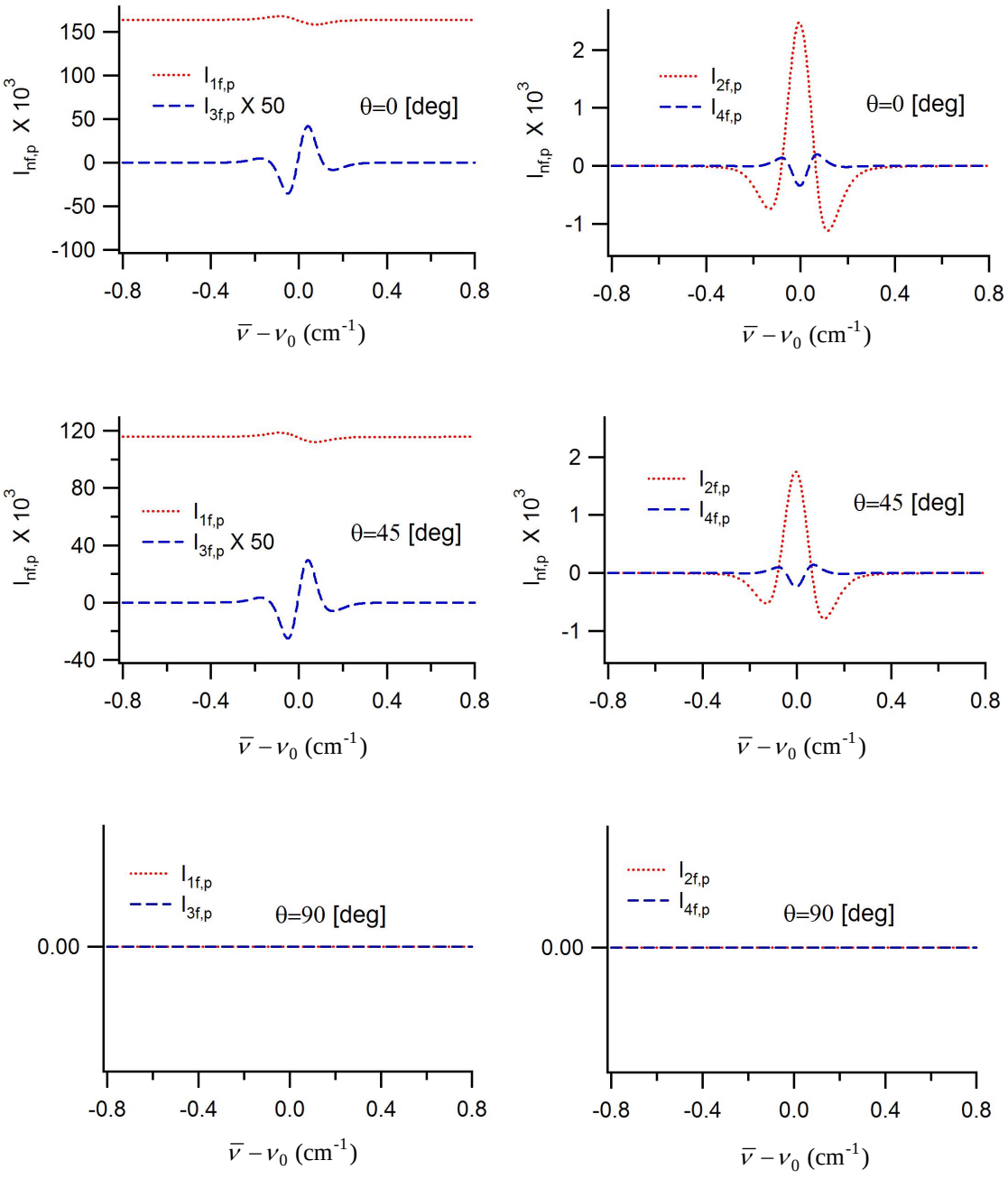

Figure 4.14: The effect of detection phase on in-phase signal $I_{nf,p}(\bar{\nu})$ for a signal with a Voigt line-shape function with $\alpha(\nu_0) = .01$, $\Delta\nu_D = .05\,\text{cm}^{-1}$ and $\Delta\nu_L = .05\,\text{cm}^{-1}$, m=1, $\psi = 0$, $K' = 1$, and linear intensity modulation ($s_{F1} = -1$, $s_{F2} = 0$, $s_f = -2$).

4.3 Methods for concentration and temperature measurement

Based on theoretical model developed in section 4.1, this section outlines the quantification of the output signal $I_{nf,p}(\bar{\nu})$ for concentration and temperature measurements. The quantification procedure is explained for a simple case, in which it is assumed there is only a single absorption transition in the measured spectra and no overlapping between transitions exists. Following the simple example a more general case, in which multiple overlapped transitions interfere is discussed.

4.3.1 Method for concentration measurement

As explained in Section 4.1, the output signal of WMS technique, $I_{nf,p}(\bar{\nu})$, can be related to an absorption feature by Equation (4.10). Since for even harmonics (n=2k, k is an integer), $I_{nf,p}(\bar{\nu})$ is maximum at the absorption center $\bar{\nu} = \nu_0$, usually even harmonics are used for concentration measurement. In this equation, absorbance $\alpha(\nu)$ is related to partial pressure of absorbing species, P_{abs}, through Equation (4.11). When all laser parameters and the spectroscopic properties of the absorption transition, including Doppler width, collisional width, and also line strength are known, through 4.11 one can calculate $I_{nf,p}(\bar{\nu})$ per unit absorbing species concentration (e.g. P_{abs}=1 atm). If the peak of the measured $I_{nf,p}(\bar{\nu})$ signal is divided by the peak of the calculated $I_{nf,p}(\bar{\nu})$, the result will be equal to the concentration of the absorbing species.

Based on the quantification method specified above, no calibration is necessary; however, many times prediction of electro-optical gain K' is difficult and therefore a

simple way to calculate electro-optical gain is measuring K' through comparing a set of measured $I_{nf,p}(\bar{\nu})$ signals at known concentration with their corresponding calculated values from Equation 4.11.

In many real applications, it is necessary to measure closely spaced rotational-vibrational transitions of absorbing species which are overlapped as a result of broadening effects. Under this circumstance, Equation 4.11 is modified to

$$I_{nf,p}(\bar{\nu}) = K' \sum_{i=1}^{N} \int_{-\pi}^{+\pi} \begin{matrix} \left[1 + s_{F1}(\bar{\nu} - \bar{\nu}_0) + s_{F2}(\bar{\nu} - \bar{\nu}_0)^2 - s_f \Delta\nu_{m,i} \cos\omega t\right] \\ \times\left\{1 - \alpha_i[\bar{\nu} - \Delta\nu_{m,i} \cos(\omega t + \psi)\right\} \cos(nwt + \theta)\, d\omega t \end{matrix} \quad (4.22)$$

where the absorbance $\alpha_i(\nu)$ is related to the concentration by

$$\alpha_i(\nu) = S_i(T) g_{V,i}(\nu - \nu_{0,i}) P_{abs} L \quad (4.23)$$

In Equation (4.22), ν_0 can be arbitrary chosen as the frequency of one the absorption line centers $\nu_{0,i}$ defined in Equation (4.23).

4.3.2 Method for temperature measurement

Diode lasers also have been used for temperature measurement (Arroyo and Hanson 1993; Allen and Kessler 1996; Baer, Nagali et al. 1996; Gharavi and Buckley 2004). The ratio of two integrated absorption lines of a single species $R_{abs} = S_{i,1} / S_{i,2}$, which is only dependent upon temperature through the corresponding line strengths, is used for temperature measurement. If the line strengths of the two transitions are sufficiently different as a function of temperature, then R_{abs} will vary with temperature, and will provide a suitable measurement metric.

Following the procedure presented in this research for concentration measurement, a new method based on WMS has been developed for temperature measurement in combustion systems. In this method, the ratio of the second harmonic (or in general even harmonics) of the two absorption transitions is formulated and used as a means for temperature measurement. If two absorption transitions *i* and *j* of a single absorbing species are detected by two different diode lasers, then the ratio of the measured second harmonics can be written as

$$\frac{I_{2f,p}(\nu_{0,i})}{I_{2f,p}(\nu_{0,j})} = \frac{K\int_{-\pi}^{+\pi}\left[1+s_{F1}(\nu_{0,i}-\bar{\nu}_0)+s_{F2}(\nu_{0,i}-\bar{\nu}_0)^2-s_f\Delta\nu_m\cos\omega t\right]\times\left\{1-\alpha_i[\nu_{0,i}-\Delta\nu_m\cos(\omega t+\psi)\right\}\cos(nwt+\theta)\,d\omega t}{K'\int_{-\pi}^{+\pi}\left[1+s'_{F1}(\nu_{0,j}-\bar{\nu}'_0)+s'_{F2}(\nu_{0,j}-\bar{\nu}'_0)^2-s'_f\Delta\nu'_m\cos\omega' t\right]\times\left\{1-\alpha_j[\nu_{0,j}-\Delta\nu'_m\cos(\omega' t+\psi')\right\}\cos(nw' t+\theta')\,d\omega' t} \tag{4.24}$$

In Equation (4.24), properties of two different lasers are assumed to be different. When detection of the absorption transitions are accessible by a single diode laser, all laser properties in the numerator and denominator can be assumed to be equal with a very good approximation except the modulation depth $\Delta\nu_m$. If the modulation depths of the single laser around well separated transitions i and j are $\Delta\nu_{m,i}$ and $\Delta\nu_{m,j}$ respectively, then Equation (4.24) can be modified as

$$\frac{I_{2f,p}(\nu_{0,i})}{I_{2f,p}(\nu_{0,j})} = \frac{\int_{-\pi}^{+\pi}\left[1+s_{F1}(\nu_{0,i}-\bar{\nu}_0)+s_{F2}(\nu_{0,i}-\bar{\nu}_0)^2-s_f\Delta\nu_{m,i}\cos\omega t\right]\times\left\{1-\alpha_i[\nu_{0,i}-\Delta\nu_{m,i}\cos(\omega t+\psi)\right\}\cos(nwt+\theta)\,d\omega t}{\int_{-\pi}^{+\pi}\left[1+s_{F1}(\nu_{0,j}-\bar{\nu}_0)+s_{F2}(\nu_{0,j}-\bar{\nu}_0)^2-s_f\Delta\nu_{m,j}\cos\omega t\right]\times\left\{1-\alpha_j[\nu_{0,j}-\Delta\nu_{m,j}\cos(\omega t+\psi)\right\}\cos(nwt+\theta)\,d\omega t} \tag{4.25}$$

Equation (4.25) shows the ratio of second harmonics at the two absorption line centers $\nu_{0,i}$ and $\nu_{0,j}$. As explained in Section 4.3.1, in the real world, in the vicinity

of the two transitions i and j, some other closely spaced transitions of the same species might exist, and these transitions are usually overlapped as result of broadening effects. For such a general case Equation (4.25) is modified to

$$\frac{I_{2f,p}(\nu_I)}{I_{2f,p}(\nu_{II})} = \frac{\sum_{i=1}^{M}\int_{-\pi}^{+\pi}\left[1+s_{F1}(\nu_{0,i}-\bar{\nu}_0)+s_{F2}(\nu_{0,i}-\bar{\nu}_0)^2-s_f\Delta\nu_{m,i}\cos\omega t\right]\times\left\{1-\alpha_i[\nu_{0,i}-\Delta\nu_{m,i}\cos(\omega t+\psi)\right\}\cos(nwt+\theta)\,d\omega t}{\sum_{j=1}^{M}\int_{-\pi}^{+\pi}\left[1+s_{F1}(\nu_{0,j}-\bar{\nu}_0)+s_{F2}(\nu_{0,j}-\bar{\nu}_0)^2-s_f\Delta\nu_{m,j}\cos\omega t\right]\times\left\{1-\alpha_j[\nu_{0,j}-\Delta\nu_{m,j}\cos(\omega t+\psi)\right\}\cos(nwt+\theta)\,d\omega t} \quad (4.26)$$

in which *M* and *N* are the number of transitions interfering with each other across region I and II of the tuning range of the diode laser. Also, ν_I and ν_{II} are the frequencies in which $I_{2f,p}(\bar{\nu})$ has a local maxima. In the in which there are only two well separated transitions i and j, ν_I and ν_{II} will become $\nu_{0,i}$ and $\nu_{0,j}$. Such simulation is illustrated in Figure 4.15.

According to Equation 4.26, the ratio of the second harmonic signal at the frequencies ν_I and ν_{II} will depend upon line strengths, Doppler width, and collisional width of the all transitions measured by the diode laser. Therefore this ratio will be purely temperature dependent if the collisional widths are known. If so, one can relate this ratio to temperature and therefore use it as means for temperature measurement.

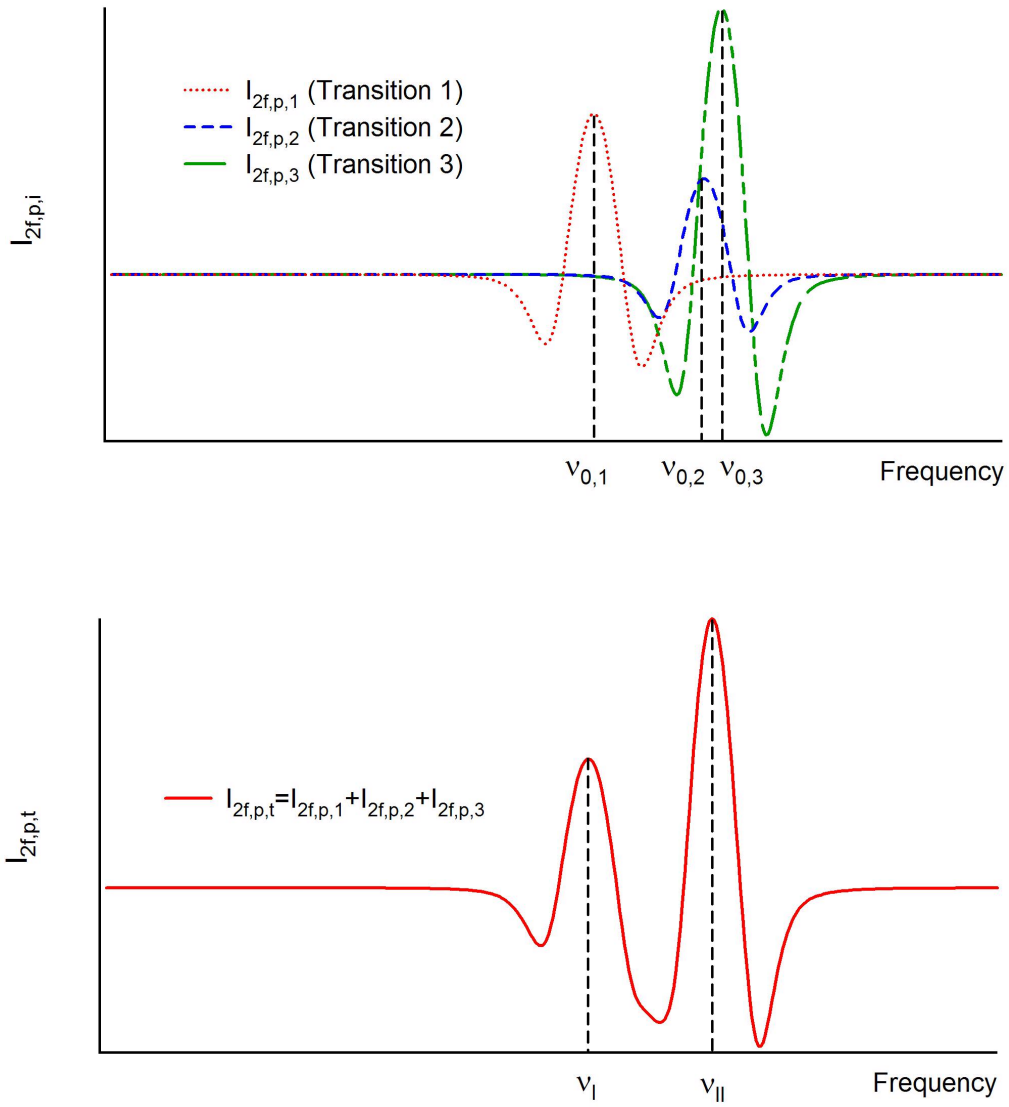

Figure 4.15: Second harmonic signal variation as a function of optical frequency for three some arbitrary overlapped absorption transitions: top trace shows the contribution of each absorption transition, bottom trace shows the second harmonic signal due to the sum of all three transitions which would be measured experimentally.

4.4 Issues and solutions for concentration and temperature measurement in a combustion system using WMS

For more than two decades WMS based on diode lasers has been used in many different applications, yet it has not found a good place in high-temperature

combustion diagnostics. WMS suffers from intensity fluctuations which is typically caused by beam steering due to changes in the refractive index of the flame zone as result of flame oscillations. Laser light scattering due to soot or other particulate material also causes intensity fluctuations. These intensity fluctuations cause changes in the measured signal unrelated to concentration variations. This problem can be partially overcome using a larger area photo diode to minimize this effect and shorter path lengths (if possible). An alternative solution is measurement of the first harmonic signal simultaneously with the second harmonic. The first harmonic signal, as discussed in Section 4.2, can provide intensity information and therefore any changes in the second (or any even) harmonic signal due to intensity variations can be distinguished.

The main barrier to application of WMS in combustion systems is, even when the intensity is constant, the second (or other even) harmonics will not linearly change with concentration and for quantification purposes, a simple calibration method will not work. For this reason, the application of WMS has been mostly limited to the trace gas measurement in which the pressure broadening and also Doppler broadening remains constant as the absorbing gas concentration changes. Under this condition, the even harmonics will vary linearly with concentration of absorbing species and a simple calibration can be used for quantification. In typical combustion systems both Doppler and collisional width vary as a result of changes in temperature and partial pressure of combustion species. For this reason a powerful theoretical model is needed to relate the measured harmonic signal to the concentration of absorbing species.

Although in the above sections, a general formula for quantification of WMS for both temperature and concentration has been derived, it will only be applicable when all of the laser parameters and the spectroscopic properties of the transitions are available. Among all of these properties, only the collisional width can not be calculated, because this parameter depends on partial pressure of all of the gas species in the probe region, and in general these partial pressures are unknown. To solve this problem, one can use the information about the pressure broadening coefficient (see Equation 2-70) of major combustion species, and based on expected concentrations for the major species such as H_2O, CO_2, etc. (for instance based on a complete combustion assumption), the total collisional width can be estimated by

$$\Delta\nu_L = \sum_i y_i \gamma_i P \qquad (4.27)$$

where P is total pressure, y_i is the mole fraction of species i and γ_i is the pressure broadening coefficient due to species i for the particular absorption transition of the absorbing molecule. If γ_i is available for main species, then estimated collisional width from Equation (4.27) will be a good approximation.

4.5 Information required for quantification of WMS for combustion diagnostics

Based on the theoretical model presented in Section 4.2 and 4.3, laser properties including $s_{F1}, s_{F2}, s_m, \psi,$ and $\Delta\nu_m$ must be measured at the laser operating condition. Chapter 6 will reveal that the measurement of these parameters is fairly straightforward. On the other hand, spectroscopic properties including line strength $S_i(T)$, and pressure broadening coefficients for each transition under the influence of

each of the major quenching gases in the combustion system, such as CO_2, H_2O, N_2, O_2, must be measured. The measurement of these parameters based on new models developed in this research is possible even for closely spaced transitions which are strongly overlapped.

In Chapter 5 all experimental methods for measuring these properties are first presented, and following that, models based on the theoretical foundation developed in this chapter are explained, and the models are verified for a set of experiments performed in the static gas cell (at known temperature and pressure) and also in a flame.

5 Measurement of spectroscopic parameters of H_2O and CH_4

Detailed mathematical models of WMS were presented in Chapter 4, based on operational laser properties as well as spectroscopic parameters of the selected absorption transitions. In this chapter measurement of the spectroscopic properties for selected absorption transitions of CH_4 and H_2O are covered in detailed. In this regard, measurements for CH_4 and H_2O were both made using direct absorption spectroscopy.

Measurement of spectroscopic parameters for CH_4 in the R(3) and R(4) manifolds of $2\nu_3$ band are covered in this chapter. Individual line strengths of each transition are determined for a range of temperatures. In addition, collision-broadened half-widths of these transitions for CO_2, N_2, H_2O, CH_4, and CO collision partners are measured as a function of temperature and pressure. From this, temperature dependence of the collision half-width for each collision partner is determined. In addition, a new method for calculation of collisional broadening at high temperatures with strongly overlapped transitions is presented (Gharavi and Buckley 2005).

For H_2O, a single diode laser absorption sensor (near 1477 nm), for the measurement of line strengths and pressure broadening coefficients of H_2O absorption transitions including 6771.747 and 6771.710 cm^{-1} (from $2\nu_1$ band) and 6771.475 cm^{-1} (from $2\nu_2+\nu_3$ band) is developed. The line strength of the transitions is measured as a function of temperature and pressure over a temperature range from 468 to 977 K. The results indicate that the selected transitions are suitable for

sensitive temperature measurements in atmospheric pressure combustion systems using integrated absorption line ratios. Comparing the results with HITRAN 96 data, it appears that these transitions will be sensitive over a wide range of temperatures (450-2000 K), suggesting applicability for combustion measurements (Gharavi and Buckley 2004). In addition, collision-broadened half-widths of these transitions for CO_2, N_2, H_2O, CH_4, and O_2 quenching gases are measured as a function of temperature and pressure. From this, the temperature dependence of the collision half-width for each quenching gas is determined.

5.1 Theory of measuring spectroscopic parameters

The transmission of light can be related to molecular species absorption by the Beer-Lambert law, given simply by:

$$\frac{I}{I_0} = \exp\left(-k_\nu L\right) \qquad (5.1)$$

Here I represents the transmitted intensity of light falling on the detector, I_0 represents the incident intensity, k_ν represents the spectral absorption coefficient, and L represents the path length that the light travels through the absorbing media. The spectral absorption coefficient k_ν (cm^{-1}) is related to the pressure of absorbing species P_{abs} (atm), the line strength of the transition i $S_i(T)$ (cm^{-2} atm^{-1}), and the line shape function $\phi_i(\nu-\nu_{0,i})$ (cm), given below, summed over several lines if more than one molecular line contributes to the absorption in a particular wavelength region.

$$k_\nu = \sum_{i=1}^{N} P_{abs} S_i(T) \phi_i(\nu - \nu_{0,i}) \qquad (5.2)$$

The temperature-dependent line strength of transition i at temperature T (in degrees Kelvin), may be expressed as (Nagali, Chou et al. 1996):

$$S_i(T) = N_L\left(\frac{273}{T}\right)\left(\frac{\pi e^2}{m_e c^2}\right)\frac{g_{1,i}}{Q(T)}\exp\left(-\frac{hcE_i''}{kT}\right)f_i\left[1-\exp\left(-\frac{hc\nu_{0,i}}{kT}\right)\right] \qquad (5.3)$$

where N_L (cm^{-3}), e (e.u.), and m_e (g) are Loschmidt's number, the electron charge, and electron mass, respectively; c (cm s^{-1}) is the speed of light; $Q(T)$ is the molecular partition function; h (J s) is Planck's constant; k (J K^{-1}) is Boltzmann's constant; and $g_{1,i}$, E_i'', and f_i are the lower-state degeneracy, the lower-state energy level, and the oscillator strength for the transition, respectively. Using Equation (5.3) one can relate the unknown line strength at temperature T to the known line strength at reference temperature T_0 by

$$S_i(T) = S_i(T_0)\frac{Q(T)}{Q(T_0)}\left(\frac{T_0}{T}\right)\exp\left[-\frac{hcE_i''}{k}\left(\frac{1}{T}-\frac{1}{T_0}\right)\right] \times\left[1-\exp\left(\frac{-hc\nu_{0,i}}{kT}\right)\right]\left[1-\exp\left(\frac{-hc\nu_{0,i}}{kT_0}\right)\right]^{-1} \qquad (5.4)$$

The line shape function in Equation (5.2) may be represented by a Lorentzian, when only collisonal effects are important, a Gaussian when the Doppler effect is dominant, or a Voigt function, where both effects are important. In many combustion applications both Doppler and pressure broadening are considrable, and therefore a Voigt function is typically used to represent the line shape. Correlations describing the Voigt function were presented in Chapter 4, Equations (4.12) through (4.16).

5.2 Measurement of CH_4 spectroscopic parameters

Many laser spectroscopic methods require some information about spectroscopic parameters such as line strength, line broadening, etc., for quantification. As discussed in this chapter WMS requires line strength and collisional broadening as a function of temperature. For measurement of methane concentrations using overtones of fundamental transitions in the near-infrared, the R(3) and R(4) transitions of the $2\nu_3$ band are among the strongest features available in a spectral region relatively free of water and other interferences (see Figure 5.1 and Appendix B1 for the spectroscopic information about these transitions). This makes these transitions good potential candidates for CH_4 measurement in combustion systems using tunable diode lasers that are readily available and inexpensive.

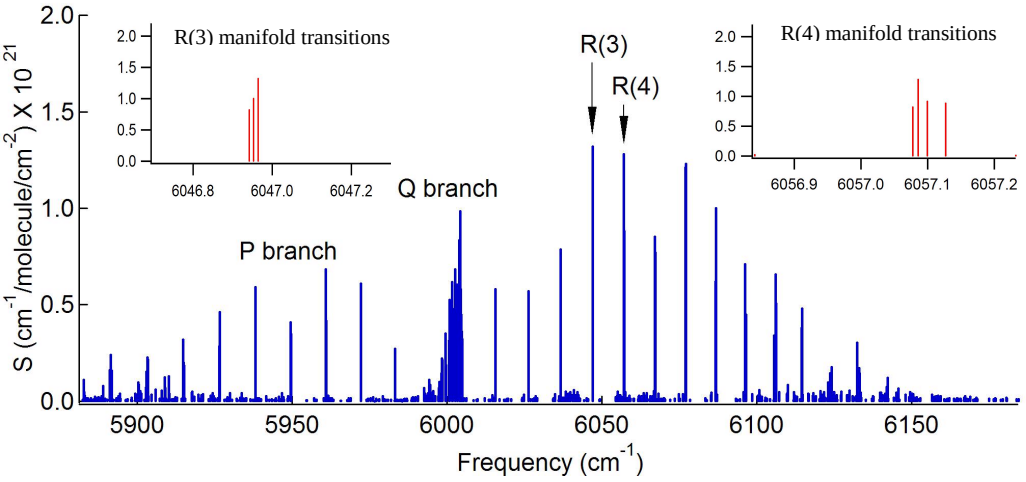

Figure 5.1: Line positions and strengths of the $2\nu_3$ band of CH_4

Previous studies have measured the line strength (Nagali, Chou et al. 1996) and collisional broadening coefficients for other CH_4 transitions as a function of

temperature (Darnton and Margolis 1973; Varanasi and Chudamani 1989). However, the R(3) and R(4) bands are comprised of lines that are sufficiently separated that one can not consider them a single transition with a hypothetical absorption frequency, a simplification that has been commonly used in the past for multiple transitions (Varanasi and Chudamani 1989). On the other hand, at high temperature and pressure these lines are strongly overlapped, such that the individual transitions are very difficult to measure. In the following, a new method for calculation of collisional broadening at higher temperatures with strongly overlapped transitions is presented.

5.2.1 Experimental details

A schematic diagram of the experiment is shown in Figure 5.2. A distributed feedback (DFB) diode laser (Corning Lasertron) operating at approximately 1651 nm, driven by an ILX Lightwave model LDC-3724B diode laser controller, generates tunable laser light in the near infrared. The laser is tuned over 0.75 cm^{-1} when the injection current from a function generator (Tektronix CFG250) is ramped with a 50 Hz sawtooth wave, to record R(3) and R(4) CH_4 absorption line transitions when the laser is operated at 35.6 and 18.1 °C, respectively. Tables 5.1 and 5.2 list the spectroscopic parameters of the R(3) and R(4) manifold from HITRAN 96 (Rothman, Rinsland et al. 1998).

The laser is coupled into a single mode fiber optic cable using bulk optics. A 1x2 fiber splitter divides the laser output into two beams. The main beam (90% of the power) is collimated by a fiber collimator and directed to a glass cell containing CH_4 and bath gases at known temperature and pressure. The absorbed beam exiting the

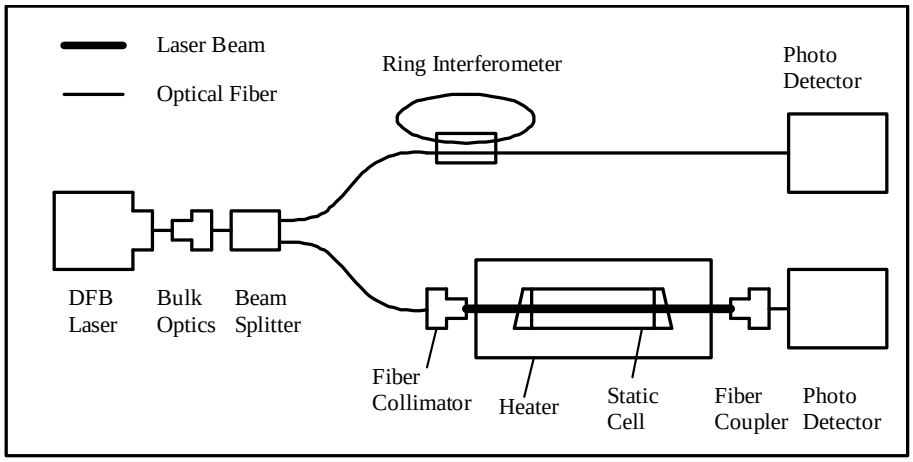

Figure 5.2: Schematic diagram of the experiment.

Table 5.1: Individual line strengths of R(3) at T=296 K

Line	ν_0 [cm^{-1}]	HITRAN 96 S_i [cm^{-2}/atm]	Measured S_i [cm^{-2}/atm]
1	6046.965	0.03271	0.03187 ± 0.00025
2	6046.953	0.02478	0.02353 ± 0.00027
3	6046.942	0.02024	0.01981 ± 0.00040
Total		0.07773	0.07521 ± 0.00060

static cell is coupled to a multimode optical fiber and is detected by a Ge photodetector (New Focus 2033) which is low-pass filtered with a bandwidth of 10 KHz. A ring interferometer (RI), with a free spectral range of 0.022675 cm^{-1} receives the secondary beam (10% of the power), which is monitored by a second Ge photodetector (New Focus 2011). The RI signal allows conversion of the time domain

Table 5.2: Individual line strengths of R(4) at T=296 K

Line	ν_0 [cm^{-1}]	HITRAN 96 S_i [cm^{-2}/atm]	Measured S_i [cm^{-2}/atm]
1	6057.127	0.02185	0.02106 ± 0.00009
2	6057.100	0.02260	0.02273 ± 0.00034
3	6057.086	0.03172	0.02774 ± 0.00021
4	6057.078	0.02029	0.02072 ± 0.00028
Total		0.09646	0.09225 ± 0.00040

in the experiment to the frequency domain as described in Chapter 3. The detected signals from both detectors are displayed on a Lecroy 9310 dual-channel oscilloscope, from which they are downloaded to a PC by a Labview program. The ring interferometer used in this experiment was designed based on information presented in a paper by Stokes et al. (Stokes, Chodorow et al. 1982). For building the ring interferometer, a single mode 95/5 directional coupler was used. More information about the designed ring interferometer is presented in Appendix C.

A 32.1-cm-long quartz static cell (designed and built in this research) with 1° wedge windows is used in these measurements. The windows are mounted in such a manner as to minimize the optical distortion associated with interference effects in the coherent light passing the static cell. The cell is surrounded by a cylindrical ceramic fiber heater extending approximately 15 cm past the end of the cell on each end, to uniformly heat the cell and the absorbing gas (CH_4). Six type-K thermocouples

measure the temperature along the cell axis (see appendix D for the 3D graph of the glass cell and heater). One of the thermocouples controls the cell temperature via a PID controller. With this arrangement, the temperature deviations along the length of the cell were less than 2% during measurements. The cell can be evacuated to less than 1 torr, and is flushed and filled with CH_4 for several times before each measurement. An MKS Baraton pressure transducer with ±1% reading accuracy measures the pressure in the cell.

For the H_2O pressure broadening measurement a slightly different setup is used. In these set of experiments, the water vapor in the headspace of a sealed flask containing liquid water is used as a source of H_2O vapor. To have access to higher water vapor pressures needed for pressure broadening measurements, part of the piping, the water flask, and also the pressure transducer are kept at approximately 45 °C by hot air from an electrical heater. In this setup a strain gage pressure transducer (Omega model PX202) is used.

5.2.2 Line strength at room temperature

Figure 5.3 illustrates the absorption signal as the laser is swept over the R(3) and R(4) transitions. The ring interferometer signal, which allows relative frequency to be readily determined, is also shown in this Figure. For each sequence of absorption measurements, the incident intensity (I_0) is obtained by collecting the transmitted signal (I) when the cell is evacuated. A 5^{th} order polynomial is fitted to this collected data. To obtain the baseline amplitude of the incident light at each absorption measurement, another fitting between the 5^{th} order fitted curve and the

array of data from the measured intensity in regions far from the CH_4 absorption region is performed.

Two new five and six-parameter models for the R(3) and R(4) transitions, suitable for treating the overlapped transitions of R(3) and R(4) are used. The general form of these models is:

$$Abs(\nu) = P_{abs} L \sum_{i=1}^{N} S_i \phi_i (\Delta\nu_D, \Delta\nu_L, \nu - \nu_{0,i}) \qquad (5.5)$$

where N is the number of transitions, three and four for R(3) and R(4) respectively. In Equation (5.5) ϕ_i is the Voigt line shape function of transition i based on Whiting's expression, with half-width for Doppler broadening $\Delta\nu_D$, Lorentzian (pressure) broadening half-width $\Delta\nu_L$, and relative central frequency of transition i of $\nu_{0,i} = \nu_0 + \delta\nu_i$, in which ν_0 is a reference frequency chosen arbitrarily where the absorbance is a maximum, and $\delta\nu_i$ is frequency spacing of individual transitions i from υ_0. In these models, $\Delta\nu_L$ for all transitions in each manifold are assumed to be equal.

For each manifold, R(3) and R(4), the measured absorbance at known conditions (room temperature / CH_4 pressure) is least square fitted using Equation (5.5), based on frequency spacing taken from Tables 1 and 2 (values from HITRAN 96 (Rothman, Rinsland et al. 1998)), and Doppler width $\Delta\nu_D$, calculated from Equation (4.13). The fitted parameters, including individual line strengths S_i, collisional width $\Delta\nu_L$, and reference frequency υ_0, are obtained after each fitting.

The acquisition of an absorption signal such as in Figure 5.3 allows the calculation of the line strengths S_i using the procedure outlined above. Line strength

is only a function of temperature. To calculate the line strengths at room temperature, measurements are made over a range of CH_4 pressures from approximately 2 to 6.5 torr for R(3) and from 4 to 16 torr for R(4). The results of the measurements for each of the lines, plus the total line strength for R(3) and R(4) manifolds, are shown in Figures 5.4 and 5.5, respectively. The averaged experimental results for each line allow the determination of an overall line strength at 296K, as shown in Tables 5.1 and 5.2. The errors indicated in the tables are the standard deviations in the data; each data point is the average of between three and five individual measurements. Additional uncertainties such as gas partial pressures are not reflected. The total uncertainties in the measured line strengths are 2.3%, the detail calculations of the total uncertainties are presented in Appendix E. As illustrated in tables 5.1 and 5.2, good agreement is found between the experimental values and the HITRAN 96 predictions at room temperature.

The measured absorption spectra corresponding to Figure 5.3 and the five- and six-parameter model fit to the data are compared for the R(3) and R(4) manifolds in Figure 5.6, respectively. The total absorbance as a function of frequency for each of these transitions is reconstructed, and the individual line contributions are also shown in the Figure. The multi-line fit and the data have close correspondence in both the R(3) and R(4) cases.

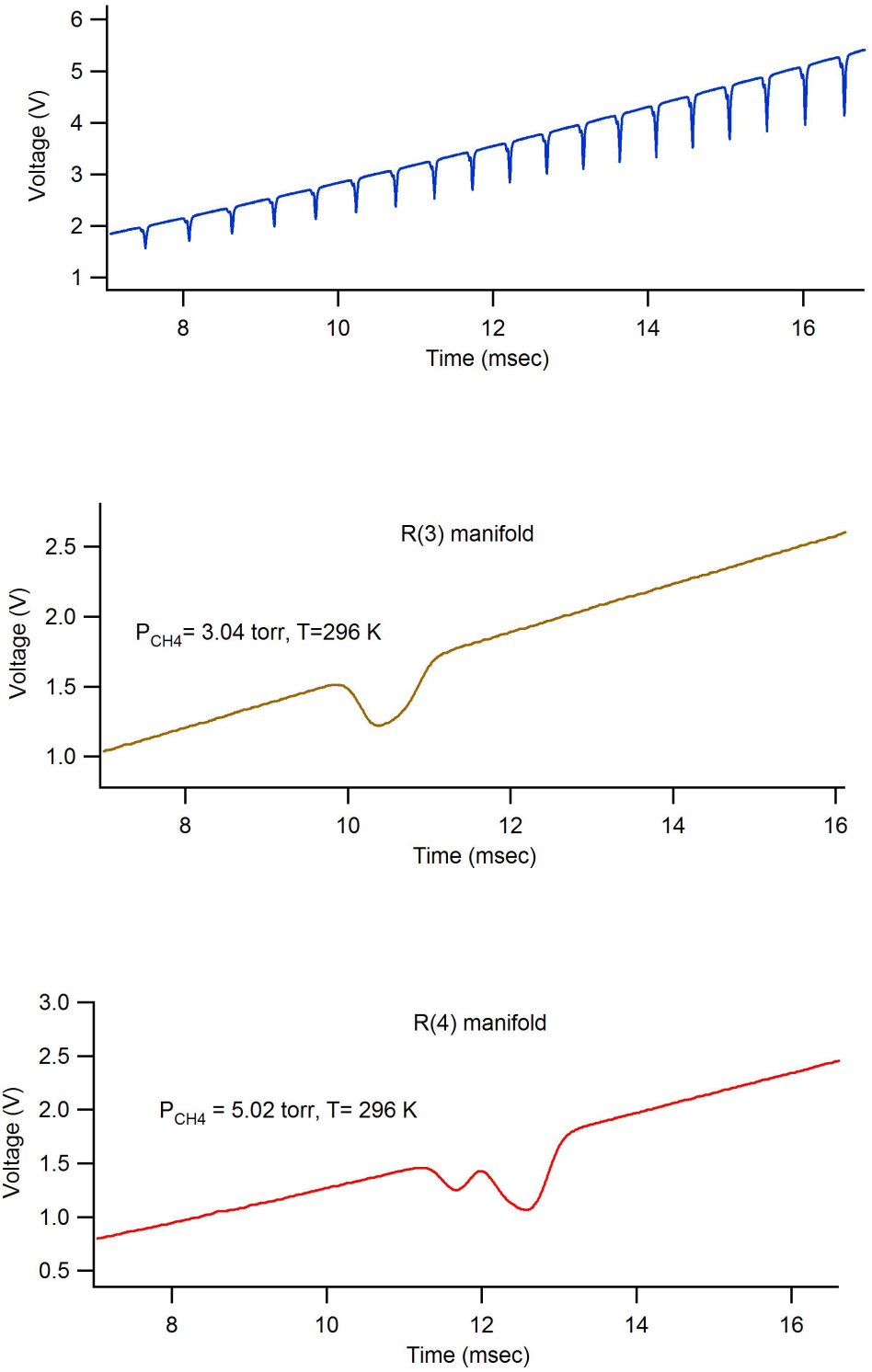

Figure 5.3: From top to bottom: Ring interferometer signal, absorption signal for R(3), and absorption signal for R(4).

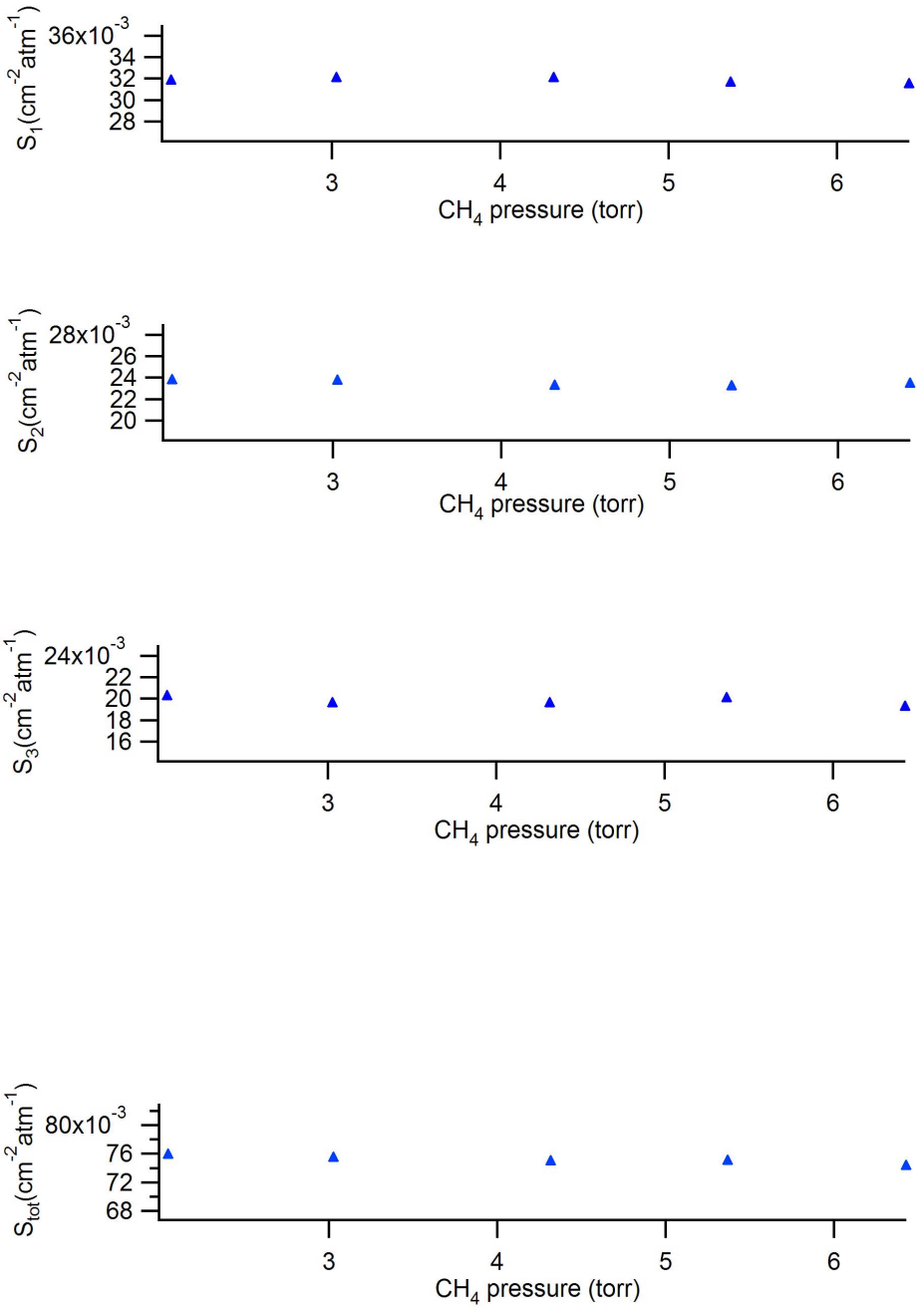

Figure 5.4: Measured room temperature (296 K) line strengths for each of the R(3) lines of CH_4, and total line strength at 296 K.

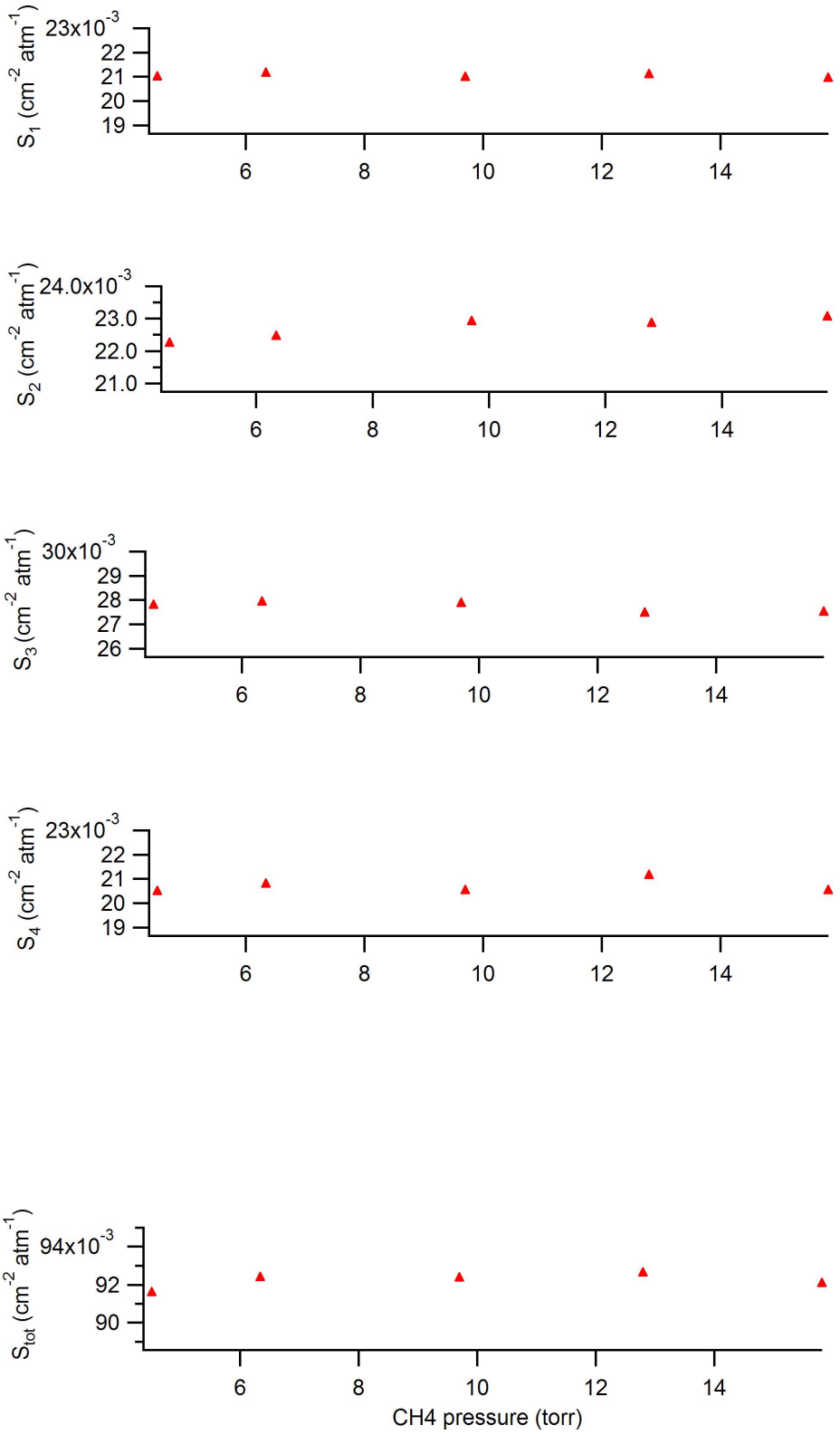

Figure 5.5: Measured room temperature (296 K) line strengths for each of the R(4) lines of CH_4, and total line strength at 296 K.

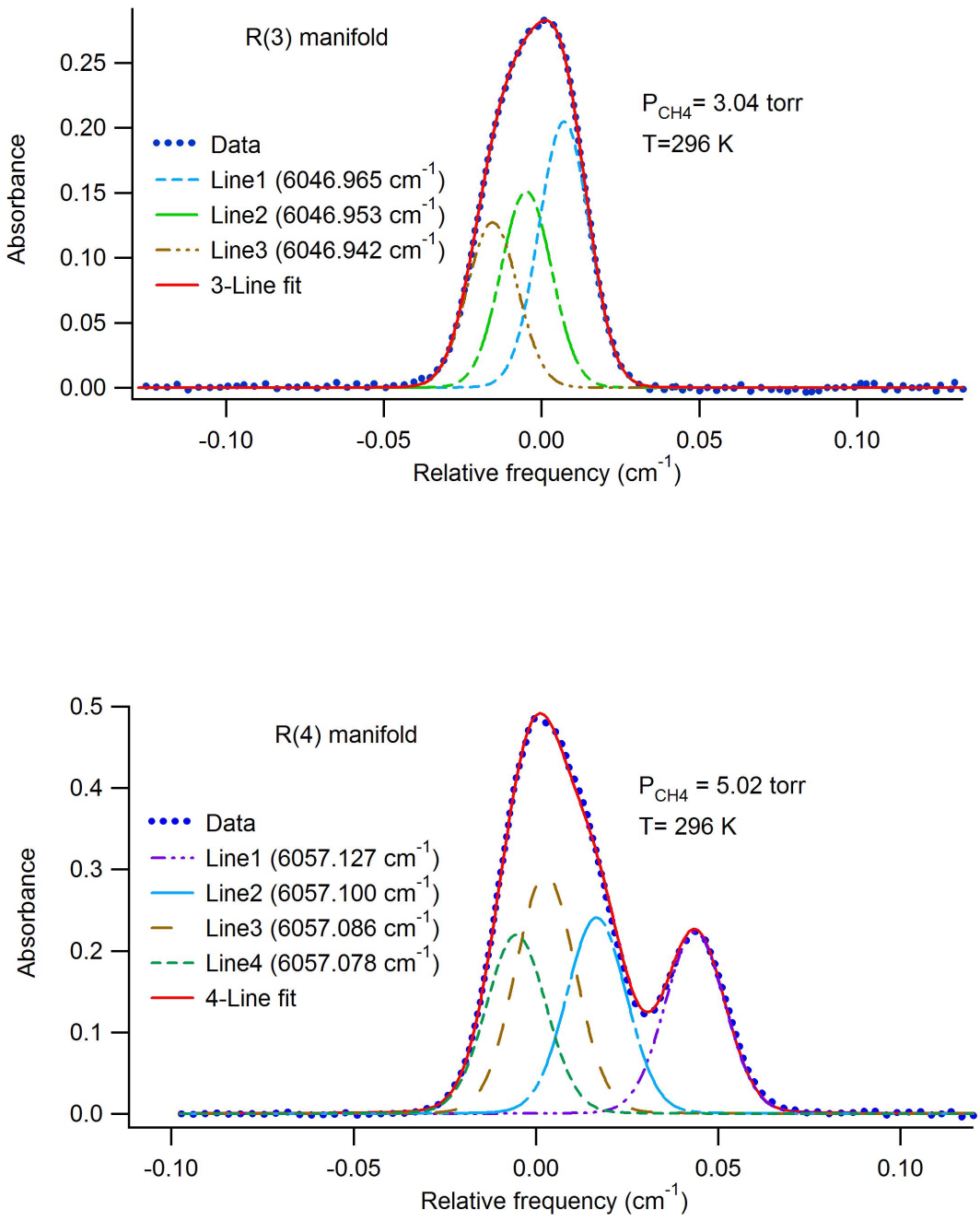

Figure 5.6: Comparison between the experimental and fitted model results for R(3) transitions (upper trace) and R(4) transitions (lower trace) at room temperature (T=296 K).

5.2.3 Line strength at elevated temperature

At higher temperatures, a similar method is applied to determine line strength. Line strengths for all of the transitions decrease exponentially with temperature, requiring increased pressure to generate a measurable signal. For these higher-pressure, higher-temperature measurements, the combination of pressure broadening and Doppler broadening, plus a significantly decreased signal, allows fitting only of the total line strength. Since lower-state energy levels (as shown in Tables 5.1 and 5.2) of the individual transitions for each manifold are very close, based on Equation (5.4), the line strength of each transition shares a similar temperature dependence. As a result, the ratio of line strengths at room temperature allows assessment of individual line strengths at high temperature from the total measured line strength, assuming that the ratio is constant with temperature.

Following the method used by Nagali et al. for a similar (R(6)) transition of CH_4 (Nagali, Chou et al. 1996), a simple harmonic oscillator model (SHM) is used for the vibrational partition function to compare the measured value of line strength at higher temperatures using Equation (5.4). The room temperature (296 K) line strength is used as a reference in the model. Tables 5.3 and 5.4 illustrate the comparison between the measured and modeled values at different temperatures for the R(3) and R(4) manifold. The errors shown in these Tables represent the standard deviation of the line strength from the measurements. Details of the overall uncertainty in the line strength are given in the Appendix E, the overall uncertainty is approximated 2.3% based on 1% uncertainty in pressure, 2% in the fit, and 0.3% in optical path. In Tables 5.3 and 5.4, numbers with asterisk means they are obtained from HITRAN.

Table 5.3: Variation of S_{tot} in R(3) with temperature

Temperature (K)	SHM (calculation) [cm^{-2}/atm]	Measured S_{tot} [cm^{-2}/atm]
296	0.07773*	0.07521 ± 0.00060
382	0.04305	0.04182 ± 0.00033
482	0.02394	0.02361 ± 0.00046
580	0.01429	0.01358 ± 0.00013
670	0.00918	0.00872 ± 0.00009
781	0.00540	0.00517 ± 0.00004
908	0.00312	0.00303 ± 0.00004

Table 5.4: Variation of S_{tot} in R(4) with temperature

Temperature (K)	SHM (calculation) [cm^{-2}/atm]	Measured S_{tot} [cm^{-2}/atm]
296	0.09646*	0.09225 ± 0.00040
382	0.05593	0.05391 ± 0.00088
482	0.03214	0.03081 ± 0.00061
580	0.01959	0.01836 ± 0.00022
670	0.01277	0.01200 ± 0.00023
781	0.00761	0.00715 ± 0.00010
908	0.00444	0.00418 ± 0.00009

5.2.4 Pressure broadening calculation

As already noted, at higher temperatures and pressures the contributions of individual lines cannot be extracted reliably from the five and six-parameter model that is applied for the room temperature measurements. Using the fact that each line changes similarly with temperature in a known manner, while relative line strengths (the ratio of individual line strength to the total line strength of the manifold) remain constant at different temperatures, the five and six-parameter model can be simplified. The corresponding three and four line strengths S_i in the five and six-parameter model can be collapsed into a single free parameter S_{tot}, as shown in Equation (5.11). Relative line strengths ω_i, which are known from room temperature measurements, are used to determine the contribution of each line in the modeling procedure.

$$Abs(\nu) = P_{abs} L \sum_{i=1}^{N} S_{tot} \omega_i \phi_i (\Delta\nu_D, \Delta\nu_L, \nu - \nu_{0,i}) \qquad (5.6)$$

Using these simplifications, Equation (5.6) describes a three-parameter model for the pressure broadening calculation based on fitting parameters including total line strength S_{tot}, collisional half-width $\Delta\nu_L$, and central frequency ν_0. An example of the three-parameter model fit to experimental data for calculating self-broadening half width at a high temperature for methane is shown in Figure 5.7.

Using this three-parameter model, the effect of quenching gases including CO_2, N_2, H_2O, CH_4, and CO on the collisional broadening is investigated as a function of temperature. Figures 5.8 and 5.9 illustrate the variation of collisional half-width for the R(3) transitions with pressure of CO_2, and N_2 at two different

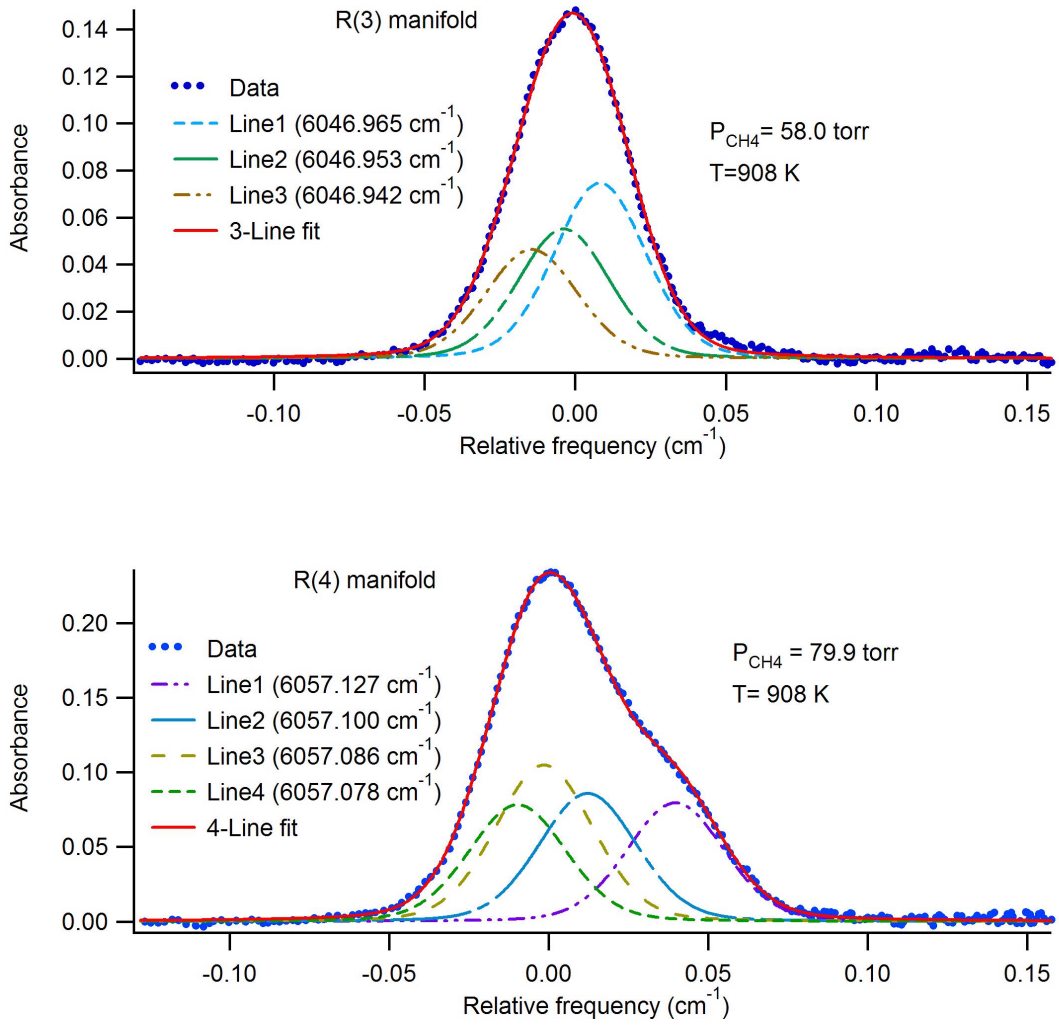

Figure 5.7: Comparison between the experimental and fitted model results for R(3) transitions (upper trace) and R(4) transitions (lower trace) at high temperature (T= 908 K).

temperatures. The slope of the graphs yields the collisional broadening coefficient γ, which is shown in the Figures. Figures 5.10 and 5.11 present the same parameters for the R(4) transitions. The results of the measured collisional broadening coefficients based on the three-parameter model at different temperatures are summarized in Tables 5.5 and 5.6 for the R(3) and R(4) transitions, respectively; the errors shown

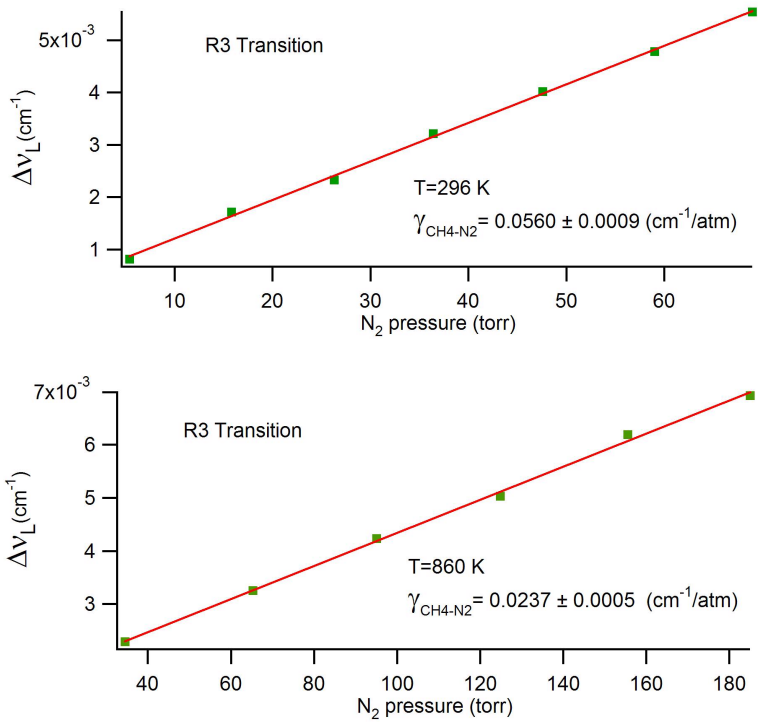

Figure 5.8: Collisional broadening half-width of CH_4 by N_2 for R(3) transitions as a function of pressure. Upper trace at room temperature (296 K), and lower trace at high temperature (860 K).

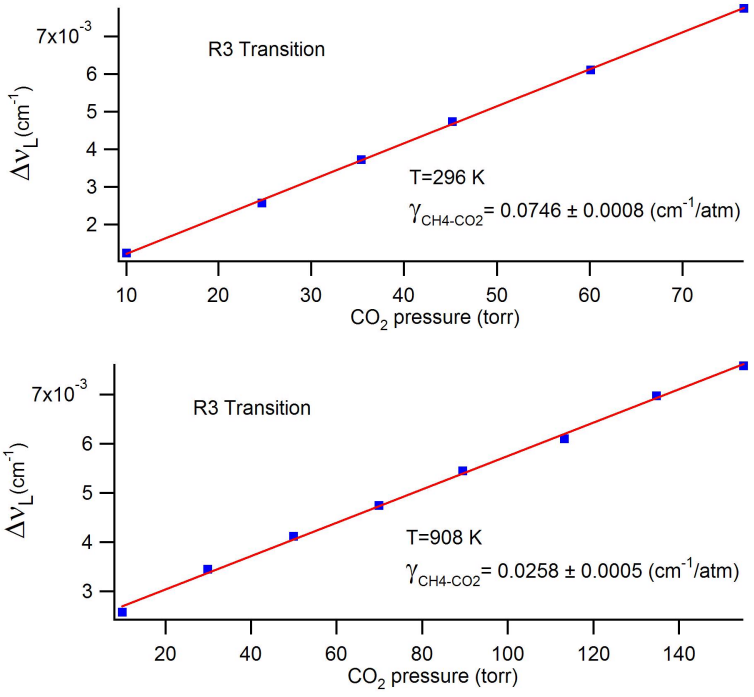

Figure 5.9: Collisional broadening half-width of CH_4 by CO_2 for R(3) transitions as a function of pressure. Upper trace at room temperature (296 K), and lower trace at high temperature (908 K).

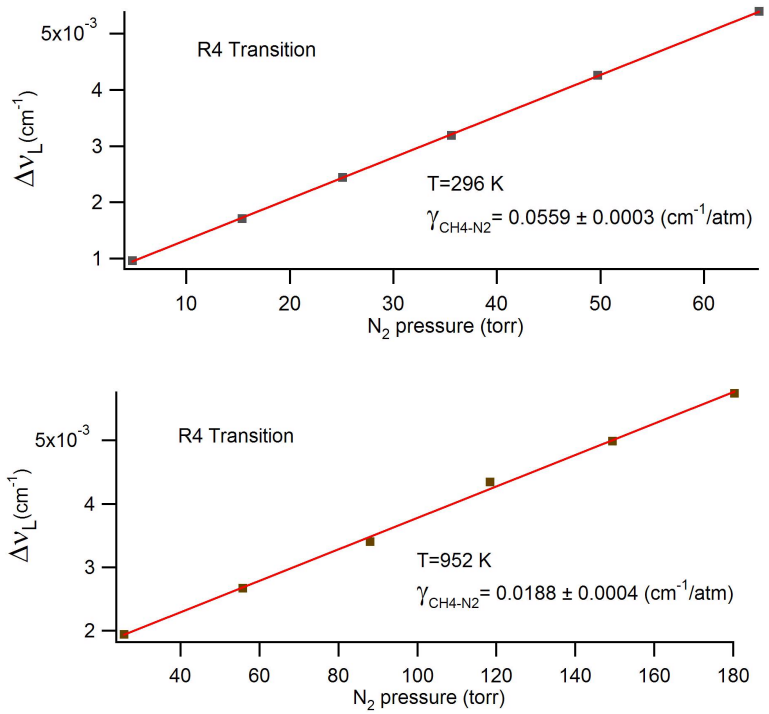

Figure 5.10: Collisional broadening half-width of CH_4 by N_2 for R(4) transitions as a function of pressure. Upper trace at room temperature (296 K), and lower trace at high temperature (952 K).

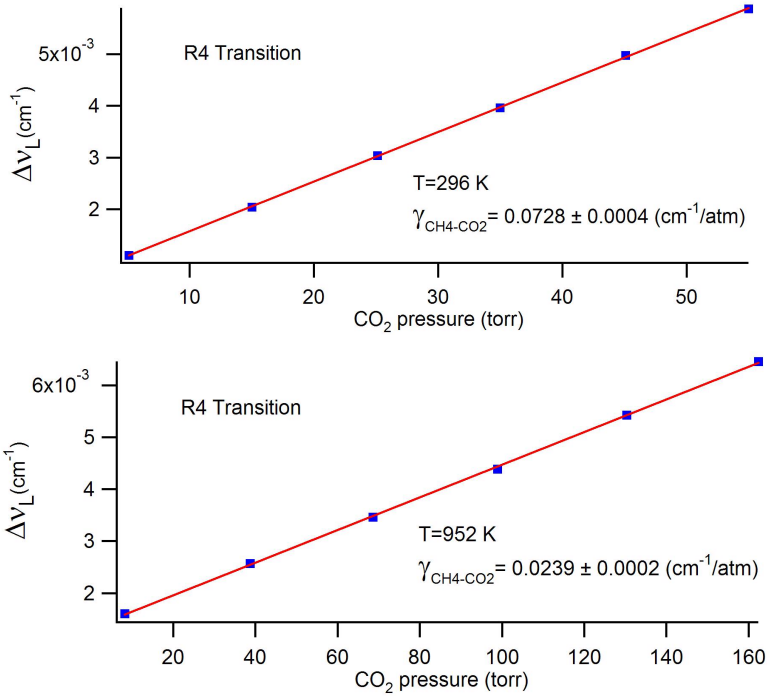

Figure 5.11: Collisional broadening half-width of CH_4 by CO_2 for R(4) transitions as a function of pressure. Upper trace at room temperature (296 K), and lower trace at high temperature (952 K).

Table 5.5: Variation of collisional half-width with temperature in R(3) manifold

Broadening Gas	γ (cm^{-1} atm^{-1})					
	296 K	482 K	670 K	813 K	860 K	908 K
N_2	0.0560 ± 0.0009	0.0371 ± 0.0005	0.0286 ± 0.0006	---	0.0237 ± 0.0005	---
CO_2	0.0746 ± 0.0008	0.0488 ± 0.0010	0.0354 ± 0.0016	---	---	0.0258 ± 0.0005
CH_4	0.0766 ± 0.0008	0.0481 ± 0.0004	0.0361 ± 0.0008	0.0297 ± 0.0007	---	---
CO	0.0579 ± 0.0006	0.0385 ± 0.0011	0.0282 ± 0.0008	---	---	0.0239 ± 0.0003

Broadening gas	γ (cm^{-1} atm^{-1})			
	316 K	390 K	482 K	580 K
H_2O	0.0759 ± 0.0017	0.0635 ± 0.0004	0.0500 ± 0.0016	0.0441 ± 0.0012

Table 5.6: Variation of collisional half-width with temperature in R(4) manifold

Broadening Gas	γ (cm^{-1} atm^{-1})			
	296 K	482 K	670 K	952 K
N_2	0.0559 ± 0.0003	0.0358 ± 0.0006	0.0267 ± 0.0002	0.0188 ± 0.0004
CO_2	0.0728 ± 0.0004	0.0444 ± 0.0006	0.0332 ± 0.0006	0.0239 ± 0.0002
CH_4	0.0731 ± 0.0022	0.0466 ± 0.0005	0.0340 ± 0.0010	0.0240 ± 0.0004
CO	0.0575 ± 0.0005	0.0360 ± 0.0013	0.0285 ± 0.0007	0.0213 ± 0.0005

Broadening Gas	γ (cm^{-1} atm^{-1})			
	316 K	390 K	482 K	580 K
H_2O	0.0762 ± 0.0013	0.0575 ± 0.0005	0.0504 ± 0.0015	0.0376 ± 0.0011

represent the standard deviation of the broadening coefficient from the measurements. The overall uncertainty in the broadening coefficients is 16% (see Appendix E).

For each quenching gas, the coefficient of broadening is expected to vary with temperature with the relationship $\frac{\gamma(T)}{\gamma(T_0)} = \left(\frac{T_0}{T}\right)^n$, where n is generally assumed to be constant. The results presented in Tables 5.5 and 5.6 are used for the calculation of the parameter n. Figure 5.12 illustrates the temperature variation of the broadening coefficient with gases N_2 and CO_2 for the CH_4 R(3) manifold. The slope of these graphs represents the parameter n, as indicated on these Figures. The corresponding results for the R(4) transition is presented in Figure 5.13. The parameter n for all of quenching gases for the R(3) and R(4) manifolds are calculated based on the measured values of pressure broadening coefficients at different temperature. These results are summarized in Table 5.7.

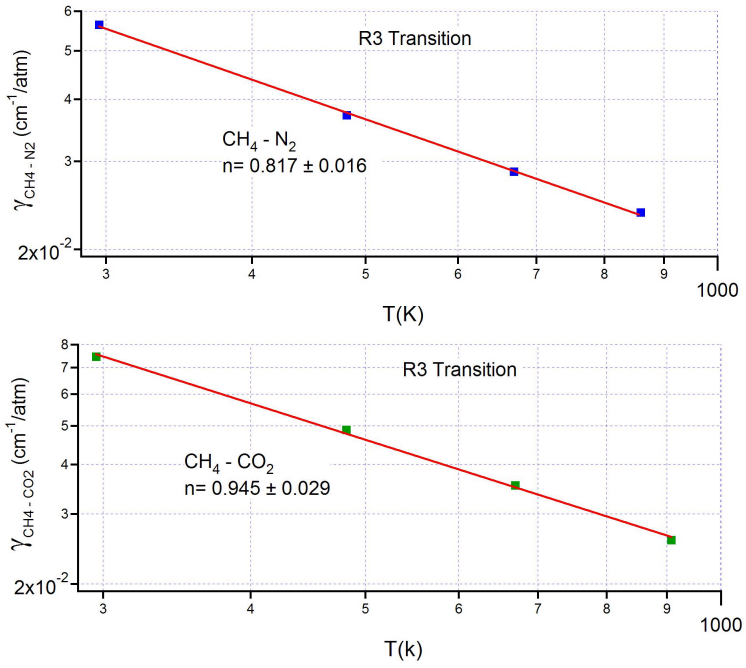

Figure 5.12: The temperature variation in broadening coefficient half-width of CH_4 by N_2 (top trace) and CO_2 (bottom race) for R(3) transitions.

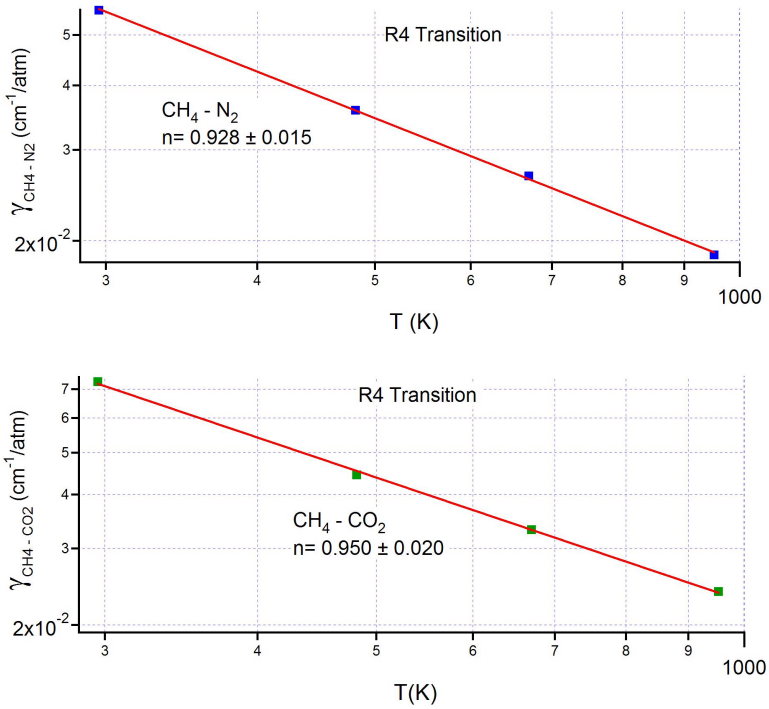

Figure 5.13: The temperature variation in broadening coefficient half-width of CH_4 by N_2 (top trace) and CO_2 (bottom race) for R(4) transitions.

Table 5.7: Temperature dependence of collisional broadening line width parameter *n* for different colliding gases. Uncertainty represents the standard deviation in the data.

Transition	*N*				
	N_2	H_2O	CO_2	CH_4	CO
R(3)	0.817 ± 0.016	0.920 ± 0.056	0.945 ± 0.029	0.931 ± 0.014	0.808 ± 0.050
R(4)	0.928 ± 0.015	0.907 ± 0.085	0.950 ± 0.020	0.952 ± 0.012	0.844 ± 0.031

5.3 Measurement of H_2O spectroscopic parameters

Water vapor, a trace species in the atmospheric air and a major product species in combustion reaction of hydrocarbons, has strong absorption line strengths in $\nu_1+\nu_3$, $2\nu_1$, and $2\nu_3$ combination and harmonic bands throughout the 1.3-1.4 μm region. H_2O transitions near 1.343 μm ($\nu_1+\nu_3$ band) and 1.392 μm ($2\nu_1$, $\nu_1+\nu_3$ bands) have been used for H_2O concentration measurements (Nagali, Furlong et al. 1995). In addition, absorption transitions of H_2O near 2.0 μm ($\nu_2+\nu_3$ band), which are approximately one order of magnitude stronger than those near 1.4 μm, have been used for H_2O concentration measurements in combustion systems (Mihalcea, Baer et al. 1998).

In addition to species measurement, tunable diode lasers can be used for temperature measurement using the variation in absorption line strengths as a function of temperature. The variation in the absorption line strength ratios of two selected H_2O transitions (Baer, Hanson et al. 1994; Nagali, Furlong et al. 1995) and also two CO_2 transitions (Ikeda, Chung et al. 2001) have been used for temperature measurement in combustion systems. A relatively recent review covering many of the more challenging combustion measurements has been contributed by Allen (Allen 1998)

In this research H_2O absorption transitions (6771.747 and 6771.710 cm^{-1} from the $2\nu_1$ band and 6771.475 cm^{-1} from the $2\nu_2+\nu_3$ band) have been identified which can be used for temperature and also H_2O concentration measurements have been identified. Detail spectroscopic information about these transitions is presented in Appendix B2. Opposed to other traditional temperature sensors that use two custom diode lasers for temperature measurement, using the selected transitions enables

temperature measurement by using a single diode laser. In the following, measurement of the spectroscopic parameters of these transitions is presented. Also, it is shown that the selected transitions have strong temperature variation such that the ratio of their integrated absorbance can be used for temperature measurement in over the wide range of temperatures expected in a combustion system.

5.3.1 Experimental details

The schematic diagram of the experimental apparatus for the line strength measurement is shown in Fig. 5.14. A fiber-pigtailed distributed feedback (DFB) diode laser (Corning Lasertron) operating at 1476.9 nm, driven by an ILX Lightwave model LDC-3724B power supply, generates tunable light. The laser tunes over 1.2 cm^{-1} when the injection current from a function generator (Tektronix CFG250) is ramp-modulated with a frequency of 50 Hz to record three H_2O absorption line transitions between 6771.47 – 6771.75 cm^{-1}. The laser output is split into two beams using a 1×2 fiber splitter. A fiber collimator collimates the main beam (90% in power) and directs it to a static glass cell containing H_2O at known temperature and pressure. The main beam exits the static cell following possible absorption and is detected by a Ge photodetector (New Focus model 2033). The other beam (10% in power) is sent to a ring interferometer (RI) with a free spectral range of 0.02296 cm^{-1} and monitored by a second Ge photodetector (New Focus model 2011). The detected signals from both detectors are displayed on a Lecroy 9310 dual-channel oscilloscope, from which they are downloaded to a PC by a Labview program. The RI signal allows conversion of the time domain in the experiment to the frequency

domain, and is used to reconstruct the incident light (unattenuated signal) entering the static cell (I_0). Before absorption measurements, the reconstruction of the incident light using the RI signal was tested by performing some measurements with no absorbing species in the optical path. After each of these measurements, calculated incident light from the RI signal was compared with the real incident light. Essentially perfect agreement between the calculated and measured incident light was observed.

During experiments, the cell is evacuated to less than 1 torr, and is flushed and filled with H_2O several times before each measurement. An MKS Baraton pressure transducer with ±1% reading accuracy measures the pressure in the cell. To reduce H_2O background absorption outside the static cell, purge tubes are placed outside the cell at each end of the heater, as shown in Figure 5.4, and these volumes were continuously purged with argon, the primary difference between this experiment setup and that shown in Figure 5.2.

For the pressure broadening measurement some changes to the previous setup are made. To have access to higher water vapor pressures needed for pressure broadening measurements, part of the piping, the water flask, and also the pressure transducer are kept at approximately 45 °C by hot air from an electrical heater. In this setup a strain gage pressure transducer (Omega model PX202) is used. Also, the purging tubes were extended all the way inside the heater to the static cell windows so that the H_2O background is minimized (almost no H_2O background absorption is observed after this modification). In addition to these changes the photodetector signals are directly

digitized by an analog input E Series Data Acquisition Card (DAQ) through a Labview program and the acquired data are downloaded to a PC.

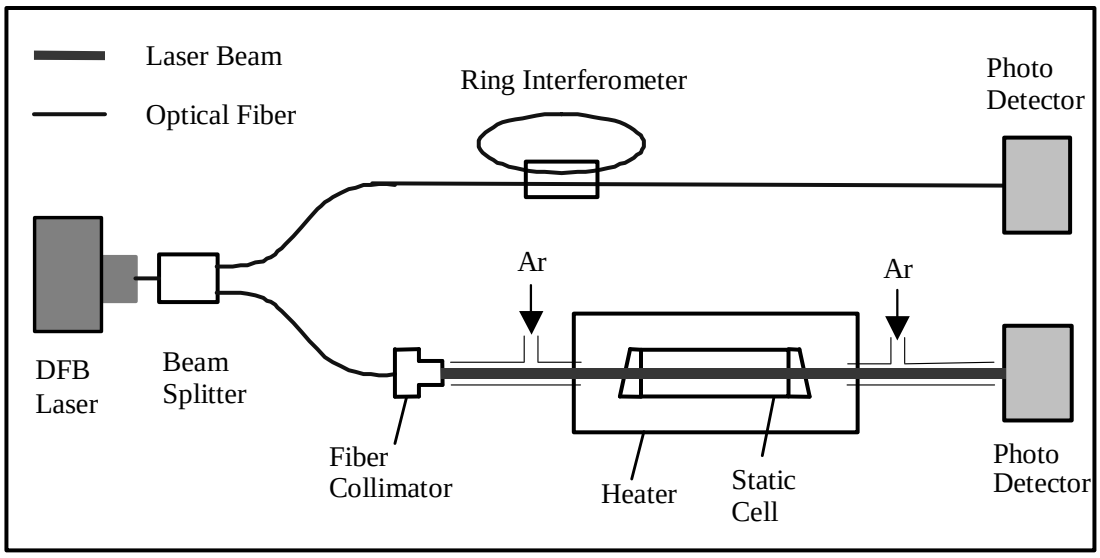

Figure 5.14: Schematic diagram of the experimental set up used to measure line strengths of H_2O.

5.3.2 Line strength measurement and temperature sensitivity of the transitions

Figure 5.15 shows samples of raw data collected when the temperature and pressure of H_2O in the cell were set to 24.6 torr and 463 K (top) and 27.6 torr and 977 K (bottom) respectively. As mentioned above, the RI signal is used to reconstruct the unattenuated signal (I_0). For this purpose, an array of data between each pair of adjacent fringes is extracted from the collected RI signal and all of the data is fitted with a single third order polynomial. Since the amplitude of the RI and I_0 signal are not the same, another fitting between the third order fitted curve and array of data from I signal (far from the H_2O absorption region) is performed. The second fitting process allows us to obtain the real amplitude of the unattenuated I_0 signal.

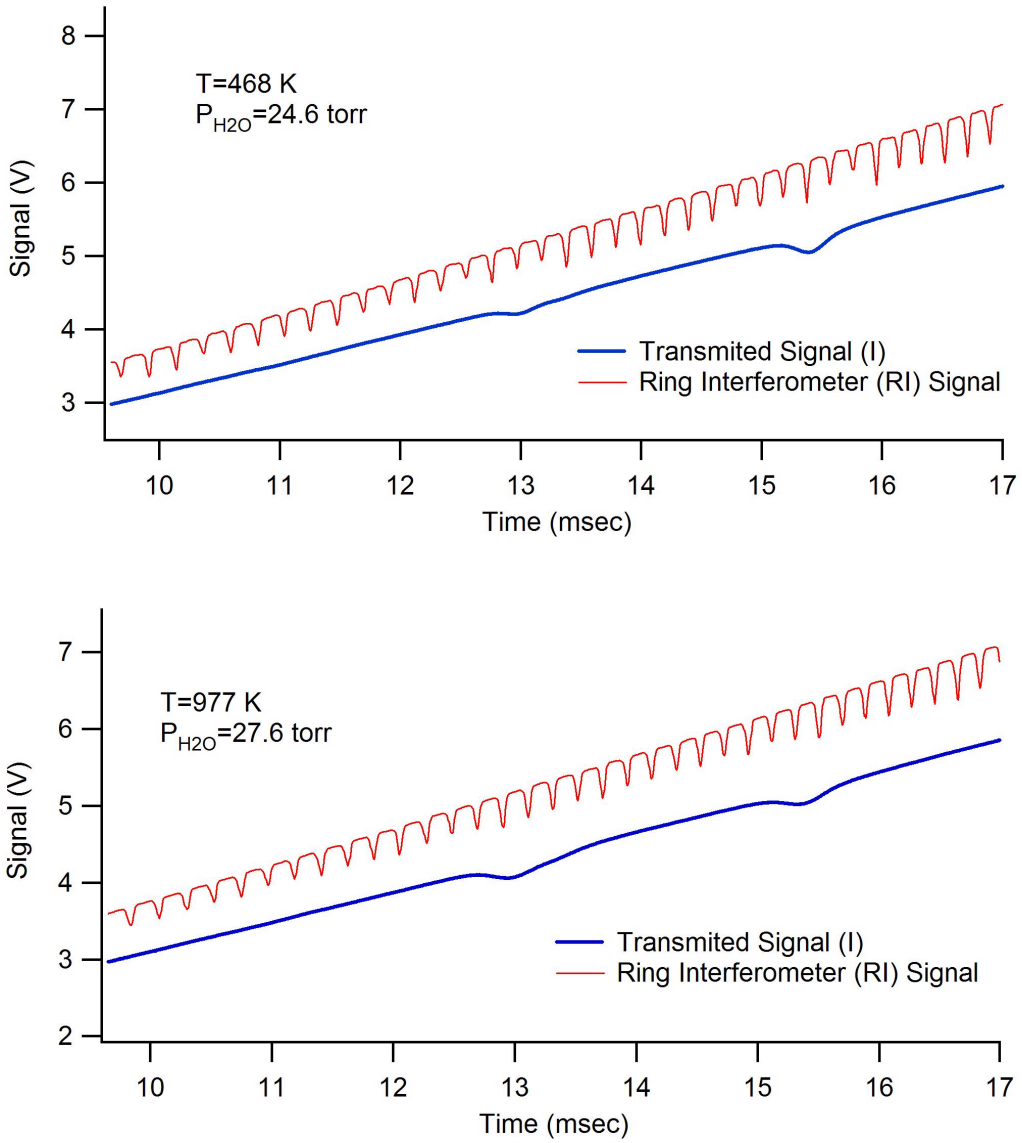

Figure 5.15: Transmitted signal (I) and RI signal at different temperature and pressure conditions. The top figure was at T= 468 K, P_{H2O}=24.6 torr and the bottom was at T= 977 K, P_{H2O}=27.6 torr.

From the HITRAN 96 database (Rothman, Rinsland et al. 1998), there are three H_2O absorption lines within the tuning range of the laser, corresponding to Figure 5.15 data, as shown in Table 5.8. In the analysis of the data, the measured absorbances are least squares fit with three Voigt line shapes corresponding to each of the three H_2O lines. In the fitting processes, the Doppler widths for each transition are

first calculated based on the temperature of water vapor in the cell using Equation (4.13) and a frequency spacing based on the HITRAN database (Table 5.8) is assumed.

Table 5.8. Frequency spacing and line strengths at T=977 K (comparison between results of HITRAN 96 and measurement).

Line	ν_0 [cm^{-1}]	HITRAN 96 S [cm^{-1}/ (molec·cm^2)]	Measured S [cm^{-1}/ (molec·cm^2)]
1	6771.747	(S_1+ S_2)	(S_1+ S_2)
2	6771.710	2.399 x 10^{-22}	(2.33± .25) x 10^{-22}
3	6771.475	1.366 x 10^{-22}	(1.39± .13) x 10^{-22}

Figure 5.16 shows the results of fitting the data from Figure 5.15. The experimental data and the fitting results are so completely overlaid that the experimental and the sum fitted line are nearly impossible to separate in the figure.

The measured line strengths for the three transitions (S_1+ S_2 and S_3) at T = 977 K are shown in Table 5.8 and compared with HITRAN results. Due to the large value of Doppler broadening at elevated temperatures, individual S_1 and S_2 line strengths cannot be precisely obtained from fitting. However;, since the lower-state energy levels for these transitions are very close (from HITRAN, E″ is 1590.6900 and 1590.6910 cm^{-1} for S_1 and S_2 respectively), one can use the fact that the ratio of these transitions in absorption will not vary with temperature. By measuring the ratio of these transitions at lower temperatures (where the Doppler broadening is small) and using this ratio in the fitting processes for the higher temperature measurements, it is

possible to determine the individual S_1 and S_2 precisely. In this study, only the variation of (S_1+ S_2) and S_3 with temperature was needed and therefore no attempt

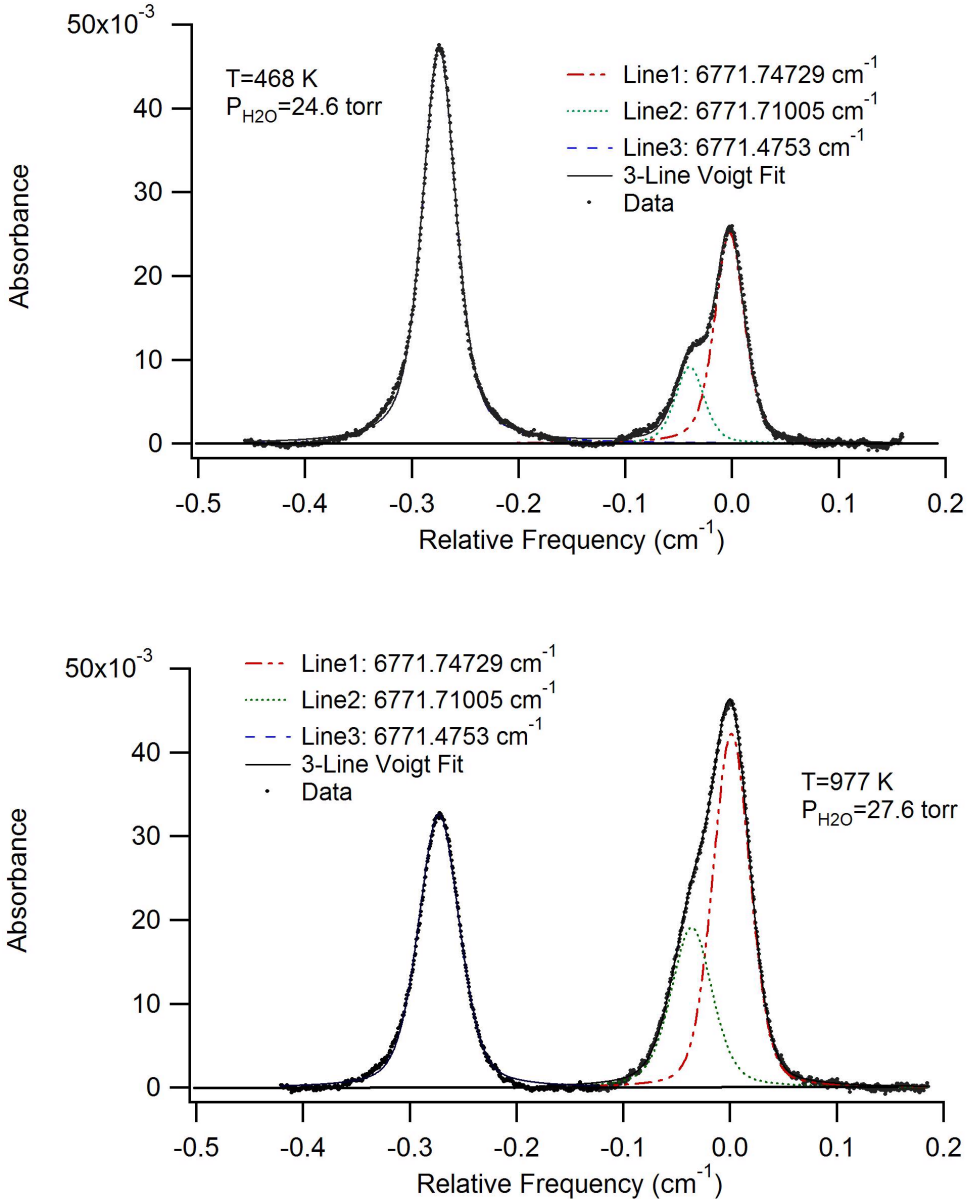

Figure 5.16: Measured and fitted results for H_2O absorbance corresponding to the data shown in Figure 2. The top figure was at T= 468 K, P_{H2O}=24.6 torr and the bottom was at T= 977 K, P_{H2O}=27.6 torr.

was made to calculate individual S_1 and S_2 during fitting processes. The measured line strengths, (S_1+ S_2) and S_3, over a range of temperatures are shown in Figure 5.17. Measurements at each condition are the average of 200 laser sweeps. Each data point in the line strength measurements (Figure 5.17) is comprised of 3 or 4 measurements, each at a different pressure. The uncertainties in the line strength measurement are shown in the Figure; the maximum uncertainty is approximately 11%, and most of the values are on the order of 3-4%.

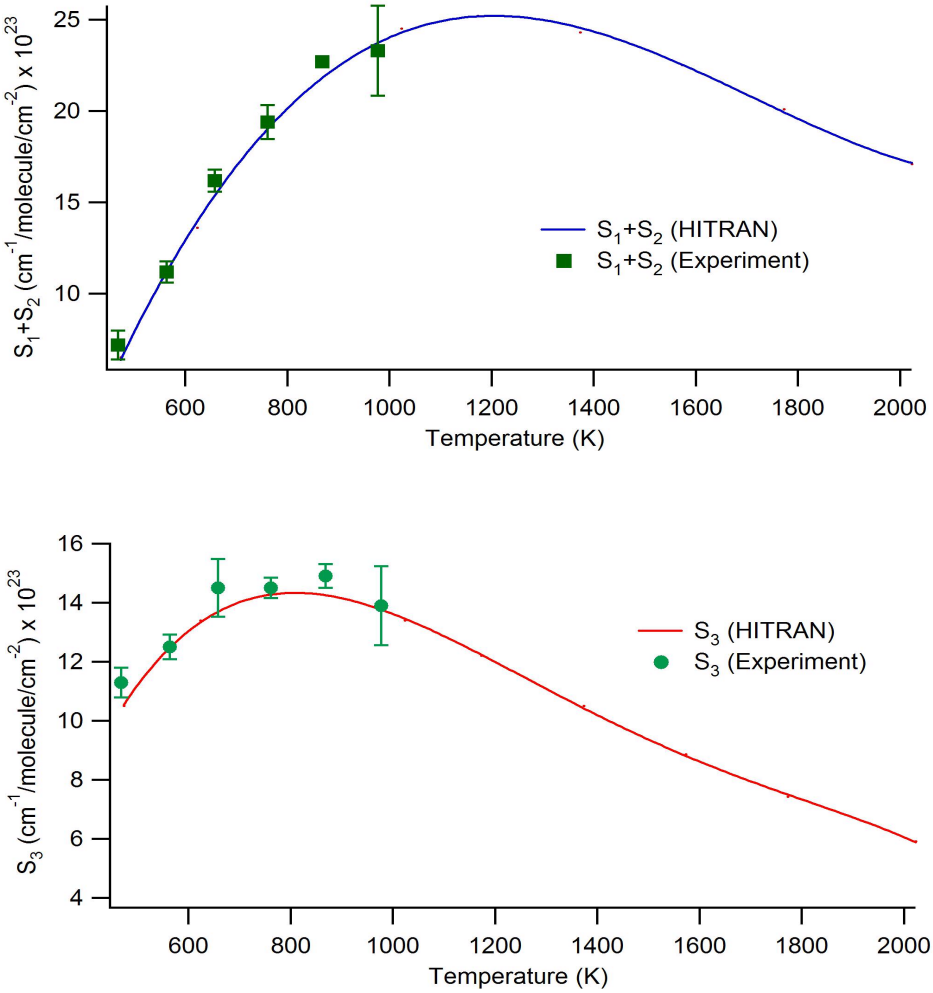

Figure 5.17: Comparison between the measured line strengths and HITRAN results. Top trace shows (S_1+S_2) and the bottom trace illustrates S_3.

The primary uncertainty in the measured values of the line strengths is related to the background H_2O absorption in the region outside the static cell. The argon purge the region outside the heaters, shown in Figure 5.14, eliminates background absorption in this low temperature region. The major background absorption is attributed to the optical path inside the heater (but outside the cell) where the purge is weaker and some atmospheric H_2O may penetrate. In this region the average temperature is approximately 30 – 50 ºC lower than the average temperature in the gas cell. For each temperature two background measurements are performed with the static cell hot and evacuated; the average of the background measurements allows calculation of the actual absorbance inside of the heated static cell. In Figure 5.17 a tolerance equal to $\pm 2\sigma$ was used as a measure for the uncertainty in the measured line strengths, where σ is the standard deviation in the measured line strengths at different H_2O pressures for each temperature. Details of the overall uncertainty in the line strength are given in the Appendix E. Based on the measurement results it appears that the HITRAN 96 database yields very good results for line strength of H_2O for these transitions at elevated temperatures.

The primary advantage of the selected frequencies is the significant variation of the line strengths with temperature, with line placement close enough to be scanned using a single diode laser. At the same time, these transitions have fairly strong line strengths, as shown in Figure 5.17. This variation in relative line intensities with changing temperature is illustrated for a particular case by comparing the graphs in Figure 5.16, which show measured water spectra at two different temperatures.

Previous diode laser temperature measurements reported in the literature (Baer, Hanson et al. 1994) and (Ikeda, Chung et al. 2001) have used two lasers.

The variation of the absorption line ratio of the first plus second line (S_1+ S_2) to the third line (S_3) with temperature is shown in Figure 5.18. The error bars shown in this Figure are calculated based on the measured line ratios at different pressures. These measured line ratios are compared with HITRAN 96 results. Using the agreement between the measured line ratio and HITRAN results, and assuming similar agreement over the range of temperatures shown in Figure 5.18, we expect that this set of lines could be used over a wide range of temperatures, from 450 to 2000 K. The HITRAN data predicts that the ratio of the first and second (overlapped) line strengths to the third transition varies between 0.57 and 2.9 over a temperature range of 450 to 2000 K. The measured uncertainty translates into an average temperature uncertainty of ± 24.9 ºC, as shown in the Figure**.**

The large, monotonic variation in the ratio of these lines makes this diagnostic suitable for simultaneous H_2O concentration and temperature measurement in atmospheric combustion systems where the pressure broadening is on the order of Doppler broadening. The suggested limitations on the upper and lower temperatures for this sensor (450 to 2000 K) are mainly due to the weaknesses of the line strengths above and below the suggested range for direct absorption measurements. Greater broadening due to increased pressure would interfere with the resolution of the lines, particularly at the upper and lower ends of the proposed temperature range where the line strengths of either (S_1+S_2) or S_3 are low as result of decreasing absorption cross-section. However, techniques such as wavelength modulation spectroscopy (WMS),

and frequency modulation spectroscopy (FMS) would likely extend the temperature range and would likely allow the sensor to be used in high-pressure combustion systems.

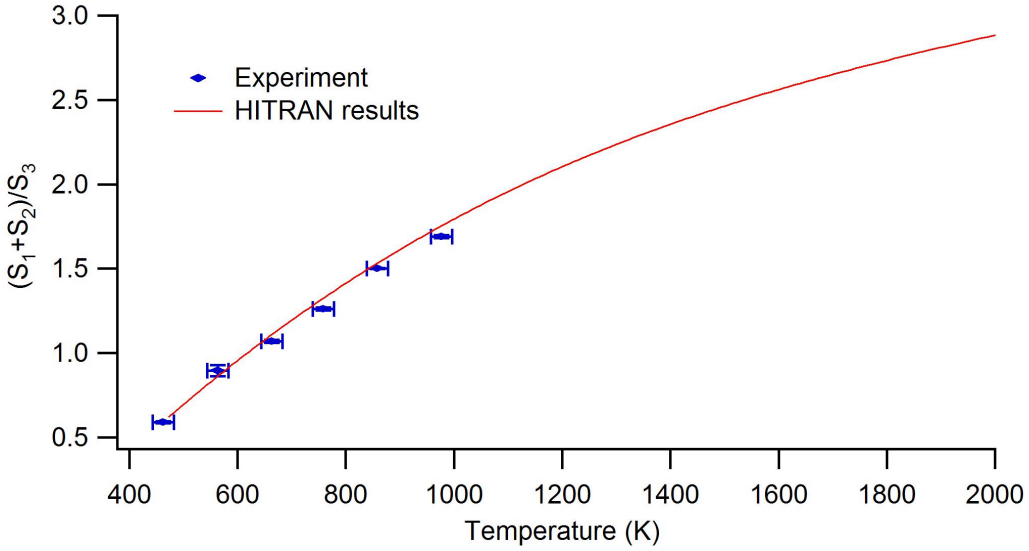

Figure 5.18: Comparison between the measured absorption ratio $(S_1+S_2)/S_3$, and HITRAN results.

5.3.3 Pressure broadening calculations

For H_2O pressure broadening calculations, the same procedure as applied for the CH_4 transitions is used. The only difference is that the parameter ω_i in Equation (5.6) for the CH_4 transitions was constant at different temperatures for all transitions; however, in the H_2O transitions only transition 1 and 2 change similarly with temperature and transitions 3 varies differently with temperature. For this reason, parameters ω_i were first calculated from line strengths predicted by HITRAN (which were validated by experiments) at the temperature of interest. Then the model explained in 5.2.4 was applied to the H_2O transitions, assuming transitions 1 and 2

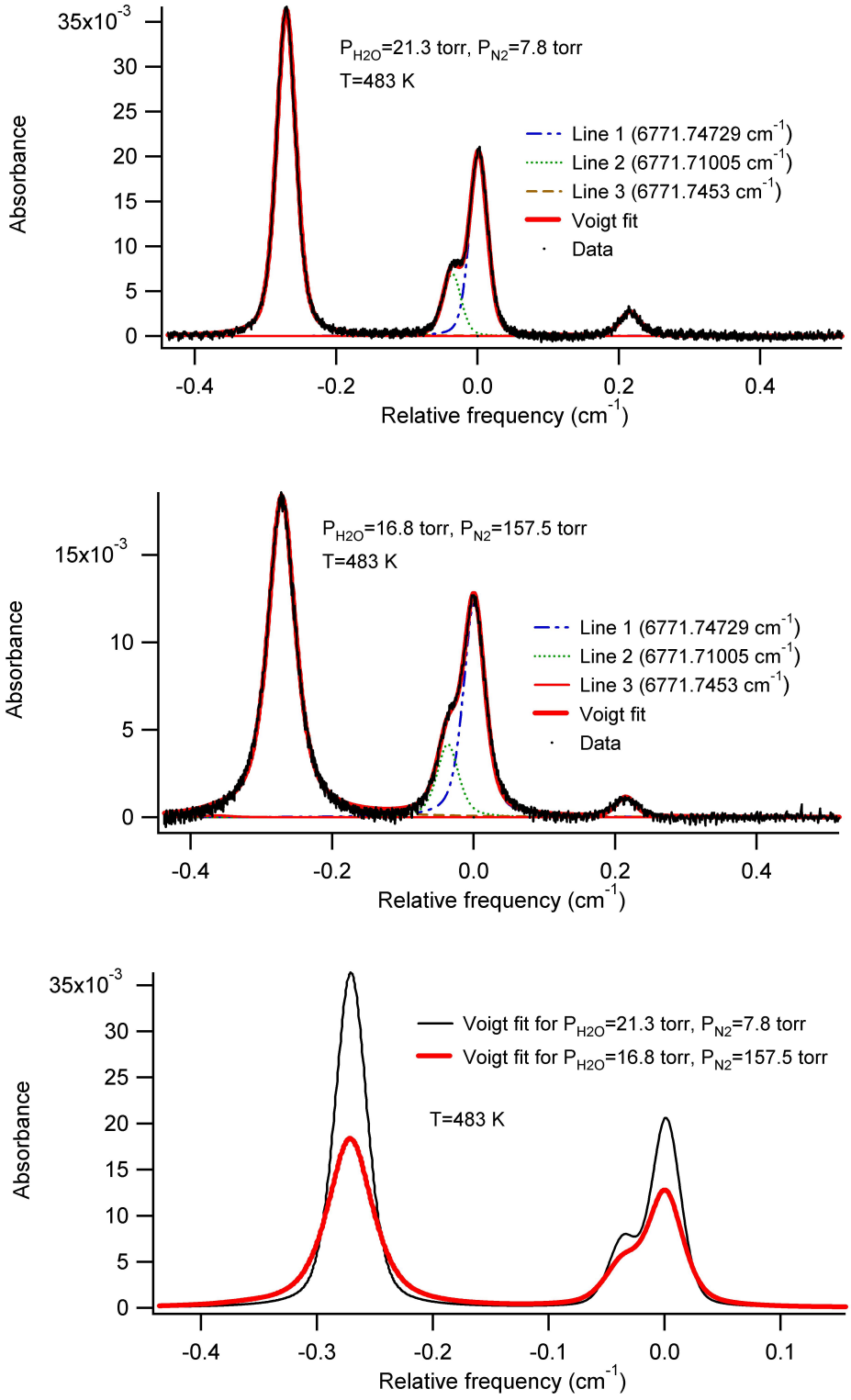

Figure 5.19: Measured and fitted results for H_2O absorbance at different pressure for calculating pressure broadening coefficient due to N_2 at T=483 K. Bottom trace compares the fitted absorption spectra.

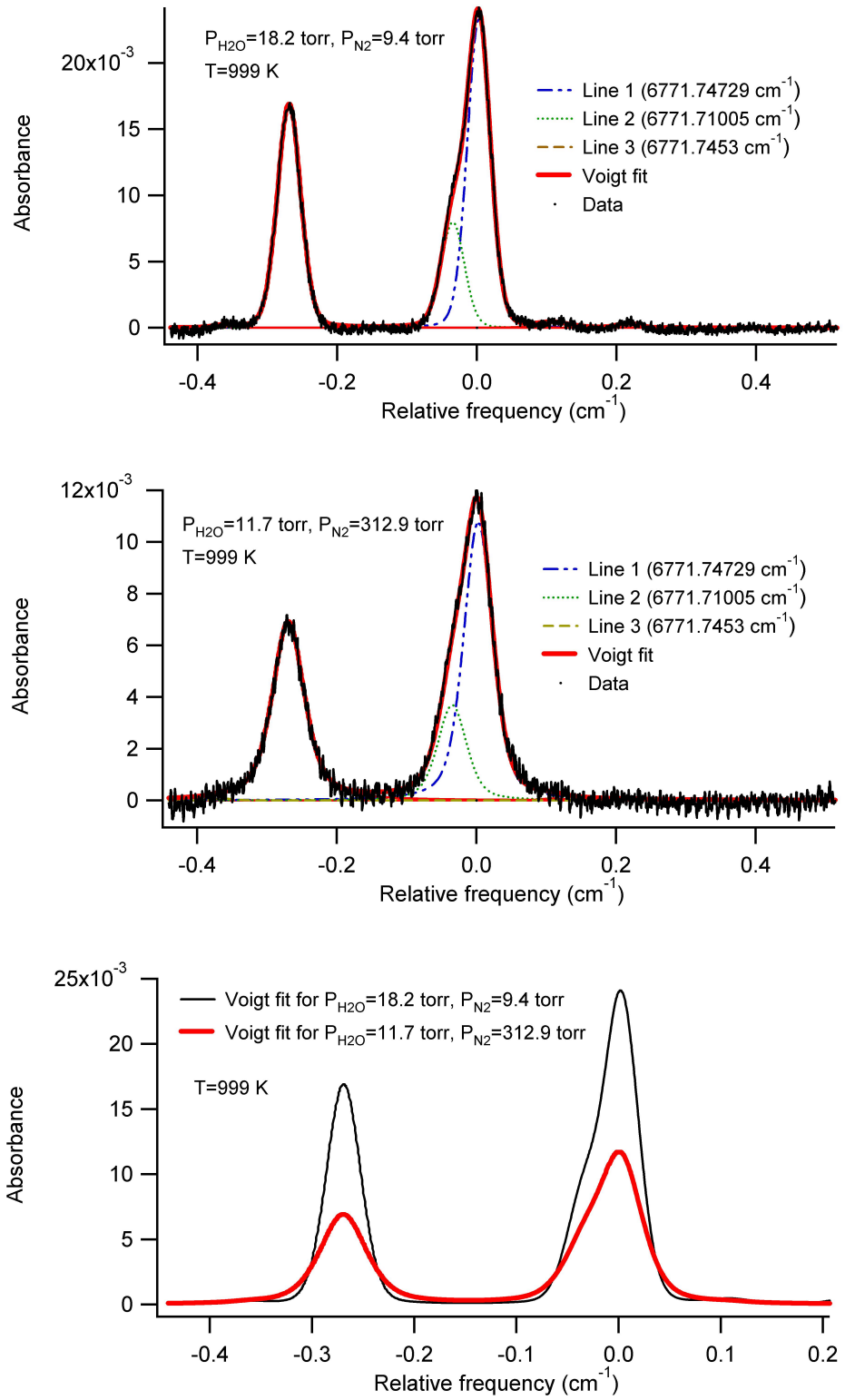

Figure 5.20: Measured and fitted results for H_2O absorbance at different pressure for calculating pressure broadening coefficient due to N_2 at T=999 K. Bottom trace compares the fitted absorption spectra.

have the same collisional half-width (because these two transitions belong to the same rotational-vibrational transition). Figures 5.19 and 5.20 (on previous pages) illustrate collisional effects caused by N_2 at T=483 and T=999 K. From the fitting results, collisional half-widths of the transitions are calculated. As observed with the CH_4 measurements, the data and the Voigt fit are nearly perfectly overlaid. The variation of collisional half-width for these transitions with pressure of N_2 at the different temperatures is shown in Figure 5.21.

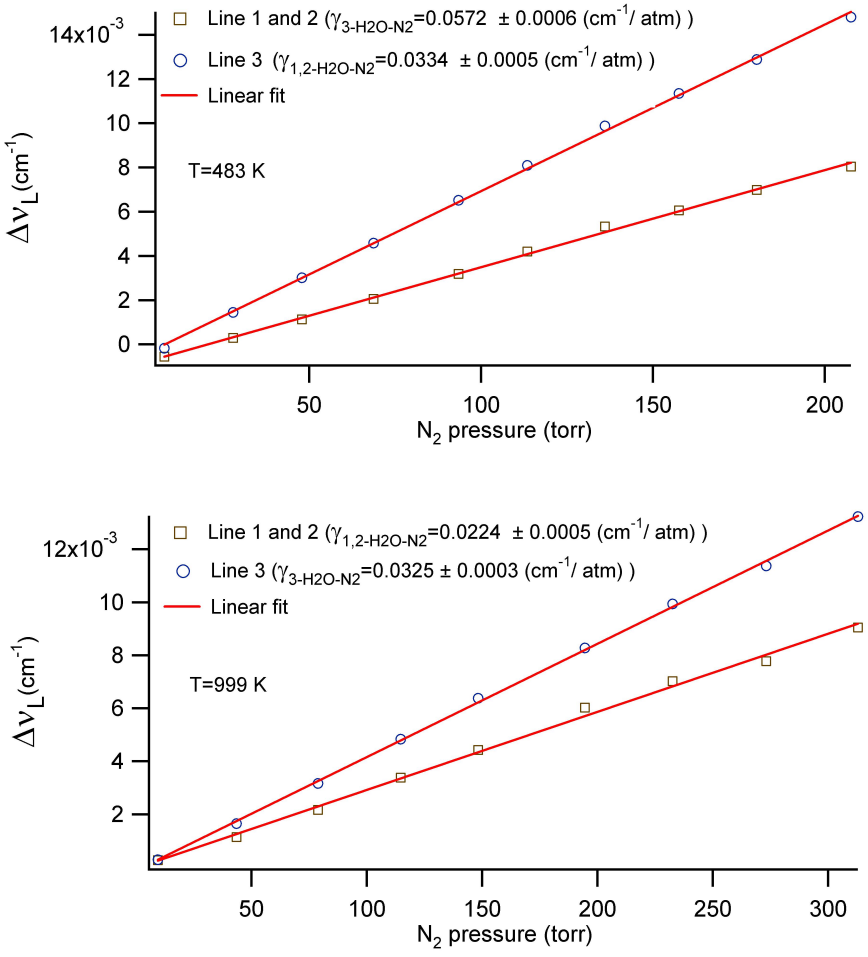

Figure 5.21: Collisional broadening half-width of H_2O transitions by N_2 as a function of pressure. Upper trace at room temperature (483 K), and lower trace at high temperature (999 K).

Also in Figure 5.22, the variation of collisional half-widths for the selected H_2O transitions with CO_2 pressure at T=483 and T=860 K are illustrated.

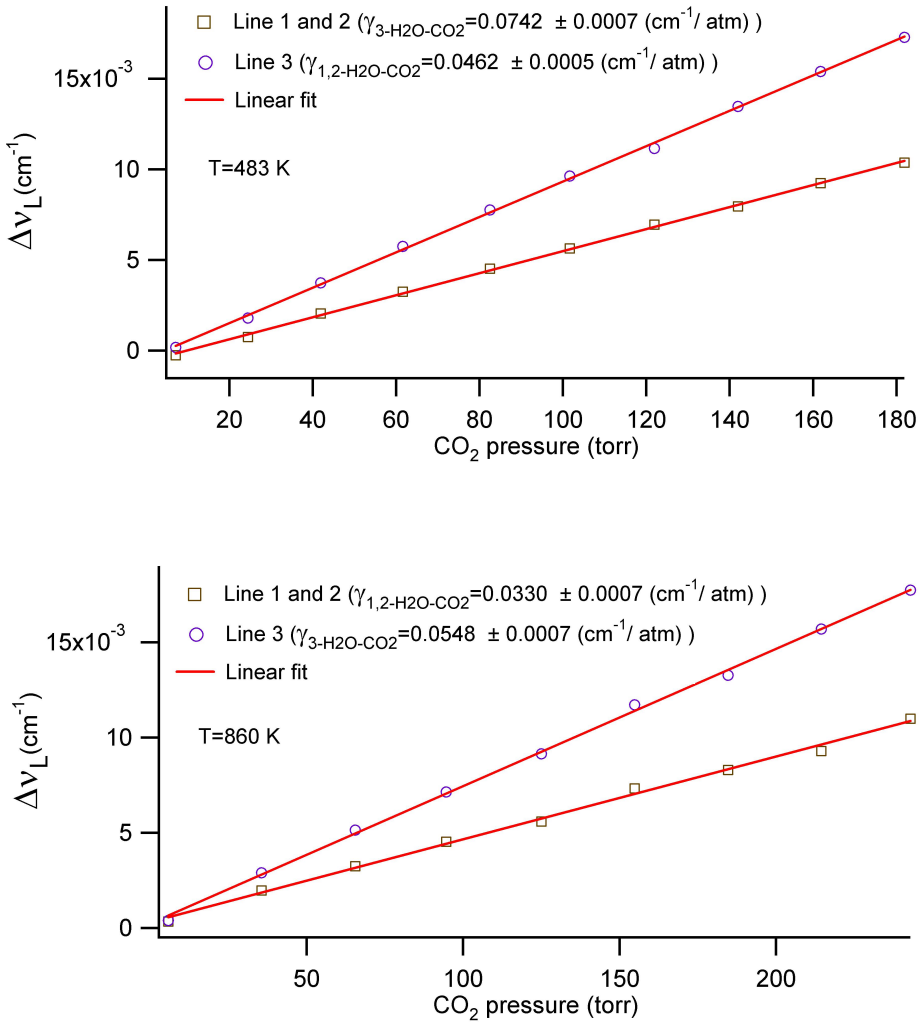

Figure 5.22: Collisional broadening half-width of H_2O transitions by CO_2 as a function of pressure. Upper trace at room temperature (483 K), and lower trace at high temperature (860 K).

The results of the measured collisional broadening coefficients at different temperatures are summarized in Tables 5.9 and 5.10 for the selected H_2O transitions. The errors shown represent the standard deviation of the broadening coefficient from

the measurements. Details of the overall uncertainty in the broadening coefficient are given in the Appendix E, the overall uncertainty is on the order of 15%.

Based on the measured broadening coefficients at different temperature (see Figure 5.23 and 5.24), similar to the treatment of R(3) and R(4) transitions of CH_4 in section 5.2.4, the temperature dependence of the collisional broadening linewidth parameter *n* is determined for each quenching gas.

Table 5.9: Variation of collisional half-width with temperature in transition 1 and 2

Broadening Gas	$\gamma_{1,2}$ (cm^{-1} atm^{-1})					
	483 K	584 K	723 K	770 K	860 K	999 K
N_2	0.0334 ± 0.0005	0.0296± 0.0003	0.0264± 0.0005	---	---	0.0224± 0.0005
CO_2	0.0462± 0.0005	0.0408± 0.0003	0.0373± 0.0006	---	0.0330± 0.0007	---
H_2O	0.1574± 0.0014	0.1510± 0.0018	---	0.1300± 0.0019	0.1180± 0.0022	0.1142± 0.0000
O_2	0.0152± 0.0002	0.0136± 0.0001	0.0125± 0.0003	---	0.0118± 0.0002	0.0106± 0.0001

Table 5.10: Variation of collisional half-width with temperature in transition 3

Broadening Gas	γ_3 (cm^{-1} atm^{-1})					
	483 K	584 K	723 K	770 K	860 K	999 K
N_2	0.0572± 0.0006	0.0490± 0.0003	0.0424± 0.0004	---	---	0.0325± 0.0003
CO_2	0.0742± 0.0007	0.0656± 0.0003	0.0611± 0.0004	---	0.0548± 0.0007	---
H_2O	0.2346± 0.0011	0.2066± 0.0026	---	0.1648± 0.0019	0.1496± 0.0017	0.1363± 0.0000
O_2	0.0239± 0.0001	0.0205± 0.0001	0.0179± 0.0002	---	0.0163± 0.0002	0.0149± 0.0001

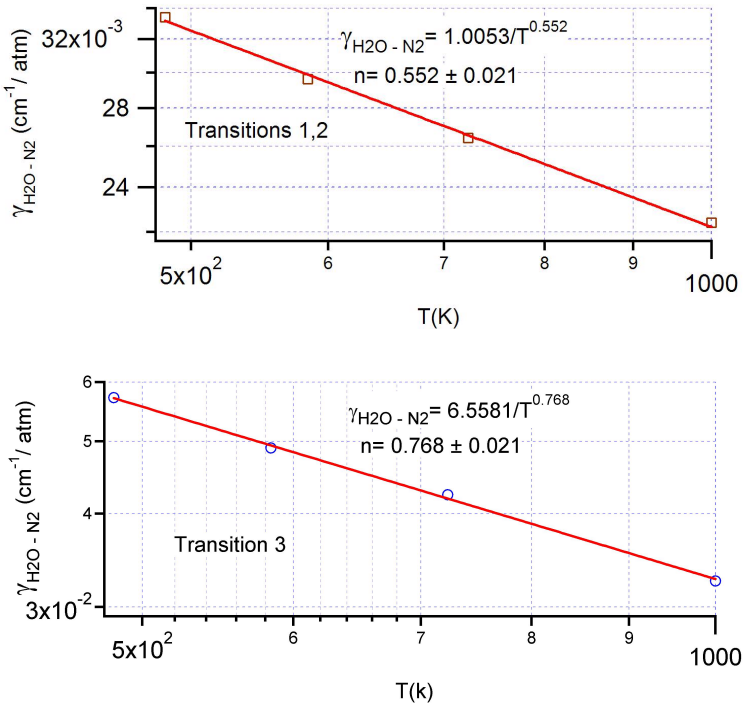

Figure 5.23: The temperature variation in broadening coefficient half-width of H_2O by N_2 for transitions 1 and 2 (top trace) and transition 3 (bottom trace).

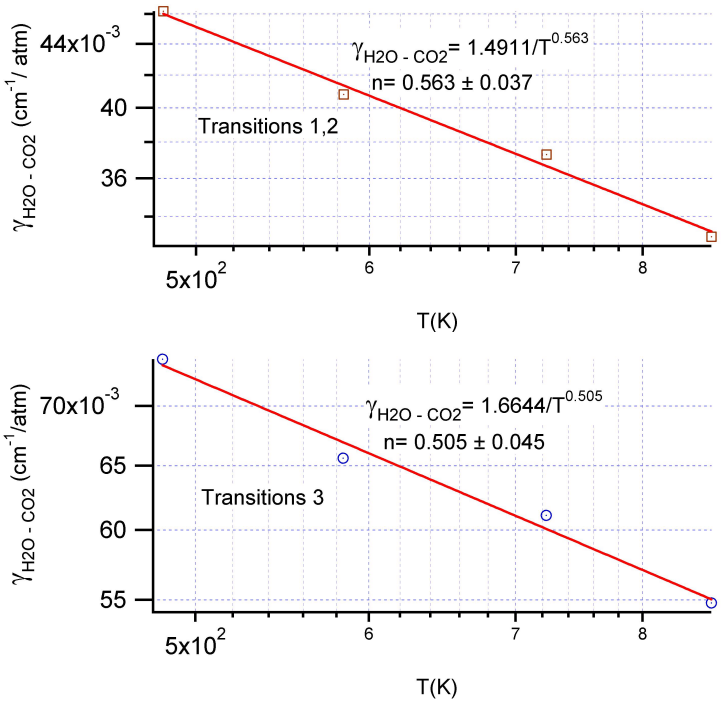

Figure 5.24: The temperature variation in broadening coefficient half-width of H_2O by CO_2 for transitions 1 and 2 (top trace) and transition 3 (bottom trace).

Figures 5.23 and 5.24 illustrate the temperature variation of the broadening coefficient with gases N_2 and CO_2 for the selected H_2O transitions. The slope of these graphs represents the parameter *n*, as indicated on these Figures. The parameter *n* for all of quenching gases for the R(3) and R(4) manifolds are calculated based on the measured values of pressure broadening coefficients at different temperature. These results are summarized in Table 5.11.

Table 5.11: Temperature dependence of collisional broadening line width parameter *n* for different quenching gases

Transition	*n*			
	N_2	H_2O	CO_2	O_2
1 and 2	0.552 ± 0.021	0.475 ± 0.049	0.563 ± 0.037	0.467 ± 0.030
3	0.768 ± 0.021	0.766 ± 0.020	0.505 ± 0.045	0.652 ± 0.030

5.4 Approximate pressure broadening calculation for some quenching gases

Among the major quenching gas species, it was not possible to measure some of the pressure broadening parameters. For the R(3) and R(4) manifolds of 2 ν_3 band of CH_4, as result of the risk of CH_4 reaction with O_2 at elevated temperatures, broadening of CH_4 at elevated temperatures was not measured. Instead, pressure broadening coefficients of these transitions with air at room temperature was measured. The measured pressure broadening of R(3) and R(4) transitions due to air at room temperature was 0.0058±0.0010 and 0.0058±0.0006 cm^{-1}/atm, respectively. Using these values, and also corresponding values for N_2 as a quenching gas from Tables 5.5 and 5.6, the pressure broadening of transition *i* due to O_2 is calculated from

$$\gamma^{i}_{CH4-air} = \gamma^{i}_{CH4-N2} * y_{N2} + \gamma^{i}_{CH4-O2} * y_{O2}$$

where y_j is mole fraction of N_2 or O_2 in air. Therefore, the broadening coefficient of R(3) and R(4) with respect to O_2 at room temperature is calculated by

$$\gamma^{i}_{CH4-O2} = \gamma^{i}_{CH4-air} / y_{O2} - \gamma^{i}_{CH4-N2} * y_{N2} / y_{O2}$$

$$= 0.058 / 0.21 - 0.056 * 0.79 / 0.21$$

$$= 0.0655\ \mathrm{cm^{-1}/atm}$$

Also the parameter n for O_2 is chosen as the average of this parameter for other quenching species, taken as $n = 0.884$ and $n = 0.916$ for the R(3) and R(4) transitions, respectively.

For H_2O transitions, broadening parameters with respect to CH_4 as a quenching species could not be measured. This problem arises as result of absorption interferences from CH_4 in the spectral region close to transition 1 and 2 of H_2O. Though CH_4 absorption in this particular region (at 6771.79 cm^{-1}) is weak, for measurement of collisional effects of CH_4, a considerable amount of CH_4 must be added to the static cell while the concentration of H_2O is kept constant. As a result of high CH_4 concentrations in the cell during measurement, absorption due to CH_4 becomes important and interferes with the H_2O absorption. Therefore, the error in the modeling becomes considerable. For this reason, pressure broadening coefficient of H_2O transitions due to CH_4 quenching gas only was measured at T=999 K. At this temperature, the aforementioned CH_4 transition becomes very weak and no interference due to CH_4 absorption is observed. The measured values of the pressure broadening coefficient of H_2O due to CH_4 as quenching species at T=999 K was measured as 0.0257±0.0002 and 0.0283±0.0002 for transitions 1,2 and 3 respectively.

As above, for CH_4 broadening of H_2O absorption, the parameter *n* is chosen as the average of its value for other quenching species given in Table 5.11. Baaed on this assumption, the value of n for transition 1,2 and transition 3 is chosen as 0.514 and 0.673 respectively.

Though the approximations introduced for calculating the collisional effects in these two cases somewhat reduces the accuracy of the calculated spectra, it should be mentioned that broadening due to these collisional effects is small in combustion systems, in which the concentration of O_2 and CH_4 is usually less than 5% in reaction zone. Therefore, even a large uncertainty in prediction of these collisional effects has little effect on the accuracy of the whole broadening calculation.

6 Temperature and concentration measurements using the WMS sensor

Theoretical information about Wavelength Modulation Spectroscopy (WMS) and the measured spectroscopic parameters of the selected CH_4 and H_2O transitions provide groundwork for CH_4, H_2O, and temperature measurements using WMS. In the first section of this chapter, a model for quantification of the WMS signal in a combustion system, based on the selected transitions, is explained. Through comparison of the model prediction and measurements performed inside a static cell at known temperature and concentration, validity of the model is tested. In the third section, the architecture of the sensor for simultaneous temperature and concentration measurement is illustrated. And finally, in the fourth section, in-flame measurements of temperature, CH_4, and H_2O concentrations measurement simultaneously are presented.

6.1 A Model for simultaneous temperature, CH_4 concentration, and H_2O concentration measurement in combustion systems

Figure 6.1 shows the flow diagram of the steps performed in the model for the quantification of WMS signals related to the selected CH_4 and H_2O transitions. Four

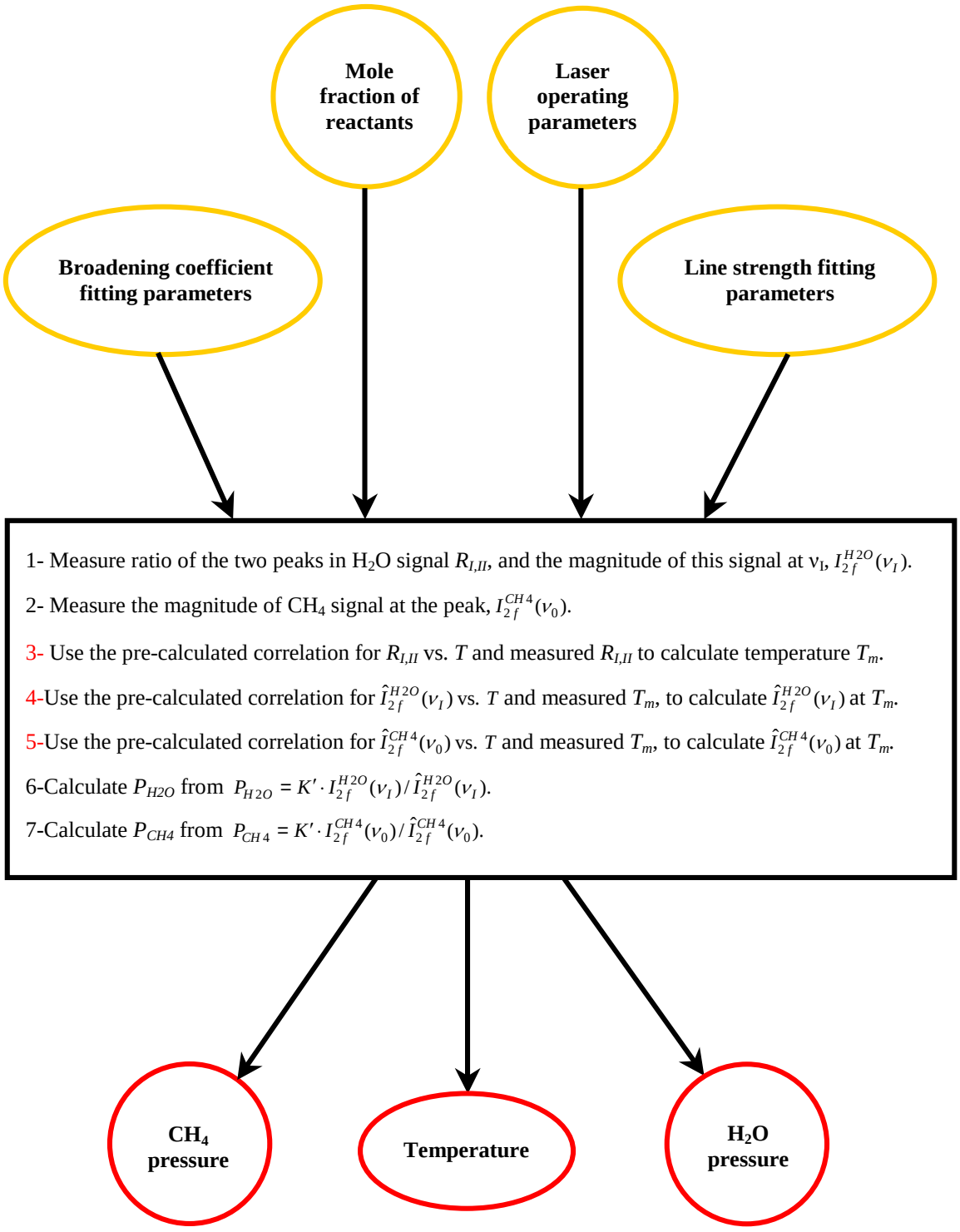

Figure 6.1: Flow diagram of the main steps performed for quantification of the sensor for temperature and species measurement in combustion system with a multiplexed WMS sensor.

sets of information are considered as inputs to the model. This information includes: line strength polynomial parameters; broadening coefficient parameters; laser operating parameters; and mole fraction of the reactants entering the combustor.

Line strength polynomial parameters can be easily obtained from least-square fitting of the calculated line strengths versus temperature using the HITRAN database for all of the selected transitions. The validity of the HITRAN database for the selected transitions has been proven in Chapter 4 and thus it is trusted. The fitting parameters of the line strengths can be seen in the C++ code in Appendix A2 and A3.

From the pressure broadening measurements, fitting parameters related to pressure broadening coefficient are calculated for all of the quenching species. These parameters can be found in the written C++ code in Appendix A2 and A3.

Laser operating parameters defined in Chapter 4 including the modulation depth, $\Delta\nu_{m,i}$, intensity-frequency parameters (s_f, s_{F1}, s_{F2}), and opto-electrical gain K' (which also depends on the photodetector and optical-electrical setup), are measured. Methods of measuring $\Delta\nu_{m,i}$ and intensity-frequency parameters are presented in Appendix F.

In the model presented in Figure 6.1, the mole fraction of the reactants entering the combustor (which are known) are used to calculate the mole fraction of major species (such as CH_4, N_2, CO_2, O_2, and H_2O) in the reaction zone, assuming that combustion reactions are complete. Using this approximation (the "complete combustion approximation") the collisional half-width of all absorption transitions *i*, $\Delta\nu_{L,i}$ (in cm^{-1}), at temperature *T*, due to quenching species *j* (including CH_4, N_2, CO_2, O_2, and H_2O) is calculated by

$$\Delta \nu_{L,i} = P \sum_{j} y_j \gamma_{i-j}(T) \qquad (6.1)$$

where, $\gamma_{i-j}(T)$ (in cm^{-1}/atm) is the collisional broadening coefficient of transition *i* at temperature *T* (calculated from fitting parameters) due to quenching gas *j*. Also, y_j is the mole fraction of major species *j*, obtained from the approximation, in the reaction zone, and *P* (in atm) is the total pressure. It should be stressed that the complete combustion approximation is only used to predict the shape of the 2f signal, not its magnitude. Through this approximation the spectra becomes only temperature dependent and the quantification becomes straightforward.

In addition to the four main inputs described above, the model uses three sets of information (steps 3, 4, and 5 in Figure 6.1) which are calculated in advance. This information, which is in reality the core of the model, is: a) information about the variation of the ratio of the two peaks in the second harmonic spectra of the selected H_2O transitions with temperature $R_{I,II}(T)$; b) information about the variation of one of the H_2O peaks in the second harmonic spectra $\hat{I}_{2f}^{H2O}(\nu_I)$ with temperature when it is normalized by power and partial pressure of H_2O; c) information about the variation of the CH_4 peak in the second harmonic spectra $\hat{I}_{2f}^{CH4}(\nu_0)$ with temperature when it is normalized by power and partial pressure of CH_4. Calculation of these three sets of information is explained in detail later, in Sections 6.1.1 and 6.1.2.

Figure 6.1 illustrates the main steps for quantification of the sensor for temperature and for H_2O and CH_4 concentration measurements. As shown in this flow diagram, in the first step, after measuring the second harmonic signal related to

the H_2O transitions, the ratio of the two H_2O peaks, $R_{I,II} = I_{2f}^{H2O}(\nu_I) / I_{2f}^{H2O}(\nu_{II})$, is measured (Figure 6.2).

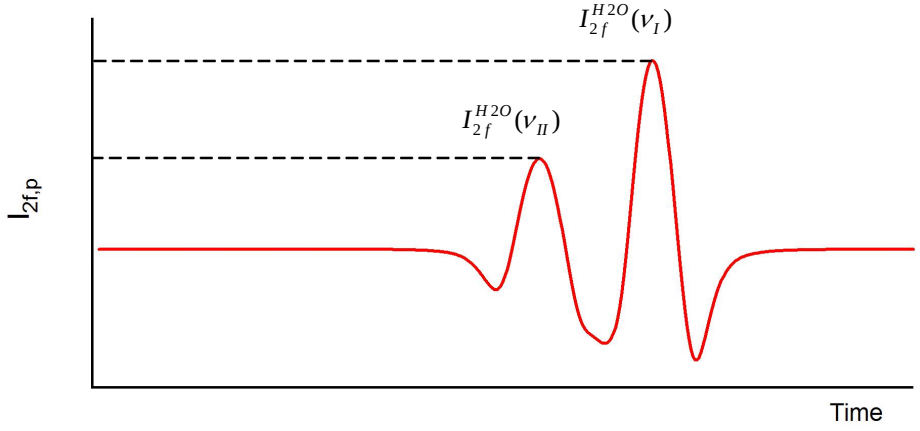

Figure 6.2: Typical second harmonic signal of H_2O related to the selected H_2O transitions

In the second step, the peak of the second harmonic signal of the CH_4 transition, $I_{2f}^{CH4}(\nu_0)$, is measured (Figure 6.3).

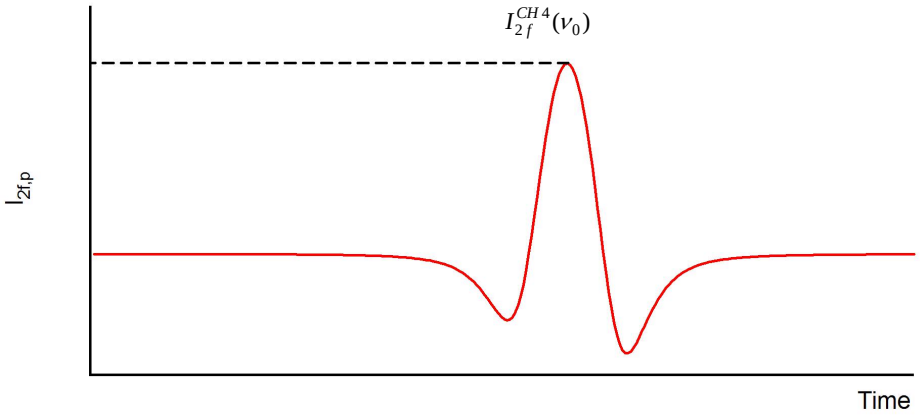

Figure 6.3: Typical second harmonic signal of CH_4 related to the selected CH_4 transitions

In the third step, by using the measured $R_{I,II}$ and pre-calculated $R_{I,II}$ vs. T correlation, the temperature, T_m, is obtained.

The measured temperature from step three, T_m, is used to calculate $\hat{I}_{2f}^{H2O}(\nu_I)$ and $\hat{I}_{2f}^{CH4}(\nu_0)$ as presented in the fourth and fifth steps, respectively, from the pre-calculated $\hat{I}_{2f}^{H2O}(\nu_I)$ vs.T and $\hat{I}_{2f}^{CH4}(\nu_0)$ vs.T correlations. Finally, in the sixth and sevenths steps, the partial pressure of H_2O and CH_4 are calculated by

$$P_{H2O} = K\frac{I_{2f}^{H2O}}{\hat{I}_{2f}^{H2O}(T_m)}, \qquad P_{CH4} = K\frac{I_{2f}^{CH4}}{\hat{I}_{2f}^{CH4}(T_m)} \tag{6.2}$$

where K is the opto-electrical gain, which is available as one of the inputs to the model. In Equation (6.2), if both the numerator and the denominator are normalized by the laser power, then K will become only dependent on electrical gain. For power normalization the corresponding first harmonic at the center of the absorption line can be used.

This model uses a straightforward procedure for quantification of the detected signal but it relies on the "complete combustion approximation". In many combustion applications (such as emission control), the interest is in analysis of exhaust gas, which is the product of an almost complete combustion process. In such applications the "complete combustion approximation," is a very good approximation and hence in these situations the model is expected to give very good estimates for temperature and concentration. However, for applications in which measurements are performed in uncompleted combustion zones, the quantification of sensor signals based on the model described above might be questionable.

6.1.1 Calculation of $\hat{I}_{2f}^{H2O}(\nu_I)$ vs. T and $R_{I,II}(T)$ vs. T correlations at optimum conditions

Based on the mole fraction of reactants (fuel and oxidizer) entering the combustor (or a premixed burner), which can be determined from the flow rate of reactants, the mole fraction of combustion species based on "complete reaction approximation" can be easily calculated. In this research we focused on CH_4/air combustion in an atmospheric premixed flame and therefore the quantification model has been applied to this particular system, the procedure could easily be extended to other combustion processes.

The computed combustion species mole fractions, pressure broadening parameters, line strength parameters, and laser operating parameters have been used in a computer code (written in C++, see Appendix A2) to calculate the normalized second harmonic signal of the H_2O spectra , $\hat{I}_{2f}^{H2O}(\bar{\nu})$, when P_{H2O}=1 torr and $K = 1$, at different temperatures. In this program the theoretical model developed for WMS in Chapter 4 has been used. Once the $\hat{I}_{2f}^{H2O}(\bar{\nu})$ spectra is calculated, $\hat{I}_{2f}^{H2O}(\nu_I)$ and $R_{I,II}$ have been extracted from the spectra as a function of temperature T, and through that the $\hat{I}_{2f}^{H2O}(\nu_I)$ vs. T and $R_{I,II}$ vs. T correlations are obtained.

In terms of optimization, generally, the sensor parameters should be chosen such that the amplitude of the second harmonic signal at a given power is a maximum, and therefore the signal to noise ratio (S/N) is optimized. In this regard, the most important parameter that affects the WMS signal is modulation depth, $\Delta\nu_m$,

which can be adjusted by changing the amplitude of the modulation current (see Chapter 4 for more detail).

When the second harmonic signal is also used for temperature measurement, changing the modulation depth causes the 2f spectra and therefore $R_{I,II}$, to vary, shows that the modulation depth changes the $R_{I,II}$ vs. T correlation. Hence, the modulation depth must be chosen such that it not only optimizes the magnitude of the 2f signal but also increases the peak ratio sensitivity to temperature. Figure 6.4 shows the changes in $R_{I,II}$ vs. T curve at different modulation depths for complete CH_4/air combustion with equivalence ratio of $\varphi = 1$.

In addition to the modulation depth, for an optimum absorption signal, an optimum detection phase $\theta_{2,\max}$ (see Chapter 4 for more detail) needs to be chosen. The optimum detection phase can be obtained by using Equation (4.19), once the laser parameter ψ, the phase difference between intensity and frequency modulation, is available.

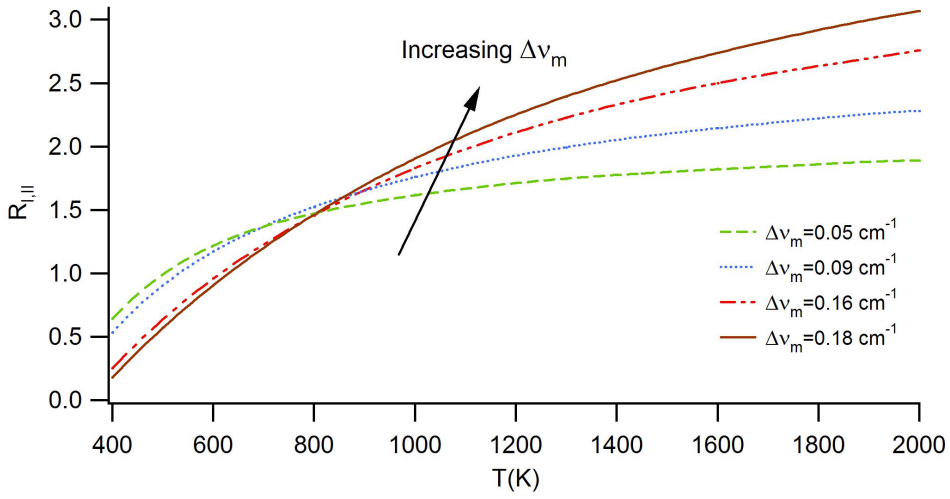

Figure 6.4: Variation in $R_{I,II}$ vs. T curve at different modulation depths and optimum detection phase $\theta = 155^{\circ}$ for CH4/air flame with φ=1.

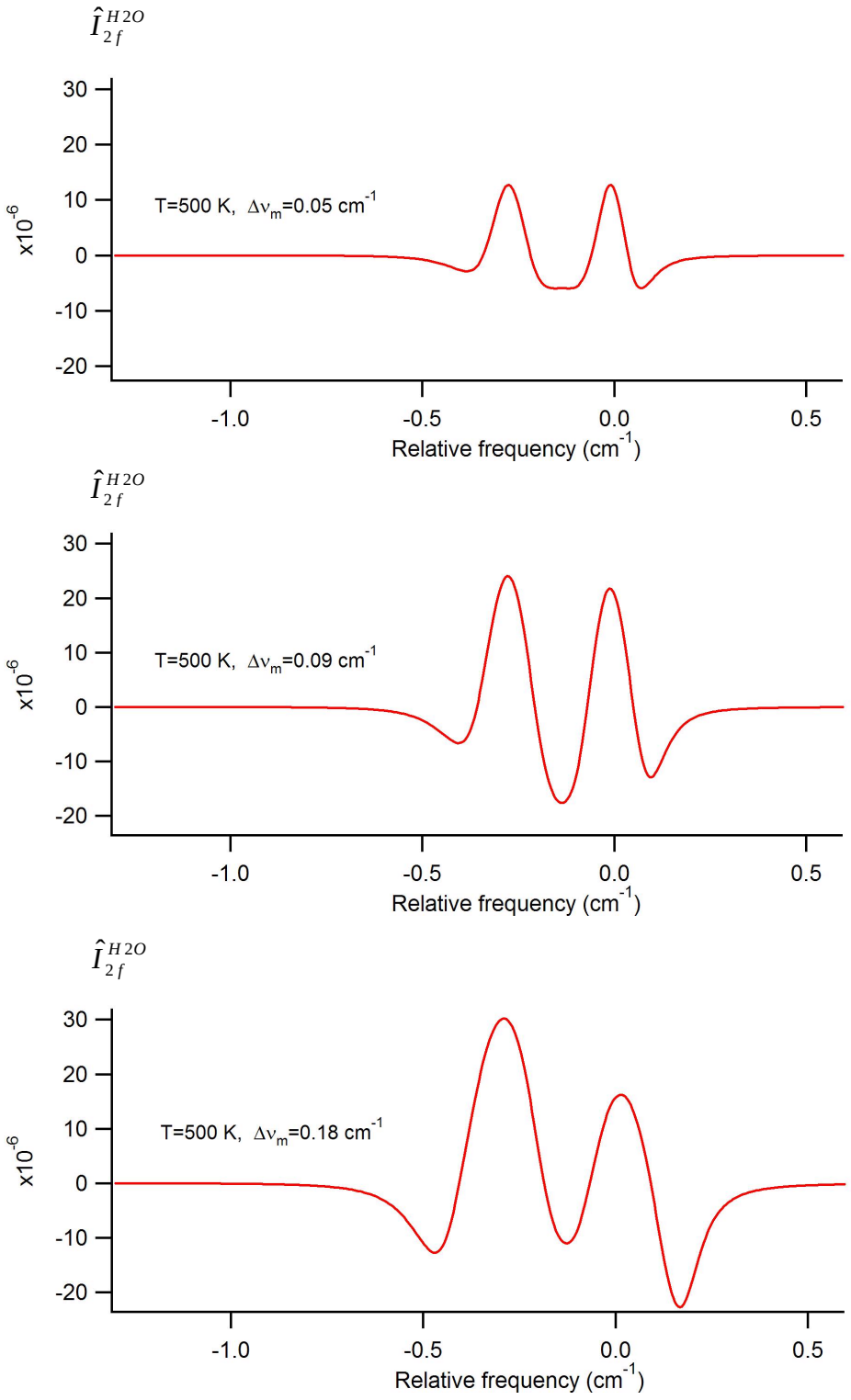

Figure 6.5: Calculated spectra of $\hat{I}_{2f}^{H2O}(\overline{\nu}-\nu_I)$ as a function of modulation depth, $\Delta\nu_m$, for CH_4/air flame with φ=1 at condition: T=500 K, $\theta = 155^\circ$ and optical path of L=10 cm.

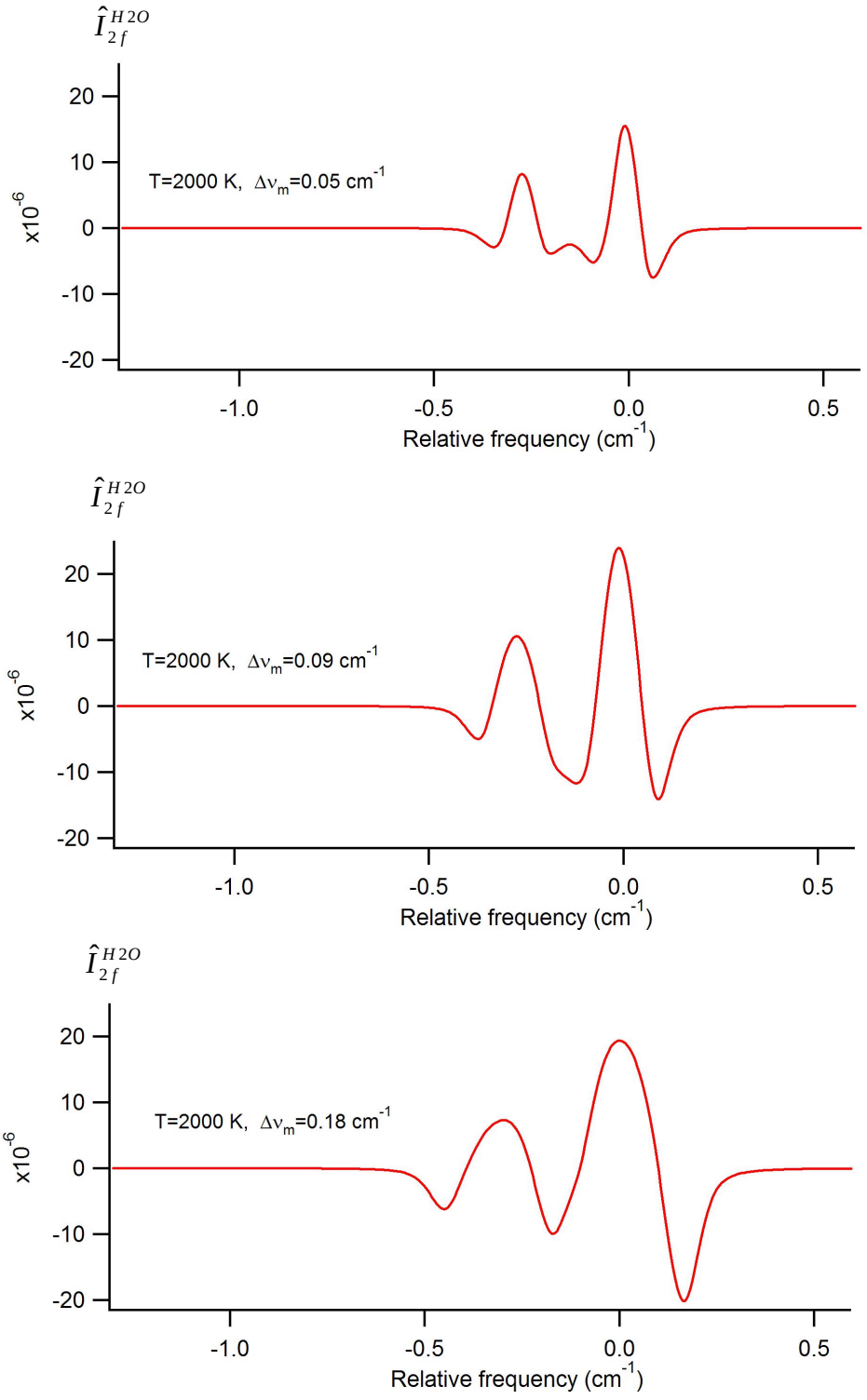

Figure 6.6: Calculated spectra of $\hat{I}_{2f}^{H2O}(\overline{\nu}-\nu_I)$ as a function of modulation depth, $\Delta\nu_m$, for CH_4/air flame with φ=1 at condition: T=2000 K, $\theta=155^\circ$ and optical path of L=10 cm.

Figures 6.5 shows the calculated spectra of $\hat{I}_{2f}^{H2O}(\bar{\nu})$ at different modulation depths at T=500 K for the CH_4/air combustion with equivalence ratio of $\varphi = 1$. Also, the spectra of $\hat{I}_{2f}^{H2O}(\bar{\nu})$ at the same condition but at T=2000 K is shown in Figure 6.6.

According to Figure 6.4, increasing the modulation depth increases the temperature sensitivity of the peak ratio $R_{I,II}$ to temperature; thus for temperature measurements it is better to choose a larger modulation depth. Also, comparing the graphs in Figure 6.5 and 6.6, it is concluded that increasing the modulation depth (in the range of 0.05 to 0.18 cm^{-1}), causes an increase in the amplitude of the second harmonic signal at T=500 K; however, at T=2000 K, the amplitude first increases sharply when modulation depth changes from 0.05 to 0.09 cm^{-1}, and then it slightly decreases when it changes from 0.09 to 0.18 cm^{-1}. Considering both effects, the temperature sensitivity and the amplitude of the second harmonic signal, it is concluded that larger modulation depth is more desirable. On the other hand, choosing a larger modulation depth has some drawbacks. The main drawbacks are first, by increasing the modulation depth, the chance of interference between closely spaced transitions becomes bigger, and therefore for quantification it is required that the spectroscopic parameters related to other transitions which interfere with the selected transitions be measured. As will be explained later in this Chapter, there are H_2O transitions which are relatively close to the selected transitions, and thus to prevent interference, there is a limit on the choice of modulation depth (of course, if the spectroscopic parameters of the adjacent transitions were available, there would be no limit on choosing modulation depth in terms of possible interference). Secondly, upon increasing the modulation depth the optical frequency will no longer

modulate purely sinusoidally. The reason is that, in general, increasing the tuning range of a diode laser typically causes the nonlinearity between current and optical frequency to become stronger, and therefore a pure sinusoidal injection current with a large amplitude won't generate a pure sinusoidal modulated optical frequency. For quantification such nonlinearities must be considered, which typically makes the modeling too complicated.

As result of these limitations, for the laser used for the H_2O absorption measurement, it is observed that the modulation depth should be less than 0.16 cm^{-1}. The limitation is due to interference of another H_2O absorption transition at 6771.197 cm^{-1} adjacent to the 3rd transition (located at 6771.475 cm^{-1}). Figures 6.7 and 6.8 compare the $\hat{I}_{2f}^{H2O}$ spectra for modulation depth of 0.09 and 0.16 cm^{-1} with and without the presence of the interfering transition at 6771.197 cm^{-1}. Since for this 4th transition the pressure broadening parameters were neither measured nor available in the HITRAN database, the air pressure broadening suggested by HITRAN is used for all colliding species for the modeling results shown in Figures 6.7 and 6.8.

From Figure 6.7, there is no significance interference from the third transition affecting the line ratio $R_{I,II}$, when the modulation depth is 0.09 cm^{-1}. Therefore, for this modulation depth, there is no need to consider the 4th transition in modeling. However, from Figure 6.8, at modulation depth of 0.16 cm^{-1} the 4th transition interferes with the 3rd transition, and the spectra of the 3rd transition is affected by absorption in the 4th transition. In this situation, in order to calculate the line ratio $R_{I,II}$, using the model, it would be necessary for the fourth transition to be included in the

model; otherwise, the calculated line ratio would not be accurate. Therefore a modulation depth of 0.09 cm^{-1} is selected for the sensor for flame measurement.

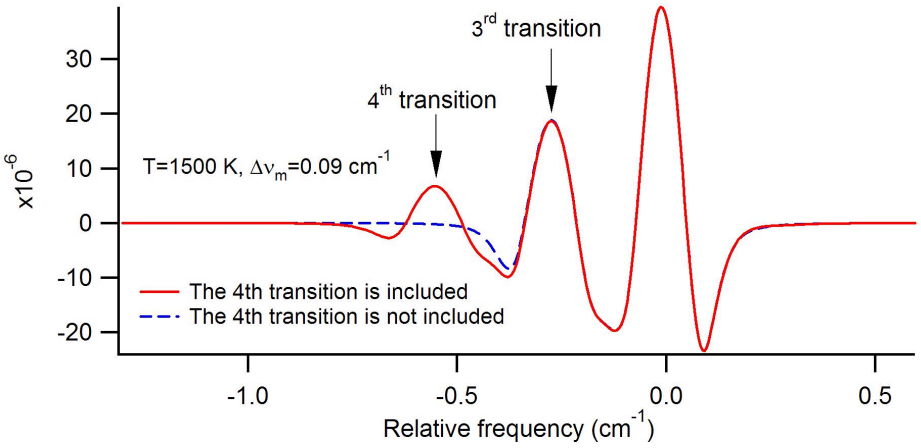

Figure 6.7: The modeled effect of the 4th transition in $\hat{I}_{2f}^{H2O}(\overline{\nu}-\nu_I)$ on the third transition for a CH_4/air flame with φ=1 at $\Delta\nu_m = 0.09\,cm^{-1}$ ($\theta = 155^\circ$, and optical path L=10 cm).

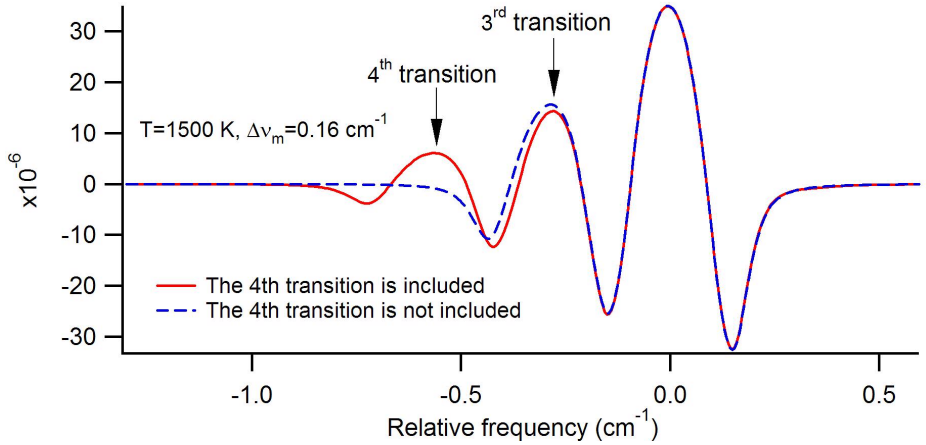

Figure 6.8: The modeled effect of the 4th transition in $\hat{I}_{2f}^{H2O}(\overline{\nu}-\nu_I)$ on the third transition for a CH_4/air flame with φ=1 at $\Delta\nu_m = 0.16\,cm^{-1}$ ($\theta = 155^\circ$, and optical path L=10 cm).

The variation of the normalized second harmonic signal of H_2O at frequency ν_I, $\hat{I}_{2f}^{H2O}(\nu_I)$, with temperature can be calculated, an example of results at modulation depth of $\Delta\nu_m = 0.09\,\text{cm}^{-1}$ and $\Delta\nu_m = 0.16\,\text{cm}^{-1}$ are illustrated in Figure 6.9.

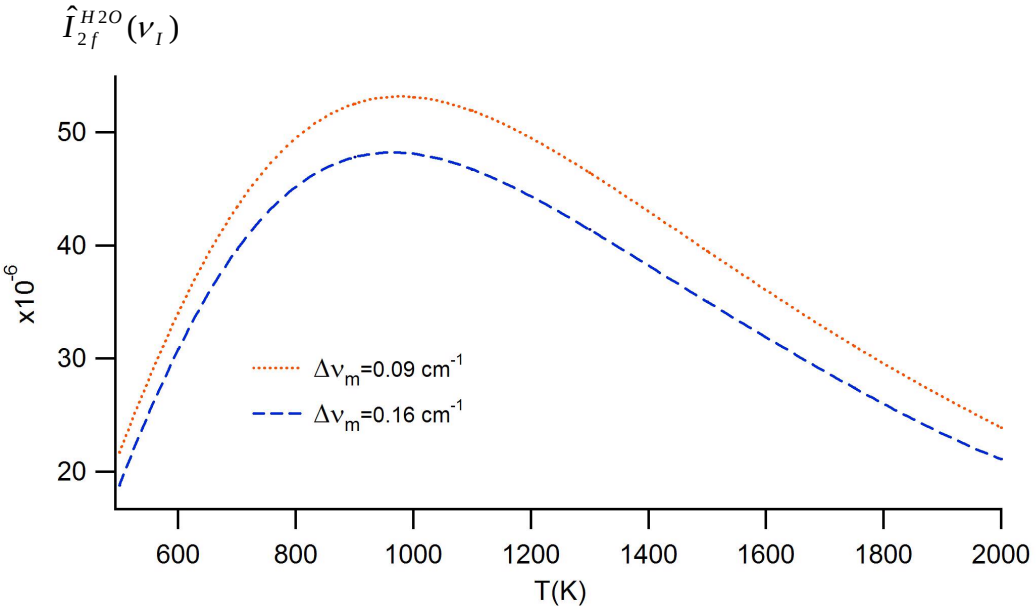

Figure 6.9: Variation of $\hat{I}_{2f}^{H2O}(\nu_I)$ with temperature at two different modulation depths for a CH_4/air flame with φ=1, at detection phase of $\theta = 155^\circ$ and optical path of L=10 cm.

From Figure 6.9, a modulation depth of 0.09 cm^{-1} gives a stronger signal; however, at this modulation depth $R_{I,II}$ is less sensitive to temperature compared to $\Delta\nu_m = 0.16\,\text{cm}^{-1}$. From results such as those presented in Figures 6.4 and 6.9, based on polynomial fitting, a correlation between $R_{I,II}$ and temperature, and between $\hat{I}_{2f}^{H2O}(\nu_I)$ and temperature can be easily obtained for every equivalence ratio at specific modulation depths.

6.1.2 Calculation of $\hat{I}_{2f}^{CH4}(\nu_0)$ vs. T correlation at optimum conditions

With the same procedure as explained in the previous section, the variation of $\hat{I}_{2f}^{CH4}(\nu_0)$ with temperature for the CH_4/air combustion with φ=1 at different modulation depths is computed. The results are shown in Figure 6.10.

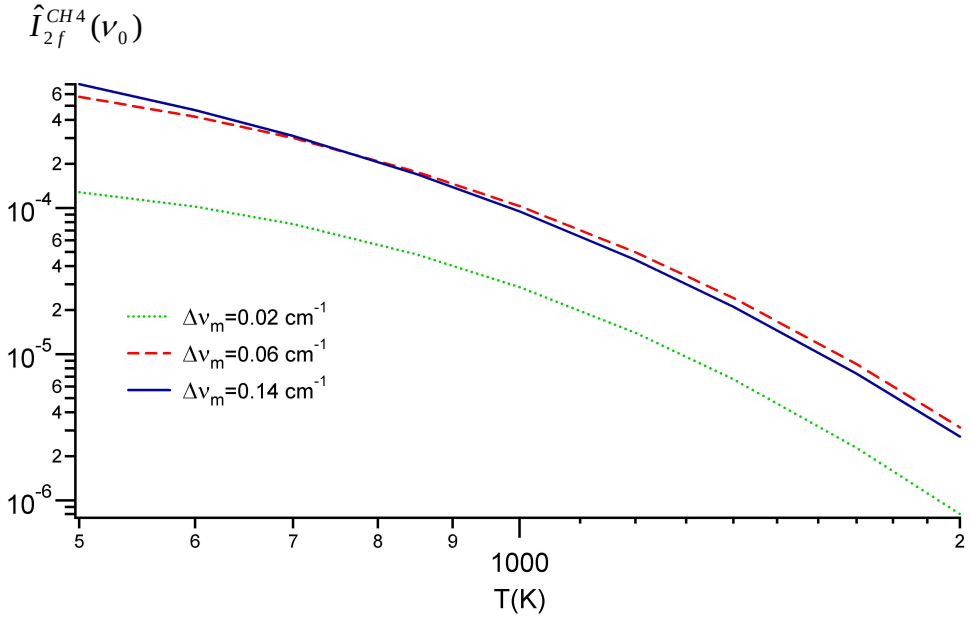

Figure 6.10: Variation of $\hat{I}_{2f}^{CH4}(\nu_0)$ with temperature at three different modulation depths for a CH_4/air flame with φ=1, at detection phase of $\theta = 140^\circ$ and an optical path of L=10 cm.

From Figure 6.10, the optimum modulation depth varies as a function of temperature. For instance, for T<700 K, a modulation depth of $\Delta\nu_m = 0.06\,\text{cm}^{-1}$ results in a stronger 2f signal than $\Delta\nu_m = 0.14\,\text{cm}^{-1}$, while at T>700 K the opposite behavior is observed. The modulation depth should be chosen such that it results in a stronger 2f signal, while minimizing interferences. Based on these factors and the results shown in Figure 6.10, modulation depth of $\Delta\nu_m = 0.057\,\text{cm}^{-1}$ is chosen for the CH_4 measurement. Using the spectra such as those shown in this Figure, correlation

between $\hat{I}_{2f}^{CH4}(\nu_0)$ and temperature can be obtained at any equivalence ratio and a fixed modulation depth.The spectra of the normalized 2f signal of CH_4, $\hat{I}_{2f}^{CH4}(\nu_0)$, at two different temperatures are shown in Figure 6.11. As we can see in this figure, the overall spectra of the R(4) transitions changes by in creasing temperature.

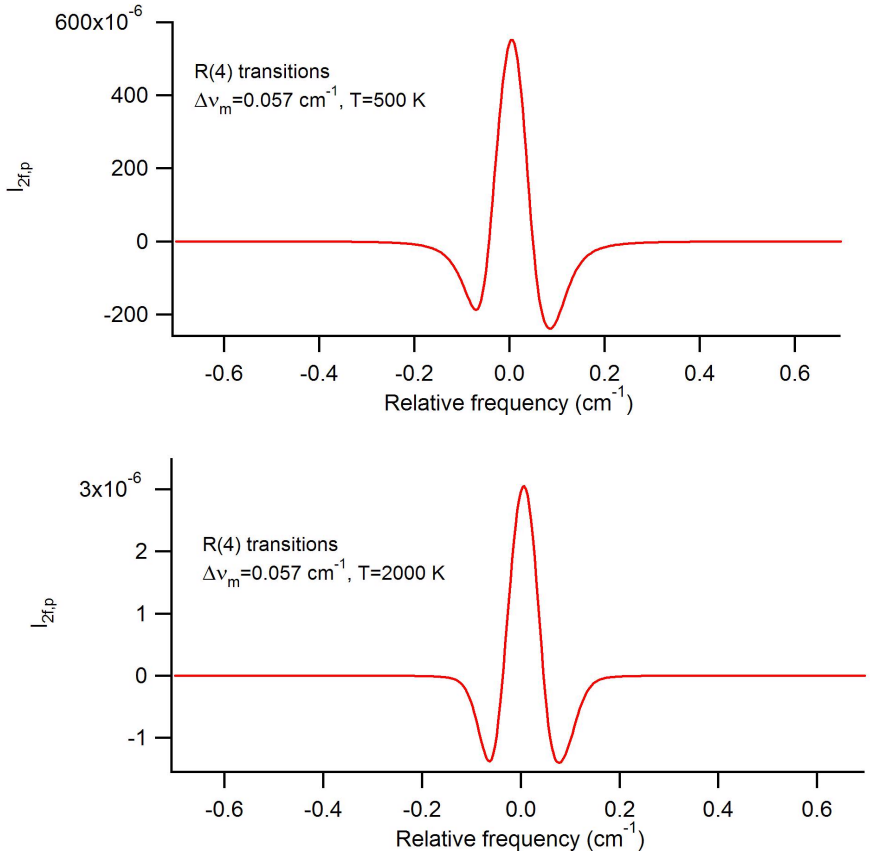

Figure 6.11: Calculated spectra of $\hat{I}_{2f}^{CH4}(\bar{\nu}-\nu_0)$ for R(4) transitions at T=500 and 2000 K for a CH_4/air flame with φ=1, at condition: $\theta = 140^\circ$ and optical path of L=10 cm.

6.2 Comparison of the modeling and experiments

In this section the results of the model are compared with experiments performed in the gas cell at known concentration and temperature. The experimental setup for this part of the measurement was the same as that for the direct absorption

measurement in Chapter 5; except in addition to the sweep signal (F=10 Hz), a modulation signal, with f=10 kHz and f=12 kHz for H_2O and CH_4 measurement, respectively, was added to the injection current. Also, the detector signal is sent to a lock-in amplifier and the second harmonic component of the photodetector signal is captured. More details of the setup for modulation is explained in the next section.

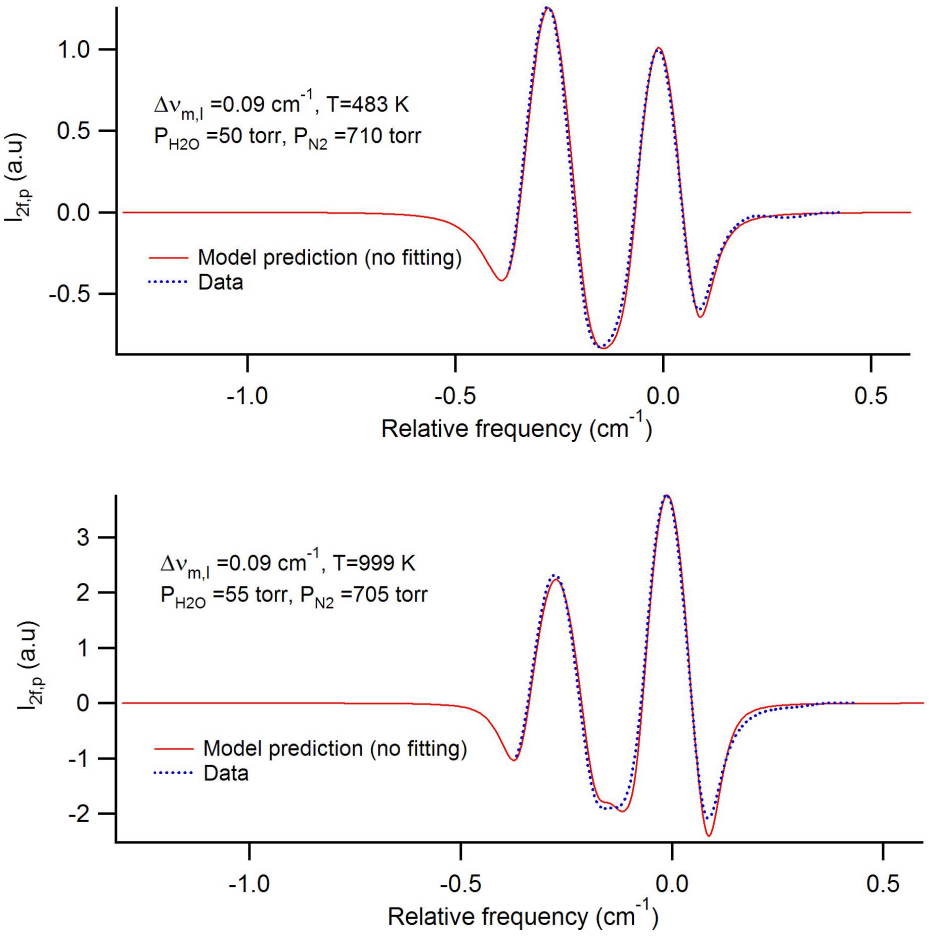

Figure 6.12: Comparison between measured and calculated 2f spectra of the selected H_2O absorption transitions for a mixture of N_2-H_2O in the gas cell.

Since the 2f signal of H_2O is used for temperature measurement, and for accurate measurement the model has to predict the spectra precisely to avoid significant error in temperature which would propagate to error in concentrations, many experiments were performed to compare the measured spectra of H_2O signal and the corresponding spectra computed (predicted) by the model for mixtures of H_2O -N_2, H_2O -CO_2, and pure H_2O at different temperatures (483-999 K).

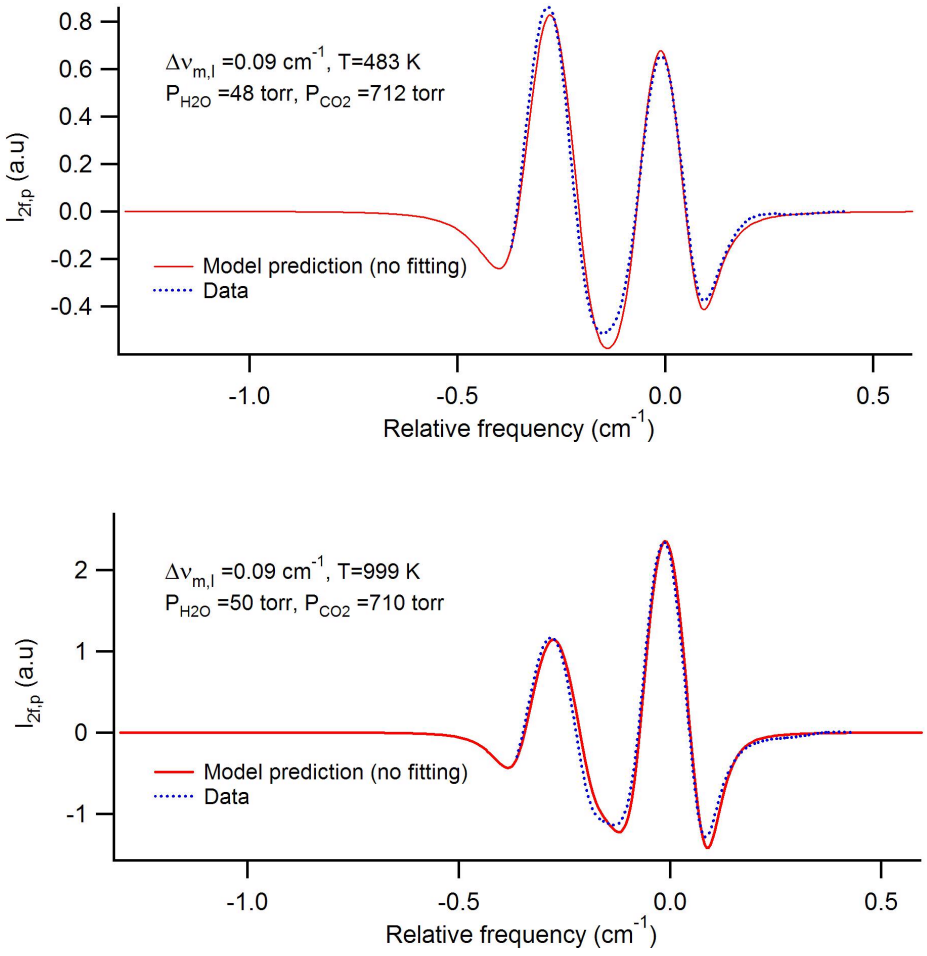

Figure 6.13: Comparison between measured and calculated 2f spectra of the selected H_2O absorption transitions for a mixture of CO_2-H_2O in the gas cell.

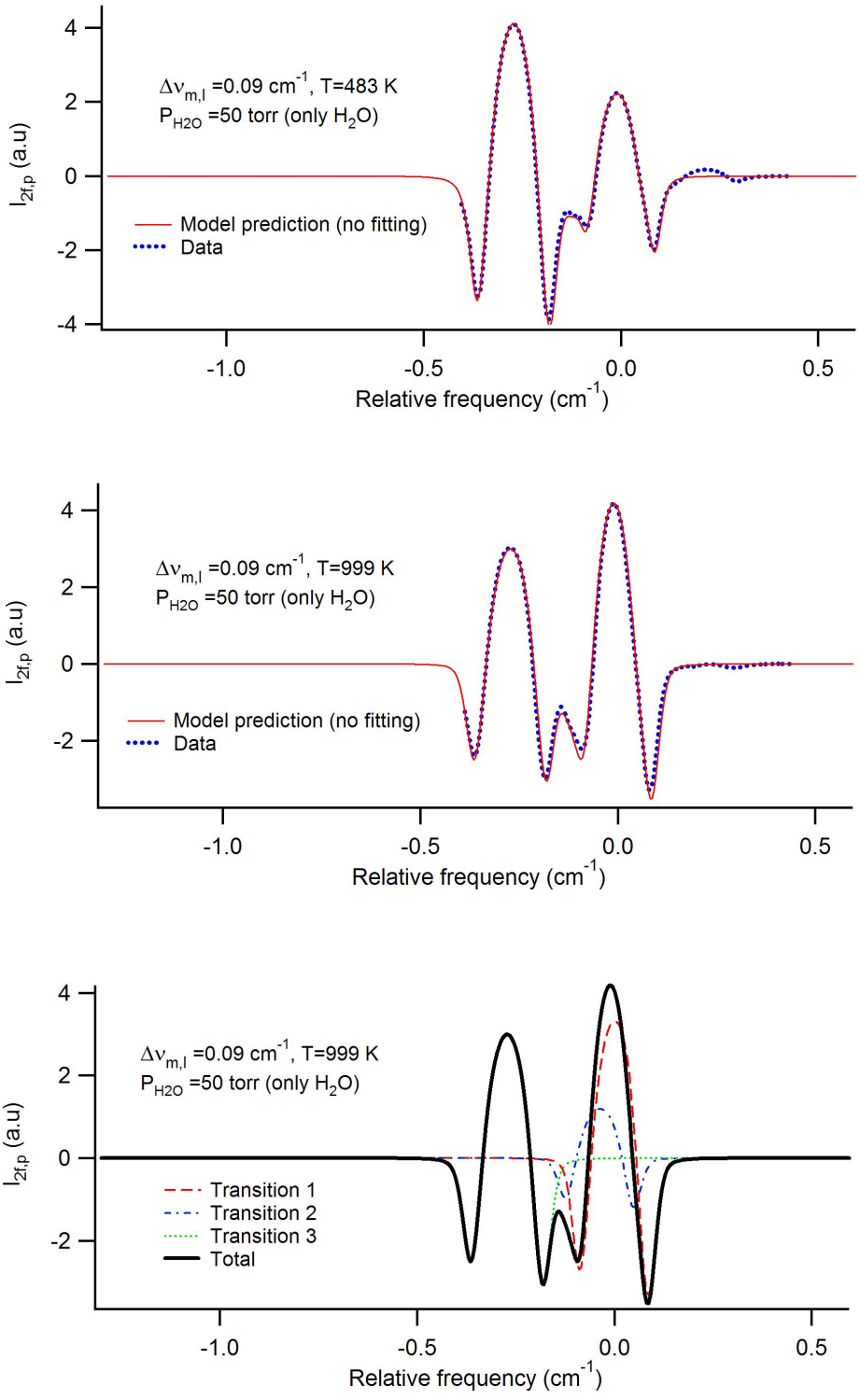

Figure 6.14: Comparison between measured and calculated 2f spectra of the selected H_2O absorption transitions for pure H_2O vapor in the gas cell. The bottom trace shows the contribution of individual transitions to the total spectra according to results of the modeling.

Figures 6.12 and 6.13 (on the previous pages) compare measured and calculated 2f spectra of the H_2O absorption transitions at temperatures of 483 K and 999 K for H_2O-N_2 for H_2O-CO_2 mixtures respectively. Also the comparison between the calculated and measured second harmonic spectra of pure H_2O vapor in the gas cell at T=483 and 999 K for modulation depth $\Delta\nu_{m,I} = 0.09\,\mathrm{cm}^{-1}$ is shown in Figure 6.14. In this figure (bottom trace) the spectra of calculated individual transitions (1 through 3) related to the middle trace (T=999 K) are shown.

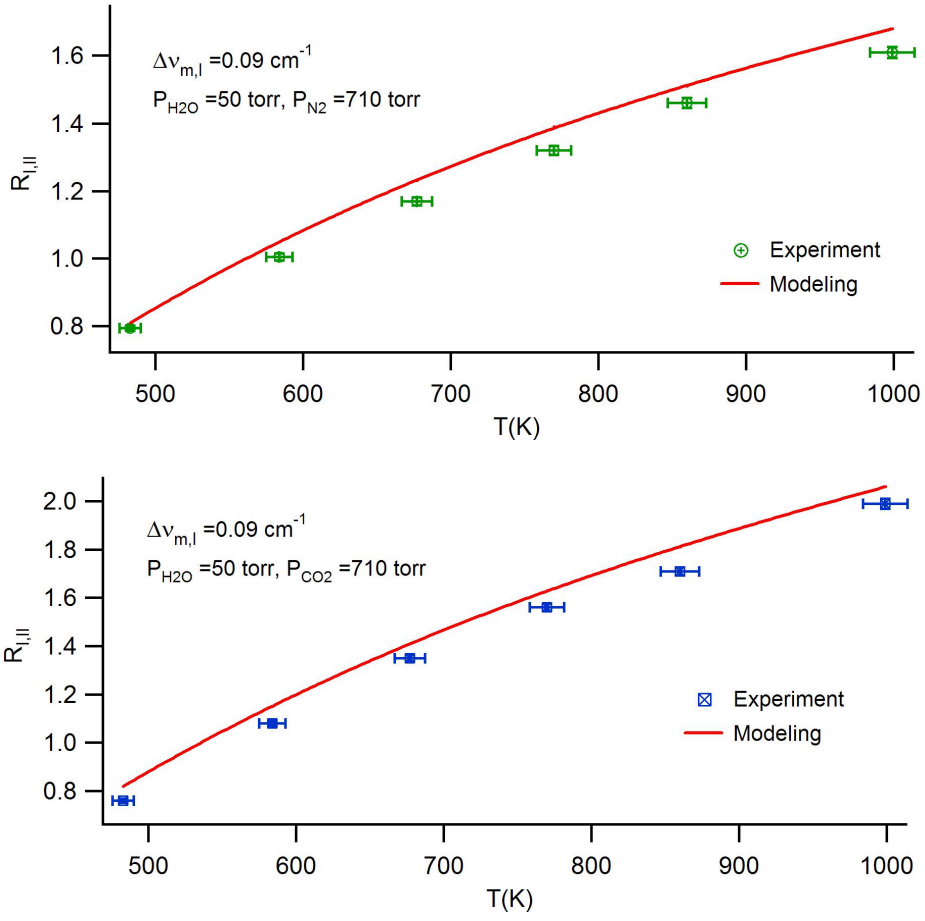

Figure 5.15: Comparison between a set of (T , $R_{I,II}$) measured by experiment in the gas cell and corresponding values calculated by the modeling results.

.

As noted above, many experiments were performed for evaluation of the accuracy of the modeling in the quantification of the second harmonic signal before using the sensor for in-flame measurement. The results shown in Figures 6.12 through 6.14 illustrate the accuracy of the mathematical model for concentration measurement, but the accuracy of the model for temperature measurements still requires assessment. For this reason, for known temperature and concentrations in the gas cell, the measured peak ratio $R_{I,II}$, at temperature recorded by thermocouple, was compared to corresponding calculated values from the modeling. The results of such comparison are shown in Figure 6.15 (on the previous page).

The results in Figure 6.15 show that the difference between the temperature measurement using the sensor (based on peak ratio) and the thermocouple used in "experiment" is about 30 ºC while the uncertainty in the thermocouple measurement is ±15 ºc (not considering a ±20 ºC uncertainty due to temperature variation along the optical path inside the gas cell). In these experiments, the measured uncertainty in the peak ratio $R_{I,II}$, based on three measurements, is about 1% (the error bar associated with $R_{I,II}$ can not be seen in the graph). These results illustrate that the optical measurement for temperature gives a very good estimate of the gas temperature, within ±30 ºC of the thermocouple measurement for the temperature range shown in Figure 6.15).

Comparison of the experimental results in the gas cell and quantification of the sensor measurement using the model show that the quantification of the sensor measurement for temperature and concentration measurement of H_2O has an accuracy of about 3% and 5% for temperature and concentration measurements respectively.

The same model is applied for quantification of CH_4 measurement. Since the model for quantification is already validated, there is no need to repeat all of the experiments performed for H_2O absorption measurement for CH_4. Figure 2.16 compares the measured and calculated spectra of R(4) transitions for a mixture of CH_4 and N_2 at T=719 K. Also in this Figure the contribution of each of the individual R(4) transitions to the total profile is shown. See Appendix A3 for the C++ program.

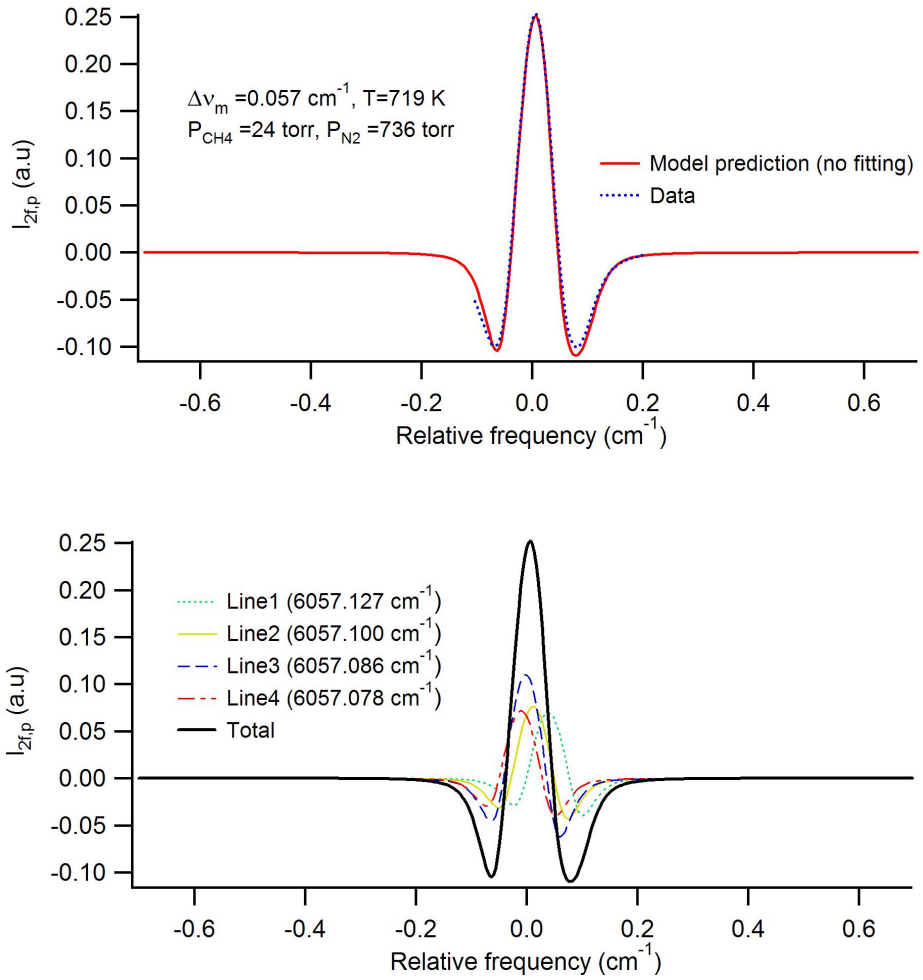

Figure 6.16: Comparison between measured and calculated 2f spectra of the selected CH_4 absorption transitions, R(4), for a known CH_4-N_2 mixture in the gas cell. The bottom trace shows the contribution of individual transitions to the total spectra according to results of the modeling.

The accuracy of quantification CH_4 concentration measurement strongly depends on the measured temperature. As we can see in Figure 6.10, the normalized signal (P_{CH4}=1 torr) decreases exponentially with increasing temperature, and therefore any error in temperature measurements would result in a considerable error in CH_4 concentration after quantification of the CH_4 signal. This behavior is mainly due to the fact that the line strength of the selected CH_4 transitions decreases exponentially with temperature.

6.3 Sensor architecture

The schematic of the sensor architecture for simultaneous temperature and CH_4 and H_2O concentration measurements, is shown in Figure 6.17. In this schematic, a ramp (or sawtooth) signal from the function generator at frequency F=10 Hz is used for tuning the optical frequency of the H_2O and CH_4 lasers. The sinusoidal signals taken from the lock-in amplifiers at frequency f_1=10 kHz and f_2=12 kHz, which are used as modulation signals, are added to the ramp signal separately using two summing circuits that have the ability to adjust the amplitude of the input signals. The output voltage from each summing circuit is sent to the Tunable Diode Laser (TDL) controller, and through that the corresponding injection current is sent to the laser. The TDL controllers also control the temperature of the lasers using thermo-electric circuits. The laser beam emitted from each laser are combined using a pellicle beam splitter and then the multiplexed light is directed through the flame region where the absorption of laser light in the reaction zone takes place. The attenuated light, as a

result of absorption in the reaction zone, is detected by a main Photo Detector (MPD) which generates a voltage signal proportional to the impinging laser intensity at the

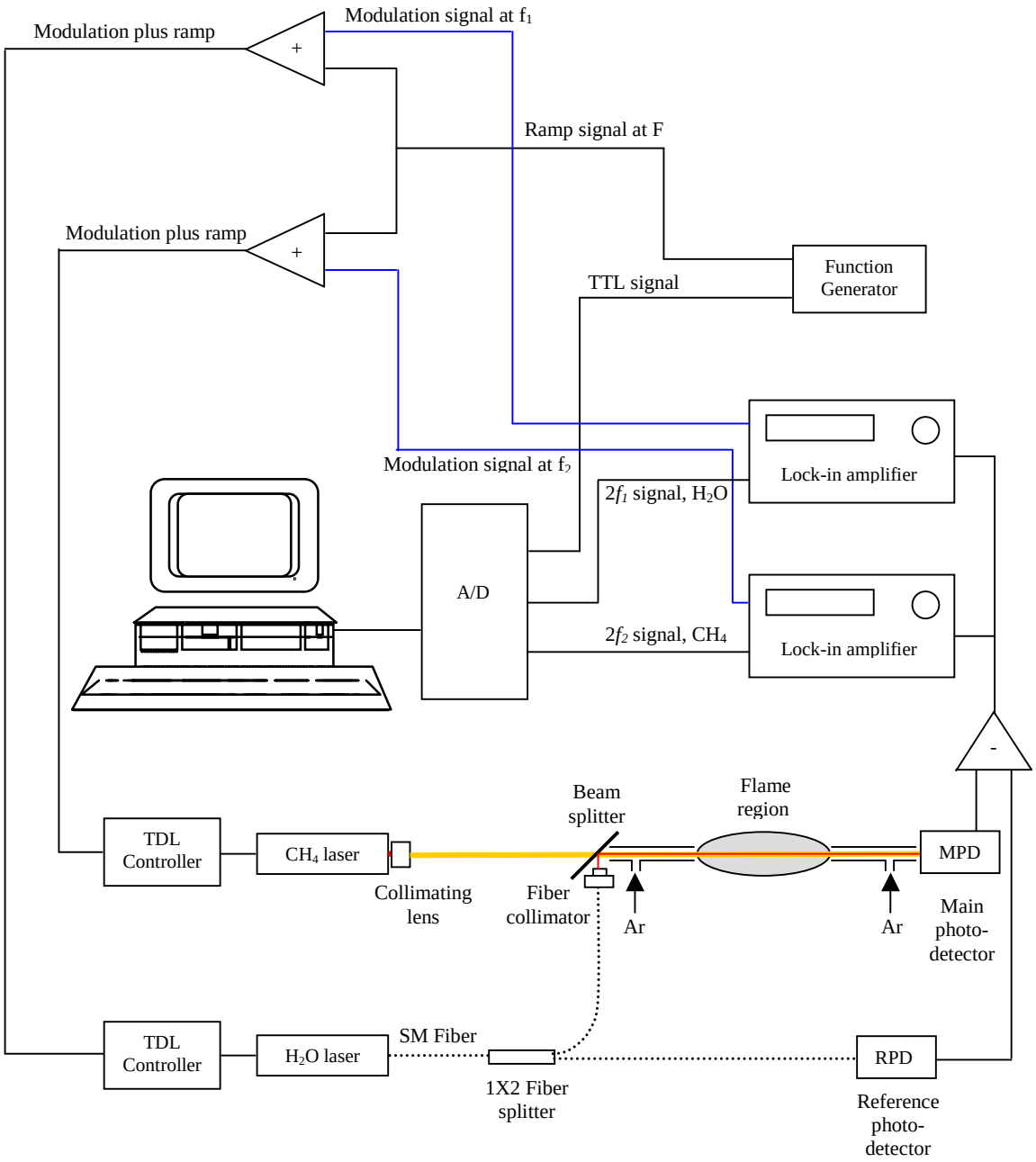

Figure 6:17: Schematic of the sensor architecture.

surface of its photodiode. Due to some nonlinearity in the optical signal of the H_2O laser, which results in a nonzero second harmonic signal at zero absorption, 10% of the laser light is separated from the main H_2O beam. This laser beam is first detected by the Reference Photo Detector (RPD), then the RPD signal is subtracted from the MPD using a subtracting circuit. In the subtracting circuit the RPD signal is adjusted so as to exactly cancel the MPD signal related to H_2O. In this manner, the second harmonic signal related to the nonlinearity in intensity of the H_2O laser is removed. The subtracted signal is then sent to two lock-in amplifiers, where demodulation of PDS is performed. From the lock-in amplifiers, the second harmonic signals related to H_2O and CH_4 are obtained. These signals, with references based on the triggering signal of the function generator (TTL signal), are digitized using an A/D converter. The data are either stored in the computer (for post processing) or processed in real-time for simultaneous temperature and concentration measurement. As explained in Chapter 5, to eliminate the background H_2O absorption related to moisture in the air, the optical path of the H_2O laser outside the reaction zone is purged either by Argon or dry air as shown in the Figure.

6.4 In-flame measurements

In this section measurements of temperature and measurements of H_2O and CH_4 concentrations in a flame, based on the setup shown in Figure 6.17, are presented. The first set of experiments performed involves measurements at different heights in the flame by changing the height of the burner using a transition stage with 0.025 mm resolution, while keeping all optics fixed.

For these measurements an adjustable slot burner with 2 mm width and length of 10.0 cm generated a premixed CH_4/air flame. The air and fuel flow rate of 9.96 and 1.78 LPM respectively were measured by two calibrated rotameters. When the burner was running, the multiplexed laser beams were directed through a very uniform flam. In addition, two type R thermocouples with diameter of 0.008 inches were used to measure the flame and post flame temperature (see Figure 6.18). As result of considerable heat conduction in thermocouple wires in the pre-flame zone, the thermocouple could not be used in these regions for temperature measurement. Therefore, thermocouple measurements were limited to flam or post-flame zones where the temperature gradients in the thermocouple wires were negligible. For the non-intrusive optical sensor, measurement of temperature at different zones (along the vertical direction) was possible.

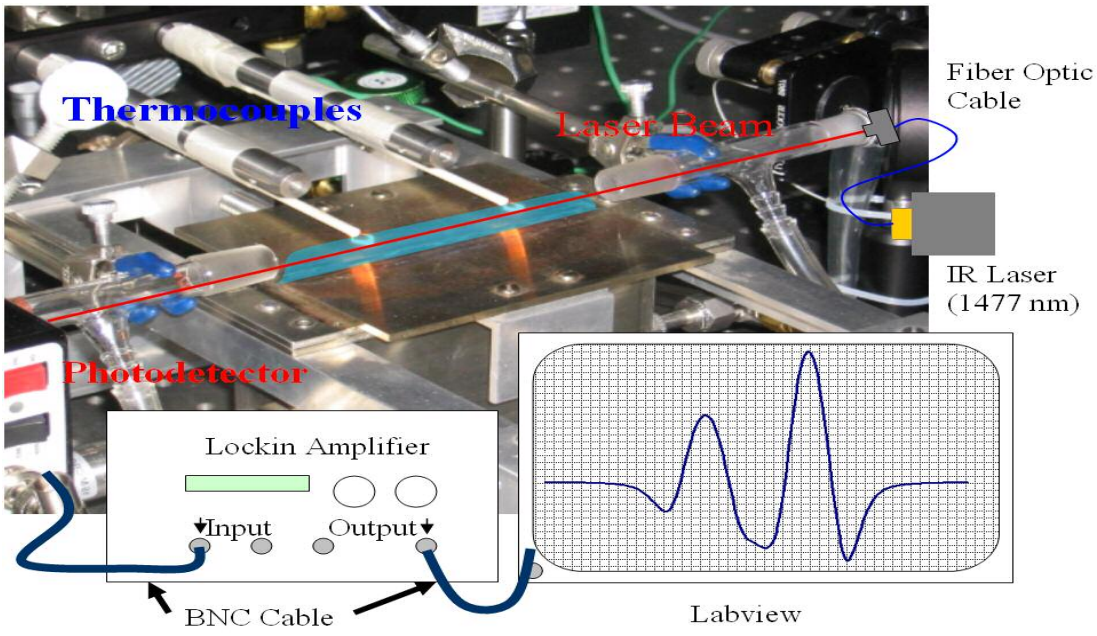

Figure: 6.18: Simplified Figure of the setup of the in-flame measurement

As discussed, $\hat{I}_{2f}^{H2O}(\nu_I)$ vs.T , $\hat{I}_{2f}^{CH4}(\nu_0)$ vs.T , and also $R_{I,II}$ vs. T correlations must be available for the mixture. These correlations are determined as shown in Figure 6.19 for this experiment.

During the measurement, the peak ratio, $R_{I,II}$, can be calculated from the measured 2f signal of H_2O. Using this ratio, the temperature along the optical path in the combustion zone is calculated as T_m (see the top trace in Figure 6.19). This temperature is used to calculate the normalized second harmonic signals of CH_4 and H_2O at that condition based on "complete combustion approximation". The graphs in the middle and bottom are pre-calculated normalized 2f signal of H_2O and CH_4 respectively. The amplitude of the second harmonic signals in these graphs are normalized to an absorbing species concentration of one torr and by intensity. For normalization with respect to optical power (intensity), they are divided by the amplitude of 1f signal at the transition frequency as discussed in Chapter 4.

The normalized signals obtained from the previous step are used to calculate the concentrations using Equation 6.2, in which K in general depends on both electrical gain and intensity. If the measured 2f signal is divided by the 1f signal at the central absorption frequency, then K in Equation (6.2), K will become independent of intensity. This allows us to use a value of K from measurement in the gas cell where the concentration and temperature are known. Based on this procedure, the constant K is determined for both H_2O and CH_4 species as 1/23.0 and 1/1.9 respectively (see Figure 6.20).

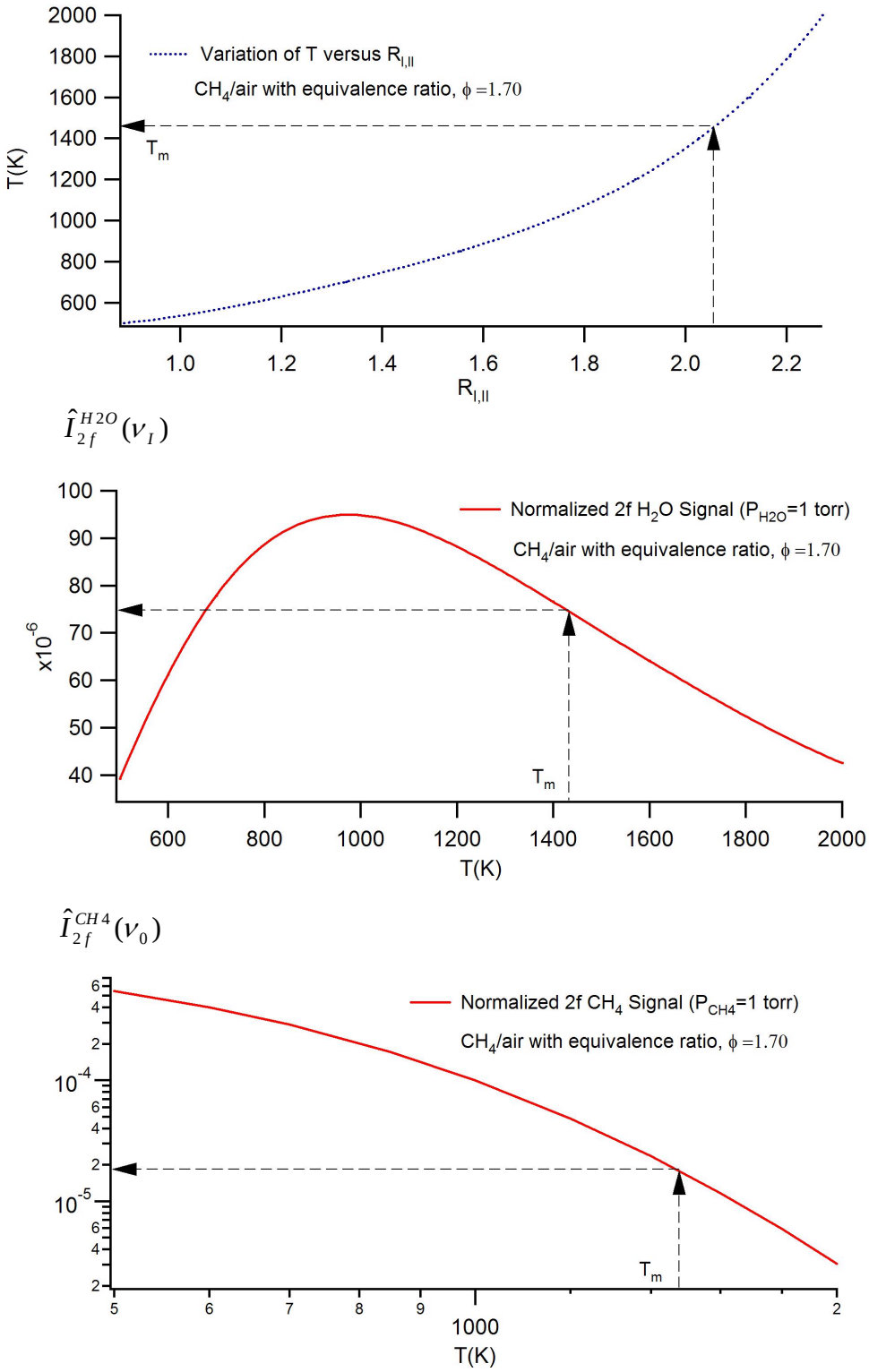

Figure 6.19: Pre-calculated correlations, $\hat{I}_{2f}^{H2O}(\nu_I)$ vs.T, $\hat{I}_{2f}^{CH4}(\nu_0)$ vs.T, and $R_{I,II}$ vs.T, for the CH_4/air flame with φ=1.70. The 2f signals are normalized by the 1f signal at the central absorption frequencies.

In this experiment a large diameter photodiode diameter is used to detect the absorption signal to minimize effects of beam steering. For all flame experiments, the intensity of the laser impinging on the photodiode was essentially constant, with the fluctuation due to beam steering less than 2%. Therefore, the amplitude of the first harmonic signals (1f) could be predetermined, using the two lock-in amplifiers available for this research, before the flame measurement. This helped us to simplify the set up and no further component needed to monitor the laser intensity during the experiment.

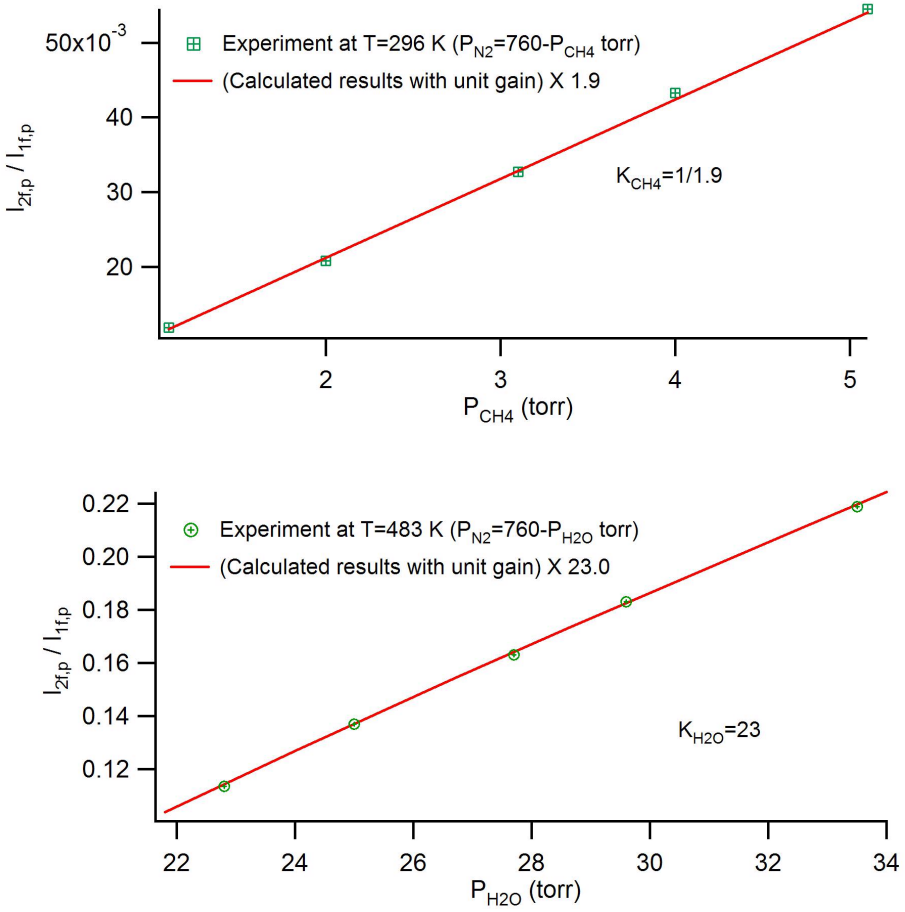

Figure 6.20: Calculation of K by comparing the measured second harmonic signal at know temperature and concentration in the gas cell and calculated second harmonic signal with unit gain.

Using the information explained above, the temperature and the concentrations of CH_4 and H_2O at 5 different heights were measured. The results of these measurements are shown in Figures 6.21 and 6.22. The uncertainty in the measured in temperature in Figure 6.21, is as result of signal fluctuation, which is attributed mainly to acoustical vibration. However for the concentrations in Figure 6.22, uncertainty is related to the both fluctuation of the signals and uncertainty in quantification as result of temperature fluctuation. The temperature uncertainty is especially dominant in CH_4 results in Figure 6.22. The bottom graph of Figure 6.19 shows that the normalized 2f signal of CH_4 decreases exponentially with temperature, and hence even a small uncertainty in temperature causes a large uncertainty in the concentration.

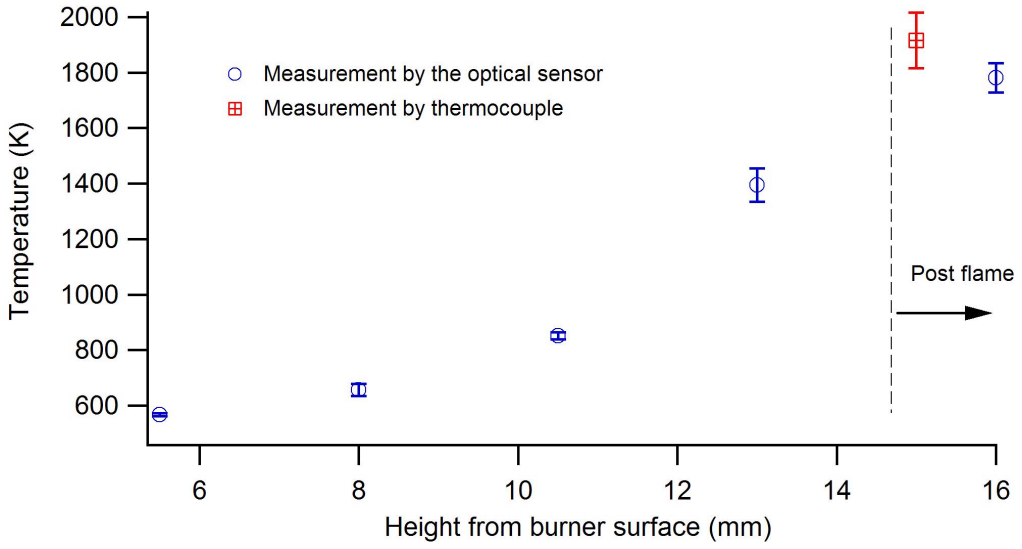

Figure 6.21: Temperature variation at different height above the burner surface using the optical sensor.

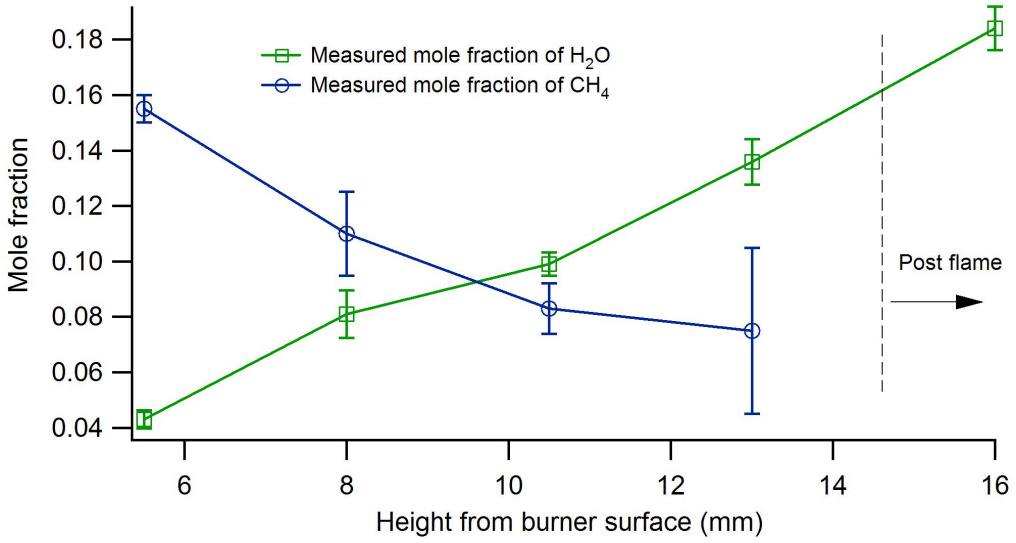

Figure 6.21: Variation of the H_2O and CH_4 concentrations at different heights above the burner surface using the optical sensor.

All the results (each point in the graphs) are the average of 4 measurements and each measurement is the average of 10 points with frequency of 10 Hz. Therefore each measurement represents the average values over 1 second and each point in the graphs indicates the average over 4 seconds.

The thermocouple values presented in Figure 6.20 are the average of 40 points over 4 seconds and are corrected for radiation loss. The method of radiation correction is presented in Appendix G. According to the results presented in Figure 6.20, the difference in measured temperature by thermocouple and optical sensor in the post-flame zone is 135 K while the uncertainty in the thermocouple measurement is ±100 K. This shows, as we expected, the optical sensor gives very a good estimate for

temperature measurement in a region where the complete combustion assumption is valid.

Also, in Figure 6.21, the mole fractions measured by the optical sensor seem reasonable. In the pos- flame zone, according to the measurement, H_2O concentration is 0.184 and based on complete combustion, the mole fraction at this region is expected to be 0.178. If the reaction is assumed to be complete, the optical sensor overestimates the concentration by 3%.

For CH_4 also very reasonable trend is observed. At a distance about 5.5 mm above the burner surface, where the reaction rate is small, the measured mole fraction at this point is 0.155 while the mole fraction of CH_4 in the reactant is 26 %. Also close to the flame-zone, from Figure 6.21, it is concluded that CH_4 concentration is not zero and this is what we expect because there has been excess fuel in the reactants.

According to this discussion, it is concluded, as for the measurement inside the gas cell, the developed optical sensor gives good estimates for temperature and concentration of CH_4 and H_2O.

7 Conclusion

In this dissertation, a sensor to measure temperature and concentrations of CH_4 and H_2O based on absorption spectroscopy was designed, built, and tested in a static cell under various conditions and in a flame. For high sensitivity, Wavelength Modulation Spectroscopy (WMS) was used to quantify the absorption of the tunable diode laser beam. In general, quantification of WMS, particularly in combustion systems, requires detailed spectroscopic information for all of the absorption features probed by the sensor. At the same time, many absorption features are usually overlapped, and therefore measurement of spectroscopic information for individual transitions may be very difficult or sometimes impossible. The lack of detailed high-temperature spectroscopic information for the near-infrared transitions of interest, combined with the complexity of WMS technique itself, have in the past been barriers for quantification of WMS in combustion systems.

In this research, a few strong absorption transitions suitable for CH_4 and H_2O measurement have been identified. In addition to having fairly strong line strength, the transitions are selected such that, they are located in the range of standard telecommunication lasers, which are readily available and inexpensive. The selected H_2O transitions are unique as they are close enough to be within the tuning of a single diode laser.

Spectroscopic properties of the selected transitions, which are overlapped under most conditions of temperature and pressure, are determined using a new technique

developed in this research, whereby individual spectroscopic properties of the transitions can be extracted from experiment. This spectroscopic information for each of the strongly overlapped transitions allows the prediction of the behavior of these transitions as a function of temperature and pressure. Using this technique, spectroscopic properties of CH_4 and H_2O for the selected transitions were determined.

For quantification of WMS in combustion systems, a mathematical model based on laser and absorption transition properties has been developed. Using the model, detailed properties of WMS when both intensity and frequency are modulated are studied. The model implements a Voigt function, and therefore is also applicable for Lorentzian and also Gaussian line-shape profiles.

Using the measured spectroscopic properties of the selected H_2O and CH_4 transitions in the WMS model allowed us to validate the accuracy of the WMS model through experiments in a static quartz cell at known temperatures and concentrations. The results of these experiments proved the accuracy of the model. Finally, the optical sensor is applied to simultaneous in-flame measurements of temperature and concentration of CH_4 and H_2O.

A primary application of the sensor described in this work might be for emission or process controls in high temperature processes including gas turbines, boilers, engine exhaust, semiconductor manufacturing, or optical fiber manufacture, among many applications. For such applications, the response time of the sensor could be improved dramatically (up to a few kHz) by centerline-locking technique. Here, instead of tuning the laser frequency across an absorption feature, through a feedback control the laser frequency is kept at the center of absorption feature and

only a modulation current is applied to the laser. Demodulation of absorption signal with such modulation scheme provides absorption information at the same rate of modulation frequency (tens of kHz).

In future work, quantification of the WMS model, which here was based on a complete combustion approximation, could be extended to the case where the reaction has progressed partially. In this case accurate quantification might be possible through an iterative method in which the absorption spectrum is modified in each iteration after calculating H_2O concentration. This particular WMS quantification could be useful for applications in which a detailed study of combustion process is needed.

Appendix A1: A program for simulation of the second harmonic spectra of a Voigt profile when Doppler and Collisional half-width are known

```
//=====================================================================
//     This Program simulates the I_nf,p (in-phase signal) when the
//     absorption spectra has a Voigt line-shape function for the
//     case when intensity modulation is taken into account.
//=====================================================================

#include <math.h>
#include <stdio.h>

int main()

{
    //  Tuning range = 1.6 cm-1 centered at nuhat=0 cm-1

    int i,j,k;
    const int nn=2000;
    const int mm=1000;

    double gamal,gamad,nu0,gamav,x,sigmanu0,a,stepwt,sum1,sum2,sum3,sum4,pi,sf,sF,sai,phi,gain;
    double snu,alpha,cos1,cos2,cos3,cos4,y,term,m,I1f[mm+1],I2f[mm+1],I3f[mm+1],I4f[mm+1],nuhat[mm+1];

    pi=atan(1.0)*4.0;
    gamal=0.05;    // Lorentzian half-width in [cm-1]
    gamad=0.05;    // Doppler half-width in [cm-1]

    sF=-1.0;       // Laser intensity-frequency parameters (assumed linear variation)
    sf=-2.0;

    sai=(-20.0/180.0)*pi;   // is phase difference b/w IM and FM in (rad)
    phi=(50.0/180.0)*pi;    // is detection phase in (rad)

    m=1.0;                  // Ratio of FM amplitude to the absorption profile half-width (Voigt half-width)

    nu0=0.0;                // central absorption frequency

    char* out="IMFMn.out";

    gamav=.5346*gamal+pow(.2166*pow(gamal,2.0)+pow(gamad,2.0),0.5);

    x=gamal/gamav;
    sigmanu0=.01;
    gain=1000.0;

    stepwt=2*pi/(nn);

    nuhat[1]=-.80;
    for(k=2;k<=mm;k++)
    nuhat[k]=nuhat[k-1]+1.6/mm;

    a=m*gamav;
```

```
    for (i=1;i<=mm;i++)
    {
        sum1=0.0; sum2=0.0; sum3=0.0; sum4=0.0;
        for(j=1;j<=nn;j++)
        {
                 y=fabs((nuhat[i]-nu0)/gamav-m*cos(-pi+(j-1)*stepwt+sai));
                alpha=sigmanu0*((1.0-x)*exp(-.693*pow(y,2.0))+x/(1.0+pow(y,2.0))+.016*(1.0-x)*x*(exp(-
                .0841*pow(y,2.25))-1.0/(1.0+.0210*pow(y,2.25))));

                snu=sF*nuhat[i]-sf*a*cos(-pi+(j-1)*stepwt);
                cos1=cos(1.0*(-pi+(j-1)*stepwt)+phi);
                cos2=cos(2.0*(-pi+(j-1)*stepwt)+phi);
                cos3=cos(3.0*(-pi+(j-1)*stepwt)+phi);
                cos4=cos(4.0*(-pi+(j-1)*stepwt)+phi);

                term=(1.0-alpha)*(1.0+snu);
                sum1=sum1+term*cos1;
                sum2=sum2+term*cos2;
                sum3=sum3+term*cos3;
                sum4=sum4+term*cos4;
        }

        I1f[i]=gain*sum1*stepwt/pi;   //  First four harmonics
        I2f[i]=gain*sum2*stepwt/pi;
        I3f[i]=gain*sum3*stepwt/pi;
        I4f[i]=gain*sum4*stepwt/pi;

    }

    //  ---------- Making output file (START)
    FILE *fpr1;
    fpr1=fopen(out,"w");

    for(k=1;k<=mm;k++)
    fprintf(fpr1,"%f %f %f %f %f\n", nuhat[k],I1f[k],I2f[k],I3f[k],I4f[k]);

    fclose(fpr1);
    //  ---------- Making output file (END)

    return 0;
}
```

Appendix A2: A program for simulation of the second harmonic spectra of the selected H_2O transitions

```
//=========================================================================
//      This Program simulates the I2f signal when the absorption
//      profile has a Voigt profile for the case when intensity
//      modulation is taken into account. In this program the effect
//      of two types intensity modulation sF, sf, and also phase shift
//      between intensity and frequency modulation, sai, are considered.
//      In addition the detection phase, phi, is also included
//              For Selected H2O transitions
//=========================================================================

#include <math.h>
#include <stdio.h>

int main()
{
    //  Tuning range = 1.6 cm-1 centered at nuhat=0 cm-1

    int i,j,k;
    const int nn=2000;
    const int mm=400;

    double a0,a12,a3,a4,aav,sum,snu,cos2,term,alpha,s1F,s2F,sf,T,Tb,Av,R,stepwt,L,Lb,sai,phi;
    double XCO2,XN2,XO2,XH2O,pCO2,pN2,pO2,pH2O,pH2Oc,pH2Ob;
    double gamaL12H2O,gamaL3H2O,gamaL0H2O,gamaL4H2O,gamaL12O2,gamaL3O2,gamaL0O2,
    gamaL4O2,gamaL12CO2,gamaL3CO2,gamaL0CO2,gamaL4CO2,gamaL12N2,gamaL3N2,
    gamaL0N2,gamaL4N2;

    double n0[7]={-1.134302397663504e-042,9.676714398274705e-039,-3.352457574161414e-
    035,5.918478065251312e-032,-5.229449580648281e-029,1.382024888890897e-026,
    8.736570371216040e-024};
    double n1[7]={1.182880452915844e-040,-9.730660245129210e-037,3.208326620720904e-033,-
    5.276879397285108e-030,4.238665213413604e-027,-1.240711482449527e-024,
    1.060758405615869e-022};
    double n3[7]={-6.705028656148200e-042,1.016906199980311e-037,-5.613008939092201e-
    034,1.541989562850704e-030,-2.263749771221360e-027,1.612103724409066e-024,
    -2.888611866904023e-022};
    double n4[7]={1.885184012772765e-041,-1.447567686064963e-037,4.293572378735591e-034,-
    5.824645724200227e-031,2.757247450868865e-028,9.006868603789042e-026,
    -4.092023902523880e-023};

    double nuhat[mm+1],I2f[mm+1],I2f1[mm+1],I2f2[mm+1],I2f3[mm+1],I2f4[mm+1],I2f0[mm+1];
    double I2fb[mm+1],I2f1b[mm+1],I2f2b[mm+1],I2f3b[mm+1],I2f4b[mm+1],I2f0b[mm+1];

    double S0,S1,S2,S3,S4,S0b,S1b,S2b,S3b,S4b;

    double HWHML0,HWHML12,HWHML3,HWHML4,HWHMD0,HWHMD1,HWHMD2,HWHMD3,
    HWHMD4,HWHMV0,HWHMV1,HWHMV2,HWHMV3,HWHMV4;
    double  HWHML0b,HWHML12b,HWHML3b,HWHML4b,HWHMD0b,HWHMD1b,HWHMD2b,
    HWHMD3b,HWHMD4b,HWHMV0b,HWHMV1b,HWHMV2b,HWHMV3b,HWHMV4b;
    double m0,m1,m2,m3,m4,nu00,nu01,nu02,nu03,nu04,xx0,xx1,xx2,xx3,xx4,y0,y1,y2,y3,y4,pi;
    double m0b,m1b,m2b,m3b,m4b,xx0b,xx1b,xx2b,xx3b,xx4b,y0b,y1b,y2b,y3b,y4b;
    double sigma00,sigma01,sigma02,sigma03,sigma04,alpha0,alpha1,alpha2,alpha3,alpha4;
    double sigma00b,sigma01b,sigma02b,sigma03b,sigma04b,alpha0b,alpha1b,alpha2b,alpha3b,alpha4b;
    double sum1,sum2,sum3,sum4,sum0,term1,term2,term3,term4,term0,snu1,snu2,snu3,snu4,snu0;
```

```
double sum1b,sum2b,sum3b,sum4b,sum0b,term1b,term2b,term3b,term4b,term0b;

char* out="I2fnw.out";

//  FSR=.022694;        Free Spectral Rang of RI

pi=atan(1.0)*4.0;

T=2000;                 // in (K)
Tb=23+273;              // Ambient temperature (in K): for the case the background H2O absorption needs
                        // is not zero
L=10.0;                 // in (cm)
Lb=0.0;                 // in (cm)
pH2Ob=10.0/760.0;


a0=0.08;                // Differnt FM amplitude at differnt region
a12=0.090;              // in (cm-1) for transition 1 and 2
a3=0.095;               // in (cm-1) for the transition 3
a4=0.10;                // a0 and a4 are FM amplitude of adjucent transition to the main transitions


s1F=-1.1928;            // laser intensity-frequency parameters
s2F= -0.3985;
sf=-2.3;

sai=(-15/180.0)*pi;     // phase differnce b/w FM and IM in (rad)
phi=(155/180.0)*pi;     // detection phase in (rad)

aav=(a12+a3)/2;         // average FM amplitude over the main transitions

Av=6.02e23;
R=82.08;

XCO2=1/(1+2+2*3.76)*100;            // methane/air combustion: mole fraction in complete
                                    //combustion approximation.
XN2=2*3.76/(1+2+2*3.76)*100;        // for Equivalence ratio=1.0
XO2=0;
XH2O=2/(1+2+2*3.76)*100;


pN2=XN2*1e-2;           // partial pressures in (atm)
pO2=XO2*1e-2;
pCO2=XCO2*1e-2;
pH2O=XH2O*1e-2;
pH2Oc=1.0;              // Normalized H2O pressure in atm (however the results are divided by 760.0 to
                        // give the normalization based on 1 torr H2O

//  Calculation of line strength at the specified temperature

S0=n0[0]*pow(T,6.0)+n0[1]*pow(T,5.0)+n0[2]*pow(T,4.0)+n0[3]*pow(T,3.0)+n0[4]*pow(T,2.0)+
n0[5]*T+n0[6];
S1=n1[0]*pow(T,6.0)+n1[1]*pow(T,5.0)+n1[2]*pow(T,4.0)+n1[3]*pow(T,3.0)+n1[4]*pow(T,2.0)+
n1[5]*T+n1[6];
S3=n3[0]*pow(T,6.0)+n3[1]*pow(T,5.0)+n3[2]*pow(T,4.0)+n3[3]*pow(T,3.0)+n3[4]*pow(T,2.0)+
n3[5]*T+n3[6];
S4=n4[0]*pow(T,6.0)+n4[1]*pow(T,5.0)+n4[2]*pow(T,4.0)+n4[3]*pow(T,3.0)+n4[4]*pow(T,2.0)+
n4[5]*T+n4[6];

S4b=3.980E-24;
S3b=3.910E-23;
S2b=1.880E-24;
```

```
S1b=5.470E-24;
S0b=8.450E-24;

S0=Av/(R*T)*S0;
S1=Av/(R*T)*S1;          // Conversion of Si to atm,cm system units
S2=S1/2.91;
S3=Av/(R*T)*S3;
S4=Av/(R*T)*S4;

S0b=Av/(R*Tb)*S0b;    // Background information
S1b=Av/(R*Tb)*S1b;    // Conversion of Si to atm,cm system units
S2b=S1b/2.91;
S3b=Av/(R*Tb)*S3b;
S4b=Av/(R*Tb)*S4b;

//  Calculation of broadening coefficient for different quenching species at the specified temperature
gamaL12H2O=3.0116/pow(T,0.475);          // Self H2O broadening coefficient of transition 1 and 2
gamaL3H2O=26.759/pow(T,0.766);          // Self H2O broadening coefficient of transition 3
gamaL0H2O=0.4389*pow(T/296,-0.68);      // Self H2O broadening coefficient of transition 0
gamaL4H2O=0.4170*pow(T/296,-0.68);      // Self H2O broadening coefficient of transition 4

gamaL12N2=1.0053/pow(T,0.552);          // H2O-N2 broadening coefficient of transition 1 and 2
gamaL3N2=6.5581/pow(T,0.768);           // H2O-N2 broadening coefficient of transition 3
gamaL0N2=0.0828*pow(T/296,-0.68);       // H2O-N2 broadening coefficient of transition 0
gamaL4N2=0.0967*pow(T/296,-0.68);       // H2O-N2 broadening coefficient of transition 4

gamaL12O2=.27008/pow(T,0.467);          // H2O-O2 broadening coefficient of transition 1 and 2
gamaL3O2=2.4758/pow(T,0.751);           // H2O-O2 broadening coefficient of transition 3
gamaL0O2=0.0828*pow(T/296,-0.68);       // H2O-O2 broadening coefficient of transition 0
gamaL4O2=0.0967*pow(T/296,-0.68);       // H2O-O2 broadening coefficient of transition 4

gamaL12CO2=1.4911/pow(T,0.563);         // H2O-CO2 broadening coefficient of transition 1 and 2
gamaL3CO2=1.6644/pow(T,0.505);          // H2O-CO2 broadening coefficient of transition 3
gamaL0CO2=0.0828*pow(T/296,-0.68);      // H2O-CO2 broadening coefficient of transition 0
gamaL4CO2=0.0967*pow(T/296,-0.68);      // H2O-CO2 broadening coefficient of transition 4

//  Calculation of effective (total) collisional halfwidths

HWHML12=gamaL12H2O*pH2O+gamaL12N2*pN2+gamaL12O2*pO2+gamaL12CO2*pCO2;
HWHML3=gamaL3H2O*pH2O+gamaL3N2*pN2+gamaL3O2*pO2+gamaL3CO2*pCO2;
HWHML0=gamaL0H2O*pH2O+gamaL0N2*pN2+gamaL0O2*pO2+gamaL0CO2*pCO2;
HWHML4=gamaL4H2O*pH2O+gamaL4N2*pN2+gamaL4O2*pO2+gamaL4CO2*pCO2;

//  Calculation of effective (total) collisional halfwidths

HWHML12=gamaL12H2O*pH2O+gamaL12N2*pN2+gamaL12O2*pO2+gamaL12CO2*pCO2;
HWHML3=gamaL3H2O*pH2O+gamaL3N2*pN2+gamaL3O2*pO2+gamaL3CO2*pCO2;
HWHML0=gamaL0H2O*pH2O+gamaL0N2*pN2+gamaL0O2*pO2+gamaL0CO2*pCO2;
HWHML4=gamaL4H2O*pH2O+gamaL4N2*pN2+gamaL4O2*pO2+gamaL4CO2*pCO2;

HWHML12b=.3853/pow(Tb,0.400)*(3.76/4.76)*1+.1456/pow(Tb,0.371)*(1/4.76)*1;
HWHML3b=15.101/pow(Tb,0.903)*(3.76/4.76)*1+2.1717/pow(Tb,0.723)*(1/4.76)*1;
HWHML4b=0.0828*pow(Tb/296,-0.68)*(3.76/4.76)*1+0.0828*pow(Tb/296,-0.68)*(1/4.76)*1;
HWHML0b=0.0967*pow(Tb/296,-0.68)*(3.76/4.76)*1+0.0967*pow(Tb/296,-0.68)*(1/4.76)*1;

HWHMD1 =.5*(7.1623e-7*6771.747*pow(T/18.0,0.5));
HWHMD2 =.5*(7.1623e-7*6771.710*pow(T/18.0,0.5));
HWHMD3 =.5*(7.1623e-7*6771.475*pow(T/18.0,0.5));
HWHMD4 =.5*(7.1623e-7*6771.1974*pow(T/18.0,0.5));
HWHMD0 =.5*(7.1623e-7*6771.96150*pow(T/18.0,0.5));

HWHMD1b =.5*(7.1623e-7*6771.747*pow(Tb/18.0,0.5));
```

```
HWHMD2b =.5*(7.1623e-7*6771.710*pow(Tb/18.0,0.5));
HWHMD3b =.5*(7.1623e-7*6771.475*pow(Tb/18.0,0.5));
HWHMD4b =.5*(7.1623e-7*6771.1974*pow(Tb/18.0,0.5));
HWHMD0b =.5*(7.1623e-7*6771.96150*pow(Tb/18.0,0.5));

HWHMV1=.5346*HWHML12+pow(.2166*pow(HWHML12,2.0)+ pow(HWHMD1,2.0),0.5);
HWHMV2=.5346*HWHML12+pow(.2166*pow(HWHML12,2.0)+ pow(HWHMD2,2.0),0.5);
HWHMV3=.5346*HWHML3+pow(.2166*pow(HWHML3,2.0)+ pow(HWHMD3,2.0),0.5);
HWHMV4=.5346*HWHML4+pow(.2166*pow(HWHML4,2.0)+ pow(HWHMD4,2.0),0.5);
HWHMV0=.5346*HWHML0+pow(.2166*pow(HWHML0,2.0)+ pow(HWHMD0,2.0),0.5);

HWHMV1b=.5346*HWHML12b+pow(.2166*pow(HWHML12b,2.0)+ pow(HWHMD1b,2.0),0.5);
HWHMV2b=.5346*HWHML12b+pow(.2166*pow(HWHML12b,2.0)+ pow(HWHMD2b,2.0),0.5);
HWHMV3b=.5346*HWHML3b+pow(.2166*pow(HWHML3b,2.0)+ pow(HWHMD3b,2.0),0.5);
HWHMV4b=.5346*HWHML4b+pow(.2166*pow(HWHML4b,2.0)+ pow(HWHMD4b,2.0),0.5);
HWHMV0b=.5346*HWHML0b+pow(.2166*pow(HWHML0b,2.0)+ pow(HWHMD0b,2.0),0.5);


xx1=HWHML12/HWHMV1;
xx2=HWHML12/HWHMV2;
xx3=HWHML3/HWHMV3;
xx4=HWHML4/HWHMV4;
xx0=HWHML0/HWHMV0;

xx1b=HWHML12b/HWHMV1b;
xx2b=HWHML12b/HWHMV2b;
xx3b=HWHML3b/HWHMV3b;
xx4b=HWHML4b/HWHMV4b;
xx0b=HWHML0b/HWHMV0b;

nu01=0;
nu02=-.03724;
nu03=-.27199;
nu04=-.5499;
nu00=+0.2142;


sigma01=S1*pH2Oc*L/(2*HWHMV1*(1.065+.447*xx1+.058*pow(xx1,2.0)));
sigma02=S2*pH2Oc*L/(2*HWHMV2*(1.065+.447*xx2+.058*pow(xx2,2.0)));
sigma03=S3*pH2Oc*L/(2*HWHMV3*(1.065+.447*xx3+.058*pow(xx3,2.0)));
sigma04=S4*pH2Oc*L/(2*HWHMV4*(1.065+.447*xx4+.058*pow(xx4,2.0)));
sigma00=S0*pH2Oc*L/(2*HWHMV0*(1.065+.447*xx0+.058*pow(xx0,2.0)));

sigma01b=S1b*pH2Ob*Lb/(2*HWHMV1b*(1.065+.447*xx1b+.058*pow(xx1b,2.0)));
sigma02b=S2b*pH2Ob*Lb/(2*HWHMV2b*(1.065+.447*xx2b+.058*pow(xx2b,2.0)));
sigma03b=S3b*pH2Ob*Lb/(2*HWHMV3b*(1.065+.447*xx3b+.058*pow(xx3b,2.0)));
sigma04b=S4b*pH2Ob*Lb/(2*HWHMV4b*(1.065+.447*xx4b+.058*pow(xx4b,2.0)));
sigma00b=S0b*pH2Ob*Lb/(2*HWHMV0b*(1.065+.447*xx0b+.058*pow(xx0b,2.0)));


m1=a12/HWHMV1;
m2=a12/HWHMV2;
m3=a3/HWHMV3;
m4=a4/HWHMV4;
m0=a0/HWHMV0;

m1b=a12/HWHMV1b;
m2b=a12/HWHMV2b;
m3b=a3/HWHMV3b;
m4b=a4/HWHMV4b;
m0b=a0/HWHMV0b;
```

```
nuhat[1]=-1.3;
for(k=2;k<=mm;k++)
    nuhat[k]=nuhat[k-1]+1.9/mm;

stepwt=2*pi/nn;

for (i=1;i<=mm;i++)
{

    sum1=0.0;sum2=0.0;sum3=0.0;sum4=0.0;sum0=0.0;
    sum1b=0.0;sum2b=0.0;sum3b=0.0;sum4b=0.0;sum0b=0.0;
    for(j=1;j<=nn;j++)
    {
        y1=fabs((nuhat[i]-nu01)/HWHMV1-m1*cos(-pi+(j-1)*stepwt+sai));
        y2=fabs((nuhat[i]-nu02)/HWHMV2-m2*cos(-pi+(j-1)*stepwt+sai));
        y3=fabs((nuhat[i]-nu03)/HWHMV3-m3*cos(-pi+(j-1)*stepwt+sai));
        y4=fabs((nuhat[i]-nu04)/HWHMV4-m4*cos(-pi+(j-1)*stepwt+sai));
        y0=fabs((nuhat[i]-nu00)/HWHMV0-m0*cos(-pi+(j-1)*stepwt+sai));

        y1b=fabs((nuhat[i]-nu01)/HWHMV1b-m1b*cos(-pi+(j-1)*stepwt+sai));
        y2b=fabs((nuhat[i]-nu02)/HWHMV2b-m2b*cos(-pi+(j-1)*stepwt+sai));
        y3b=fabs((nuhat[i]-nu03)/HWHMV3b-m3b*cos(-pi+(j-1)*stepwt+sai));
        y4b=fabs((nuhat[i]-nu04)/HWHMV4b-m4b*cos(-pi+(j-1)*stepwt+sai));
        y0b=fabs((nuhat[i]-nu00)/HWHMV0b-m0b*cos(-pi+(j-1)*stepwt+sai));

        alpha1=sigma01*((1.0-xx1)*exp(-.693*pow(y1,2.0))+xx1/(1.0+pow(y1,2.0))+
        .016*(1.0-xx1)*xx1*(exp(-.0841*pow(y1,2.25))-1.0/(1.0+.0210*pow(y1,2.25))));
        alpha2=sigma02*((1.0-xx2)*exp(-.693*pow(y2,2.0))+xx2/(1.0+pow(y2,2.0))+
        .016*(1.0-xx2)*xx2*(exp(-.0841*pow(y2,2.25))-1.0/(1.0+.0210*pow(y2,2.25))));
        alpha3=sigma03*((1.0-xx3)*exp(-.693*pow(y3,2.0))+xx3/(1.0+pow(y3,2.0))+
        .016*(1.0-xx3)*xx3*(exp(-.0841*pow(y3,2.25))-1.0/(1.0+.0210*pow(y3,2.25))));
        alpha4=sigma04*((1.0-xx4)*exp(-.693*pow(y4,2.0))+xx4/(1.0+pow(y4,2.0))+
        .016*(1.0-xx4)*xx4*(exp(-.0841*pow(y4,2.25))-1.0/(1.0+.0210*pow(y4,2.25))));
        alpha0=sigma00*((1.0-xx0)*exp(-.693*pow(y0,2.0))+xx0/(1.0+pow(y0,2.0))+
        .016*(1.0-xx0)*xx0*(exp(-.0841*pow(y0,2.25))-1.0/(1.0+.0210*pow(y0,2.25))));

        alpha1b=sigma01b*((1.0-xx1b)*exp(-.693*pow(y1b,2.0))+xx1b/(1.0+pow(y1b,2.0))+
        .016*(1.0-xx1b)*xx1b*(exp(-.0841*pow(y1b,2.25))-1.0/(1.0+.0210*pow(y1b,2.25))));
        alpha2b=sigma02b*((1.0-xx2b)*exp(-.693*pow(y2b,2.0))+xx2b/(1.0+pow(y2b,2.0))+
        .016*(1.0-xx2b)*xx2b*(exp(-.0841*pow(y2b,2.25))-1.0/(1.0+.0210*pow(y2b,2.25))));
        alpha3b=sigma03b*((1.0-xx3b)*exp(-.693*pow(y3b,2.0))+xx3b/(1.0+pow(y3b,2.0))+
        .016*(1.0-xx3b)*xx3b*(exp(-.0841*pow(y3b,2.25))-1.0/(1.0+.0210*pow(y3b,2.25))));
        alpha4b=sigma04b*((1.0-xx4b)*exp(-.693*pow(y4b,2.0))+xx4b/(1.0+pow(y4b,2.0))+
        .016*(1.0-xx4b)*xx4b*(exp(-.0841*pow(y4b,2.25))-1.0/(1.0+.0210*pow(y4b,2.25))));
        alpha0b=sigma00b*((1.0-xx0b)*exp(-.693*pow(y0b,2.0))+xx0b/(1.0+pow(y0b,2.0))+
        .016*(1.0-xx0b)*xx0b*(exp(-.0841*pow(y0b,2.25))-1.0/(1.0+.0210*pow(y0b,2.25))));

        snu1=s1F*nuhat[i]+s2F*pow(nuhat[i],2.0)-sf*a12*cos(-pi+(j-1)*stepwt);
        snu2=snu1;
        snu3=s1F*nuhat[i]+s2F*pow(nuhat[i],2.0)-sf*a3*cos(-pi+(j-1)*stepwt);
        snu4=s1F*nuhat[i]+s2F*pow(nuhat[i],2.0)-sf*a4*cos(-pi+(j-1)*stepwt);
        snu0=s1F*nuhat[i]+s2F*pow(nuhat[i],2.0)-sf*a0*cos(-pi+(j-1)*stepwt);

        cos2=cos(1.0 *(-pi+(j-1)*stepwt)+phi);

        term1=(1.0-alpha1)*(1.0+snu1);
        term2=(1.0-alpha2)*(1.0+snu2);
        term3=(1.0-alpha3)*(1.0+snu3);
        term4=(1.0-alpha4)*(1.0+snu4);
        term0=(1.0-alpha0)*(1.0+snu0);

        term1b=(1.0-alpha1b)*(1.0+snu1);
```

```
            term2b=(1.0-alpha2b)*(1.0+snu2);
            term3b=(1.0-alpha3b)*(1.0+snu3);
            term4b=(1.0-alpha4b)*(1.0+snu4);
            term0b=(1.0-alpha0b)*(1.0+snu0);

            sum1=sum1+term1*cos2;
            sum2=sum2+term2*cos2;
            sum3=sum3+term3*cos2;
            sum4=sum4+term4*cos2;
            sum0=sum0+term0*cos2;

            sum1b=sum1b+term1b*cos2;
            sum2b=sum2b+term2b*cos2;
            sum3b=sum3b+term3b*cos2;
            sum4b=sum4b+term4b*cos2;
            sum0b=sum0b+term0b*cos2;

        }
        I2f1[i]=sum1*stepwt/pi;
        I2f2[i]=sum2*stepwt/pi;
        I2f3[i]=sum3*stepwt/pi;
        I2f4[i]=sum4*stepwt/pi;
        I2f0[i]=sum0*stepwt/pi;

        I2f1b[i]=sum1b*stepwt/pi;
        I2f2b[i]=sum2b*stepwt/pi;
        I2f3b[i]=sum3b*stepwt/pi;
        I2f4b[i]=sum4b*stepwt/pi;
        I2f0b[i]=sum0b*stepwt/pi;

        I2f[i]=I2f1[i]+I2f2[i]+I2f3[i]+I2f4[i]+I2f0[i];
        I2fb[i]=I2f1b[i]+I2f2b[i]+I2f3b[i]+I2f4b[i]+I2f0b[i];

    }

    //  ---------- Making output file (START)
    FILE *fpr1;
    fpr1=fopen(out,"w");

    for(k=1;k<=mm;k++)
        fprintf(fpr1,"%f %f %f\n", nuhat[k],I2f[k]);

    fclose(fpr1);
    //  ---------- Making output file (END)

    return 0;
}
```

Appendix A3: A program for simulation of the second harmonic spectra of the R(4) manifold of the $2\nu_3$ band of CH_4

```
//=========================================================================
//      This Program simulates the I2f signal when the absorption
//      profile has a Voigt profile for the case when intensity
//      modulation is taken into account. In this program the effect
//      of two types intensity modulation sf, sF, and also phase shift
//      between intensity and frequency modulation, sai, are considered.
//      In addition the detection phase, phi, is also included.
//              ***    R(4) transition of CH4   ***
//=========================================================================

#include <math.h>
#include <stdio.h>

int main()
{
    //  Tuning range for simulation= 1.6 cm-1 centered at nuhat=0 cm-1

    int i,j,k;
    const int nn=2000;
    const int mm=400;

    double cc,kk,bb,hh,ssigma,Qnucl,Qrot,Qvib,QT0,QT,nu1,nu2,nu3,nu4;

    double am,cos2,s1F,s2F,sf,T,Av,R,stepwt,L,sai,phi;
    double XCO2,XN2,XO2,XH2O,XCH4,pCO2,pN2,pO2,pH2O,pCH4,pCH4c;
    double gamaL1H2O,gamaL2H2O,gamaL3H2O,gamaL4H2O,gamaL1O2,gamaL2O2,gamaL3O2,gamaL4O2,
    gamaL1CO2,gamaL2CO2,gamaL3CO2,gamaL4CO2,gamaL1N2,gamaL2N2,gamaL3N2,gamaL4N2,
    gamaL1CH4,gamaL2CH4,gamaL3CH4,gamaL4CH4;

    double nuhat[mm+1],I2f[mm+1],I2f1[mm+1],I2f2[mm+1],I2f3[mm+1],I2f4[mm+1];

    double S1,S2,S3,S4;

    double HWHML1,HWHML2,HWHML3,HWHML4,HWHMD1,HWHMD2,HWHMD3,HWHMD4,
    HWHMV1,HWHMV2,HWHMV3,HWHMV4;
    double m1,m2,m3,m4,nu01,nu02,nu03,nu04,xx1,xx2,xx3,xx4,y1,y2,y3,y4,pi;
    double sigma01,sigma02,sigma03,sigma04,alpha1,alpha2,alpha3,alpha4;
    double sum1,sum2,sum3,sum4,term1,term2,term3,term4,snu1,snu2,snu3,snu4;

    char* out="I2CH4R4.out";


    pi=atan(1.0)*4.0;

    T=2000;             // in (K)
    L=10.0;             // in (cm)
    pCH4c=1.0;          // in (atm), however in the graphs in the dissertation it is devided by 760
                        // for normalization per 1 torr

    am=0.057;           // amplitude of FM (cm-1)
```

```
s1F=-1.869;                 // Laser intensity-frequency parameters
s2F=-.900;
sf=-3.5;

sai=(0.0/180.0)*pi;         // phase difference b/w FM and IM in (rad)
phi=(140.0/180.0)*pi;       // detection phase in (rad)

Av=6.02e23;
R=82.08;

XCO2=1/(1+2+2*3.76)*100;              // methane/air combustion   phi=1.0
XN2=2*3.76/(1+2+2*3.76)*100;
XO2=0;
XH2O=2/(1+2+2*3.76)*100;
XCH4=0.0;

pN2=XN2*1e-2;     // partial pressure of species in (atm)
pO2=XO2*1e-2;
pCO2=XCO2*1e-2;
pH2O=XH2O*1e-2;
pCH4=XCH4*1e-2;

//  Calculation of line strength at a given temeprature based on SHM
Qnucl=16.0;
QT0=585.132;
bb=5.24;
ssigma=12.0;
cc=2.998e+10;
kk=1.38066e-23;
hh=6.62608e-34;
nu1=2914.2;
nu2=1526.0;
nu3=3020.3;
nu4=1306.2;

Qrot=(1/ssigma)*pow( (pi/pow(bb,3.0)) * pow((kk*T/(hh*cc)),3.0),0.5 );
Qvib=pow(1- ( exp(-hh*cc*nu1/(kk*T)) ) ,-1.0) * pow(1- ( exp(-hh*cc*nu2/(kk*T)) ) ,-2.0) *
 pow(1- ( exp(-hh*cc*nu3/(kk*T)) ) ,-3.0) * pow(1- ( exp(-hh*cc*nu4/(kk*T)) ) ,-3.0);

QT=Qnucl*Qrot*Qvib;

S1=(0.021854*QT0*296.0)/(QT*T) * exp( -hh*cc*104.7800/kk*(1.0/T-1.0/296.0) ) *
( 1- ( exp(-hh*cc*6057.127/(kk*T)) ) ) * 1.0/ ( 1- ( exp(-hh*cc*6057.127/(kk*296.0)) ) );
S2=(0.022598*QT0*296.0)/(QT*T) * exp( -hh*cc*104.7747/kk*(1.0/T-1.0/296.0) ) *
( 1- ( exp(-hh*cc*6057.100/(kk*T)) ) ) * 1.0/ ( 1- ( exp(-hh*cc*6057.100/(kk*296.0)) ) );
S3=(0.031716*QT0*296.0)/(QT*T) * exp( -hh*cc*104.7728/kk*(1.0/T-1.0/296.0) ) *
( 1- ( exp(-hh*cc*6057.086/(kk*T)) ) ) * 1.0/ ( 1- ( exp(-hh*cc*6057.086/(kk*296.0)) ) );
S4=(0.020293*QT0*296.0)/(QT*T) * exp( -hh*cc*104.7760/kk*(1.0/T-1.0/296.0) ) *
( 1- ( exp(-hh*cc*6057.078/(kk*T)) ) ) * 1.0/ ( 1- ( exp(-hh*cc*6057.078/(kk*296.0)) ) );

//  Calculation of broadening coefficient for different quenching species at the specified temperature
gamaL1H2O=14.098/pow(T,0.907);          // CH4-H2O broadening coefficient of transition 1
gamaL2H2O=gamaL1H2O;                    // CH4-H2O broadening coefficient of transition 2
gamaL3H2O=gamaL1H2O;                    // CH4-H2O broadening coefficient of transition 3
gamaL4H2O=gamaL1H2O;                    // CH4-H2O broadening coefficient of transition 4

gamaL1N2=10.984/pow(T,0.928);           // CH4-N2 broadening coefficient of transition 1
gamaL2N2=gamaL1N2;                      // CH4-N2 broadening coefficient of transition 2
gamaL3N2=gamaL1N2;                      // CH4-N2 broadening coefficient of transition 3
gamaL4N2=gamaL1N2;                      // CH4-N2 broadening coefficient of transition 4

gamaL1O2=12.021/pow(T,0.916);           // CH4-O2 broadening coefficient of transition 1
```

```
gamaL2O2=gamaL1O2;                  // CH4-O2 broadening coefficient of transition 2
gamaL3O2=gamaL1O2;                  // CH4-O2 broadening coefficient of transition 3
gamaL4O2=gamaL1O2;                  // CH4-O2 broadening coefficient of transition 4

gamaL1CO2=16.213/pow(T,0.950);          // CH4-CO2 broadening coefficient of transition 1
gamaL2CO2=gamaL1CO2;                // CH4-CO2 broadening coefficient of transition 2
gamaL3CO2=gamaL1CO2;                // CH4-CO2 broadening coefficient of transition 3
gamaL4CO2=gamaL1CO2;                // CH4-CO2 broadening coefficient of transition 4

gamaL1CH4=16.466/pow(T,0.952);          // CH4-CH4 broadening coefficient of transition 1
gamaL2CH4=gamaL1CH4;                // CH4-CH4 broadening coefficient of transition 2
gamaL3CH4=gamaL1CH4;                // CH4-CH4 broadening coefficient of transition 3
gamaL4CH4=gamaL1CH4;                // CH4-CH4 broadening coefficient of transition 4

//  Calculation of effective (total) collisional halfwidths

HWHML1=gamaL1H2O*pH2O+gamaL1N2*pN2+gamaL1O2*pO2+gamaL1CO2*pCO2+
gamaL1CH4*pCH4;
HWHML2=gamaL2H2O*pH2O+gamaL2N2*pN2+gamaL2O2*pO2+gamaL2CO2*pCO2+
gamaL2CH4*pCH4;
HWHML3=gamaL3H2O*pH2O+gamaL3N2*pN2+gamaL3O2*pO2+gamaL3CO2*pCO2+
gamaL3CH4*pCH4;
HWHML4=gamaL4H2O*pH2O+gamaL4N2*pN2+gamaL4O2*pO2+gamaL4CO2*pCO2+
gamaL4CH4*pCH4;

//  Calculation of Doppler halfwidths

HWHMD1 =.5*(7.1623e-7*6057.127*pow(T/16.0,0.5));
HWHMD2 =.5*(7.1623e-7*6057.100*pow(T/16.0,0.5));
HWHMD3 =.5*(7.1623e-7*6057.086*pow(T/16.0,0.5));
HWHMD4 =.5*(7.1623e-7*6057.078*pow(T/16.0,0.5));

HWHMV1=.5346*HWHML1+pow(.2166*pow(HWHML1,2.0)+ pow(HWHMD1,2.0),0.5);
HWHMV2=.5346*HWHML2+pow(.2166*pow(HWHML2,2.0)+ pow(HWHMD2,2.0),0.5);
HWHMV3=.5346*HWHML3+pow(.2166*pow(HWHML3,2.0)+ pow(HWHMD3,2.0),0.5);
HWHMV4=.5346*HWHML4+pow(.2166*pow(HWHML4,2.0)+ pow(HWHMD4,2.0),0.5);

xx1=HWHML1/HWHMV1;
xx2=HWHML1/HWHMV2;
xx3=HWHML3/HWHMV3;
xx4=HWHML4/HWHMV4;

nu01=.0412;
nu02=0.0137;
nu03=0.0;
nu04=-.0083;

sigma01=S1*pCH4c*L/(2*HWHMV1*(1.065+.447*xx1+.058*pow(xx1,2.0)));
sigma02=S2*pCH4c*L/(2*HWHMV2*(1.065+.447*xx2+.058*pow(xx2,2.0)));
sigma03=S3*pCH4c*L/(2*HWHMV3*(1.065+.447*xx3+.058*pow(xx3,2.0)));
sigma04=S4*pCH4c*L/(2*HWHMV4*(1.065+.447*xx4+.058*pow(xx4,2.0)));


m1=am/HWHMV1;
m2=am/HWHMV2;
m3=am/HWHMV3;
m4=am/HWHMV4;

nuhat[1]=-0.7;
for(k=2;k<=mm;k++)
    nuhat[k]=nuhat[k-1]+1.4/mm;
```

```
    stepwt=2*pi/nn;

    for (i=1;i<=mm;i++)
    {
        sum1=0.0;sum2=0.0;sum3=0.0;sum4=0.0;
        for(j=1;j<=nn;j++)
        {
             y1=fabs((nuhat[i]-nu01)/HWHMV1-m1*cos(-pi+(j-1)*stepwt+sai));
             y2=fabs((nuhat[i]-nu02)/HWHMV2-m2*cos(-pi+(j-1)*stepwt+sai));
             y3=fabs((nuhat[i]-nu03)/HWHMV3-m3*cos(-pi+(j-1)*stepwt+sai));
             y4=fabs((nuhat[i]-nu04)/HWHMV4-m4*cos(-pi+(j-1)*stepwt+sai));

            alpha1=sigma01*((1.0-xx1)*exp(-.693*pow(y1,2.0))+xx1/(1.0+pow(y1,2.0))+
            .016*(1.0-xx1)*xx1*(exp(-.0841*pow(y1,2.25))-1.0/(1.0+.0210*pow(y1,2.25))));
            alpha2=sigma02*((1.0-xx2)*exp(-.693*pow(y2,2.0))+xx2/(1.0+pow(y2,2.0))+
            .016*(1.0-xx2)*xx2*(exp(-.0841*pow(y2,2.25))-1.0/(1.0+.0210*pow(y2,2.25))));
            alpha3=sigma03*((1.0-xx3)*exp(-.693*pow(y3,2.0))+xx3/(1.0+pow(y3,2.0))+
            .016*(1.0-xx3)*xx3*(exp(-.0841*pow(y3,2.25))-1.0/(1.0+.0210*pow(y3,2.25))));
            alpha4=sigma04*((1.0-xx4)*exp(-.693*pow(y4,2.0))+xx4/(1.0+pow(y4,2.0))+
            .016*(1.0-xx4)*xx4*(exp(-.0841*pow(y4,2.25))-1.0/(1.0+.0210*pow(y4,2.25))));

            snu1=s1F*nuhat[i]+s2F*pow(nuhat[i],2.0)-sf*am*cos(-pi+(j-1)*stepwt);
            snu2=snu1;
            snu3=snu1;
            snu4=snu1;

            cos2=cos(2.0 *(-pi+(j-1)*stepwt)+phi);

             term1=(1.0-alpha1)*(1.0+snu1);
            term2=(1.0-alpha2)*(1.0+snu2);
            term3=(1.0-alpha3)*(1.0+snu3);
            term4=(1.0-alpha4)*(1.0+snu4);

            sum1=sum1+term1*cos2;
            sum2=sum2+term2*cos2;
            sum3=sum3+term3*cos2;
            sum4=sum4+term4*cos2;

        }
        I2f1[i]=sum1*stepwt/pi;
        I2f2[i]=sum2*stepwt/pi;
        I2f3[i]=sum3*stepwt/pi;
        I2f4[i]=sum4*stepwt/pi;

        I2f[i]=I2f1[i]+I2f2[i]+I2f3[i]+I2f4[i];

    }

    //  ---------- Making output file (START)
    FILE *fpr1;
    fpr1=fopen(out,"w");

    fprintf(fpr1,"x=[\n");

    for(k=1;k<=mm;k++)
        fprintf(fpr1,"%f %f\n", nuhat[k],I2f[k]);

    fclose(fpr1);
    //  ---------- Making output file (END)

    return 0;
}
```

Appendix B1: Some spectroscopic parameters of R(3) and R(4) manifolds of the $2\nu_3$ band of CH_4

The vibrational quantum numbers of R(3) and R(4) manifolds of the $2\nu_3$ band of CH_4 transitions are listed in Tables B1.1 and B1.2, respectively.

Table B1.1: Vibrational quantum numbers of the $2\nu_3$ band of R(3) manifold of CH_4 absorption transitions (Extracted from HITRAN database).

ν	E''	v1'	v2'	v3'	v4'	n/C'		V1''	v2''	v3''	v4''	n/C''
6046.9420	62.8768	0	0	2	0	1F2	<-	0	0	0	0	1A1
6046.9527	62.8758	0	0	2	0	1F2	<-	0	0	0	0	1A1
6046.9647	62.8782	0	0	2	0	1F2	<-	0	0	0	0	1A1

Table B1.2: Vibrational quantum number of the $2\nu_3$ band of R(4) manifold of CH_4 absorption transitions (Extracted from HITRAN database).

ν	E''	v1'	V2'	v3'	v4'	n/C'		v1''	v2''	v3''	v4''	n/C''
6057.0778	104.776	0	0	2	0	1F2	<-	0	0	0	0	1A1
6057.0861	104.7728	0	0	2	0	1F2	<-	0	0	0	0	1A1
6057.0998	104.7747	0	0	2	0	1F2	<-	0	0	0	0	1A1
6057.1273	104.78	0	0	2	0	1F2	<-	0	0	0	0	1A1

More information about the spectroscopic parameters of CH_4 can be found in the paper by Brown et al. (Brown, Benner et al. 2003)

Appendix B2: Some spectroscopic parameters of the selected H_2O transitions

Global and local quanta indexes, which are used to describe a particular transition, for selected absorption transitions are listed in Table B2.1.

Table B2.1: Global and local quanta index of the selected H_2O absorption transitions (Extracted from HITRAN database).

N	E''	v_1'	v_2'	v_3'	v_1''	v_2''	v_3''	J'	K'_a	K'_c	F'	J''	K''_a	K''_c	F''
6771.4753	931.237	0	2	1	0	0	0	6	4	2	7	4	3	562	6
6771.7101	1590.691	2	0	0	0	0	0	7	6	2	8	7	1	462	6
6771.7473	1590.69	2	0	0	0	0	0	7	6	1	8	7	2	462	6

More information about HITRAN transition parameters can be found in the paper by Rothman et al. (Rothman, Barbe et al. 2003)

Appendix C: Design and building the Ring Interferometer

The ring interferometer is designed based on information presented in paper by Stokes (Stokes, Chodorow et al. 1982) Based on information presented in this paper, a 95/5 single mode directional coupler is used for building the interferometer. One of the input/out ports of the coupler is first cut in such a way that by splicing the ends of these ports together, a ring with an approximate length of 30 cm has been made. See Figure C.1.

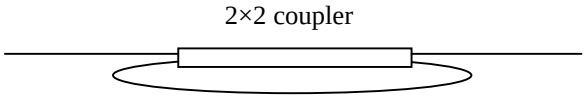

Figure C.1: Schematic of the ring interferometer

The Free Spectral Range (FSR) of such interferometer will be $1/nL$ cm^{-1}, where n is refractive index of waveguide and L is the length of the ring in cm. Since the waveguide of the coupler is made of fused silica, and fused silica has an approximate refractive index of 1.5 for infrared light, the FSR of the designed ring interferometer is approximately $1/(1.5\times30)=0.022$ cm^{-1}. Since during building the ring interferometer there was some uncertainty in measuring the length of the ring, it is decided to calculate FSR more precisely. For measuring FSR, the spectra of the ring interferometer signal, as shown in Figure 5.15, was compared to absorption spectra of two H_2O transitions, shown in Figure 5.15, where their frequency spacing is well known from HITRAN database. By comparison of these spectra, the FSR for the H_2O

laser (1477 nm) is obtained as 0.0022694 ± 0.0000020cm^{-1}. Also for CH4 laser, the FSR is calculated by

$$\frac{\mathrm{FSR}_{\mathrm{H2O}}}{\mathrm{FSR}_{\mathrm{CH4}}} = \frac{n_{\mathrm{CH4}}}{n_{\mathrm{H2O}}} = \frac{1.4634}{1.4622} \qquad \text{(C.1)}$$

Therefore for CH_4 laser, the FSR is calculated as 0.0022675 ± 0.0000020cm^{-1}.

Appendix D: Glass Cell and its accessories

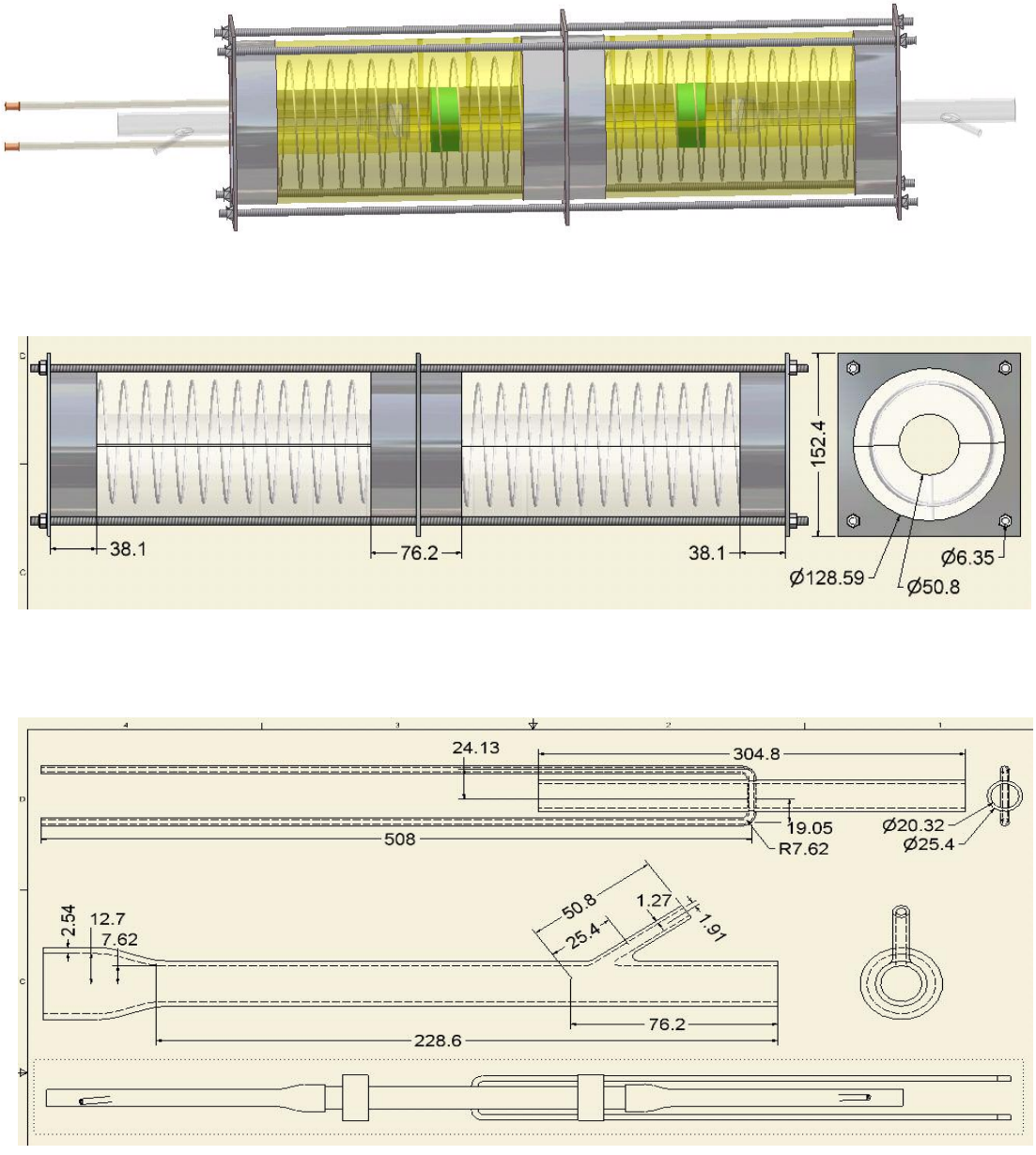

Figure D.1: From top to bottom: Glass Cell and heater assembly, heater dimensions, and Glass Cell and its accessories dimensions

Appendix E: Absolute error analysis for linestrength S_T and pressure broadening coefficient γ

In the following the uncertainty in the linestrength and also pressure broadening coefficients of the selected CH_4 transitions are explained in detail and for H_2O transitions only the results are presented.

E.1 Uncertainty in LineStrength S_T of the CH_4 transitions

From measurements of linestrength S_T can be determined from partial pressure of the absorbing species P_{abs}, the path length, and the wavelength-integrated absorbance over the line, as

$$S_T = \frac{1}{P_{abs} \cdot L} \int \ln\left(\frac{I_0}{I}\right) d\nu \qquad \text{E.1}$$

From this expression the estimated uncertainties ($\Delta P/P$), ($\Delta L/L$), and ($\Delta\alpha/\alpha$), where α is the value of the integral, can be obtained in the usual way

$$\frac{\Delta S_T}{S_T} = \sqrt{\left(\frac{\Delta P}{P}\right)^2 + \left(\frac{\Delta L}{L}\right)^2 + \left(\frac{\Delta \alpha}{\alpha}\right)^2} \qquad \text{E.2}$$

with the uncertainty ($\Delta P/P$)=1%, due to pressure gauge, and estimating ($\Delta L/L$)=0.3% (1 mm in 32.1 cm), and ($\Delta\alpha/\alpha$)=2% from the uncertainty in the fit, we arrive from Equation (E.2) at a combined uncertainty estimate for S_T of 2.3%.

E.2 Uncertainty in the pressure broadening coefficients of the CH_4 transitions

As $\gamma = \frac{\Delta\nu_L}{p}$, one can calculate the relative error in pressure broadening coefficient as

$$\frac{\delta\gamma}{\gamma} = \sqrt{\left(\frac{\delta\Delta\nu_L}{\Delta\nu_L}\right)^2 + \left(\frac{\delta p}{p}\right)^2} \tag{E.3}$$

During the fitting processes, the uncertainty in Voigt half-width $\Delta\nu_v$ and the Doppler half-width $\Delta\nu_D$, is propagated to the Lorentzian half-width $\Delta\nu_L$, by

$$\delta\Delta\nu_L = \sqrt{\left(\frac{\partial\Delta\nu_L}{\partial\Delta\nu_V}\right)^2 (\delta\Delta\nu_V)^2 + \left(\frac{\partial\Delta\nu_L}{\partial\Delta\nu_D}\right)^2 (\delta\Delta\nu_D)^2} \tag{E.4}$$

Using Whitting's expression,

$$\Delta\nu_V = 0.5346\Delta\nu_L + (0.2166\Delta\nu_L^2 + \Delta\nu_D^2)^{0.5} \tag{E.5}$$

one can calculate the derivative terms in Eq. (E.4) as shown in Eqs. (E.6)

$$\frac{\partial\Delta\nu_L}{\partial\Delta\nu_V} = 7.7254 - \frac{6.7257}{\sqrt{1 + 0.3195(\Delta\nu_D/\Delta\nu_V)^2}}$$

$$\frac{\partial\Delta\nu_L}{\partial\Delta\nu_D} = -\frac{2.1488}{\sqrt{0.3195 + (\Delta\nu_V/\Delta\nu_D)^2}} \tag{E.6}$$

In these experiments, the maximum fractional error in pressure broadening $\frac{\delta\gamma}{\gamma}$ occurs at the highest temperature T=952 K, for the N_2 measurement which exhibits the maximum error in $\frac{\delta\Delta\nu_L}{\Delta\nu_L}$. At this condition $\Delta\nu_D = 0.0167\,\text{cm}^{-1}$,

$0.0018 \le \Delta\nu_L \le 0.0057\,\text{cm}^{-1}$, and $0.0177 \le \Delta\nu_V \le 0.020\,\text{cm}^{-1}$, therefore $0.83 \le \frac{\Delta\nu_D}{\Delta\nu_V} \le 0.95$. Using this in Equation (E.6) we get

$$1.64 \le \frac{\partial\Delta\nu_L}{\partial\Delta\nu_V} \le 1.80 \text{, and } 1.94 \le \frac{\partial\Delta\nu_L}{\partial\Delta\nu_D} \le 2.14. \qquad \text{(E.7)}$$

For this condition the maximum error in Voigt half-width, which is due to the limited number of points in each sweep, is estimated as

$$\max \delta\Delta\nu_V = (1/149) * 0.020 = 0.00013\,\text{cm}^{-1} \qquad \text{(E.8)}$$

in which 1/149 represents the relative error in the Voigt half-width corresponding 1 data point error in the 149 points of each collected sweep over the line.

The maximum error in Doppler half-width based on 2% uncertainty in temperature can be calculated as:

$$\delta\Delta\nu_D = 1.79\times10^{-7}\nu_0\sqrt{\frac{1}{TM}}\delta T = 1.79\times10^{-7}\times6057.1\times\sqrt{\frac{1}{16\times952}}\times(0.02\times952) = 0.00017\ \text{cm}^{-1}$$

(E.9)

Using Eq. (E.7), Eq. (E.8), and Eq. (E.9) in Eq. (E.4), the maximum uncertainty in Lorentzian half-width is estimated as

$$\delta\Delta\nu_L = \sqrt{(1.8)^2(0.00013)^2 + (2.14)^2(0.00017)^2} = 0.00043\,\text{cm}^{-1} \qquad \text{(E.10)}$$

For the worst case, the pressure broadening coefficient is calculated based on the maximum absolute error of 0.00043 cm^{-1} over six different pressures. For the rang of pressures studied, the Lorentzian half-width is in the range of $0.0018 \le \Delta\nu_L \le 0.0057$. This means that in the worst case the pressure broadening

coefficient is calculated based on six values for Lorentzian half-widths each having a relative error in the range of $0.075 \le \frac{\delta \Delta \nu_L}{\Delta \nu_L} \le 0.24$.

Taking the maximum relative error in the measured Lorentzian half-width due to temperature and Voigt half-width uncertainty to be the average of range:

$$\max \frac{\delta \Delta \nu_L}{\Delta \nu_L} = 0.16 \qquad \text{(E.11)}$$

From this, the maximum absolute error in pressure broadening coefficient due to 1% uncertainty in pressure, 2% uncertainty in temperature, and 1/149=0.7% in Voigt half-width for the worst case measurement would be:

$$\max \frac{\delta \gamma}{\gamma} = \sqrt{(0.16)^2 + (.01)^2} = 0.16$$

For the lower temperature measurements the absolute error becomes much smaller.

Using the same procedure explained above, the uncertainty in linestrength and pressure broadening coefficients of the selected H_2O transitions are estimated as 7% and 15%, respectively.

Appendix F: Measurement of amplitude of modulation and intensity-frequency parameters

F.1 Calculation of s_{F1}, and s_{F2}

These parameters are directly calculated from the second-order least square fitting of the intensity variation of the ring interferometer signal versus frequency. Since these parameters are normalized with respect to intensity at one of the absorption transitions (for H_2O they are normalized at the absorption peak located between transition 1 and 2, while for CH_4 they are normalized at the absorption peak of the manifold), the absorbance must be calculated in order to determining the location (frequency) where the parameters should be normalized. Typical values of these parameters for H_2O and CH_4 lasers can be found in Appendix A2 and A3 in the C++ program written for modeling the WMS signal of the selected transitions.

F.2 Calculation of amplitude of modulation $\Delta\nu_m$

Amplitude of modulation varies as the laser frequency is tuned over absorption transitions. At a given optical frequency, the amplitude of modulation can be obtained by detecting the ring interferometer signal when the central frequency of laser is fixed, at the given frequency, and only modulation current is applied to the laser. Based on the number of fringes during half cycle of the modulation and also Free Spectral Rang (FSR) of the ring interferometer, the amplitude of modulation $\Delta\nu_m$

can be calculated. Figure F.1 shows the frequency modulation of the H_2O laser around optical frequency of ν_{II}=6771.47 cm^{-1}.

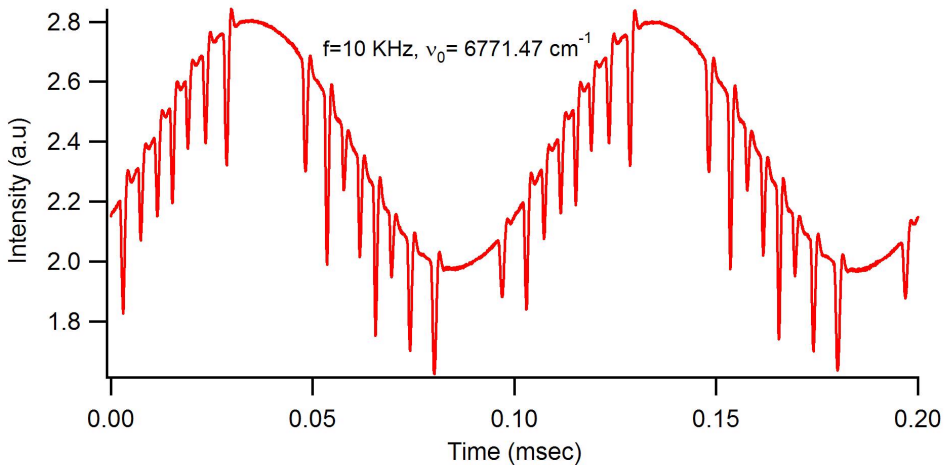

Figure F.1: Ring interferometer signal of the H_2O laser when it is modulated around ν_{II}=6771.47 cm^{-1} at f=10 kHz.

According to this figure, $\Delta\nu_m$ is approximately equivalent to 4FSR but more accurate value of $\Delta\nu_m$ can be obtained by comparing the calculated 2f signal with experiments at known condition. In this case, by only adjusting the $\Delta\nu_m$ in the modeling, and comparing the results with measured 2f signal at known condition, $\Delta\nu_m$ can be calculated more precisely.

F.3 Calculation of s_f

For calculating s_f, it is needed the ring interferometer signal at a given optical frequency is measured at the ramp frequency (see Figure F.2). Comparing this signal with corresponding signal at modulation frequency (such as the signal shown in Figure F.1), and also the calculated value for s_{F1}, as explained in section F.1, this parameter can be calculated.

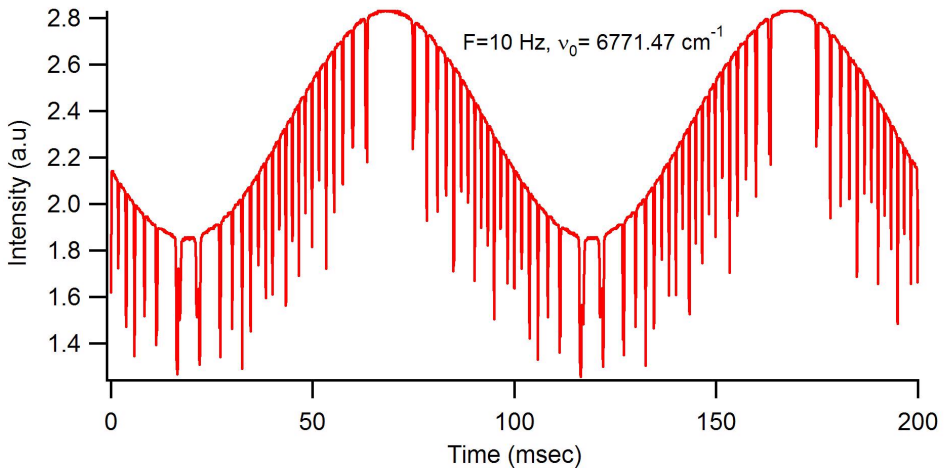

Figure F.2: Ring interferometer signal of the H_2O laser when it is modulated around ν_{II}=6771.47 cm^{-1} at F=10 Hz.

Then s_f, can be calculated by

$$s_f = S_{F1} \frac{\Delta \nu_m\big|_F}{\Delta \nu_m\big|_f} \cdot \frac{\Delta I\big|_f}{\Delta I\big|_F} \qquad \text{(F.1)}$$

where, subscripts f and F represent calculated parameters when the modulation frequency is f and F, respectively. ΔI represents amplitude of intensity modulation (amplitude of intensity as shown in Figures F.1 and F.2 without considering fringes). Calculated values of s_f can be found in the written C++ program for modeling 2f signal presented in Appendixes A2 and A3.

F.4 Calculation of phase between frequency and intensity modulation ψ

Based on Equation (4.19), the detection phase θ is adjusted such that the magnitude of the measured 2f signal at the center of a particular transition frequency becomes maximum. At this condition, based on the measured $\theta_{2,\max}$, using Equation (4.19) one can calculate ψ.

The measured values of ψ for H_2O and CH_4 lasers at the selected modulation frequencies (10 kHz for H_2O laser and 12 kHz for CH_4 laser) are -15^o and 140^o, respectively.

Appendix G: Temperature correction of the thermocouple measurements for radiation loss

The in-flame temperature measurement using thermocouple must be corrected for radiation loss. The method of temperature correction used in this dissertation was based on a information presented in a paper by Weissweiler (Weissweiler 1994). According to this method, the corrected temperature T_c (in K) is calculated by

$$T_c = T_d + \frac{\varepsilon \cdot \sigma \cdot d \cdot T_d^4}{2 \cdot \lambda} \cdot A \qquad \text{G.1}$$

where T_d is measured (displayed) temperature in K, λ (in W/mK) is thermal conductivity of the thermocouple wire, d is bead diameter (in m), ε is the emissivity, and σ is Boltzmann constant (σ = 5.67×10^{-8} W/m^{2}K^4) and A is the view factor. The thermal conductivity of the type R thermocouple at temperature T_d is calculated from (1994)

$$\lambda = 4.6942\times10^{-3} + 8.1225\times10^{-5}T_d - 1.4547\times10^{-8}T_d^2 \qquad \text{G.2}$$

For the in-flame measurement, explained in Chapter 6, type-R thermocouples with a thinness of 0.008 in. were used. In that experiment, the view factor of A=1 is considered as the surrounding temperature around the bid was almost the same as room temperature. The emissivity of type-R thermocouple is approximately 0.2. The bid diameter based on the manufacturer specification sheet is 2.5 of the wire diameter. Therefore, d =$2.5\times0.008\times0.0254=5.1\times10^{-4}$ m.

The corrected temperature T_c for one the measured values of T_d =1693 K is calculated in the following.

$$\lambda = 4.6942\times10^{-3} + 8.1225\times10^{-5}T_d - 1.4547\times10^{-8}T_d^2$$

$$= 4.6942\times10^{-3} + 8.1225\times10^{-5}(1693) - 1.4547\times10^{-8}(1693)^2 = 0.108\ \text{W/mK}$$

Using the calculated thermal conductivity at T_d =1693 K, the corrected temperature is calculated by

$$T_c = 1693 + \frac{0.2\times5.67\times10^{-8}\times5.1\times10^{-4}\times1693^4}{2\times0.108}\times1$$

$$= 1693\,\text{K} + 220\,\text{K} = 1913\,\text{K}$$

This procedure was applied for all in-flame temperature measured by thermocouples and their corresponding corrected temperatures were calculated.

References

Abramowitz, M. and I. A. Stegun (1972). Handbook of Mathematical Functions. Dover, New York.

Allen, M. G. (1998). "Diode Laser Absorption Sensors for Gas-Dynamic and Combustion Flows." Measurement Science and Technology 9: 545-562.

Allen, M. G. and W. J. Kessler (1996). "Simultaneous water vapor concentration and temperature measurements using 1.31 um diode lasers." AIAA 34: 483-8.

Arndt, R. (1965). "Analytical line shapes for Lorentzian signals broadened by modulation." J. of Applied Physics 36: 2522-2524.

Arroyo, M. P. and R. K. Hanson (1993). "Absorption measurements of water-vapor concentration, temperature and line-shape parameters using a tunable InGaAsP diode laser." Applied Optics 32: 6104-16.

Avetisov, V. G. and P. Kauranen (1996). "Two-tone frequency-modulation spectroscopy for quantitative measurements of gaseous species: theoretical, numerical, and experimental investigation of line shapes." Applied Optics 35: 4705-4723.

Avetisov, V. G. and P. Kauranen (1997). "High-resolution absorption measurements by use of two-tone frequency-modulationspectroscopy with diode lasers." Applied Optics 36: 4043-4054.

Baer, D. S., R. K. Hanson, et al. (1994). "Multiplexed Diode-Laser Sensor System for Simultaneous H2o, O-2, and Temperature-Measurements." Optics Letters 19(22): 1900-1902.

Baer, D. S., V. Nagali, et al. (1996). "Scaned- and fixed-wavelength absorption diagnostics for combustion measurements using multiplexed diode lasers." AIAA 34: 489-93.

Bernath, P. F. (1995). Spectra of atoms and molecules. New York, Oxford University Press.

Bomse, D., J. A. Silver, et al. (1992). "Frequency modulation and wavelength modulation spectroscopes: Comparison of experimental methods using a lead-salt diode laser." Applied Optics 31: 718-731.

Brown, L. R., D. C. Benner, et al. (2003). "Methane line parameters in HITRAN." J. of Quantitative Spectroscopy & Radiative Transfer 82: 219-238.

CHou, S. L., D. S. Baer, et al. (1997). "Diode Laser Absorption Measurements of CH3CL and CH4 near 1.65 micrometers." Applied Optics 36(15): 3288-3293.

Cooper, D. E. and T. F. Gallagher (1985). "Double frequency modulation spectroscopy: high modulation frequency with low-bandwidth detectors." Applied Optics 24: 1327-1334.

Cooper, D. E. and R. E. Warren (1987). "Two-tone optical hetrodyne spectroscopy with diode lasers: theory of line shapes and experimental results." J. Opt. Soc. Am. B 4: 470-480.

Darnton, L. and J. S. Margolis (1973). Journal of Quantitative Spectroscopy & Radiative Transfer 13: 969-976.

Dore, L. (2003). "Using Fast Fourier Transform to compute the line shape of frequency-modulated spectral profiles." J. of Molecular Spectroscopy 221: 93-98.

Durry, G. and G. Megie (1999). "Atmospheric CH4 and H2O monitoring with near-infrared InGaAs laser diodes by the SDLA, a balloonborne spectrometer for tropospheric and stratospheric in situ measurement." Applied Optics 38: 7342-7354.

Feher, M. and P. A. Martin (1995). "Tunable Diode Laser Monitoring of Atmospheric Trace Gas Constituents." Spectrochemica Acta, Part A 51: 203-210.

Gehrtz, M., W. Lenth, et al. (1986). "High frequency-modulation spectroscopy with a lead-salt diode laser." Optics Letters 11: 132-134.

Gharavi, M. and S. G. Buckley (2004). "Single Diode Laser Sensor for Wide-Range H_2O and Temperature Measurements." Applied Spectroscopy 58(4): 468-473.

Gharavi, M. and S. G. Buckley (2005). "Diode laser absorption spectroscopy measurement of linestrengths and preasure broadening coefficients of the methane 2nu3 band at elevated temperature." J. of Molecular Spectroscopy 229: 78-88.

Hanson, R. K., P. A. Kuntx, et al. (1977). "High-resolution pectroscopy of combustion gases using a tunable IR diode laser." Applied Optics 16: 2045-7.

Henkley, E. D. (1976). Opt. And Quantum Electron. 8: 155-167.

Ikeda, Y., D.-H. Chung, et al. (2001). Laser Techniques Applied to Fluid Mechanics, Springer-Verlag.

Janik, G., C. Carlise, et al. (1985). "Frequency modulation spectroscopy with second harmonic detection." Applied Optics 24: 3318-3319.

Janik, G. R., C. B. Carlisle, et al. (1986). "Two-tone frequency-modulation spectroscopy." J. Opt. Soc. Am. B 3: 1070-1074.

Jin, W., Y. Z. Xu, et al. (1997). "Investigation of interferometric noise in fiber-optic gas sensors with use of wavelength modulation spectroscopy." Applied Optics 36: 7239-7246.

Kluczynski, P. and O. Axner (1999). "Theoritical description based on Fourier analysis of wavelength-modulation spectrometry in terms of analytical and background signals." Applied Optics 38(27): 5803-5815.

Kluczynski, P., A. M. Lindberg, et al. (2001). "Background signals in wavelength-modulation spectrometry with frequency-doubled diode-laser light. I. Theory." Applied Optics 40(6): 783-793.

Kluczynski, P., A. M. Lindberg, et al. (2001). "Background signals in wavelength-modulation spectrometry with frequency-doubled diode-laser light. II. Experiment." Applied Optics 40(6): 794-805.

Ku, R. T. and E. D. Hinkley (1975). Applied Optics 14: 854-861.

Lenth, W. (1983). "Optical heterodyne spectroscopy with frequency and amplitude-modulated semiconductor lasers." Optics Letters 11: 575-577.

Lenth, W. (1984). "High frequency heterodyne spectroscopy with current-modulated diode lasers." IEEE J. of Quantum Electron. QE-20: 1045-1050.

Lenth, W., C. Ortiz, et al. (1982). "Frequency modulation excitation spectroscopy." Opt. Commun. 41: 369-373.

McQuarrie, D. A. and J. D. Simon (1997). Physical chemistry : a molecular approach. Sausalito, Calif., University Science Books.

Mihalcea, R. M., D. S. Baer, et al. (1998). "Advanced Diode Laser Absorption Sensor for In Situ Combustion Measurements of CO_2, H_2O, and Gas Temperature." Proceedings of the Combustion Institute 27: 95-101.

Mihalcea, R. M., M. E. Webber, et al. (1998). "Diode-laser absorption measurements of CO2, H2O, N2O, and NH3 near 2.0 µm." Applied Physics B 67: 283-288.

Milhalcea, R. M., D. S. Baer, et al. (1997). "Diode Laser Sensor for measurements of CO, CO2, and CH4 in Combustion Flows." Applied Optics 36(36): 8745-8752.

MIT(website) "http://ocw.mit.edu/NR/rdonlyres/Chemistry/5-33Advanced-Chemical-Experimentation-and-InstrumentationFall2002/97B37CC7-4463-4D39-8A6F-89856ECF8A8A/0/spec5.pdf."

Nagali, V., S. I. Chou, et al. (1996). "Tunable Diode Laser Measurements of Methane at Elevated Temperatures." Applied Optics 35(21): 4026-4032.

Nagali, V., S. L. Chou, et al. (1996). "Tunable diode-laser absorption measurements of methane at elevated temperatures." Applied Optics 35: 4026-4032.

Nagali, V., E. R. Furlong, et al. (1995). presented at the 31st Joint Propulsion Conference, San Diego, CA, 1995 (unpublished).

Nagali, V., E. R. Furlong, et al. (1995). Diode-Laser Sensor System for Multi-Species and Multi-Parameter Measurements in Combustion Flows. 31st Joint Propulsion Conference, San Diego, CA.

Nelson, D. D. (1998). "Tunable Diode Laser System for the remote sensing of On-Road Veicle Emissions." Applied Physics B 67(4): 433-441.

Olivero, J. J. and R. L. Longbothum (1977). "Empirical fits to the Voigt line width: A brief review." J. Quant. Spectr. Rad. Trans. 17: 233.

Philippe, L. C. and R. K. Hanson (1993). "Laser diode wavelength-modulation spectroscopy for simultanious measurement of temperature, pressure, and velocity in shock-heated oxygen flows." Applied Optics 32(30): 6090-6103.

Pokrowsky, P., W. Zapka, et al. (1983). "High frequency wavelength spectroscopy with diode lasers." Opt. Commun. 44: 175-179.

Reid, J. and D. Labrie (1981). "Second-harmonic detection with tunable diode lasers - comparison of experiment and theory." Applied Physics B 26: 203-210.

Rothman, L., C. Rinsland, et al. (1998). "The HITRAN Molecular Spectroscopic Database and HAWKS (HITRAN Atmospheric Workstation." J Quant. Spectrosc. Radiat. Transfer 60: 665-710.

Rothman, L. S., A. Barbe, et al. (2003). "The HITRAN molecular spectroscopic database: edition of 2000 including updates through 2001." Journal of Quantitative Spectroscopy & Radiative Transfer 82: 5-44.

Schilt, S., L. Thevenaz, et al. (2003). "Wavelength modulation spectroscopy: combined frequency and intensity modulation." Applied Optics 42(33): 6728-6738.

Silver, J. A. (1992). "Frequency-modulation spectroscopy for traces species detection: theory and comparison among experimental methods." Applied Optics 31: 707-717.

Steele, R. (1997). "1997 Review and forecasts of laser markets, part II." Laser Focus World: 84-107.

Stokes, L. E., M. Chodorow, et al. (1982). "All-single-mode fiber resonator." Optical Society of America 7(6): 288-290.

Uehara, K. and H. Tai (1992). "Remote detection of metane using a 1.66 µm diode laser." Applied Optics 31: 809-814.

Varanasi, P. and S. Chudamani (1989). "Measurements of Collision-Broadened Line Widths in the n_4 - Fundamental Band of CH_4 C^{12} at Low Temperatures." Journal of Quantitative Spectroscopy & Radiative Transfer 41(5).

Verein Deutscher Ingenieure, VDI-Warmeatlas, 7. erweiterte Auflage (1994).

Wahlquist, H. (1961). "Modulation braodening of unsaturated lorentzian lines." Journal of Chemical Physics 35(5): 1708-1710.

Weissweiler, T. (1994). Measurements of stable species and soot volume fraction in a propane-air counterflow diffusion flame, RWTH Aachen, Germany.

Whiting, E. (1968). "An empirical approximation to the Voigt profile." J. Quant. Spectr. Rad. Trans. 8(6): 1379-1384.

Whittaker, E. A., C. M. Shum, et al. (1988). "Reduction of residula amplitude modulation in frequency-modulation spectroscopy by using harmonic frequency modulation." J. Opt. Soc. Am. B 5: 1253-1256.

Wilson, G. V. H. (1963). "Modulation Broadening of NMR and ESR Line Shapes." J. of Applied Physics 34: 3276-3285.